Star Formation in Massive Protoclusters and First Exploration of Environmental Dependence

Yu Cheng
Hebei, China

B.A. Astronomy, Nanjing University, 2015
M.S. Astronomy, University of Virginia, 2018

A Dissertation Presented to the
Graduate Faculty of the
University of Virginia
in Candidacy for the Degree of
Doctor of Philosophy

Department of Astronomy

University of Virginia
July 2021

Committee Members:
Jonathan Tan
John Tobin
Zhi-Yun Li
Catherine Dukes

Abstract

While it now known that most stars are born in relatively massive clusters, i.e., with masses $\gtrsim 1000\,M_\odot$, several fundamental questions remain open, including "what is the timescale of the process?" and "what sets the star formation efficiency?" Furthermore, there is no consensus on a general theory that predicts the outcome of star formation, e.g., the stellar initial mass function (IMF) or multiplicity/clustering properties, from given interstellar medium conditions. Development of such a theory requires testing by observations of forming clusters that span a wide range of environments and evolutionary stages. Now with the unprecedented sensitivity and resolution provided by facilities like the Atacama Large Mm/sub-mm Array (ALMA) and the forthcoming James Webb Space Telescope (JWST), it is possible to study star cluster formation in detail — star by star — in relatively distant regions throughout our Galaxy.

In this dissertation, I first present a case study of massive star cluster formation in G286.17+0.14 (hereafter G286), which is located at a distance of 2.5 $\pm$ 0.3 kpc in the Carina spiral arm. We have conducted a multi-wavelength survey with facilities including ALMA (millimeter) and Hubble Space Telescope (HST)/ Very Large Telescope (VLT) / Gemini (near-infrared [NIR]). This allows us to trace both the gas/dust component and the young stellar object (YSO) population. From the mm continuum we identified about 100 cores and derived the Core Mass Function (CMF). For $M \gtrsim 1\ M_\odot$, the fiducial dendrogram-identified CMF can be fit with a power law

of the form $\mathrm{d}N/\mathrm{dlog}M \propto M^{-\alpha}$ with $\alpha \simeq 1.24 \pm 0.17$, which is slightly shallower than, but still consistent with, the index of the Salpeter stellar IMF of 1.35. This further strengthens the case of a correspondence between CMF and IMF that has been seen previously in local regions, but now is found in a more distant, massive protocluster. The kinematics and dynamics of the gas in G286 was studied using spectral lines, including $C^{18}O(2-1)$ and those from deuterated species like N_2D^+, DCO^+ and DCN. The 0.02-pc-scale dense cores, and pc-scale filamentary structures in G286 show internal kinematics that are consistent with being in virial equilibrium. However, the velocity distribution of the whole cloud appears to be composed of two spatially distinct velocity groups, indicating that the dense molecular gas has not yet relaxed to virial equilibrium, perhaps due to there being recent or continuous infall into the system. With multi-epoch HST J/H band data we also characterize the stellar variability of the young stars. By comparing the NIR photometry for data taken in 2014 and 2017 for around 6000 stars, we found significant variability in about 7% of the sample. This percentage is higher (14%) for objects that show NIR color signatures of having a protostellar disk. An object with extreme variability was also found, with a K band brightening of 3.5 magnitudes. Follow-up observations indicate this object is a very low mass ($<0.12M_\odot$) example of an FU Ori type (accretion burst) source, which would be the lowest mass example of this class.

In the next part of the thesis I explore the environmental dependence of star formation by extending the developed analysis methods to other regions. One example is the Center Ridge Clump (CRC) of the Vela C giant molecular cloud (GMC). This dense clump was selected as showing the lowest level of sub-mm polarization angle dispersion in BLASTPOL mapping of the region and so is expected to be strongly magnetized. We have characterized the dense cores in the CRC with ALMA band 6 (1.3 mm) and 7 (0.87 mm) observations. We identified 11 dense cores from their continuum emission, with masses ranging from 0.1 to 4.5 $M_\odot$. Their deuteration ratios, determined from N_2H^+(3-2) and N_2D^+(3-2), span from 0.09 to 1.28, with the latter being one of the highest values yet measured. These ratios appear to be a good tracer of core evolution. Overall this region has a relatively low dense gas fraction compared with other typical clouds with similar column densities, which may be a result of its strong magnetic field.

As an attempt to extend the analysis to different environments and also study the detailed star formation process on protostellar disk scales, we also present ALMA band 6 and 7 and VLA Ka band (9 mm) observations toward NGC 2071 IR, an intermediate-mass star formation region in the L1630 cloud of Orion B. We characterize the continuum and associated molecular line emission towards the most luminous protostars, i.e., IRS1 and IRS3, as well as other protostellar objects, on $\sim$ 40 au scales. IRS1 is partly resolved in millimeter and centimeter continuum and shows a potential disk. IRS3 has a clear disk appearance in millimeter continuum and is further resolved into a binary system in our 9 mm map. Both sources exhibit clear velocity gradients across their protostellar disks in multiple spectral lines. We use an analytic method to fit the Keplerian rotational motion of the disks, and derive constraints on physical parameters, such as the dynamical mass of the central object. For both IRS1 and IRS3, the inferred ejection directions from different tracers, including radio jets, water masers, molecular outflows and H_2 emission, are not always consistent and can be misaligned by up to $\sim$50°. IRS3 is better explained by a single precessing jet with its axis wiggling over a range of position angles. A similar mechanism may be present in IRS1, but unresolved multiplicity is also a possibility.

We conclude with a discussion of the prospects for extending such studies of star formation, where individual stars and disks are characterized across the full range of the mass spectrum, to other regions in the Galaxy.

Acknowledgements

I want to thank my advisor Jonathan Tan, for his instructions and guidance throughout my graduate career. His passion and enthusiasm for research are contagious. I have always been benefiting from his insightful feedback and comments. I am also very lucky to have John as my Reber fellow supervisor. I appreciate his encouragement and patience when we work together and I have learned a lot from the inspiring discussions. I also want to express my appreciation to Zhi-Yun Li, for his helpful comments and advice on my research, and always-in-time reply of emails whenever I'm in trouble. The thanks also extend to Dukes Catherine, who kindly serves on my committee and provides helpful comments. And special thanks to the Astronomy Department and Graduate School of Arts & Sciences for allowing me to work remotely overseas during the pandemic.

Thanks to Morten Andersen, my collaborator and host during my visit in Gemini South. It was a wonderful trip in Chile. Thanks to Keping Qiu, my undersgraduate supervisor, for the helpful suggestions on my academic career and kind host every time I visit Nanjing. Thanks to all my academic colleagues, which I can never exhaustively list, Xing Walker, Yao-Lun, Ruben, Juan, Wanggi, Kei, Yichen, Viviana, Junhao, Shuo... for their generous share of knowledge and expertises. I'm grateful for my cohort and friends in Charlottesville, Gainsville as well as in Nanjing, Mengyao, Xiaoshan, Yiqing, Ci, Xinlun, Pallavi, Chenxing, Yuzhu, Xiao, Bo, Shuang and many

many others - I can always recall many beautiful memories with you guys together. Thank my family for your unconditional love and support, even without knowing much what exactly I am doing... Also thank Emily for your company. I hope you would not gain too much weight next time I see you - it is not healthy.

Table of Contents

List of Figures

List of Tables

Chapter 1

Introduction

1.1 Overview of Star Cluster Formation

Most stars are born in relatively massive ($\gtrsim 1000\,M_{\odot}$) clusters (e.g., Lada & Lada, 2003; Gutermuth et al., 2009), which are thus the basic building blocks of galaxies. Star clusters originate from a large reservoir of gas and dust, i.e., the protocluster "clump", which is typically part of a giant molecular cloud (GMC). The formation process is thought to be controlled by an intricate interplay between the self-gravity of the interstellar medium and various opposing agents, such as turbulence, magnetic fields, and mechanical and radiative feedback. Despite the efforts in observations and simulations (e.g., Krause et al., 2020), several fundamental questions about star cluster formation are still debated, including: "what is the timescale of the process?"; "what sets the star formation efficiency?"; and "do clusters form via a monolithic collapse or a collection of mergers of subclusters?" These affect the ability of a cluster to remain gravitationally bound, which on large scales influences global interstellar medium (ISM) feedback, e.g., concentrated feedback from clusters can create superbubbles (e.g., Krause et al., 2013) and on small scales controls the feedback environments and tidal perturbations of protoplanetary disks (Adams, 2010).

Tan et al. (2006) and Nakamura & Li (2007) proposed that formation times are relatively long compared to the local free-fall time, especially for those clusters with high ($\gtrsim$30%) overall star formation efficiency, since simulations of self-gravitating, turbulent, magnetized gas show low formation efficiency of just $\sim$2% per free-fall time (Krumholz & McKee, 2005; Padoan & Nordlund, 2011). Such gas would take many, $\gtrsim$10, local free-fall times to build up the high, $\gtrsim$20%, total efficiencies observed in many systems (e.g., Lada & Lada, 2003), such as the Orion Nebula Cluster (ONC). Note, efficiencies $\sim$30% are needed to create a gravitationally bound cluster if gas dispersal is gradual (e.g., Lada et al., 1984). If the formation time is long compared to the free-fall time, then the system of stars and gas has time to approach approximate virial equilibrium, with important implications for the conditions of the gas from which most stars and planetary systems form.

On the other hand, Elmegreen et al. (2000); Elmegreen (2007); Hartmann & Burkert (2007) and Hartmann et al. (2012) have argued for cluster formation in just one or a few free-fall times. In high star formation efficiency clusters this would require the gas to form stars with $\gtrsim$10% efficiencies per free-fall time, which is possible only if turbulence has dissipated. The gas is then undergoing rapid global collapse and the proper motions of stars formed from this gas will show distinct, correlated kinematic signatures of this infall.

Overall, there is no consensus on a general theory that predicts the outcome of star formation, e.g., the stellar initial mass function (IMF) or multiplicity/clustering properties, from given ISM conditions. Development of a complete theory of star formation requires testing by observations that span a wide range of environments and evolutionary stages, while still resolving units of star formation, i.e., self-gravitating gas cores and individual stars.

1.2 Characterization of the Gas/Dust Component

1.2.1 Core Mass Function

Stars are known to form from cold dense cores in molecular clouds. These "prestellar cores" can be defined theoretically as gravitationally-bound, local density maxima that collapse via a single rotationally-supported disk into a single star or small N multiple. In the context of Core Accretion models (e.g., Padoan & Nordlund, 2002; Padoan et al., 2007; McKee & Tan, 2003; Hennebelle & Chabrier, 2008; Kunz & Mouschovias, 2009), the stellar mass is assumed to be related to the mass of its parental core, modulo a relatively constant core to star formation efficiency, $\epsilon_{\rm core}$, perhaps set mostly by outflow feedback (Matzner & McKee, 2000; Zhang et al., 2014), with radiative feedback expected to influence only the most massive stars (Tanaka et al., 2017). In this framework, we expect the stellar IMF to be strongly influenced by the prestellar CMF, i.e., the PSCMF. However, there are alternative models, especially Competitive Accretion (Bonnell et al., 2001; Bate, 2012), which explain the IMF without a CMF that extends to higher masses. Therefore, the study of the CMF, and ideally the PSCMF, is crucial for understanding the origin of the IMF and its connection to the large-scale physical and chemical conditions of molecular clouds.

Early observations based on submillimeter dust continuum emission(e.g., Motte et al., 1998; Testi & Sargent, 1998; Johnstone et al., 2000) found evidence for an approximately log-normal CMF peaking near $\sim 1\,M_\odot$, with a power law tail at higher masses of the form

$$\frac{{\rm d}N}{{\rm dlog}M} \propto M^{-\alpha}. \tag{1.1}$$

These studies found values of $\alpha \simeq 1.0$ to 1.5, based on samples of several tens of sources. In this form, the Salpeter (1955) $\gtrsim 1\,M_\odot$ power law description of stellar masses has an index $\alpha = 1.35$, indicating a potential similarity of the CMF and IMF. Alves et al. (2007) used NIR dust extinction to characterize about 160 cores to find similar results, with the peak of the CMF now better measured close to $1\,M_\odot$ and the CMF suggested to be a simple translation of the IMF requiring $\epsilon_{\rm core} \simeq 0.3$ (see Figure 1.1). More recent results from the Gould Belt Survey with *Herschel*, *Spitzer* and the James Clerk Maxwell Telescope (JCMT) have also detected samples of hundreds of cores (e.g., André et al., 2010; Sadavoy et al., 2010; Salji et al., 2015; Marsh et al., 2016) and have added to the evidence for a similarity in shape of the CMF and IMF.

Extending to more distant ($\gtrsim 2$ kpc), high-mass star-forming regions has been more challenging, in particular requiring higher angular resolution interferometric observations. Beuther et al. (2004) (see also Rodón et al., 2012) reported a CMF of 1.3 mm emission cores in IRAS 19410+2336 ($d \sim 2$ kpc) with $\alpha \simeq 1.5 \pm 0.3$, based on a sample of 24 sources ranging in mass from $\sim 2 - 25\,M_\odot$. Bontemps et al. (2010) detected a similar number of sources in Cygnus X ($d = 1.7$ kpc), but these were identified from the follow-up of five quite widely-separated clumps, so that the CMF was not derived from uniform mapping of a contiguous region. Zhang et al. (2015) studied the core population via 1.3 mm emission in the Infrared Dark Cloud (IRDC) G28.34 P1 clump ($d \simeq 5$ kpc) with ALMA, finding 38 cores. They concluded there was a dearth of lower-mass ($\sim 1 - 2\,M_\odot$) cores compared to the prediction resulting from a scaling down to these masses with a Salpeter mass function. Ohashi et al. (2016) studied the IRDC G14.225-0.506 ($d = 2$ kpc) CMF via 3 mm emission with ALMA at $\sim 3''$ resolution, identifying 48 sources with the clumpfind algorithm (Williams et al., 1994) from two separate fields. They derived $\alpha = 1.6 \pm 0.7$, with the masses ranging from $1.5 - 22\,M_{\odot}$.

1.2.2 Kinematics and Dynamics

From the observational side, measuring the structural and kinematic properties of the dense gas component in the protocluster is needed to provide constraints for different theoretical models. Previously, Walsh et al. (2004) found small velocity differences between dense cores and surrounding envelopes for a sample of low-mass cores. Kirk et al. (2007, 2010) surveyed the kinematics of over 150 candidate dense cores in the Perseus molecular cloud with pointed N_2H^+ and $C^{18}O$ observations and found subvirial core to core velocity dispersions in each region. A similar small core velocity dispersion was also found in the Ophiuchus cloud (André et al., 2007). Qian et al. (2012) searched for ^{13}CO cores in the Taurus molecular cloud and found the core velocity dispersion exhibits a power-law behavior as a function of the apparent separation, similar to Larson's law for the velocity dispersion of larger scale molecular gas, which suggests the formation of these cores has been influenced by large-scale turbulence.

With the unprecedented sensitivity and spatial resolution of ALMA, more light has been shed on massive star forming regions from the "clump" scale (of about a few parsecs) to the "core" scale (~ 0.01 to 0.1 pc) (e.g., Beuther et al., 2017; Fontani et al., 2018; Lu et al., 2018). Multiple coherent velocity components from filamentary structures have been reported in some massive IRDCs (Henshaw et al., 2013, 2014; Sokolov et al., 2018), similar to the structures seen in the nearby Taurus region by Hacar et al. (2013). "Hub-filament" systems have also been reported in some massive star forming regions across a variety of evolutionary stages, perhaps indicating presence of converging flows that channel gas to the junctions where star formation is most active (e.g., Hennemann et al., 2012; Peretto et al., 2014; Lu et al., 2018; Yuan

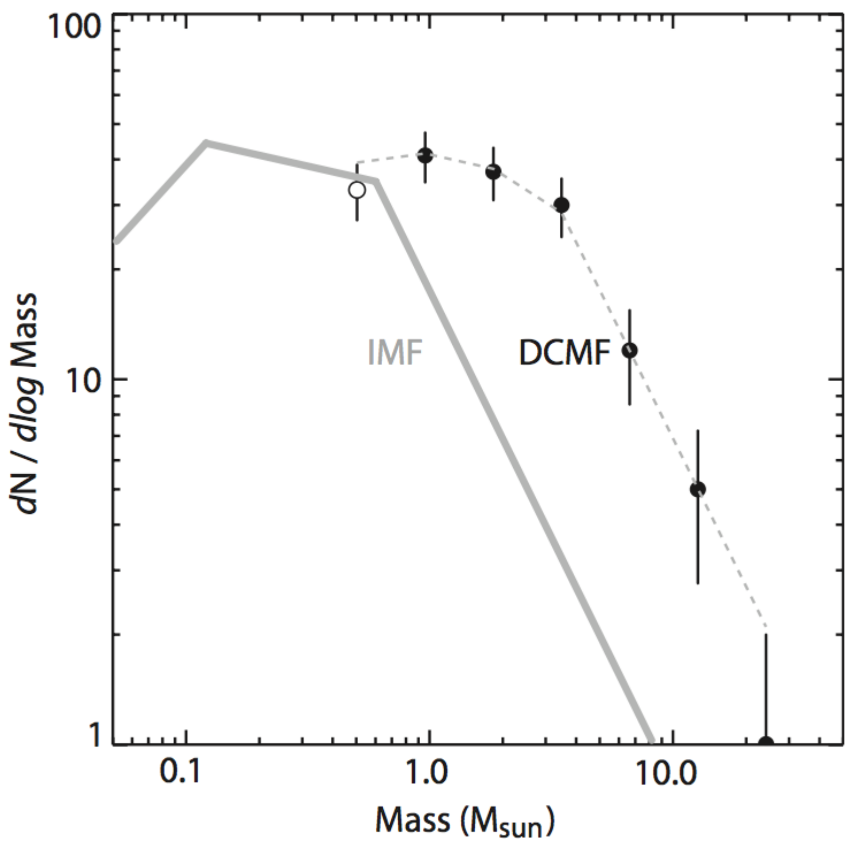

Figure 1.1: Adapted from Alves et al. (2007). Mass function of dense molecular cores plotted as filled circles with error bars. The grey line is the stellar IMF for the Trapezium cluster (Muench et al. 2002). The dashed grey line represents the stellar IMF in binned form matching the resolution of the data and shifted to higher masses by about a factor of 4. The dense core mass function is similar in shape to the stellar IMF function, apart from a uniform star formation efficiency factor.

et al., 2018). However, complete surveys for the dense gas component of massive protoclusters down to the individual core scale, are still rare (e.g., Ohashi et al., 2016; Ginsburg et al., 2017) and a large spatial dynamic range is required to perform a multi-scale kinematics analysis.

1.3 Individual Star Formation

The formation and evolution of star clusters is a multi-scale process that includes formation of the constituent individual stars. For isolated low-mass star formation, the core accretion model has become well established (Shu et al., 1987), which includes evolution in four stages: first, cores form within molecular clouds as magnetic support is lost through ambipolar diffusion; second, a protostar with a surrounding disk forms at the center of a cloud core collapsing from the inside-out; third, a protostellar outflow breaks out along the rotational axis of the system, creating a bipolar outflow; fourth, the infall terminates, revealing a newly formed star with a circumstellar disk.

Unlike the case for low-mass stars, a complete and detailed picture for high mass star formation is not firmly established, mainly due to the difficulty of observations toward massive star formation given the typically large distances and high extinction of the regions. High mass stars are defined as those with masses $> 8\ M_\odot$, have luminosities $> 10^3\ L_\odot$ and main sequence spectral types of B3 or earlier (e.g., Martins et al., 2008). Given their powerful radiative, mechanical and chemical feedback to their environment, massive stars impact a vast range of scales and processes, from the evolution of galaxies to the formation of planets around low-mass stars in the same cluster or association. Formation theories range from Core Accretion (e.g., McKee & Tan, 2003), in which massive stars form via collapse of a massive core, to Competitive Accretion (e.g., Bonnell et al., 2001), in which massive stars have most of the mass reservoir joining later and form hand in hand with the formation of a cluster of mostly low-mass stars.

Intermediate-mass protostars can be observationally defined as having luminosities between ~ 50 and 2000 $L_\odot$ and will eventually reach final masses of 2 to 8 $M_\odot$ (Beltrán, 2015). Intermediate-mass protostars constitute the link between low- and high-mass protostars, and hence provide a natural laboratory to test star formation theories that unify the two mass regimes. Unlike their low-mass counterparts, intermediate-mass stars produce significantly more UV photons and tend to form in more densely clustered environments (e.g., Fuente et al., 2007). In observational terms, intermediate-mass star-forming regions are on average closer and less extincted than high-mass ones, making it easier to trace the primordial configuration of the molecular cloud and to study the earliest stages of star formation.

1.4 Characterization of Young Stellar Populations

1.4.1 Initial Mass Function

A star's mass at birth, or "inital mass", determines its evolution, lifetime and iteraction with the surrounding environment. The shape of the IMF and whether it is universal are important topics in modern astrophysics. An accurate parameterized description of the IMF is a crucial sub-grid input in simulations of star and galaxy formation from star cluster to cosmological scales. For example, the IMF is a key ingredient in our understanding of the chemical evolution of galaxies and the mass-to-light ratios of unresolved stellar populations. Finally, any successful theory of star formation needs to be able to reproduce the IMF and predict whether it varies or not.

Salpeter (1955) proposed a functional description of IMF of the form

$$\frac{dN}{d\log M} \propto M^{-\alpha}, \tag{1.2}$$

where M is the mass and $\alpha = 1.35$. Other commonly used functional forms to described the IMF include the Kroupa IMF (Kroupa & Boily, 2002), which is a piecewise powerlaw function:

$$\frac{dN}{d\log M} \propto \begin{cases} M^{0.7\pm0.7}, 0.01 \ M_\odot \leq M < 0.08 \ M_\odot \\ M^{-0.3\pm0.5}, 0.018 \ M_\odot \leq M < 0.50 \ M_\odot \\ M^{-1.3\pm0.3}, 0.5 \ M_\odot \leq M, \end{cases} \tag{1.3}$$

and the Chabrier IMF (Chabrier, 2005), which connects a lognormal at the low-mass end to a high-mass power law tail:

$$\frac{dN}{d\log M} \propto \begin{cases} exp\left[-\frac{(logM - log0.2)^2}{2\times0.55^2}\right], M \leq 1 \ M_\odot \\ M^{-1.35}, M > 1 \ M_\odot. \end{cases} \tag{1.4}$$

Continuing efforts have been made on both observational and theoretical sides to measure and understand the shape of the IMF. Observations in nearby clusters have revealed remarkably universal IMFs (Bastian et al., 2010), which appear to follow a Salpeter power law index above 1 $M_\odot$. Such a scale-free power law has been proposed to result from competitive accretion models (e.g., Bate, 2005; Bonnell et al., 2007; Bate, 2009) or from turbulence-driven fragmentation models (e.g., Padoan & Nordlund, 2004; Hennebelle & Chabrier, 2008). In local regions, the IMF turns over with a peak near 0.25 $M_\odot$. The cause for the turnover is uncertain. For example, it may be due to suppression of forming such low-mass pre-stellar cores (PSCs) (Bate, 2009; Krumholz et al., 2011) or from the heating effects associated with local feedback (Krumholz et al., 2014).

However, in spite of much progress in measuring the IMF, its origin and environmental dependence are still under active debate. For example, the universality of the IMF is a conclusion mostly made from observations in the Solar neighborhood. In contrast, recent observations give some hints about possible deviations from a universal IMF in extreme environments, such as the Central Molecular Zone (Hosek et al., 2019), starburst galaxies (Zhang & Tan, 2018) and low-metallicity environments (Marks et al., 2012).

1.4.2 Stellar Variability

Variability is ubiquitous among young stellar objects (YSOs). A low level of variability (i.e., typically below a few 0.1 mag) has been observed in most YSOs in the optical and NIR (e.g., Parihar et al., 2009). Mechanisms to produce such variations include rotationally modulated cool spots, hot spots on the stellar surface, extinction changes, and changes in the inner circumstellar disk (e.g., Wolk et al., 2013). Some of these mechanisms, like hot spots and varying extinction, may also produce variability with larger amplitudes (see, e.g., Grankin et al., 2007; Bouvier et al., 2013). Apart from these common causes of variability, a small fraction of YSOs show evidence for eruptive behavior, with variations larger than 1 magnitude in the optical or NIR bands over a few years or decades. This type of variability is thought to be related to the process of accretion from the circumstellar disk on to the protostar. During these bursts the YSO may increase its mass accretion rate by several orders of magnitude compared with quiescent phases, resulting in strong variability. While this episodic accretion scenario is well established, the driving force of this phenomenon is still poorly understood (e.g., Audard et al., 2014). Understanding the underlying mechanisms is crucial not only for building a complete picture of star formation, but also for the potential implications on the planet formation process (e.g., Zhu et al., 2009).

The nature of YSOs favors observations at NIR and mid-IR (MIR) wavelengths, which allow for direct detection of optically thick disks, e.g., via excess K-band flux (Lada & Adams, 1992). Over recent years there has been an increasing interest to search for eruptive variables with long-term NIR observations. Scholz (2012) used archival NIR photometry to investigate the long-term variability in a few nearby low-mass star-forming regions and found a low fraction ($\sim$2% in the YSO sample) of large amplitude variable objects. A higher incidence of K band variations > 1 mag ($\sim 13 \pm 7$%) has been reported in Class I YSOs in the dark cloud L1003 in Cygnus OB7 (Rice et al., 2012; Wolk et al., 2013). A panoramic search by the UKIRT Infrared Deep Sky Survey (UKIDSS; Lawrence et al., 2007) found a strong concentration of high-amplitude IR variables towards star-forming regions (Contreras Peña et al., 2014), and this is confirmed by recent VVV survey (VISTA Variables in the Via Lactea; Minniti et al. (2010)), in which more than 100 eruptive YSOs were detected (Contreras Peña et al., 2017a).

1.4.3 Protostellar Disks

Disks of gas and dust around young protostars are fundamental to protostellar mass accretion and act as the mass reservoir from which stars and planetesimals form (e.g., Armitage, 2011; Williams & Cieza, 2011). Circumstellar disks are expected to be present around both extremely young protostars that are still deeply embedded in the natal dense envelope and more evolved pre-main sequence stars, at which point the envelope has dissipated. The advent of new facilities such as the Atacama Large

Millimeter/submillimeter Array (ALMA) and the Jansky Very Large Array (JVLA) have boosted the study of the formation and evolution of disks around young solar-type stars. Questions concerning disk masses, disk radii, disk evolution, and the presence of planetesimals in the youngest protostellar disks are only beginning to be addressed (e.g., Andrews et al., 2016; Carrasco-González et al., 2016). Surveys to date span a wide range of physical conditions and ages, with the σ Ori (Ansdell et al., 2017) and Orion Nebula Cluster (ONC) (e.g., Eisner et al., 2018) typical of massive, young star-forming regions. Regions like Lupus, Taurus and Chamaeleon I probe a lower-mass, more isolated regime of star formation (e.g., Ansdell et al., 2016). Observations of the Upper Scorpius OB association, on the other hand, provide a window on a more evolved population (Barenfeld et al., 2016).

1.5 Outline of the Thesis

The outline of this thesis is as follows. A multi-wavelength study of the massive protocluster G286 is presented in §2, §3 and §4. In §2 we mainly use millimeter continuum data to measure the CMF. In §3 we investigate the kinematics and dynamics of G286 with spectral lines from dense gas tracers. In §4 we characterize the stellar variability in this region with 2-epoch HST data in the near-IR band. In order to study the environmental dependence of cluster formation, in §5 we extend the analysis to a strongly magnetized cloud in the Vela C region and present the ALMA observations in band 6 and band 7, including characterization of dense cores and a discussion on the overal star formation efficiency in this region. Finally we present in §6 a case study of individual star formation on the protostellar disk scale, i.e., IRS1 and IRS3 in the intermediate-mass star-forming region in NGC 2071IR, with a focus on the properties of their disks and outflows.

Chapter 2

Core Mass Function in the Massive Protocluster G286.21+0.17

2.1 Introduction

The stellar initial mass function (IMF) is of fundamental importance throughout astrophysics. However, in spite of much progress in measuring the IMF (see reviews of, e.g., Bastian et al. 2010; Kroupa et al. 2013), its origin and environmental dependence are still under active debate. Stars are known to form from cold dense cores in molecular clouds. These "prestellar cores" can be defined theoretically as gravitationally-bound, local density maxima that collapse via a single rotationally-supported disk into a single star or small N multiple. In the context of Core Accretion models (Padoan & Nordlund, 2002; Padoan et al., 2007; McKee & Tan, 2003; Hennebelle & Chabrier, 2008; Kunz & Mouschovias, 2009, e.g.,), the stellar mass is assumed to be related to the mass of its parental core, modulo a relatively constant core to star formation efficiency, $\epsilon_{\rm core}$, perhaps set mostly by outflow feedback (Matzner & McKee, 2000; Zhang et al., 2014), with radiative feedback expected to influence only the most massive stars(Tanaka et al., 2017). In this framework, we expect the IMF to be strongly influenced by the prestellar CMF, i.e., the PSCMF. However, there are alternative models, especially Competitive Accretion(Bonnell et al., 2001; Bate, 2012), which explain the IMF without a CMF that extends to higher masses. Therefore, the study of the CMF, and ideally the PSCMF, is crucial for understanding the origin of the IMF and its connection to the large-scale physical and chemical conditions of molecular clouds.

Early observations based on submillimeter dust continuum emission(e.g., Motte et al., 1998; Testi & Sargent, 1998; Johnstone et al., 2000) found evidence for an approximately log-normal CMF peaking near $\sim 1\,M_\odot$, with a power law tail at higher masses of the form

$$\frac{\mathrm{d}N}{\mathrm{dlog}M} \propto M^{-\alpha}. \tag{2.1}$$

These studies found values of $\alpha \simeq 1.0$ to 1.5, based on samples of several tens of sources. In this form, the Salpeter (1955) $\gtrsim 1\,M_\odot$ power law fit to stellar masses has an index $\alpha = 1.35$, indicating a potential similarity of the CMF and IMF. Alves et al. (2007) used near-infrared dust extinction to characterize about 160 cores to find similar results, with the peak of the CMF now better measured close to $1\,M_\odot$ and the CMF reported to be a simple translation of the IMF requiring $\epsilon_{\rm core} \simeq 0.3$. More recent results from the Gould Belt Survey with *Herschel*, *Spitzer* and JCMT have also detected samples of hundreds of cores (e.g., André et al., 2010; Sadavoy et al., 2010; Salji et al., 2015; Marsh et al., 2016) and have added to the evidence for a similarity in shape of the CMF and IMF.

Extending to more distant ($\gtrsim 2$ kpc), high-mass star-forming regions has been more challenging, in particular requiring higher angular resolution interferometric observations. Beuther et al. (2004)(see also Rodón et al., 2012) reported a CMF of 1.3 mm emission cores in IRAS 19410+2336 ($d \sim 2$ kpc) with $\alpha \simeq 1.5 \pm 0.3$, based on a sample of 24 sources ranging in mass from $\sim 2 - 25\ M_\odot$. Bontemps et al. (2010) detected a similar number of sources in Cygnus X ($d = 1.7$ kpc), but these were identified from the follow-up of five quite widely-separated clumps, so that the CMF was not derived from uniform mapping of a contiguous region. Zhang et al. (2015) studied the core population via 1.3 mm emission in the Infrared Dark Cloud (IRDC) G28.34 P1 clump ($d \simeq 5$ kpc) with ALMA, finding 38 cores. They concluded there was a dearth of lower-mass ($\sim 1 - 2\ M_\odot$) cores compared to the prediction resulting from a scaling down to these masses with a Salpeter mass function. Ohashi et al. (2016) studied the IRDC G14.225-0.506 ($d = 2$ kpc) CMF via 3 mm emission with ALMA at $\sim 3''$ resolution, identifying 48 sources with the clumpfind algorithm (Williams et al., 1994) from two separate fields. They derived $\alpha = 1.6 \pm 0.7$, with the masses ranging from $1.5 - 22\ M_\odot$.

G286.21+0.17 (hereafter G286) is a massive protocluster associated with the η Car giant molecular cloud at a distance of 2.5 ± 0.3 kpc, in the Carina spiral arm(e.g., Barnes et al., 2010; Andersen et al., 2017a) G286 has been claimed to be $\sim 10^4\ M_\odot$ (B10), which would make it the most massive and densest of the 300 HCO^+(1-0) clumps studied by Barnes et al. (2011) and Ma et al. (2013), but an assessment of its dust mass from *Herschel* imaging data suggests a lower mass of $\sim 2000\ M_\odot$ (Ma et al., in prep.). From modeling of HCO^+ and $H^{13}CO^+$ spectra, B10 found a global infall rate $\sim 3 \times 10^{-2}\ M_\odot\ \mathrm{yr}^{-1}$, one of the largest such infall rates yet measured.

Here we present the ALMA Band 6 (230 GHz) continuum observation of G286 and an analysis of the CMF in this region. This paper is organized as follows: in §2 we describe the observational setup and analysis methods; in §3 we present our results, including an exploration of different analysis techniques for identifying cores and the resulting CMFs; in §4 we discuss and summarize our conclusions.

2.2 Observations and Analysis Methods

2.2.1 Observational Set-Up

The observations were conducted with ALMA during Cycle 3 (Project ID 2015.1.00357.S, PI: J. C. Tan), during a period from Dec. 2015 to Sept. 2016. To map the entire field of G286 ($\sim$5.3′×5.3′), we divided the region into five strips, denoted as G286_1, G286_2, G286_3, G286_4, and G286_5, each about 1′ wide and 5.3′ long and containing 147 pointings of the 12-m array. Figure 2.1a illustrates the spatial extent of the five strips, together with red circles showing the 12-m array mosaic footprints overlaid on strip G286_5 as an example. The position of field center is R.A.=10:38:33, decl.=-58:19:22. We employed the compact configuration C36-1 to recover scales between 1.5″ and 11.0″. Additionally, a 35-pointing mosaic was performed for each strip using the 7-m array, probing scales up to 18.6″. Total power observations of the region were also carried out (relevant only for the line observations).

Two scheduling blocks happened to be observed when the array configuration was in a transition phase, i.e., moving from a very extended configuration (C37/C38-1) to our proposed compact configuration. Thus we obtained extra *uv* coverage for two strips, G286_1 and G286_2, where $\sim$90% of the continuum emission is located. This enables us to detect and characterize structures at a higher resolution ($\sim$1″, 2500 au) in these regions, which will be the focus of the results presented in this paper.

During the observations, we set the central frequency of the correlator sidebands to be the rest frequency of the N_2D^+(3-2) line at 231.32 GHz for SPW0, and the $C^{18}O$(2-1) line at 219.56 GHz for SPW2, with a velocity resolution of 0.046 and

0.048 km s^{-1}, respectively. The second baseband SPW1 was set to 231.00 GHz, i.e., 1.30 mm, to observe continuum with a total bandwidth of 2.0 GHz. The frequency coverage for SPW3 ranges from 215.85 to 217.54 GHz to observe DCN(3-2), DCO^+(3-2), SiO($v = 0$)(5-4) and $CH_3OH(5_{1,4} - 4_{2,2})$. The molecular line data from this observation will be presented and analyzed in a future paper, while here we focus on the results of the broad continuum band, i.e., tracing dust emission.

Both the 7-m and 12-m array data were calibrated with the data reduction pipeline using *Casa* 4.7.0. The continuum visibility data was constructed with all line-free channels. We performed imaging with *tclean* task in *Casa* and during cleaning we combined data for all five strips to generate a final mosaic map. The 7-m array data was imaged using a Briggs weighting scheme with a robust parameter of 0.5, which yields a resolution of $7.32'' \times 4.42''$. For the combined data, we used the same Briggs parameter. In addition, since we have extra *uv* coverage for part of the data, we also apply a $0.6''$ *uvtaper* to suppress longer baselines, which results in $1.62'' \times 1.41''$ resolution.

The lowest noise level in the image varies from 0.2 mJy beam^{-1} to 0.46 mJy beam^{-1}, depending on which strip is being considered. The 1σ noise of the central strip is 0.45 mJy beam^{-1}. We also do the cleaning separately for the central two strips with a smaller *uvtaper* value to utilize the long baseline data, which results in a resolution of $1.07'' \times 1.02''$. The 1σ noise level in this image is 0.45 mJy beam^{-1}.

2.2.2 Core Identification

To study the CMF we first need to identify the "cores." A variety of algorithms have been used to detect and characterise dense cores in previous studies of continuum maps (e.g., Williams et al., 1994; Kramer et al., 1998; Rosolowsky et al., 2008), and in practice, the results in terms of core number and statistical properties can vary

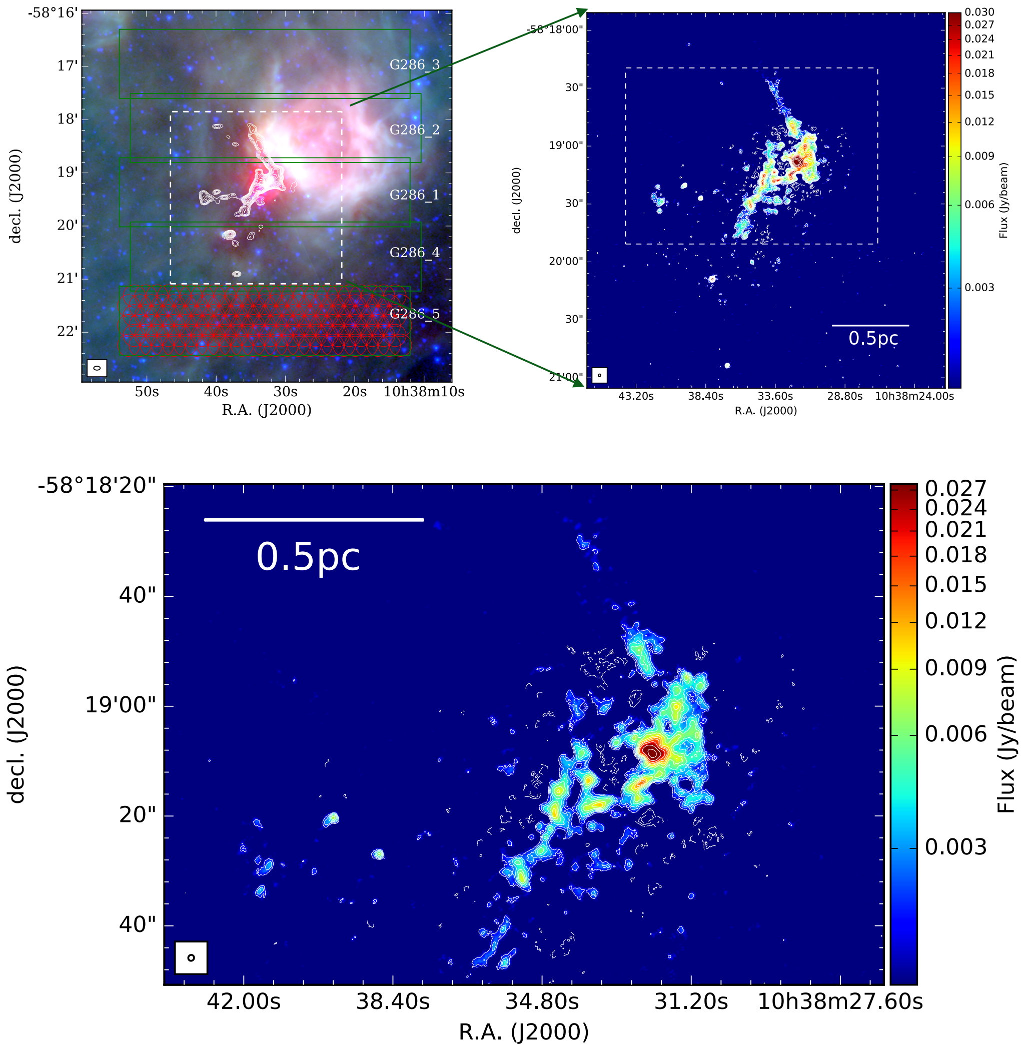

Figure 2.1: *(a) Top Left:* Three color image of G286 constructed by combining *Spitzer* IRAC 3.6 μm (blue), 8.0 μm (green), and *Herschel* PACS 70 μm (red). White contours show ALMA 7-m array image starting from 4σ. The G286 field is divided into five strips, as shown by the green rectangles. Each strip is covered with 147 pointings of the 12-m array, illustrated for strip G286_5 as an example with red circles marking the FWHM field of view of each pointing. The white dashed rectangle is the region shown in (b). *(b) Top Right:* Image with combined 12-m array and 7-m array data. The resolution is $1.62'' \times 1.41''$. The contour levels are at (4, 8, 10, 12, 15, 20, 25, 30, 40, 50, 75, 100, 150)$\times$0.45 mJy beam^{-1} (color scale in Jy beam^{-1}). The white dashed rectangle is the region shown in (c). *(c) Bottom:* Image with combined 12-m array and 7-m array data, but now imaged at $1.07'' \times 1.02''$. Our CMF analysis is carried out for this region.

with the different algorithms and input parameters (e.g. Pineda et al., 2009). To understand how the derived CMF depends on these identification methods, we thus adopt two well-documented and widely used algorithms to analyse our data and test the effects of variation of their parameters.

The Dendrogram Method

The dendrogram algorithm is described by Rosolowsky et al. (2008) and implemented in *astrodendro*. The dendrogram is an abstraction of the changing topology of the isosurfaces as a function of contour level. This method can describe hierarchical structures in a 2-D or 3-D datacube. There are two types of structures returned in the results: leaves, which have no sub-structure; and branches, which can split into multiple branches or leaves. Here we only use the leaf structure as a representation of dense cores.

There are three main parameters in this algorithm: $F_{\rm min}$, δ, and $S_{\rm min}$. First, $F_{\rm min}$ is the minimum value to be considered in the dataset. In the fiducial case we adopt $F_{\rm min} = 4\sigma$. Second, δ describes how significant a leaf has to be in order to be considered as an independent entity. We adopt a fiducial value of $\delta = 1\sigma$, which means a core must have a peak flux reaching 5σ above the noise. The minimum area a structure must have to be considered as a core is given by $S_{\rm min}$. In general the size of the beam is a good choice, but in a crowded field a detected core can be smaller than one beam size due to blending, especially when a large value of $F_{\rm min}$ is used. We thus set $S_{\rm min} = 0.5 S_{\rm beam}$ as our fiducial choice. We will also explore the effects of varying these choices of $F_{\rm min}$, δ, and $S_{\rm min}$.

The Clumpfind Method

The clumpfind algorithm(Williams et al., 1994) works by first contouring the data at a multiple of the rms noise of the observation, then searching for peaks of emission that locate the structure, then following them down to lower intensities. It was designed to study molecular clouds using 3-D datacubes and has also been widely used to describe dense cores (e.g., Reid & Wilson, 2005; Pineda et al., 2009).

The most sensitive parameters for clumpfind are the lowest contour level ($F_{\rm min}$) and level spacing (Δ). $F_{\rm min}$ is the same as that in the dendrogram method, and we adopt 4σ as a fiducial value. Δ refers to the contour level spacing and hence is somewhat different from the δ parameter of the dendrogram method. We choose $\Delta = 3\sigma$ in the fiducial case, similar to previous implementations in the literature. As with the dendrogram method, cores are requires to have a minimum area $S_{\rm min}$, and we adopt $S_{\rm min} = 0.5 S_{\rm beam}$ as a fiducial threshold. Again, we investigate the effects of variations in the values of $F_{\rm min}$, Δ, and $S_{\rm min}$.

2.2.3 Core Mass Estimation

We estimate core masses by assuming optically thin thermal emission from dust. The total mass surface density corresponding to a given specific intensity of mm continuum emission is

$$
\begin{aligned}
\Sigma_{\rm mm} &= 0.369 \frac{F_\nu}{\rm mJy} \frac{(1'')^2}{\Omega} \frac{\lambda_{1.3}^3}{\kappa_{\nu,0.00638}} \\
&\quad \times \left[\exp\left(0.553 T_{d,20}^{-1} \lambda_{1.3}^{-1}\right) - 1\right] \ {\rm g\ cm^{-2}} \\
&\to 0.272 \frac{F_\nu}{\rm mJy} \frac{(1'')^2}{\Omega} \ {\rm g\ cm^{-2}},
\end{aligned} \tag{2.2}
$$

where F_ν is the total integrated flux over solid angle Ω, $\kappa_{\nu,0.00638} \equiv \kappa_\nu/(6.38 \times 10^{-3}\ {\rm cm^2\ g^{-1}})$ is the dust absorption coefficient, $\lambda_{1.3} = \lambda/1.30$ mm and $T_{d,20} = T_d/20$ K with T_d being the dust temperature. To obtain the above fiducial normalization of κ_ν, we assumed an opacity per unit dust mass $\kappa_{\rm 1.3mm,d} = 0.899\ {\rm cm^2 g^{-1}}$ (moderately coagulated thin ice mantle model of Ossenkopf & Henning (1994), which then gives

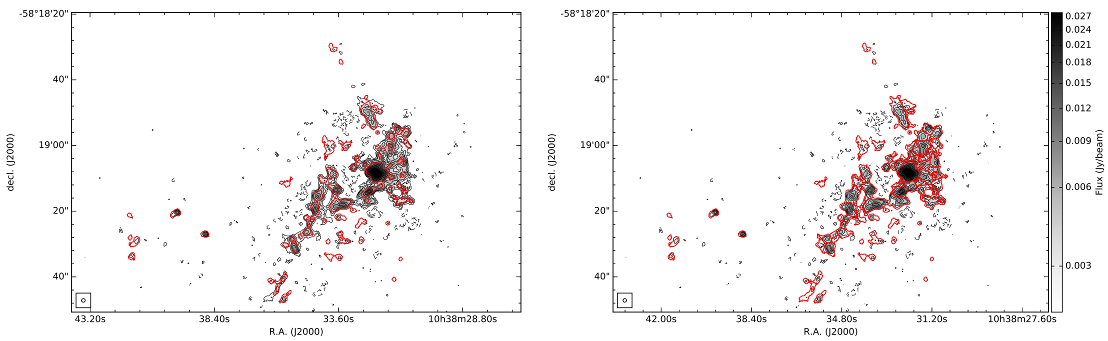

Figure 2.2: *(a) Left:* Cores found with the dendrogram method using our fiducial criteria: $F_{\rm min} = 4\sigma$, $\delta = 1\sigma$ and $S_{\rm min} = 0.5 S_{\rm beam}$. The image is shown in gray scale overlaid on black contours starting from 4σ and increasing in steps of 2σ. The red contours indicate the boundaries of the detected cores. *(b) Right:* Same as (a), but now showing the results of the clumpfind method. The criteria are $F_{\rm min} = 4\sigma$, $\Delta = 1\sigma$ and $S_{\rm min} = 0.5 S_{\rm beam}$.

$\kappa_{1.3\mathrm{mm}} = 6.38 \times 10^{-3}\ \mathrm{cm}^2\ \mathrm{g}^{-1}$ using a gas-to-refractory-component-dust ratio of 141 (Draine, 2011). The numerical factor following the $\rightarrow$ in the final line shows the fiducial case where $\lambda_{1.3} = 1$ and $T_{d,20} = 1$.

Note that since we do not have detailed temperature information for each source, for simplicity we have adopted an uniform value of $T_d = 20$ K for all cores in our fiducial analysis. Such temperatures are expected to be representative of average temperatures in protostellar cores (e.g., Zhang et al., 2015) However, we recognize that somewhat warmer temperatures may result either from strong external heating by nearby, luminous sources in the embedded protocluster or by stronger than average internal heating in protostellar cores. On the other hand, the temperature could be lower in prestellar or early-stage protostellar cores. If temperatures of 15 K or 30 K were to be adopted, then the mass estimates would differ by factors of 1.48 and 0.604, respectively.

Given the above values of Σ_{mm}, then the core mass is

$$\begin{aligned} M &= \Sigma_{\mathrm{mm}} A = 0.113 \frac{\Sigma_{\mathrm{mm}}}{\mathrm{g\ cm^{-2}}} \frac{\Omega}{(1'')^2} \left(\frac{d}{1\ \mathrm{kpc}}\right)^2 M_\odot \\ &\rightarrow 0.192 \frac{F_\nu}{\mathrm{mJy}} \left(\frac{d}{2.5\ \mathrm{kpc}}\right)^2 M_\odot \end{aligned} \tag{2.3}$$

where A is the projected area of the core, d is the source distance, and the final evaluation is for fiducial temperature assumptions of 20 K (following eq. Equation 2.3). Thus the 1σ noise level in the image corresponds to a core mass of $\sim 0.1\ M_\odot$.

Overall, we estimate absolute mass uncertainties of about a factor of two, which we expect to be caused mostly by temperature variations. Relative core mass estimates will be somewhat more accurate, although still potentially with uncertainties of this magnitude due to core to core temperature and opacity variations.

2.2.4 Core Flux Recovery and Completeness Corrections

We calculate two corrections factors that are needed to estimate a "true" CMF from a "raw" observed CMF. First, since both dendrogram and clumpfind methods adopt a threshold value (i.e., 4σ) and pixels below this level are not assigned to any core structures, we expect the estimated core flux (i.e., mass) is a fraction of the true flux. We estimate the flux recovery fraction, $f_{\rm flux}$, as a function of true core mass by carrying out experiments of artificial core insertion into the *ALMA* images. These same experiments also allow us to assess the second factor, i.e., the number recovery fraction, $f_{\rm num}$, again as a function of true input core mass. These correction factors are also expected to depend on core density profile and the local clump environment, e.g., degree of crowding.

We adopt the following methods for these experiments of artificial core insertion and recovery. The artificial cores are assumed to have the same shape as the synthesized beam, i.e., the limiting case appropriate for small, unresolved cores. The locations of the artificial cores are chosen randomly, but with a probability density that is scaled to match the flux profile we derive from the 7-m array image, which has the effect of placing more cores in crowded regions. In each experiment, we insert 10 cores (i.e., $\sim$10% of the total number to avoid excessive blending) of a given total flux, i.e., of a given mass. We run the core detection algorithms to determine the average flux levels recovered in detected cores and the probability for artificial cores of a given mass to be found. This is repeated 30 times to obtain a large sample for more accurate estimates.

With $f_{\rm flux}(M)$ estimated in this way, we then first transform the raw CMF into a flux-corrected CMF, which involves estimating the average (median) flux correction factor for a given observed mass. Then, given our estimate of $f_{\rm num}(M)$, we transform the flux-corrected CMF into an estimate of the true CMF, i.e., by assuming the completeness correction factor at a given mass is equal to the inverse of $f_{\rm num}$. The derived forms of $f_{\rm flux}(M)$ and $f_{\rm num}(M)$ are shown in the next section for our fiducial case.

2.3 RESULTS

2.3.1 1.3 mm Continuum Image

Figure 2.1 presents the 1.3 mm continuum map constructed with the 7-m array data in the top left panel, 12-m and 7-m array combined data in the top right panel, and the highest resolution combined image in the bottom panel. The image with only 7-m data reveals two main filaments: a northern one with a NE–SW orientation and a southern one with a NW–SE orientation. These two filaments converge at a clump with bright mm continuum emission. Several other isolated clumps are also revealed. The southern filament and central hub are further resolved into a cluster of dense cores. The image combining all data has a spatial dynamic range that recovers structures from $\sim 1''$ to $\sim 20''$.

Figure 2.2 shows the high resolution ($\sim 1''$) 1.3 mm continuum image with the core boundaries overlaid for both the dendrogram and clumpfind methods. Inspection of these images allows one to assess how the core identification algorithms operate on the imaging data. One sees cores with a range of sizes, some being many times the size of the beam. Note that the central, brightest and most massive "core" is identified in a similar way with both algorithms. However, we expect that there is a high probability that such massive, large area "cores" will appear fragmented when imaged at higher angular resolution (see also §section 2.4).

Another feature revealed by Figure 2.2 is clumpfind's method of partitioning all the flux above the minimum threshold contour level. This is to be contrasted with the method adopted by the dendrogram algorithm, with the effect being to tend to make the cores identified by clumpfind more massive than their dendrogram counterparts.

2.3.2 The Core Population and CMF

In Figure 2.3 we show the "raw" CMFs (black histograms) derived from our fiducial dendrogram (top panel) and clumpfind (bottom panel) methods. The fiducial dendrogram method ($F_{\rm min} = 4\sigma$, $\delta = 1\sigma$, $S_{\rm min} = 0.5 S_{\rm beam}$) identifies 76 cores, while the fiducial clumpfind method ($F_{\rm min} = 4\sigma$, $\Delta = 3\sigma$, $S_{\rm min} = 0.5 S_{\rm beam}$) finds 83 cores. Note, we adopt uniform binning in $\log M$, with 5 bins per dex. Poisson counting errors are shown for each bin. Figure 2.3 also displays the flux corrected CMFs (blue histograms, with errors again estimated as a Poisson value) and subsequently number corrected, i.e., "true," CMFs (red histograms, with error assumed to be the same fractional value as in the blue histograms), for each case. The fitting of power law functions to the high-mass end of the CMFs is discussed below.

The correction factors used in Figure 2.3 are shown in Figure 2.4. The flux correction factor, which is based on median values of $f_{\rm flux}$ (excluding values > 1, which we attribute to false assignments; and extrapolating with constant values for $M \lesssim 0.3\,M_\odot$), rises from about 0.6 at the low-mass end (when cores are detected) to close to unity at the high-mass end. The values of $f_{\rm flux}$ for dendrogram and clumpfind are similar to each other, with clumpfind recovering slightly more flux over most of the mass range.

The number recovery fractions, $f_{\rm num}$, show a larger dynamic range, rising from ~ 0.1 at the low-mass end to near unity at the high-mass end (these remain slightly less than one due to the possibility of blending with existing massive cores). Again, the values of this correction factor are similar for both dendrogram and clumpfind.

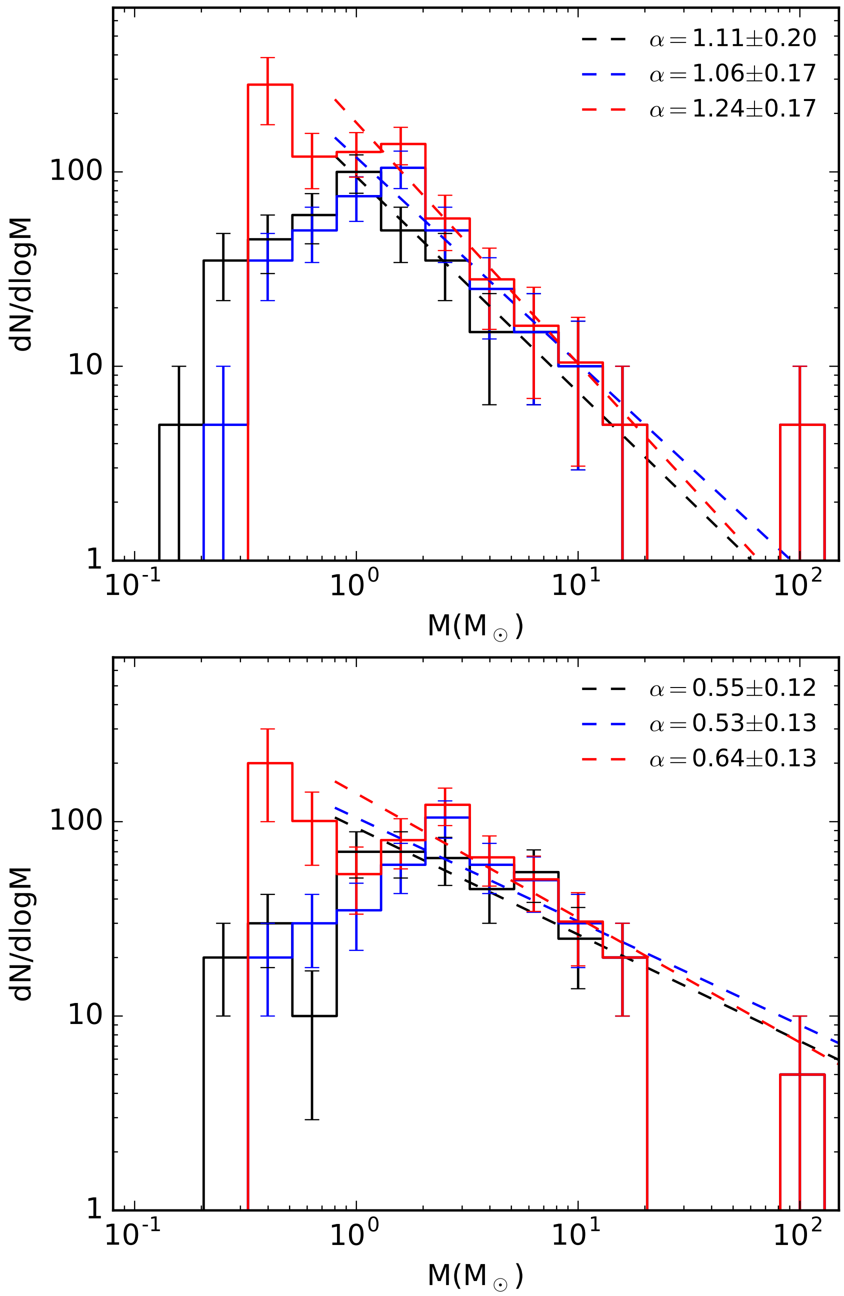

Figure 2.3: *(a) Top:* CMF for the dendrogram method. The original CMF is shown in black and after mass (flux) correction for each core is shown in blue. The blue CMF is then corrected for the number recovery fraction, as illustrated in red. The dashed lines in black, blue and red show the best power law fit result for the high-mass end ($M > 0.8\ M_\odot$) for the corresponding CMFs. *(b) Bottom:* As (a), but now for the clumpfind method.

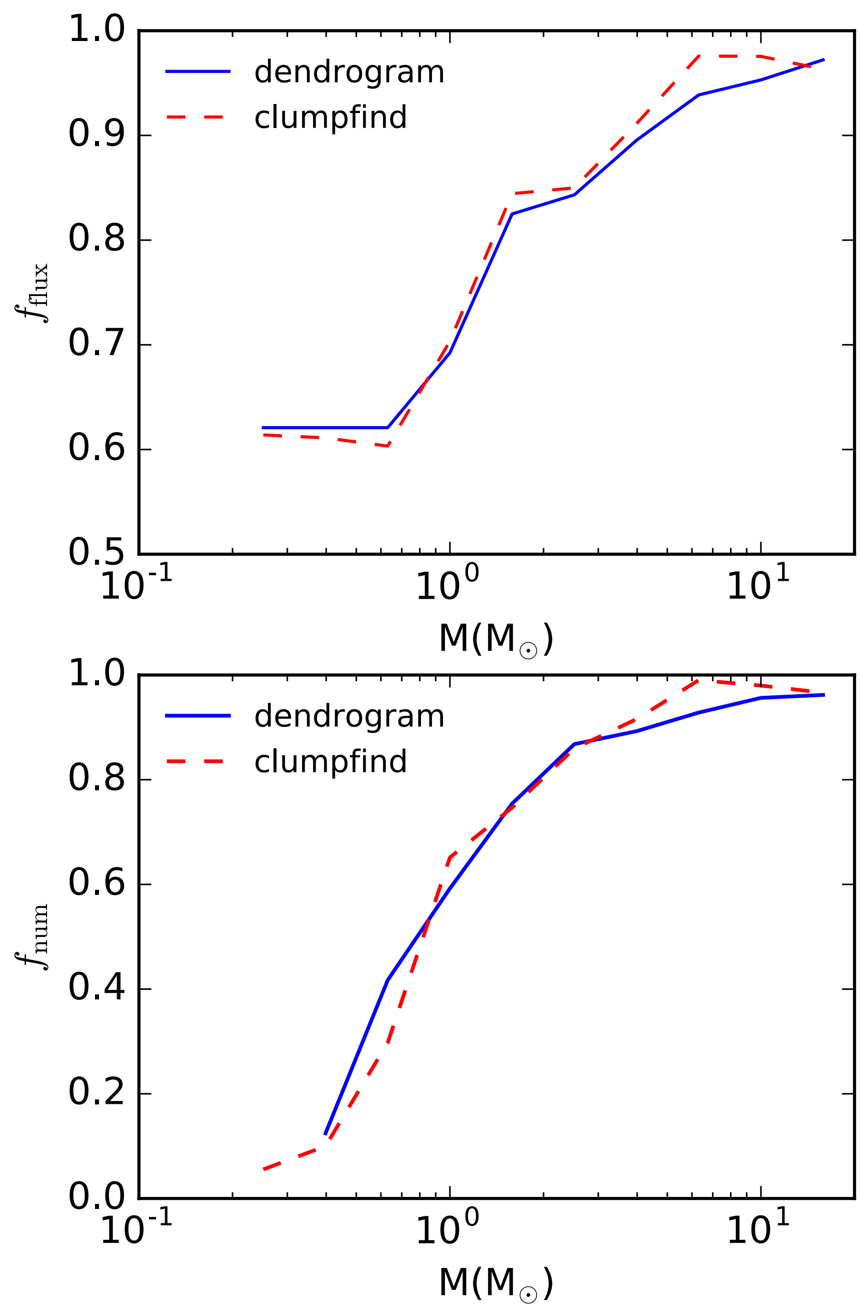

Figure 2.4: *(a) Top:* Flux recovery fraction, $f_{\rm flux}$, versus core mass, M, for dendrogram and clumpfind algorithms, as labelled. *(b) Bottom:* Number recovery fraction, $f_{\rm num}$, versus core mass, M, for dendrogram and clumpfind algorithms, as labelled.

We estimate that we are about 50% complete by number for $\sim 1 M_\odot$ cores. The direct effect of the number correction can be seen by comparing the blue and red histograms in Fig. Figure 2.3.

We characterize the high-end ($> 0.8\ M_\odot$, i.e., starting with the bin centered on $1\ M_\odot$) part of the raw dendrogram CMF by fitting a power law of the form given by equation (Equation 2.1). We find $\alpha = 1.11 \pm 0.20$. Fitting the same mass range for the flux corrected CMF yields $\alpha = 1.06 \pm 0.17$, while that for the fully (flux and number) corrected, i.e., "true", CMF yields $\alpha = 1.24 \pm 0.17$. Thus these correction factors have only a modest impact on the shape of the CMF for $M \gtrsim 0.8\ M_\odot$, with the true CMF being slightly steeper than the raw CMF, mostly due the effects of the number correction.

We note that there is sparse sampling of the high-mass end of the CMF, i.e., there is a single, massive ($\sim 100\ M_\odot$) "core." Our fitting method, which we note minimizes χ^2 in log space, treats the empty bins as effective upper limits. However, if we were to exclude this source and fit the CMF only over the range from 0.8 to $\sim 20 M_\odot$, then we would derive $\alpha = 1.11 \pm 0.22$ and $\alpha = 1.15 \pm 0.17$ for the raw and true CMFs, respectively, i.e., there is only a very minor effect.

Inspection of the true CMF indicates that the power law behavior may continue down to lower masses. If we fit to the range $M \gtrsim 0.3\ M_\odot$, we derive a moderately shallower value of $\alpha = 0.83 \pm 0.11$. From these results, we see that there is potential evidence for a break in the CMF near $1\ M_\odot$, but that a single power law is still a reasonable description of the flux and number corrected, i.e., true, CMF across most of the mass range probed, i.e., from $\sim 0.3\ M_\odot$ to $\sim 100\ M_\odot$.

For the CMF resulting from the fiducial clumpfind algorithm, the power law description of the raw CMF also appears potentially valid for $M \gtrsim 0.8\ M_\odot$. For this we derive $\alpha = 0.55 \pm 0.12$, which is significantly shallower than the 1.11 ± 0.20 derived over the same mass range for the dendrogram raw CMF. Thus, note, there are a larger number of massive cores found with the clumpfind method than with the dendrogram method. Then, on applying the flux and number corrections, the "true" CMF found via clumpfind displays a local peak at about 2.5 $M_\odot$, but with numbers of lowest-mass cores still potentially rising slowly. If we attempt the same uniform metric of a single power law fit above 0.8 $M_\odot$, then we find $\alpha = 0.64 \pm 0.13$. If we fit only from the bin containing the true CMF peak and extending to higher masses, then we find $\alpha = 0.78 \pm 0.14$, which is still shallower than the equivalent dendrogram result.

Thus we see that whether or not there is a peak or break defining a characteristic mass in the CMF depends on the method of core identification used and whether or not completeness corrections are applied. In particular, while the two methods find similar number of cores, we can explain the differences in their final CMFs mostly as a result of how mass is then assigned to the identified structures. As discussed above, clumpfind partitions all the flux above a given threshold to the sources, while dendrogram does not, i.e., its cores sit on plateaux that are described by branches in its structural decomposition.

The values of high-end slopes of the CMFs are relatively unaffected by the application of the completeness corrections. We note that the stellar IMF at $\gtrsim 1\, M_\odot$ also follows a power law form with $\alpha \simeq 1.35$ (Salpeter, 1955), and this value is very similar to those seen in the dendrogram CMFs, while the clumpfind CMFs are shallower. As previous studies of more local regions have found (see §section 2.1), this may indicate that core to star formation efficiency is relatively constant with increasing mass, at least over the range of masses that is effectively probed here, i.e., from ~ 1 to $\sim 100\, M_\odot$. The outflow and radiative feedback models of Tanaka et al. (2017) for star formation in clumps with $\Sigma_{\rm cl} \simeq 1\, {\rm g\, cm^{-2}}$, i.e., the value most relevant to G286,

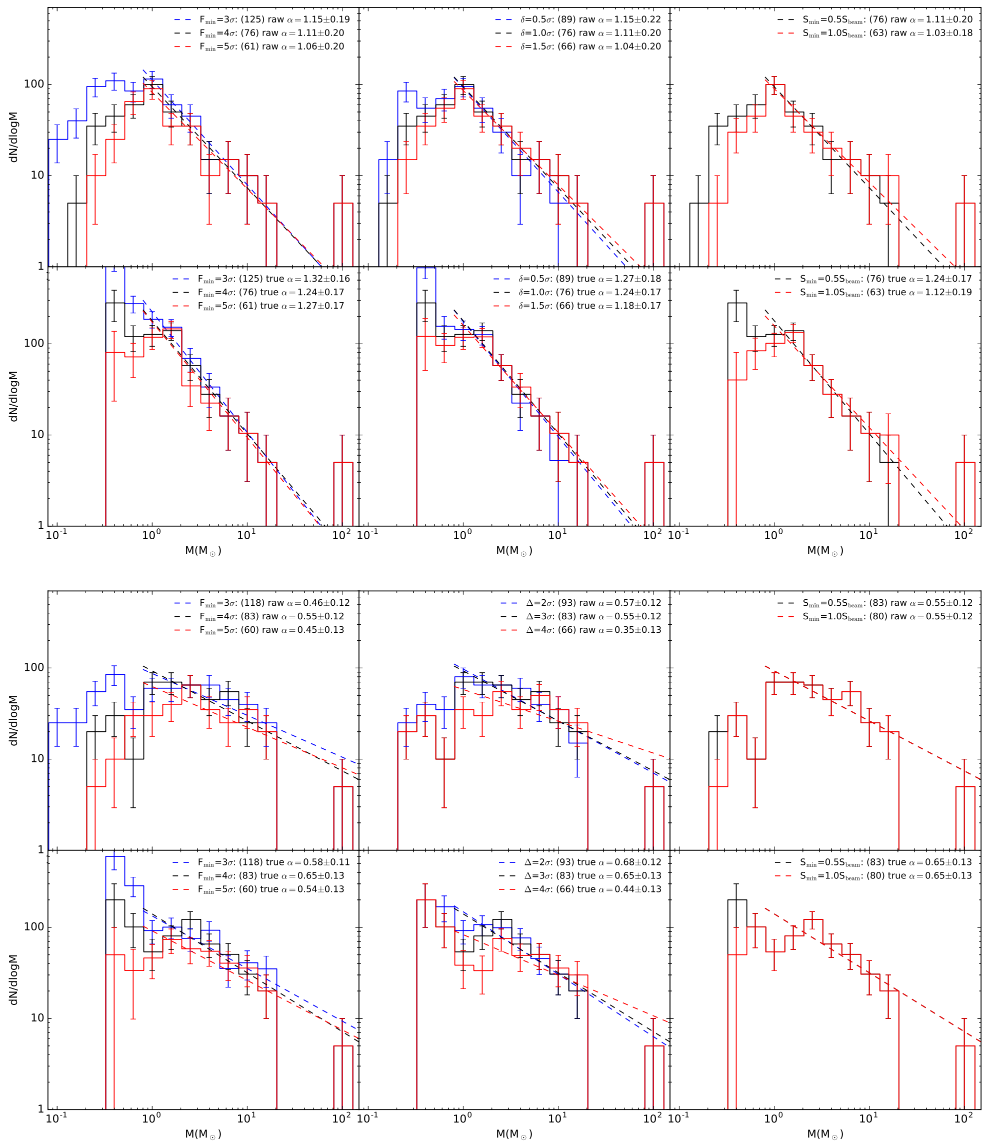

Figure 2.5: Raw CMFs derived with results from the dendrogram method shown on the top panels, and the clumpfind method on the bottom panels. For each algorithm we show different results by varying $F_{\rm min}$, δ (for dendrogram and Δ for clumpfind) and $S_{\rm min}$ (columns, left to right). In each panel, the results with different parameter selections are illustrated in different colors (see text). The number in the brackets denotes how many cores are detected. Also shown is the power law index, α, from fitting the high-mass end ($M > 0.8\,M_\odot$ for both dendrogram and clumpfind).

predict that these efficiencies should drop from ϵ =0.48 to 0.37 as the stellar mass increases from 5 $M_{\odot}$ to 40 $M_{\odot}$, i.e., as core masses increase from about 10 $M_{\odot}$ to about 100 $M_{\odot}$. Such a relatively small change in ϵ is still compatible with the results we have presented, since they lack significant numbers of cores $> 20\,M_{\odot}$ to place very stringent constraints in this regime. Other caveats should also be considered that may affect the derived CMFs, including possible systematic temperature variations with increasing continuum flux, i.e., if brighter cores are warmer, we will have over-estimated their masses. However, with the data in hand, it is not currently possible to assess how important this effect may be.

In Figure 2.5 we show the dependence of the CMFs that result from varying the three main parameters associated with each core identification method. We focus on the total core numbers found, the shape of the raw and true CMFs, and the high-end slope of the power law fits. In relation to the fiducial dendrogram method, if we lower the minimum threshold to $F_{\rm min} = 3\sigma$, 125 cores are now found (total core numbers are listed in parentheses in the legend in Fig. Figure 2.5), with the increase mostly being for sub-solar mass cores. If we set $F_{\rm min} = 5\sigma$, then only 61 cores are recovered. Varying δ to 0.5σ or 1.5σ has a more modest effect, as does increasing the minimum size of a core to 1 beam area. We see from comparing the raw CMFs and their derived values of α that the shape above $1\,M_{\odot}$ is relatively robust to these variations. In fact, we note that all the variation we see in α of these raw CMFs due to different dendrogram parameter choices is smaller than the uncertainty arising from Poisson counting statistics in this fiducial estimate. The completeness-corrected "true" CMFs found by the different dendrogram methods are generally very similar to one another if one restricts attention to $M \gtrsim 1\,M_{\odot}$, where the power law fits are always found to be slightly steeper than those of the raw CMFs. However, the shapes of these true CMFs below 1 $M_{\odot}$ are quite strongly affected by the choice of core definition within the dendrogram framework. This can affect whether or not a characteristic core mass is seen in the CMFs.

We have seen that the fiducial clumpfind method yields similar core numbers as the dendrogram analysis. Figure 2.5 shows that this is also true if we consider variations in its parameters $F_{\rm min}$ and Δ, in correspondence with the variations of the equivalent dendrogram parameters. However, unlike dendrogram, clumpfind does not see a significant reduction in the numbers of cores found if the minimum core size is doubled. Again, most values of the high-end α of these raw and true CMFs are similar to the fiducial values of their respective cases, i.e., 0.55 and 0.65, with only the $\Delta = 4\sigma$ case yielding significantly shallower slopes.

Next, we examine how the CMFs vary if the analyzed image has a lower angular resolution of $\simeq 1.5''$. Figure 2.6 compares the raw CMFs derived from the $1''$ and $\simeq 1.5''$ images. As expected, core masses tend to shift to higher values when identified from the lower resolution image. This leads to a flattening in the shape of the high-end CMFs, i.e., a reduction in the derived values of α, which can be quite significant, i.e., $\Delta\alpha \simeq -0.3$ for the raw CMF found by the fiducial dendrogram method. However, after completeness corrections are applied, the effect on α is more modest. These results indicate that even the high-end part of the CMFs can vary somewhat as the resolution is changed, and the trend may continue in the opposite direction if one were to image at higher resolutions. Indeed, this is expected if the more massive, larger cores are seen to fragment at significant levels when imaged at higher resolution. Such cores are known to fragment to some extent, although there are observed cases of quite limited fragmentation (e.g., Csengeri et al. 2017). This effect should be kept in mind when comparing CMFs derived from protoclusters that are observed with different resolutions, e.g., as may occur due to being at different distances.

Finally, in Figure 2.7 we examine how the CMFs vary if the analyzed image is

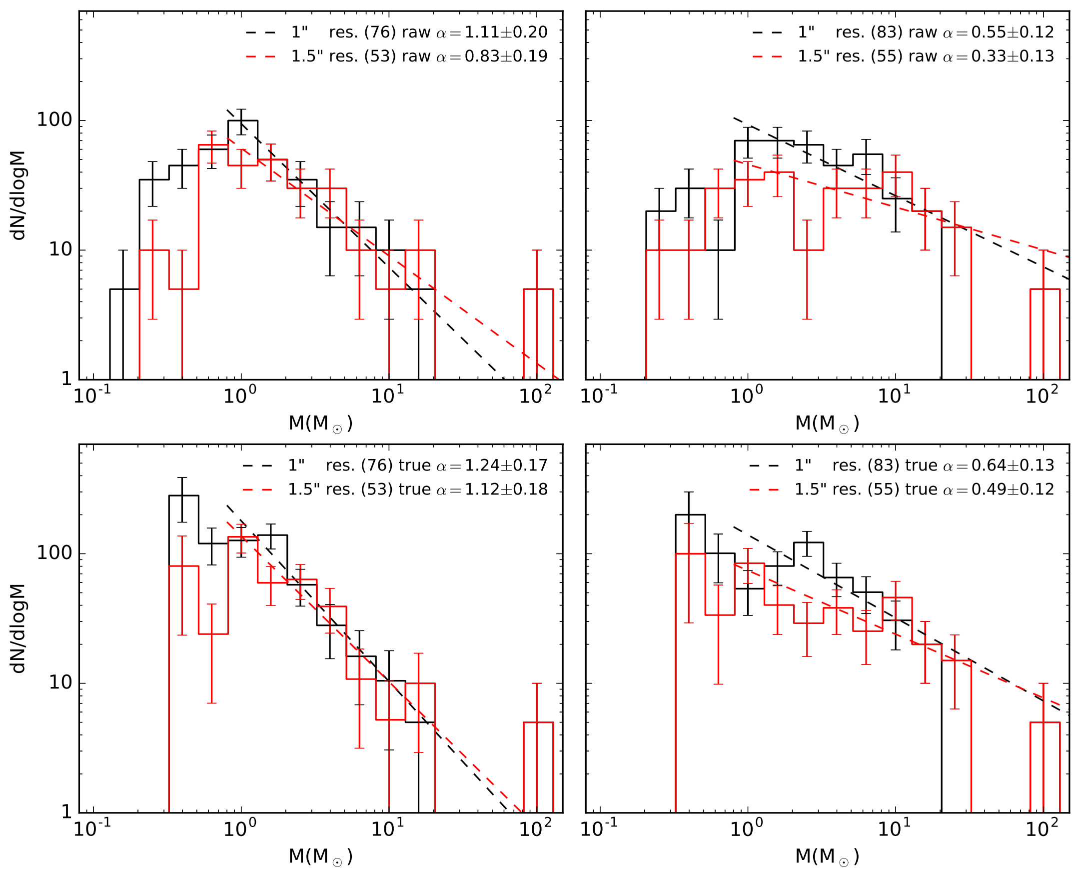

Figure 2.6: CMFs derived for images with lower spatial resolution, i.e., "1.5″" (actually $1.62'' \times 1.41''$), shown as red histograms and fitted power laws. These are compared to the fiducial results from analysis of the "1″" images (actually $1.07'' \times 1.02''$), shown in black. *Top left:* Raw CMFs with the fiducial dendrogram method. *Bottom left:* Completeness-corrected true CMFs with the fiducial dendrogram method. *Top right:* Raw CMFs with the fiducial clumpfind method. *Bottom right:* Completeness-corrected true CMFs with the fiducial clumpfind method.

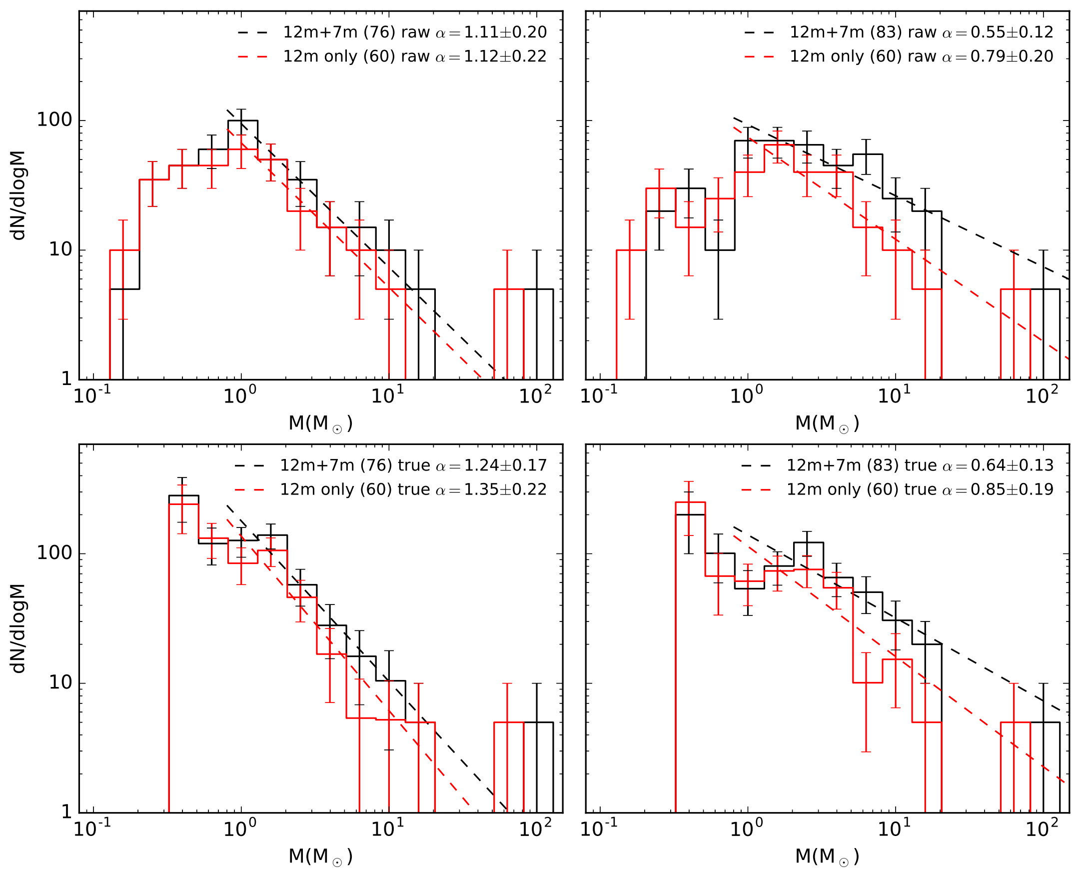

Figure 2.7: CMFs derived for images derived from only the 12m-array data, shown as red histograms and fitted power laws. These are compared to the fiducial results from analysis of our 12m + 7m array combined images, shown in black. *Top left:* Raw CMFs with the fiducial dendrogram method. *Bottom left:* Completeness-corrected true CMFs with the fiducial dendrogram method. *Top right:* Raw CMFs with the fiducial clumpfind method. *Bottom right:* Completeness-corrected true CMFs with the fiducial clumpfind method.

lacking the larger spatial scales obtained from the 7m-array data. Such an analysis is useful for understanding how the results of other observational programs that measure CMFs without such data may be affected. Our 12m only image has an rms noise level of 0.47 mJy beam^{-1}. For the dendrogram method we find that the CMF derived from the 12m only image contains slightly fewer cores (60) than found in the combined image (76), but has a high-end power law slope index that is very similar. For the completeness-corrected CMF the 12m-array only CMF has a high-end power law index that is about 0.1 steeper than that derived from the 12m + 7m image. Similar results are also found for clumpfind derived raw and true CMFs, with the difference now being about 0.2 in the magnitude of α. Thus the value of the high-end power law slope of the true CMF appears to be slightly over estimated if the image is lacking the larger spatial scales provided by 7m-array data.

2.4 Discussion and Conclusions

We have studied the CMF in the central region of the massive protocluster G286.21+0.17, with cores identified by their 1.3 mm dust continuum emission in a high spatial dynamic range image observed with the 7-m and 12-m arrays of ALMA. We explored the effects of using two different core identification algorithms, dendrogram and clumpfind, including a systematic study of the effects of varying their three main core selection parameters. We also examined the effects of varying angular resolution and largest recovered angular scale of the analyzed continuum image.

Our fiducial methods, including flux and number corrections estimated by artificial core insertion and recovery, yield CMFs that show high-end ($M \gtrsim 1\ M_\odot$) power law indices of $\alpha = 1.24 \pm 0.17$ for dendrogram and 0.64 ± 0.13 for clumpfind. These results are quite robust to variations of choices of core selection parameters.

With the dendrogram method, which we consider to be preferable to clumpfind as a means for identifying and characterizing cores that are embedded in a clump environment, these power law indices are similar to the Salpeter stellar IMF index of 1.35. This further strengthens the case of a correspondence between CMF and IMF seen in local regions, but now in a more distant, massive protocluster. As discussed in §section 2.1, such a correspondence is a general feature and/or expectation of Core Accretion models of star formation, in contrast to Competitive Accretion models. However, caveats remain, including potential systematic changes in core temperature for brighter cores and the fact that the measured CMF is expected to be composed of a mixture of prestellar and protostellar cores, i.e., tracing different evolutionary stages (see also discussion of Clark et al. (2007).

We do find that whether or not a peak is seen in the CMF near 1 $M_\odot$ depends on which core finding algorithm is used, i.e., dendrogram or clumpfind, the choices of parameters associated with the algorithm, and whether or not completeness corrections are carried out. Thus we cannot make firm conclusions about the presence of a peak or characteristic core mass near 1 $M_\odot$. Such a peak might be expected if there is close correspondence of CMF shape with stellar IMF shape. Our fiducial dendrogram result (see Fig. Figure 2.3a) shows only a very tentative hint of there being a break in the power law description of the CMF to shallower slopes for masses $\lesssim 1\,M_\odot$.

We re-emphasize that the relation of the CMF identified purely from sub-mm/mm dust continuum emission to the stellar IMF is uncertain. We expect that many of the cores identified by these methods, being the brighter cores, will be protostellar sources. Examples of massive prestellar cores identified by their high levels of deuteration, i.e., via N_2D^+ line emission, can show relatively weak mm continuum emission, perhaps indicating that they are significantly colder than their surrounding clump material (Kong et al. 2017a,b). For constraining theoretical models, it is desirable to have a measure of the PSCMF, and it remains to be seen how effective interferometric studies of mm continuum emission in distant massive protoclusters are at measuring this PSCMF (see, e.g., Fontani et al. 2009).

The observations carried out here also included N_2D^+(3-2) and ^{12}CO(2-1), amongst other species. In a future paper, these line data will be analyzed to place better constraints on the PSCMF and its relation to the CMFs presented here. We note that core finding methods that also utilize molecular line emission may also make it easier to break-up spatially confused structures.

Another caveat in the accuracy of CMF determination relates to the effects of spatial resolution and the possibility of fragmentation of identified "cores" into smaller structures as the resolution is increased. Such an effect has been seen before in numerous studies, but at varying levels (e.g., Beuther et al., 2004; Bontemps et al., 2010; Zhang et al., 2015; Csengeri et al., 2017) Cases of limited fragmentation may indicate an important role for magnetic fields in stabilizing the more massive cores (see, e.g., Kunz & Mouschovias, 2009; Tan et al., 2013; Fontani et al., 2016). Our investigation of how the true dendrogram CMF varies as the resolution is changed from about 1.5″ to 1″ shows that there is a slight steepening of the power law index, by about 0.1, as one goes to the higher resolution. However, the size of this change is smaller than the uncertainties arising solely from counting statistics, so larger samples of cores are needed to verify this trend. Higher sensitivity and higher angular resolution studies of the G286.21+0.17 are also desirable to investigate the particular fragmentation properties of the identified cores.

Taking the above caveats of CMF definition in mind, we still regard characterization of the mm continuum image via identification of discrete cores by specified, well-defined algorithms as a useful exercise for assessing the fragmentation in the cloud and as a first step for measuring the true CMF and, eventually, the PSCMF. Furthermore, the same core finding algorithms can also be applied to simulated molecular clouds to make a direct, statistical comparison of their structures with those of real systems, and in this way constrain the physics of star and star cluster formation.

Chapter 3

Gas Kinematics/Dynamics of G286.21+0.17

3.1 Introduction

While it is generally agreed that most stars form in clusters and/or associations rather than in isolation (e.g., Lada & Lada, 2003; Gutermuth et al., 2009; Bressert et al., 2010), there is no consensus for how this comes about. Several fundamental questions about star cluster formation are still debated. For example, is the process initiated by internal processes within a Giant Molecular Cloud (GMC), such as decay of support by supersonic turbulence or magnetic fields, or external processes, such as triggering by cloud-cloud collisions or feedback-induced shock compression (see e.g., Tan, 2015).

Once underway, is cluster formation a fast or a slow process relative to the local freefall time ($t_{\rm ff}$)? Tan et al. (2006) and Nakamura & Li (2007) proposed that formation times are relatively long, i.e., $\sim 10 t_{\rm ff}$, especially for those clusters with high ($\gtrsim$ 30%) overall star formation efficiency, since simulations of self-gravitating, turbulent, magnetized gas show low formation efficiency of just ~2% per free-fall time (Krumholz & McKee, 2005; Padoan & Nordlund, 2011). Alternatively, Elmegreen (2007), Hartmann & Burkert (2007) and Hartmann et al. (2012) have argued for cluster formation in just one or a few free-fall times. Another question is: what sets the overall star formation efficiency during cluster formation? The formation timescale and overall efficiency are likely to affect the ability of a cluster to remain gravitationally bound, which on large scales influences global ISM feedback, e.g., concentrated feedback from clusters can create superbubbles (e.g., Krause et al., 2013), and on small scales controls the feedback environments and tidal perturbations of protoplanetary disks (e.g., Adams, 2010).

Star cluster formation is likely to be the result of a complex interaction of numerous physical processes including turbulence, magnetic fields and feedback. From the observational side, measuring the structure and kinematic properties of the dense gas component is needed to provide constraints for different theretical models. Previously, Walsh et al. (2004) found small velocity differences between dense cores and surrounding envelopes for a sample of low-mass cores. Kirk et al. (2007, 2010) surveyed the kinematics of over 150 candidate dense cores in the Perseus molecular cloud with pointed N_2H^+ and $C^{18}O$ observations and found subvirial core to core velocity dispersions in each region. A similar small core velocity dispersion was also found in the Ophiuchus cloud (André et al., 2007). Qian et al. (2012) searched for ^{13}CO cores in the Taurus molecular cloud and found the core velocity dispersion exhibits a power-law behavior as a function of the apparent separation, similar to LarsonâĂŹs law for the velocity dispersion of the gas, which suggests the formation of these cores has been influenced by large-scale turbulence.

These observations have generally focused on nearby low-mass star-forming regions. With the unprecedented sensitivity and spatial resolution of ALMA, more light has been shed on massive star forming regions from the "clump" scale (of about a few parsecs) to the "core" scale ($\sim$ 0.01 to 0.1 pc) (e.g., Beuther et al., 2017; Fontani et al., 2018; Lu et al., 2018). Multiple coherent velocity components from filamentary structures have been reported in some massive Infrared Dark Clouds (IRDCs) (Henshaw et al., 2013, 2014; Sokolov et al., 2018), similar to the structures seen in the nearby Taurus region by Hacar et al. (2013). "Hub-filament" systems have also been reported in some massive star forming regions across a variety of evolutionary stages, perhaps indicating presence of converging flows that channel gas to the junctions where star formation is most active (e.g., Hennemann et al., 2012; Peretto et al., 2014; Lu et al., 2018; Yuan et al., 2018).

However, complete surverys for the dense gas component of massive protoclusters down to the individual core scale, are still rare (e.g., Ohashi et al., 2016; Ginsburg et al., 2017) and a large spatial dynamic range is required to perform a multi-scale kinematics analysis.

Until recently only very few nearby regions were known that were candidates for very young and still forming massive star clusters. One particular promising star-forming clump is G286.21+0.17 (in short G286). It is a massive protocluster associated with the η Car giant molecular cloud at a distance of 2.5 $\pm$ 0.3 kpc, in the Carina spiral arm (e.g., Barnes et al., 2010). We performed a core mass function (CMF) study towards this region based on ALMA Cycle 3 observations in Cheng et al. (2018).

Here we present a follow-up study of multiple spectral lines to investigate the gas kinematics and dynamics of G286 from clump to core scales. The paper is organized as follows: in section 6.2 we describe the observational setup and analysis methods; the results are presented in section 6.3. We discuss the kinematics and dynamics for parsec-scale filaments and dense cores separately in section 3.4 and section 6.4, and then summarize our findings in section 5.5.

3.2 Observational Data

3.2.1 ALMA Observations

The observations were conducted with ALMA in Cycle 3 (Project ID 2015.1.00357.S, PI: J. C. Tan), during a period from Dec. 2015 to Sept. 2016. More details of the observations can be found in Cheng et al. (2018). In summary, we divided the region into five strips, denoted as G286_1, G286_2, G286_3, G286_4 and G286_5, each about 1′ wide and 5.3′ long and containing 147 pointings of the 12-m array (see Figure 6.1). The position of field center is R.A.=10:38:33, decl.=-58:19:22. We employed the compact configuration C36-1 to recover scales between 1.5″ and 11.0″. This is complemented by observations with the ACA array, which probes scales up to 18.6″. Total power (TP) observations were also carried out to recover the total flux (of line emission), which gives a resolution of about 30″.

During the observations, we set the central frequency of the correlator sidebands to be the rest frequency of the N_2D^+(3-2) line at 231.32 GHz for SPW0, and the $C^{18}O$(2-1) line at 219.56 GHz for SPW2, with a velocity resolution of 0.046 and 0.048 $\mathrm{km\,s^{-1}}$, respectively. The second baseband SPW1 was set to 231.00 GHz, i.e., 1.30 mm, to observe the continuum with a total bandwidth of 2.0 GHz, which also covers CO(2-1) with a velocity resolution of 0.64 $\mathrm{km\,s^{-1}}$. The frequency coverage for SPW3 ranges from 215.85 to 217.54 GHz to observe DCN(3-2), DCO^+(3-2), SiO($v = 0$)(5-4) and $CH_3OH(5_{1,4} - 4_{2,2})$. This paper will focus mostly on dense gas tracers $C^{18}O$, N_2D^+, DCO^+ and DCN.

The raw data were calibrated with the data reduction pipeline using *Casa* 4.7.0. The continuum visibility data were constructed with all line-free channels. We per-

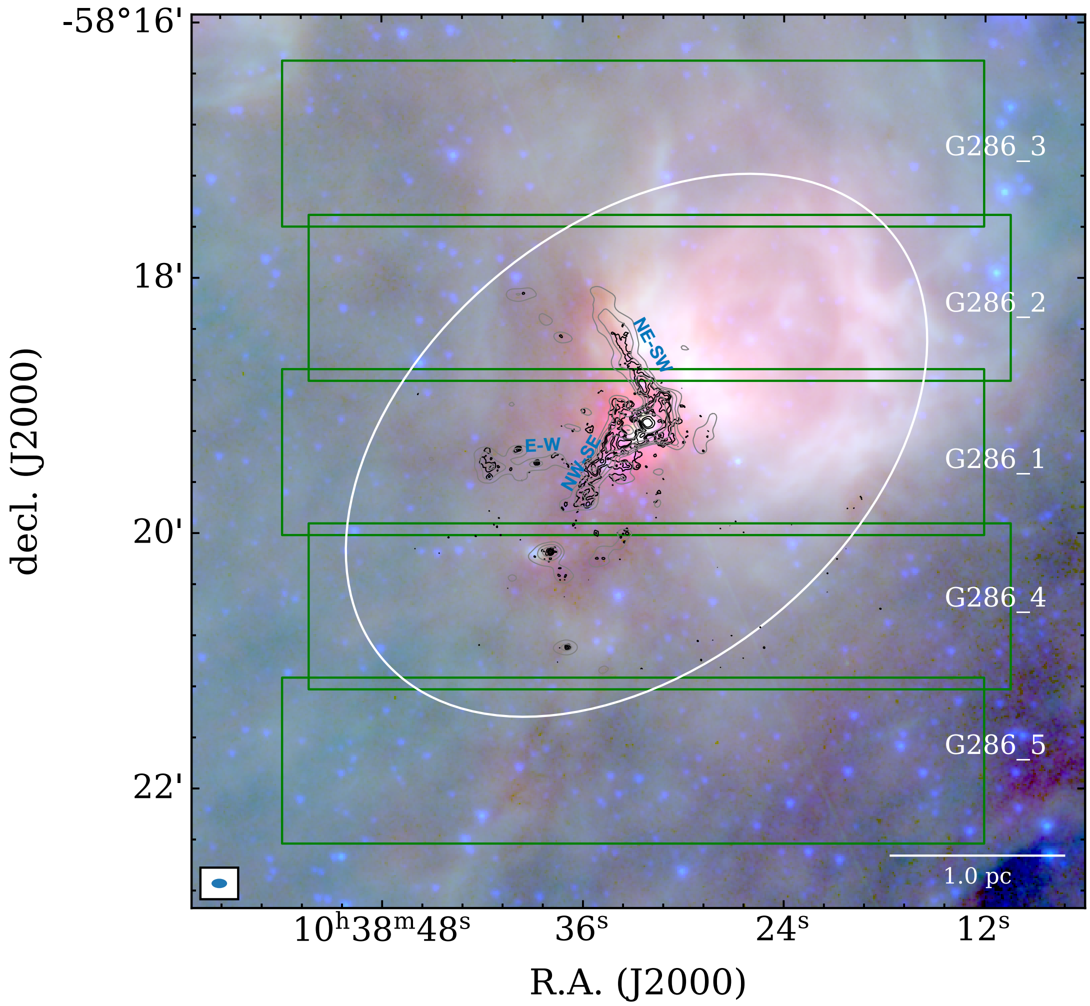

Figure 3.1: Three color image of G286 constructed by combining Spitzer IRAC 3.6 μm (blue), 8.0 μm (green), and Herschel PACS 70 μm (red). Black contours show the 1.3 mm continuum image combining ALMA 12-m and 7-m array data (with a resolution of $1.62'' \times 1.41''$). The contour levels are $1\sigma \times$ (4, 10, 20, 50, 100) with σ=0.45mJy beam^{-1}. Grey contours show the 1.3 mm continuum image with only 7-m array data (with a resolution of $7.32'' \times 4.42''$, shown in lower left corner). The contour levels are $1\sigma\times$ (4, 10, 20, 50, 100) with σ=1.7mJy beam^{-1}. The position of three filamentary structures are marked in blue text. The G286 field is divided into five strips, as shown by the green rectangles. Each strip is covered with 147 pointings of the 12-m array. The white ellipse denotes the boundary defined by Mopra HCO$^+$(1-0) emission (Barnes et al., 2011), with the major and minor axes equal to twice the FWHM lengths of the 2D gaussian fits to its emission.

formed imaging with *tclean* task in *Casa* and during cleaning we combined data for all five strips to generate a final mosaic map. Two sets of images were produced for different aspects of the analysis, one including the TP and 7-m array data and one combining TP, 7-m and 12-m data. The 7-m array data was imaged using a Briggs weighting scheme with a robust parameter of 0.5, which yields a resolution of $7.32'' \times 4.42''$. For the combined data, we used the same Briggs parameter. In addition, since we have extra *uv* coverage for part of the data, we also apply a $0.6''$ *uvtaper* to suppress longer baselines, which results in $1.62'' \times 1.41''$ resolution. Both image sets are then feathered with the total power image to correct for the missing large scale structures. Our sensitivity level is about 30 mJy per beam per 0.1 km/s for N_2D^+ and $C^{18}O$. A sensitivity of 45 mJy per beam per 0.1 km/s is achieved for DCO^+(3-2), DCN(3-2), SiO(5-4) and $CH_3OH(5_{1,4} - 4_{2,2})$.

3.2.2 Herschel Observations

The FIR dust continuum images of G286 were taken from *Herschel* Infrared GALactic plane survey (Hi-GAL; Molinari et al., 2010, 2016). The data includes Photodetector Array Camera and Spectrometer (PACS) (70 and 160 μm) and Spectral and Photometric Imaging REceiver (SPIRE) (250, 350, and 500 μm) images. We performed pixel by pixel graybody fits to derive the mass surface density (Σ) of the G286 region, following the procedures in Lim et al. (2016). The background was estimated as the median intensity value between 2 and 4 times the ellipse aperture shown in Figure 6.1. To better probe the smaller, higher Σ structures, we generated a higher-resolution Σ map by regridding the $\lambda \sim$160 to 500μm images to match the 250μm data (see Lim et al., 2016, for details).

3.3 General Results

An overview of the observed region and the layout of the ALMA observations is shown in Figure 6.1. With the large spatial dynamic range of the ALMA dataset, we will present the large scale structures traced with single dish TP observations first, followed by higher resolution 7-m and 12-m array observations.

3.3.1 Observations with the Total Power (TP) Array

Figure 3.2a shows the spectra of CO(2-1) and $C^{18}O$(2-1) averaged inside a 2.5′ radius aperture centered on the phase center. The CO(2-1) line has a maximum around the known systemic velocity of about -20 $\mathrm{km\,s^{-1}}$. A secondary, much weaker peak is seen around -9 $\mathrm{km\,s^{-1}}$. This component is also seen in the Mopra CO(2-1) map, which appears to be a diffuse structure larger than our field of view. We expect that this feature is probably contributed by a foreground or background cloud along line of sight and there is no indication of an interaction between this cloud and G286. Emission from $C^{18}O$(2-1) is only seen from the main -20 $\mathrm{km\,s^{-1}}$ component.

Figure 3.2b shows the spectra of the deuterated dense gas tracer N_2D^+(3-2) and DCO^+(3-2), averaged over the same region, and compared to $C^{18}O$(2-1), zooming-in to the velocity range of the main -20 $\mathrm{km\,s^{-1}}$ component. Deuterated species, such as DCO^+ and N_2D^+ are expected to be tracers of cold, dense gas, including material that is contained in pre-stellar cores (e.g., Crapsi et al., 2005; Bergin & Tafalla, 2007; Kong et al., 2015), and typically optical thin even at the core scale, as found in some examples in IRDCs (Tan et al., 2013). Interestingly, the $C^{18}O$(2-1) line exhibits a main gaussian-like profile with a slight skewness (or second component) to the redshifted side. The spectrum from DCO^+(3-2) shows a more pronounced double-peaked profile, with one component at about -20.5 $\mathrm{km\,s^{-1}}$ and the other at -18.5 $\mathrm{km\,s^{-1}}$.

The double-peak profile, i.e., with a stronger blue wing, has also been seen in the HCO^+(1-0) and HCO^+(4-3) line in Barnes et al. (2010), with similar central velocities for both peaks. It was interpreted by Barnes et al. (2010) as a canonical inverse P-Cygni profile indicating gravitational infall (Zhou et al., 1993). However, in this picture we would expect a single gaussian profile for optical thin tracers at the self-absorption velocity, in contrast to our DCO^+(3-2) spectrum. We will return in section 6.4 to the question of whether the claimed inverse P-Cygni profile in HCO^+ is really tracing global clump infall or whether it is arising from distinct spatial and kinematic substructures in the protocluster.

To further explore the kinematic structure of the clump, we present the CO(2-1) channel map from $-55.0\,\mathrm{km\,s^{-1}}$ to 15.0 $\mathrm{km\,s^{-1}}$ in Figure 3.3(a), where we have averaged four velocity channels in each displayed panel. The CO emission is widespread around the systemic velocity (-23 $\mathrm{km\,s^{-1}}$ to -17 $\mathrm{km\,s^{-1}}$). Bluewards of the line center the emission retains extension towards the southeast and then at the highest blueshifted velocities, e.g., $v \lesssim -45\,\mathrm{km\,s^{-1}}$, appears more concentrated. The redshifted emission shows more complex structure, including from emission features already mentioned at around $v = -9\,\mathrm{km\,s^{-1}}$, which may be from an unrelated cloud along the line of sight. However, high velocity ($\Delta v \gtrsim 25\,\mathrm{km\,s^{-1}}$) redshifted gas is still seen near the phase center. These high velocity features, both blue- and redshifted, are likely to be caused by protostellar outflow activity from within the G286 star-forming clump.

The clump-averaged spectra could be affected by multiple factors including collapse, rotation and outflows. To better resolve the kinematics near the systemic velocity where ^{12}CO(2-1) is expected to be mostly optically thick, in Figure 3.3(b) we show the $C^{18}O$(2-1) channel map from -23.0 $\mathrm{km\,s^{-1}}$ to -17.0 $\mathrm{km\,s^{-1}}$. This $C^{18}O$ emission at around -20 $\mathrm{km\,s^{-1}}$ is moderately elongated in the North-South direction. In

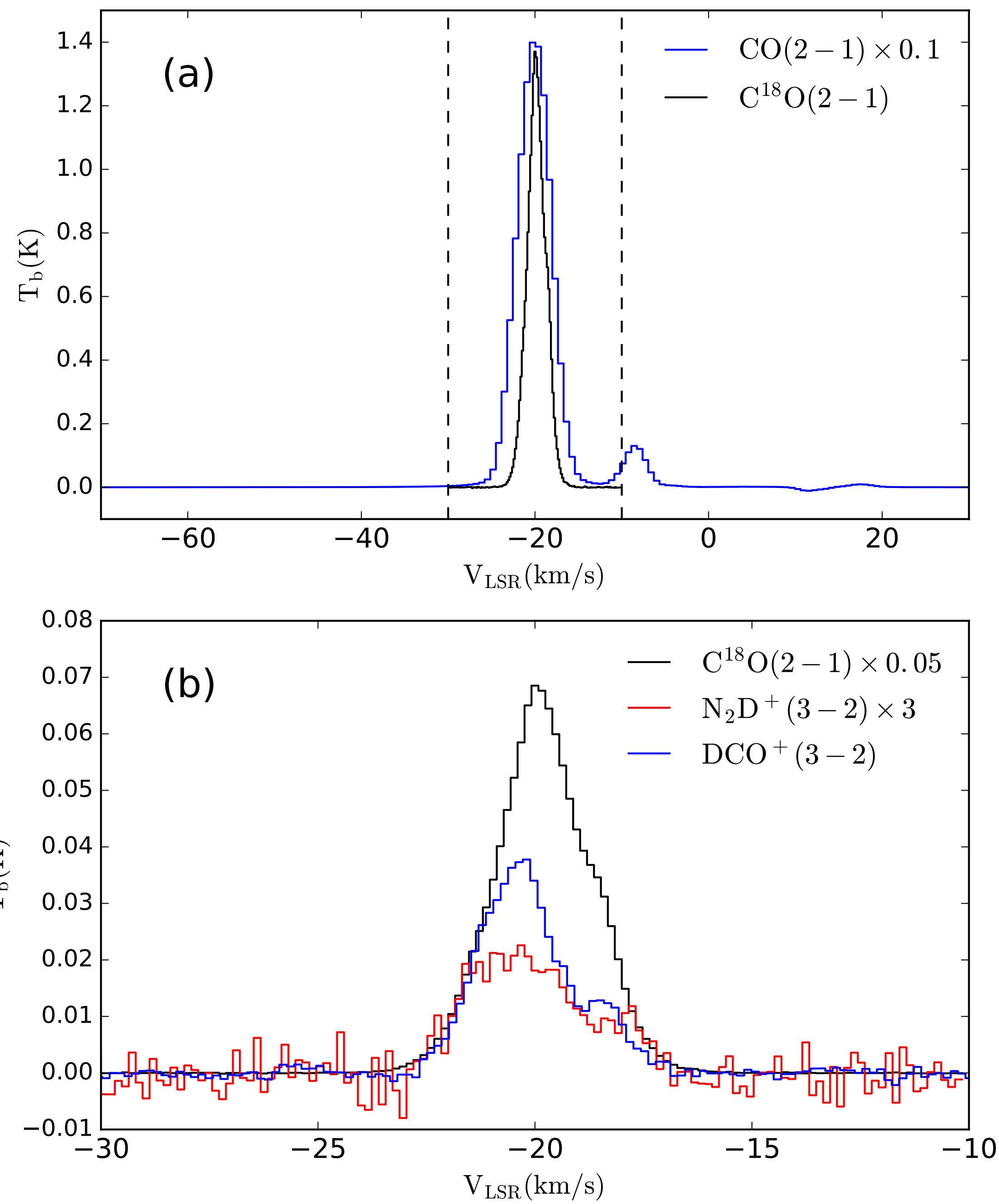

Figure 3.2: *(a)* Averaged CO(2-1) and $C^{18}O$(2-1) TP spectra extracted over a 2.5′ radius aperture centered on the phase center. Note the flux scale of CO(2-1) has been reduced by a factor of 10. *(b)* Same as *(a)* but for $C^{18}O$(2-1), N_2D^+(3-2) and DCO^+(3-2) in a smaller velocity range from -30 to -10 $km\,s^{-1}$. The flux scale of $C^{18}O$(2-1) is reduced by a factor of 20 and that of N_2D^+(3-2) is increased by a factor of 3 for ease of comparison. Note the N_2D^+(3-2) emission is affected by hyperfine structure, while the DCO^+(3-2) is not.

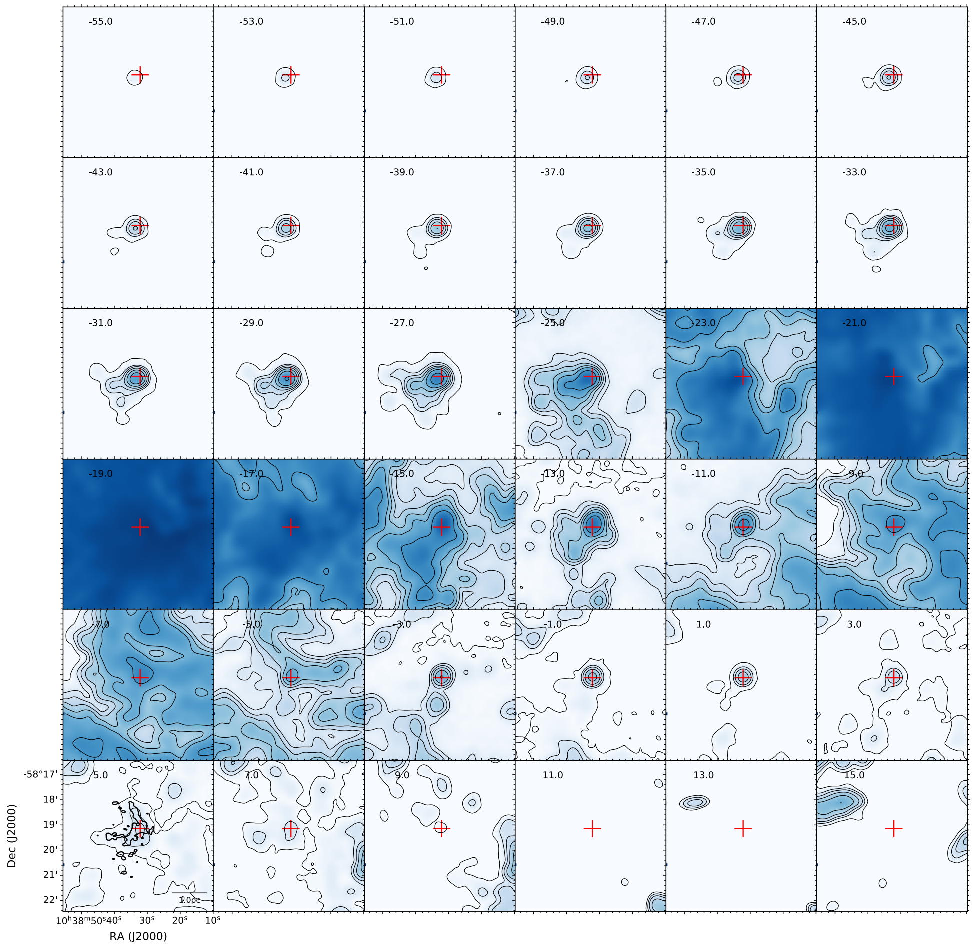

(a)

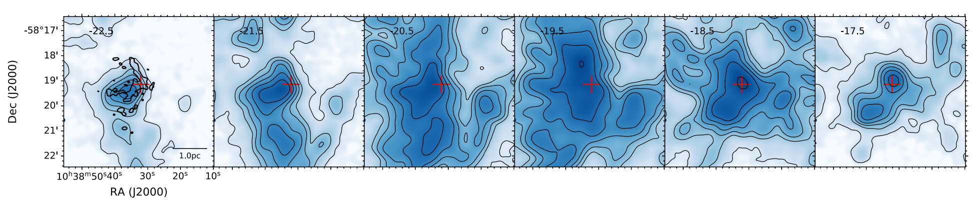

(b)

Figure 3.3: *(a)* Channel maps of TP CO(2-1) emission integrated over every 2.0 $\mathrm{km\,s^{-1}}$, as indicated in the upper left of each panel (indicating central velocity of the range), from -55.0 to +15.0 $\mathrm{km\,s^{-1}}$. The contour levels are 1 $\mathrm{Jy\,beam^{-1}\ km\,s^{-1}} \times$ (1, 5, 10, 20, 40, 80, 200). The red cross in each panel marks the phase center of the observation (R.A.=10:38:33, decl.=-58:19:22). The thick black contour in the lower left panel shows the 4σ level of the 7-m continuum emission. *(b)* Channel maps of TP $\mathrm{C^{18}O}$(2-1) emission integrated over every 1.0 $\mathrm{km\,s^{-1}}$, with ranges from -22.5 to -17.5 $\mathrm{km\,s^{-1}}$. The contour levels are 1 $\mathrm{Jy\,beam^{-1}\ km\,s^{-1}} \times$ (1, 5, 10, 20, 40, 80, 200). The thick black contour in the left panel shows the 4σ level of the 7-m continuum emission.

the central 2′ region, the $C^{18}O$(2-1) at blueshifted velocities is mostly extended to the southeast, while at the corresponding redshifted velocities, there is a more complex, widespread morphology, including some material at northeastern and southeastern locations.

3.3.2 Observations of the 7-m and 12-m arrays

Figure 3.4 presents summary maps of four spectral lines $C^{18}O$(2-1), N_2D^+(3-2), DCO^+(3-2) and DCN(3-2) from left to right overlaid on 1.3 mm continuum image in black contours. The top two rows show the moment 0 and moment 1 map of the 7-m array images, respectively. As shown in the moment 0 map, $C^{18}O$ traces structures that are more spatially extended than other lines. N_2D^+ and DCO^+ are more closely associated with the dust continuum, but their distributions are slightly different. N_2D^+ is mainly detected towards the NW-SE filament and the southern part of the NE-SW filament. Note also that not all the regions with strong dust continuum have detections of N_2D^+. In particular, there is a deficiency of N_2D^+ emission towards the central brightest clump. DCO^+ emission, on the other hand, appears slightly more extended. There is also an E-W filamentary feature to the east of NW-SE filament. This E-W filament is not seen clearly in continuum emission, where we only observe a few cores strung out along the EW direction, but these do appear to be connected by weak diffuse dust emission seen at a 3-σ level. Additionally, DCO^+ is also detected towards a few positions to the south of NW-SE filament. The spatial distribution of DCN emission is dramatically different from N_2D^+ and DCO^+: it is strongly concentrated towards the clump in the center, where no detection or only weak detection is seen for N_2D^+ and DCO^+. DCN emission becomes weaker away from the center.

The different morphological distributions of the deuterated species may be due

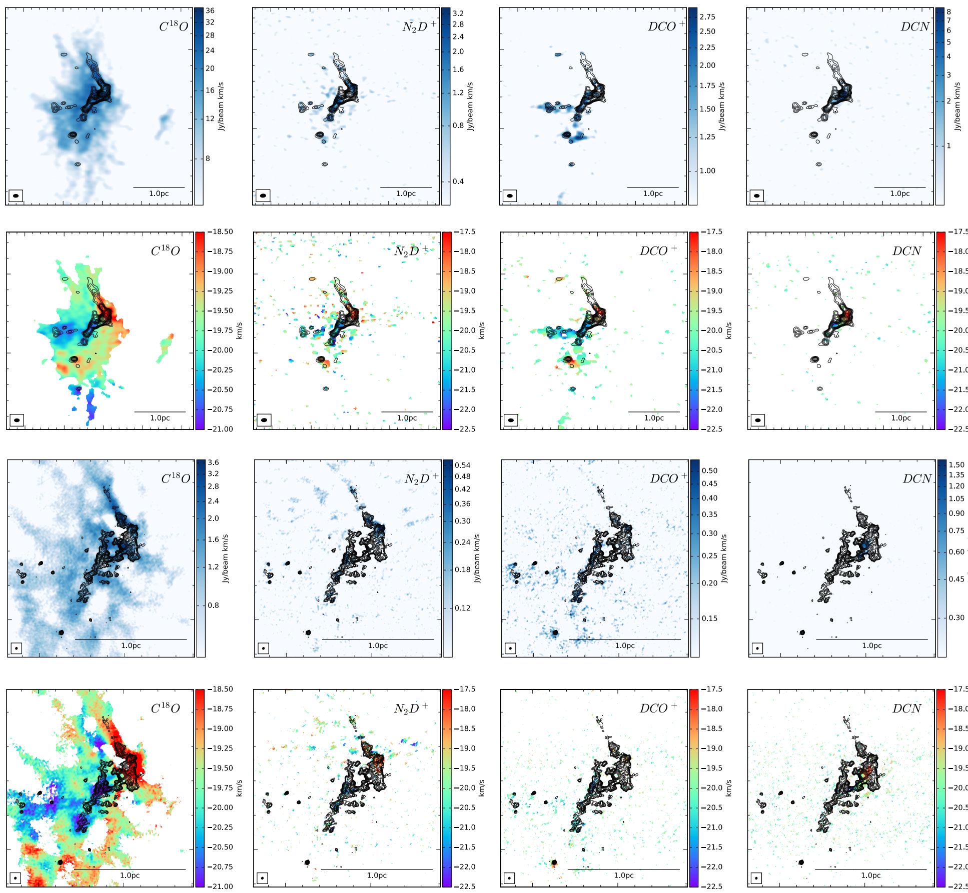

Figure 3.4: Summary figure for the 7-m and 12-m line observations. Columns from left to right show the results of $C^{18}O$(2-1), N_2D^+(3-2), DCO^+(3-2) and DCN(3-2), respectively. From top to bottom, the color scales show the maps of 7-m moment 0, 7-m moment 1, 7-m+12-m moment 0, 7-m+12-m moment 1. The color bar at the right corner indicates the flux scale in Jy beam^{-1} for moment 0 maps, and velocity in km s^{-1} for moment 1 maps. The black contours illustrates the 1.3 mm continuum emission for comparision, with the first two rows showing 7-m cotinuum image and last two rows 7-m+12-m image.

chemical differentiation. In general, N_2D^+ is known as a good tracer of cold ($T \lesssim$ 20 K), dense gas, where H_2D^+ builds up in abundance, but where CO is mostly frozen out on to dust grains (e.g., Fontani et al., 2015). Formation of DCO^+ requires both H_2D^+ and gas phase CO (e.g., Millar et al., 1989), which requires a temperature $\lesssim$

30 K but not too cold to cause significant CO freeze-out. On the other hand, the primary DCN formation mechanisms are thought to require CH_2D^+ instead of H_2D^+, which is energetically favorable up to ∼80 K (e.g., Millar et al., 1989; Turner, 2001). Additionally, sputtering from grain mantles can also lead to enhancement of DCN abundance in shocked regions (e.g., Busquet et al., 2017). Hence we would generally expect more DCN emssion in relatively later evolutionary stages. The concentrated distribution of DCN, combined with more wide-spread N_2D^+ and DCO^+ emission, indicates a sceneario that star formation, especially more massive, luminous star formation, has taken place first in the central regions of G286 compared to in the more extended filaments.

The second row of Figure 3.4 shows the moment 1 map of the 7-m array images. The $C^{18}O$ moment 1 map reveals redshifted emission associated with the NE-SW filament and then continuing to the south of NW-SE filament, while the NW-SE filament and E-W filament are mainly associated with blueshifted gas. Other dense gas tracers show similar velocity patterns as $C^{18}O$, but with the emission mainly detected towards dense continuum clumps. In particular, DCN illustrates the blue-red velocity transition across the central clump in the NW-SE direction.

A zoom-in view of G286 is presented in the third and fourth row of Figure 3.4, illustrating the moment 0 and moment 1 map of combined 12-m+7-m array image with a resolution of $\sim 1.5''$. The continuum image reveals a higher level of fragmentation and many well-defined dense cores, with a typical size of a few thousand AU. The E-W filament and part of the NE-SW filament are resolved out in this continuum image. The intensity and velocity distribution of $C^{18}O$ appears more complicated seen in high resolution. Other dense gas tracers like N_2D^+ still have good association with continuum at the core scale, and the velocity pattern is also consistent with that seen in the 7-m image.

Table 3.1: Properties of the NE-SW Filament

Properties	Strip 1	Strip 2	Strip 3	Strip 4	Total
$\overline{\Sigma}_{\rm sed}$ (g cm^{-2})	0.25	0.17	0.13	0.12	0.17
$M_{\rm sed}$ ($M_\odot$)	53	36	27	26	142
$M_{\rm 1.3mm}$ ($M_\odot$)	25	17	21	11	74
$m_{\rm sed,f}$ ($M_\odot$ pc^{-1})	254	170	130	123	170
$\overline{v}_f$ (km s^{-1})	-17.85	-18.59	-19.01	-19.40	-18.73
$\sigma_{\rm C^{18}O}$(km s^{-1})	0.40	0.52	0.53	0.61	0.52[a]
σ_f(km s^{-1})	0.48	0.58	0.59	0.66	0.58
$m_{\rm vir,f}$ ($M_\odot$ pc^{-1})	106	158	160	204	158
$m_f/m_{\rm vir,f}$	2.39	1.08	0.81	0.60	1.08

[a] For velocity dispersion we take the linear average of 4 strips.

In Figure 3.5 we present the 12-m + 7-m C^{18}O image with integrated emission in different velocity intervals shown in different colors, i.e., -23.0 to -20.5 km s^{-1} in blue, -20.5 to -19.5 km s^{-1} in green and -19.5 to -17.0 km s^{-1} in red. Besides the velocity structures seen in Figure 3.4, this plot also reveals highly filamentary C^{18}O features around the systemic velocity. These filaments are more spatially extended than the continuum. While some of this morphology may be affected by artificial sidelobes from imperfect cleaning of the interferometric data, at least some of the C^{18}O(2-1) filaments have corresponding detections in the continuum and hence are most likely to be real features.

3.4 Filamentary Virial Analysis

As shown in Figure 6.1, the millimeter continuum emission reveals two main filaments: a northern one with a NE-SW orientation and a southern one with a NW-SE orientation. Here we perform a filamentary virial analysis following Fiege & Pudritz (2000). Since the NE-SW filament is mostly filtered out at higher resolution, we utilize the 7-m array data (continuum and C^{18}O) for this section.

Figure 3.6 illustrates the C^{18}O(2-1) emission, integrated over every 0.5 km s^{-1} from -22.0 to -17.0 km s^{-1}. As in Figure 3.5, filamentary structures are seen near

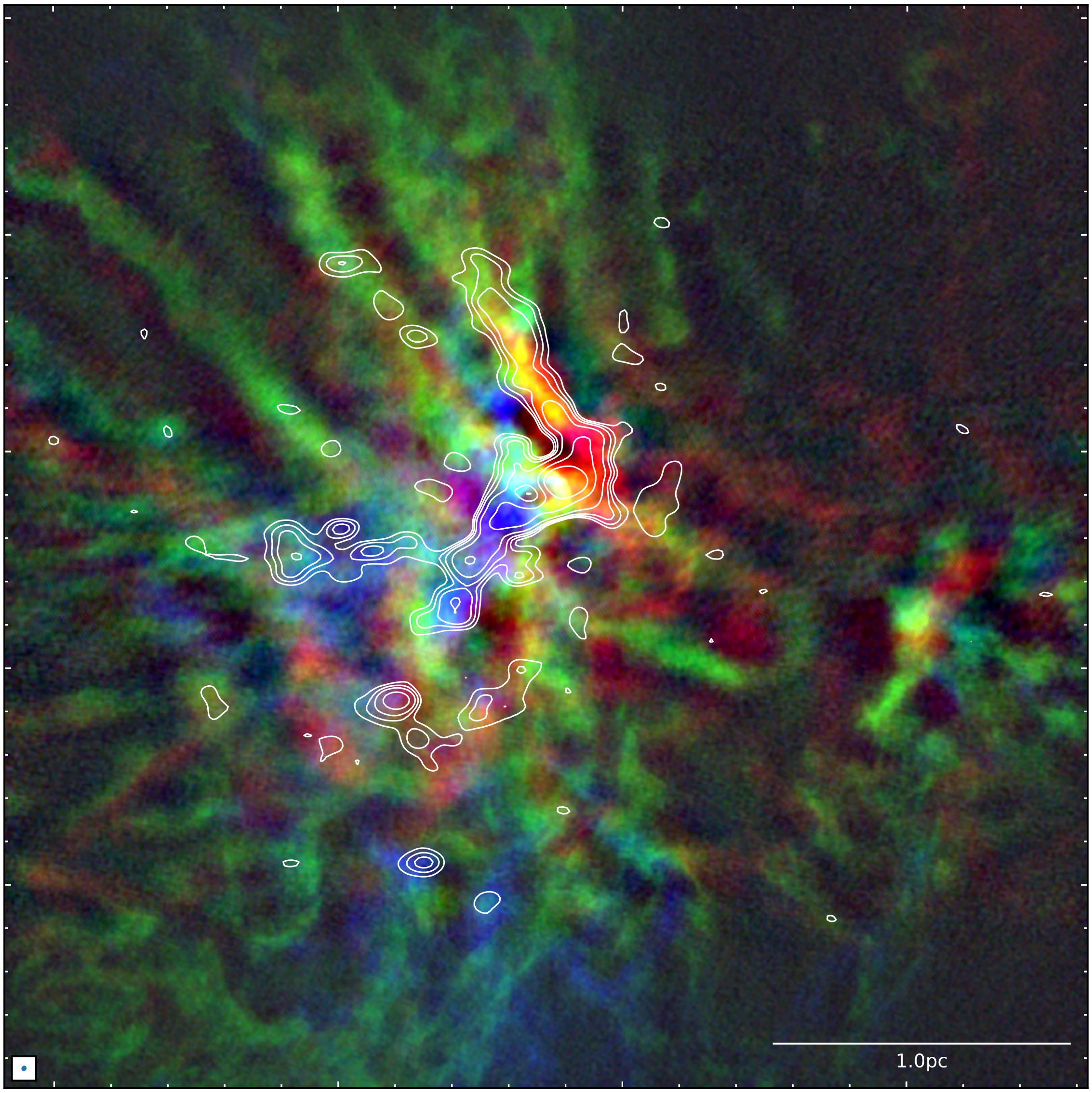

Figure 3.5: Three color image constructed with integrated 12-m + 7-m $C^{18}O$(2-1) emission (-23.0 – -20.5 $km\,s^{-1}$ in blue, -20.5 – -19.5 $km\,s^{-1}$ in green and -19.5 – -17.0 $km\,s^{-1}$ in red). The synthesized beam ($1.56'' \times 1.40''$) is shown in the lower left corner. The 7-m continuum image is shown in white contours for comparison. The contour levels are 1.7 mJy $beam^{-1} \times$ (3, 6, 10, 20, 50, 100).

the systemic velocity of -20 $km\,s^{-1}$. At least three of the $C^{18}O$(2-1) filaments have corresponding detections in the continuum at a 2σ level and hence are most likely real features, rather than sidelobe artifacts. The most prominent filament is associated with the NE-SW continuum filament and is clearly seen from -20.0 km s^{-1} to -17.0 km s^{-1}. The NW-SE filament appears more complicated in C^{18}O(2-1) and is not well described as being a coherent C^{18}O filamentary structure. Therefore we carry out a virial analysis only for the NE-SW filament.

As shown by Fiege & Pudritz (2000), a pressure-confined, non-rotating, self-gravitating, filamentary (i.e., length $\gg$ width) magnetized cloud that is in virial equilibrium satisfies

$$\frac{P_e}{P_f} = 1 - \frac{m_f}{m_{\rm vir,f}}\left(1 - \frac{M_f}{|W_f|}\right) \tag{3.1}$$

where P_f is the mean total pressure in the filament, P_e is the external pressure at its surface, m_f is its mass per unit length, $m_{\rm vir,f} = 2\sigma_f^2/G$ is its virial mass per unit length, and M_f and W_f are the gravitational energy and magnetic energy per unit length, respectively. Here, because of the observational difficulties of measuring the surface pressure and magnetic fields, we ignore the surface term and magnetic energy term, i.e., only considering the balance between gravity and internal pressure support.

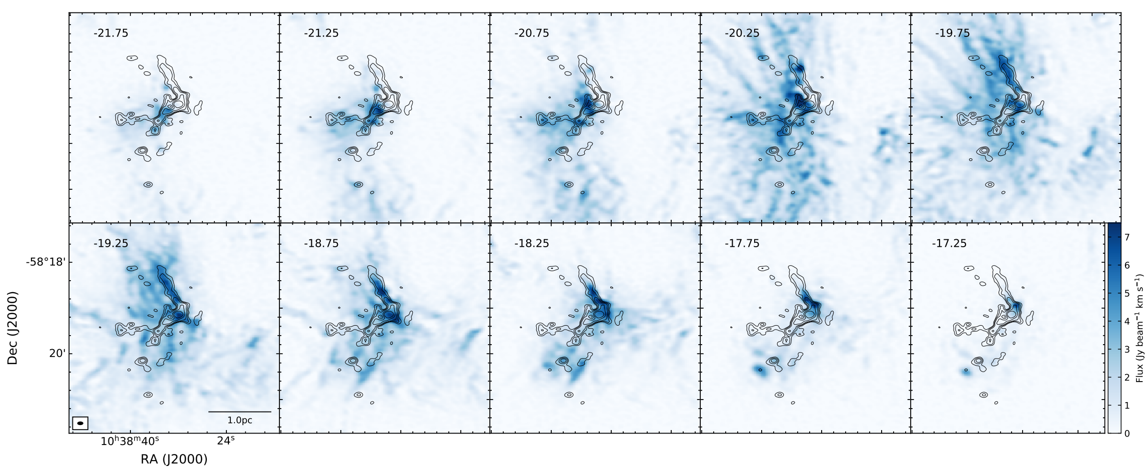

Figure 3.6: 7-m C^{18}O(2-1) emission integrated over 0.5 km s^{-1} intervals, as indicated in the upper left of each panel, from -22.0 to -17.0 km s^{-1}. The black contours show the 7m array 1.3 mm continuum emission. The contour levels are 1.7 mJy beam$^{-1}\times$ (4, 10, 20, 50, 100).

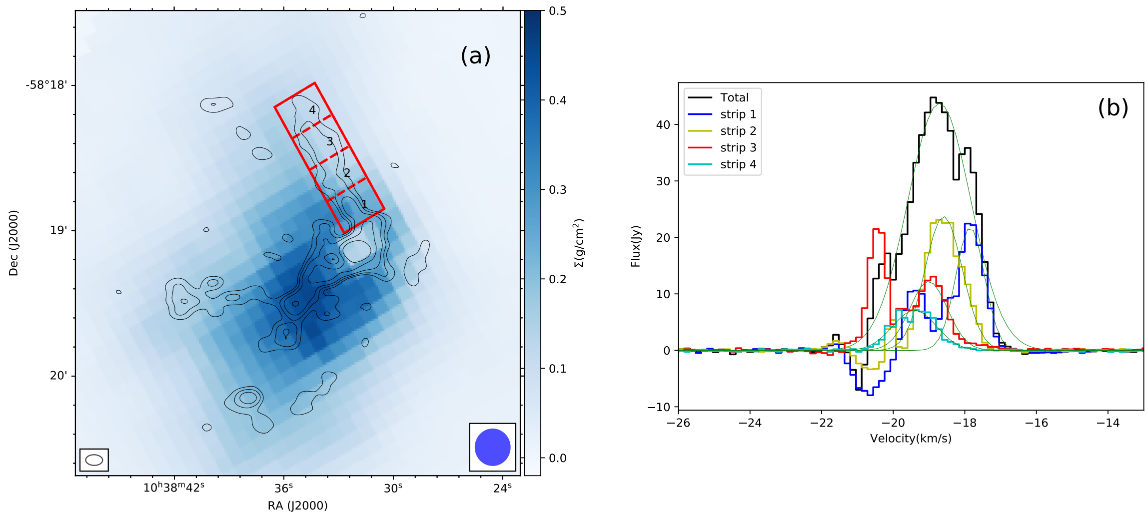

Figure 3.7: *(a)* Column density map made with *Herchel* sub-mm continuum data, overlaid on the 7-m array continuum emission in contours. The contour levels are 1.7mJy beam$^{-1}\times$ (4, 10, 20, 50, 100). The *ALMA* synthesized beam is shown in the lower left corner, while the resolution of the *Herschel*-derived mass surface density map is shown in the lower right. The red rectangles dilineate the position of the NE-SW filament and its division into four strips, numbered 1 to 4 from south to north. *(b)* $C^{18}O$(2-1) spectra of the four strips of the NE-SW filament and the total (see legend). The green lines show primary gaussian component fits to these spectra.

To measure the properties of the filament we show in Figure 3.7a a $60'' \times 20''$ rectangle that closely encompasses the NE-SW filament, which we use to define the filament boundary. From the *Herschel*-SED-derived mass surface density map we find average values of $\Sigma_{\rm sed}$ in the strips ranging from 0.25 g cm^{-2} (in Strip 1 that is closest to the center of G286) to 0.12 g cm^{-2} (in Strip 4) (see section 3.4). The mass in each region is then estimated, with values of between $M_{\rm sed}$ = 26 and 53 $M_\odot$. For comparision, we also calculate masses from the 1.3 mm continuum flux, assuming a temperature of 20 K and other dust properties following Cheng et al. (2018). We find the 1.3 mm-derived mass estimates are about a factor of two smaller than that measured from the *Herschel*-SED fitting method. Since the *ALMA* 7-m array observations only probe scales up to $\sim 19''$, they are likely to be missing some flux from the filament leading to an underestimation of the masses, and so here we adopt the *Herschel*-SED-derived mass estimates for the virial analysis.

The 60″ length of the filament corresponds to 0.73 pc at an assumed distance of 2.5 kpc. We assume a 10% uncertainty in the distance (e.g., Barnes et al., 2010). Without direct observational constraints, we further assume the filament axis is inclined by an angle $i = 60°$ to the line of sight (90° would be in the plane of the sky). If an inclination angle of 90 or 30° were to be adopted, then the length estimates would differ by factors of 1.15 and 0.577, respectively. Thus the actual the length of the filament is assumed to be 0.84 pc (or 3/4 of this from the centers of Strip 1 to Strip 4). Thus the overall mass per unit length of the filament is $m_{\rm sed,f} \sim 170\ M_\odot\ {\rm pc}^{-1}$, with Strip 1 having a higher value of $\sim 250\ M_\odot\ {\rm pc}^{-1}$.

The mean line-of-sight velocity and velocity dispersion of the filament are measured from the average $C^{18}O$ spectra inside the rectangular regions. To reduce contamination from surrounding ambient gas at the systemic velocity, we utilize the image cube made with only the 7-m array data (i.e., without feathering with the TP data), as illustrated in Figure 3.7b. We perform gaussian fitting to measure the average centroid velocity $\overline{v}_f$ and velocity dispersion $\sigma_{C^{18}O}$.

The values of $\overline{v}_f$ show a steady progression from $-17.85\ {\rm km\,s^{-1}}$ in Strip 1 to $-19.40 {\rm km\,s^{-1}}$ in Strip 4, which corresponds to an overall velocity gradient of $2.84 {\rm km\,s^{-1}\,pc^{-1}}$ using plane-of-sky projected distance or $2.46\ {\rm km\,s^{-1}\,pc^{-1}}$ for the assumed 60° inclination. We can compare these kinematics to the IRDC filament studied by Hernandez et al. (2011, 2012), which has a length of 3.77 pc on the sky (4.35 pc for the assumed 60° inclination) and also had its $C^{18}O$(2-1) emission analyzed in 4 strips. Here the velocities did not show a steady progression, but showed differences of about $0.5\ {\rm km\,s^{-1}}$ from strip to strip, i.e., corresponding to velocity gradients of about $0.53\ {\rm km\,s^{-1}\,pc^{-1}}$ in the plane of the sky. The larger and more systematic velocity gradient shown in the NE-SW filament in G286 may be the result of acceleration due to infall into the protocluster potential. Strip 4 has a mean velocity similar to that of the ambient, larger-scale gas in the region, while Strip 1, closer in projection to the protocluster center, is redshifted with respect to this velocity. Thus in this scenario the Strip 4 end of the filament is closer to us than the protocluster center.

If the velocity change from Strip 4 to Strip 1, i.e., $+1.55\,\mathrm{km\,s^{-1}}$, is due to infall in the protocluster potential, then we can use this information to constrain the mass of the protocluster. Assuming an uniform distribution of matter in a spherical protocluster clump of radius L, the change in potential from the edge to the center is $GM/(2L)$. If material starts at rest at radius L, i.e., the Strip 4 position, and then accelerates to velocity v_1, of which we observe v_1 cos$i$, then the mass inside radius L is

$$M = \frac{232}{\cos^2 i \sin i} \left(\frac{v_{1,\mathrm{obs}}}{\mathrm{km/s}}\right)^2 \left(\frac{L_{\mathrm{obs}}}{\mathrm{pc}}\right) M_\odot. \tag{3.2}$$

For an observed length L_{obs} from the center of Strip 4 to the center of Strip 1 of 0.55 pc (i.e., 3/4 of 0.73 pc) and a line of sight velocity difference of $1.55\,\mathrm{km\,s^{-1}}$, we thus estimate the dynamical mass to be $1410\,M_\odot$, assuming $i = 60°$. If an inclination angle of 30° or 70° is adopted, the mass would be 814 or $2780\,M_\odot$, respectively. This estimation is consistent with that derived from *Herschel*-SED fitting ($\sim 1500\,M_\odot$, Ma et al., in prep.).

Considering the internal dynamics of the filament, in order to account for support against gravity from both thermal and non-thermal motions of the gas, we subtract the thermal component of broadening of the $C^{18}O$(2-1) line from the measured velocity dispersion (in quadrature, assuming a temperature of 20 K) and add back the sound speed to obtain the total 1D velocity dispersion, σ_f, i.e.,

$$\sigma_f = \left(\sigma_{\rm nth}^2 + \sigma_{\rm th}^2\right)^{1/2} = \left(\sigma_{\rm C^{18}O}^2 - \frac{k_B T}{\mu_{\rm C^{18}O} m_p} + \frac{k_B T}{\mu_p m_p}\right)^{1/2} \tag{3.3}$$

where $\mu_p = 2.33$ is the mean molecular weight assuming $n_{\rm He} = 0.1 n_{\rm H}$ and $\mu_{\rm C^{18}O}$ is the molecular weight of $C^{18}O$. We have then carried out a virial analysis for each of the four strips (see section 3.4). Note, for Strips 1 and 3 we fit the spectra with two gaussian components and utilize the component that is more clearly associated with the filament. For example, in Strip 3, the velocity component near -20.5 $\mathrm{km\,s^{-1}}$ is contributed by another gas clump to the north-west of the filament.

The values of $m_f/m_{\rm vir,f}$ of the four strips range from 0.60 to 2.39. Given the systematic uncertainties in measuring the masses and lengths of the structures that combine to be at least $\sim$ 50%, these values are consistent with the filament being in approximate virial equilibrium, even without accounting for surface pressure and magnetic support terms. We also note that the values of $m_f/m_{\rm vir,f}$ grow, i.e., becoming less gravitationally bound, as one progresses from Strip 4 to Strip 1. This may indicate that infall motions and/or tidal forces towards the center of the protocluster act to stabilize the filament.

3.5 Kinematic properties of the dense core sample

Cheng et al. (2018) analysed the mass distribution of dense cores towards the central region of G286 (about $2.2' \times 1.5'$), where the uv coverage of the observation allows imaging with $\sim 1''$ resolution. Here we carry out a kinematic follow-up study on the dense core sample in this region.

Figure 3.8 shows the integrated intensity map of $C^{18}O$(2-1), N_2D^+(3-2), DCO^+(3-

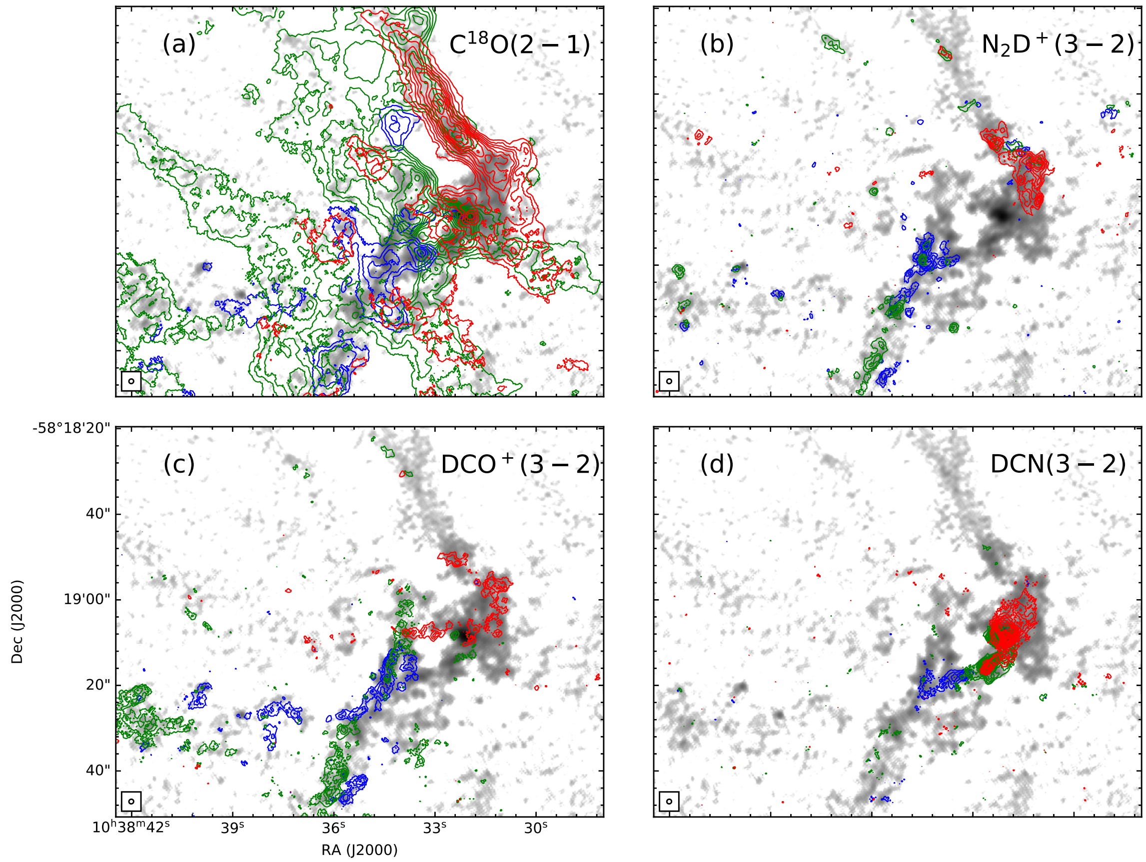

Figure 3.8: *(a)* $C^{18}O$ integrated intensity map using combined 7-m + 12-m array data. Red, green and blue contours show emission integrated from -23 to -21 $km\,s^{-1}$, -21 to 19 $km\,s^{-1}$ and -19 to -17 $km\,s^{-1}$, respectively. The contours start from 4σ in step of 2σ, with $\sigma = 0.1$ Jy beam$^{-1}\cdot$ km s^{-1}. The grey scale image is the 1.0″resolution 7-m + 12-m array combined 1.3 mm continuum image. *(b)* Same as panel (a), but for N_2D^+(3-2). The contours start from 4σ in step of 2σ, with $\sigma = 0.025$ Jy beam$^{-1}\cdot$ km s^{-1}. *(c)* Same as panel (a), but for DCO^+(3-2). The contours start from 4σ in step of 2σ, with $\sigma = 0.03$ Jy beam$^{-1}\cdot$ km s^{-1}. *(d)* Same as panel (a), but for DCN(3-2). The contours start from 4σ in step of 2σ, with $\sigma = 0.03$ Jy beam$^{-1}\cdot$ km s^{-1}.

2) and DCN(3-2) in the central region, with three velocity ranges shown in different colors. This map is similar to the 12-m + 7-m moment maps in Figure 3.4, but emphasizes relatively weaker features that might be missing in Figure 3.4 due to higher noise resulting from its wider velocity range. Most cores in this region have significant detection from at least one of the three dense gas tracers: N_2D^+(3-2),

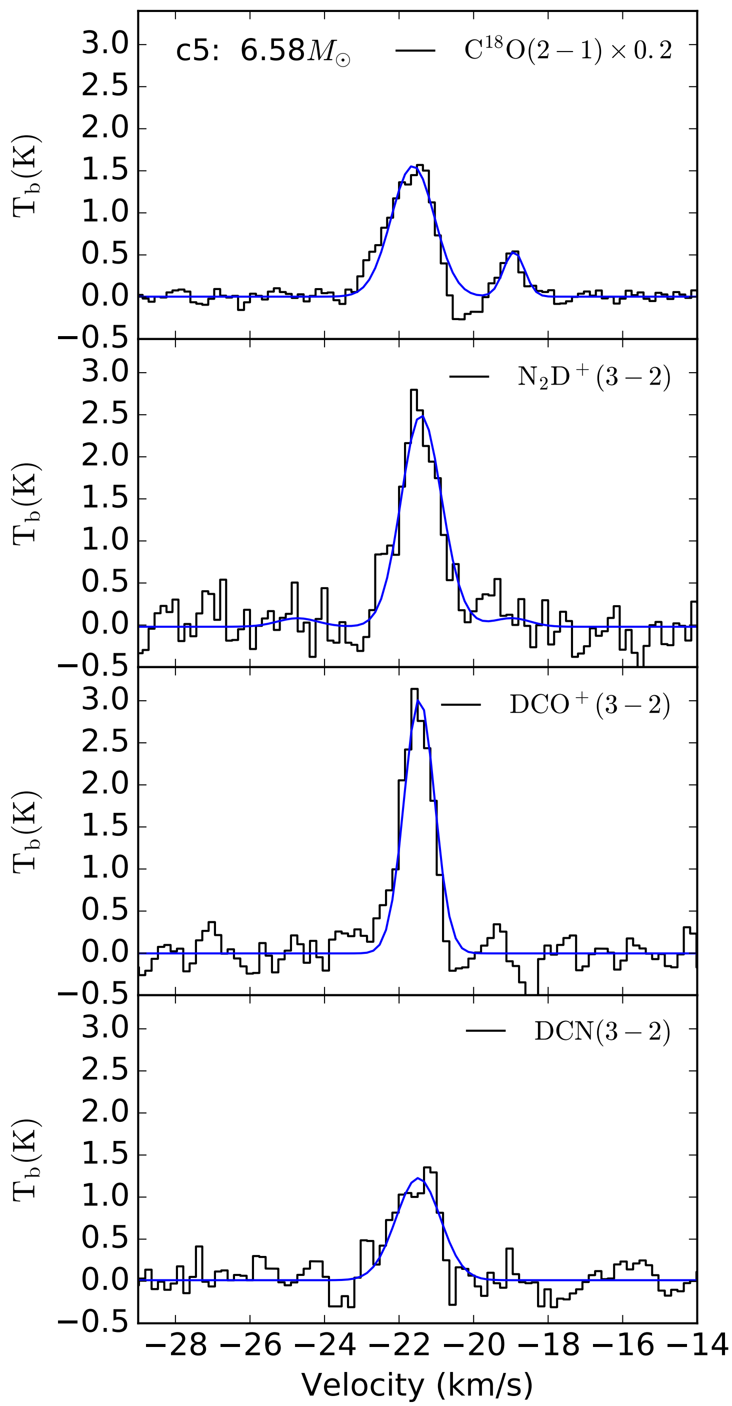

Figure 3.9: An example of the spectral line fitting for G286c5. Here we use one gaussian component to fit the spectra of N_2D^+(3-2), DCO^+(3-2) and DCN(3-2), and two components for $C^{18}O$(2-1).

DCO^+(3-2) and DCN(3-2), and this allows us to measure the centroid velocity and velocity dispersion for each dense core.

3.5.1 Review of the core sample based on dust continuum emission

Cheng et al. (2018) reported different numbers of identified cores, ranging from 60 to 125, depending on the detection algorithm and parameter choices of these algorithms. Here we adopt the fiducial dendrogram identified core sample with a base threshold of 4σ, a delta threshold of 1σ, along with a minimum area of half a synthesized beam size. This parameter combination yields 76 cores.

In Table A.1 we list the properties of the dense core sample. The cores are here named as G286c1, G286c2, etc., with the numbering order from highest to lowest core mass. The masses are estimated to range from 0.19 $M_\odot$ to 80 $M_\odot$, assuming a constant temperature of 20 K for each core (see Cheng et al. (2018) for more details). The radius is evaluated as $R_c = \sqrt{A/\pi}$, where A is the projected area of the core. The median radius is 0.011 pc, similar to the spatial resolution ($\sim$1″, 2500 AU), indicating many cores are not well resolved. Note that we adopt the core area returned by *Dendrogram*, which is defined with an isophotal boundary at a certain flux level, i.e., the level where two cores merge together or the 4σ flux threshold for isolated cores. So the core area or radius could be underestimated in a crowded field.

We then evaluate the mean mass surface density of the cores as $\Sigma_c \equiv M/A$. The median mass surface density of our sample is ~ 0.65 g cm^{-2} and all the cores have values $\gtrsim 0.4$ g cm^{-2}. We also evaluate the mean H nuclei number density in the cores, $n_{\mathrm{H},c} \equiv M_c/(\mu_\mathrm{H} V)$, where $\mu_\mathrm{H} = 1.4 m_\mathrm{H}$ is the mean mass per H assuming $n_\mathrm{He} = 0.1\ n_\mathrm{H}$ and $V = 4\pi R_c^3/3$. The mean value of $\log_{10}(n_{\mathrm{H},c}/\mathrm{cm}^{-3})$ is 6.88, with a standard deviation of 0.24.

3.5.2 Spectral fitting

We extract the average $C^{18}O$(2-1), N_2D^+(3-2), DCO^+(3-2) and DCN(3-2) spectra of each core, which are shown in Figure A.1 and Figure A.2. Among the four tracers $C^{18}O$ is the strongest for almost all the cores, and sometimes the $C^{18}O$ profiles can be complex. Other lines are relatively weak and only detected for part of the core sample.

To measure the centroid velocity and velocity dispersion of each core we only fit spectra with well defined profiles, i.e., those with a peak greater than a certain threshold value. Here we adopt a 4σ criterion for this threshold value. Since the noise levels of the average spectra vary for different cores (depending on the pixel numbers in the core, etc.), we estimate the rms noise separately for each core and each line using the signal-free channels. This signal to noise criterion gives 74 cores detected in $C^{18}O$(2-1)(97%), 27 in N_2D^+(3-2)(36%), 45 in DCO^+(3-2)(59%) and 29 in DCN(3-2)(38%). We also checked the single pixel spectra at the continuum peak of each core and found that the vast majority have similar line profiles as the averaged spectra, but the signal to noise ratios are usually lower, so we proceed with our analysis using the core-averaged spectra.

We characterize the $C^{18}O$(2-1) spectra with 1-d gaussian fitting using the *curve_fit* function in the *Scipy.optimize* python module. Most cores can be well described with a single gaussian component. In general, we expect that $C^{18}O$(2-1) traces lower density envelope gas surrounding the dense core and thus could be more affected by multiple components along the line of sight. In 31 cores where a spectrum has more complex profiles and hence can not be well approximated by a single gaussian, we allow for a second gaussian component.

For the DCO^+(3-2) and DCN(3-2) lines we also perform the gaussian fitting with *curve_fit* function. For the N_2D^+(3-2) line, to account for the full blended hyperfine components, we use the hyperfine line fitting routine in *pyspeckit* (Ginsburg & Mirocha, 2011), with the relative frequencies and optical depths for N_2D^+ taken from Dore et al. (2004) and Pagani et al. (2009). These dense gas tracers are usually well described with one gaussian component. Figure 3.9 shows a example of the line fitting. In particular, in one case (i.e., G286c3), two separate components were clearly required for a good fit for N_2D^+ and DCO^+. These two components are mostly likely to belong to two separate entities that are not resolved in their continuum emission.

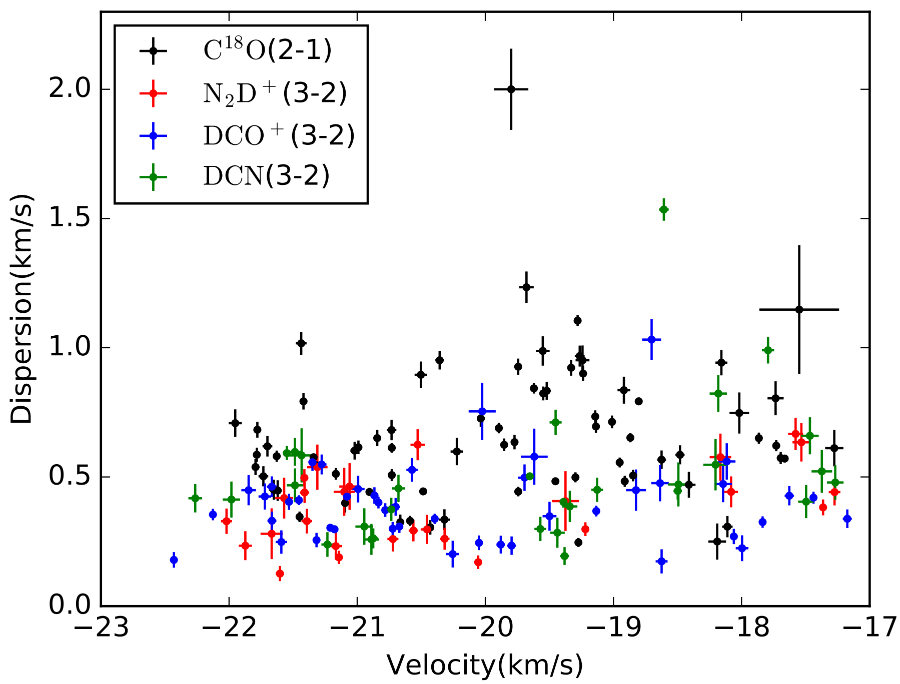

Figure 3.10: The centroid core velocity and velocity dispersion of each core measured with $C^{18}O$(2-1), N_2D^+(3-2), DCO^+(3-2) and DCN(3-2).

3.5.3 Comments on individual cores

G286c1: This is the most massive core in G286, with a mass of 80 $M_\odot$ and an equivalent radius of 0.036 pc. G286c1 is associated with strong infrared emission and a wide angle bipolar CO outflow (Cheng et al. in prep.), and hence it is already in a relatively evolved protostellar stage. If we adopt a higher temperature such as 70 K, typical of massive protostellar sources (e.g., Zhang & Tan, 2018), then its mass would be $\sim 20\,M_{\odot}$. G286c1 is not detected in N_2D^+(3-2), but we see broad line profiles from DCO^+(3-2), DCN(3-2) and $C^{18}O$(2-1). In particular, there is very strong DCN(3-2) emission from -22 to -15 $\mathrm{km\,s^{-1}}$, which is even broader than $C^{18}O$. Our high resolution ALMA observation in Cycle 5 has revealed further fragmentation and substructures in G286c1 (Cheng et al., in prep.). Here, we still use a one-gaussian component to model the spectral lines of G286c1, and the resulting fitting parameters should be treated more cautiously as reflecting the average properties of the core.

G286c3: This is also a massive core, with $\sim 12\,M_{\odot}$. We have detected $C^{18}O$(2-1), N_2D^+(3-2), DCO^+(3-2) and DCN(3-2) towards G286c3. Interestingly, these spectra of $C^{18}O$, N_2D^+ and DCO^+ all exhibit a double-peak profile, with one peak centered around -19.5 $\mathrm{km\,s^{-1}}$ and another at $\sim$ -18$\mathrm{km\,s^{-1}}$, though DCN is only detected in one velocity component. Since we expect the deuteratated species such as N_2D^+ and DCO^+ to be optically thin, these line profiles are more likely to be contributed by two separate entities inside G286c3 instead of a central dip caused by self-absorption. A detailed inspection from the continuum also reveals that G286c3 is very elongated in the NE-SW direction. Thus it is possible that there are further sub-fragmentations in G286c3 that are not identified by our fiducial dendrogram algorithm: e.g., there could be two cores overlapping along the line of sight. Here we use two-component gaussian fitting to model the spectrum of $C^{18}O$, N_2D^+ and DCO^+, and treat them as two individual cores (i.e., two data points per line in Figure 3.10). We split the mass of G286c3 assuming that the mass of each component is proportional to the $C^{18}O$ flux for relavent analysis.

G286c4: This core has an estimated mass of $\sim 9\,M_{\odot}$. There is no N_2D^+ detection, but we see very strong $C^{18}O$, DCO^+ and DCN emission. DCN(3-2) has a very strong peak centered at -19.5 $\mathrm{km\,s^{-1}}$, similar to $C^{18}O$ and DCO^+. Additionally, there are two secondary peaks at around velocity -16 $\mathrm{km\,s^{-1}}$ and -23 $\mathrm{km\,s^{-1}}$. These may be a real features resulting from unresolved condensations, or more dynamical activities like outflows, but we are unsure about its origin with the current information. Here for DCN we only fit the central major velocity component that is consistent with other tracers.

G286c8, G286c20 and G286c41: These are special in terms of their DCO^+(3-2) spectra. All three cores have a DCO^+ peak around -18 $\mathrm{km\,s^{-1}}$. For G286c20 and G286c41, DCO^+ has a large velocity offset ($\sim$1 $\mathrm{km\,s^{-1}}$) compared with other tracers, like $C^{18}O$. For G286c8, this offset is even larger ($\sim$3 $\mathrm{km\,s^{-1}}$) and there is another obvious DCO^+ peak around -21 $\mathrm{km\,s^{-1}}$, similar with the peaks of $C^{18}O$ and DCN lines. A possible explanation is that G286c8 has a core velocity around -21 $\mathrm{km\,s^{-1}}$, as traced by multiple tracers, while the DCO^+ feature around -18 $\mathrm{km\,s^{-1}}$ is not associated with the dense core. From the continuum map we find that all these three cores are close together and lie on a filamentary feature that is only seen in DCO^+. This filamentary feature is clear in the DCO^+ channel map and does not appear to be associated with dense dust continuum. Hence we exclude this DCO^+ velocity component near -18 $\mathrm{km\,s^{-1}}$ for G286c8, G286c20 and G286c41 in our analysis.

3.5.4 Line parameters of different tracers

The best-fit parameters of centroid velocity and velocity dispersion are displayed along with the spectral lines in Figure A.1 and Figure A.2. Figure 3.10 illustrates the distribution of these parameters, along with their individual uncertainties. As can be seen, the centroid velocities range from -22.5 to -17.0 $\mathrm{km\,s^{-1}}$ and there is a modest clustering near -21.5 $\mathrm{km\,s^{-1}}$. The velocity dispersions range from 0.1 to 1.0 $\mathrm{km\,s^{-1}}$ for deuterated species, while those of $C^{18}O$ are systematically larger.

N_2D^+ and DCO^+ usually give smaller velocity dispersions, with a median value of 0.35 and 0.36 $\mathrm{km\,s^{-1}}$, respectively. DCN-measured dispersions are larger, with a median value of 0.43 $\mathrm{km\,s^{-1}}$. Centroid velocity uncertainties range from 0.01 to 0.08 $\mathrm{km\,s^{-1}}$, while velocity dispersion uncertainties vary from 1% to 20%, with a few cases $\gtrsim$30%, depending on the signal to noise ratio and shape of the line profiles.

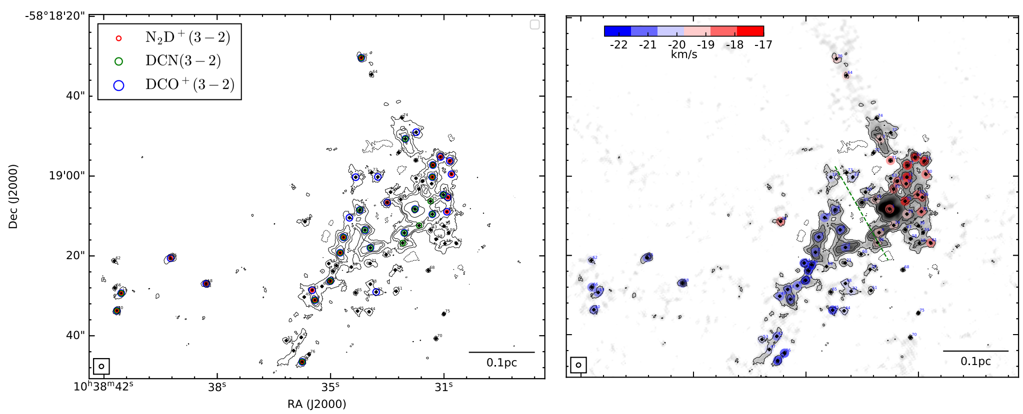

Figure 3.11: *Left:* Line detection status for each core overlaid on the 1.0″ resolution 1.3 mm continuum image in contours. The black crosses denote positions of cores identified via 1.3 mm continuum by Cheng et al. (2018). A red circle indicates a detection of N_2D^+(3-2); a blue circle of DCO^+(3-2); and a green circle of DCN(3-2). *Right:* Core velocity map overlaid on the 1.0″ resolution 1.3 mm continuum image shown in contours and greyscale. The core velocity is determined by averaging the results from N_2D^+, DCO^+ and DCN(see text). The colored circles indicate the velocity of the 54 dense core that are detected in at least one deuterated tracer.

Figure 3.11 illustrates the line detection situation of the core sample, with different colored circles denoting detections in N_2D^+(3-2), DCO^+(3-2) and DCN(3-2). $C^{18}O$(2-1) is detected for almost all the cores (except c68, c75) and hence is not shown here. As already apparent in Figure 3.8, DCN(3-2) is mostly detected in the central region, while N_2D^+(3-2) and DCO^+(3-2)-detected cores are more widespread. Overall we have 54 cores that are detected in at least one of these three dense gas tracers. In particular, all the cores with N_2D^+ detection also have strong DCO^+ emission.

The cores that are detected in more than one line are of particular interest, since differences in fitted parameters could be a reflection of chemical differentiation. There are 14 cores that are detected in all three lines; 26 cores that are detected in both N_2D^+ and DCO^+; 14 in both N_2D^+ and DCN; and 21 in both DCO^+ and DCN. Figure 3.12 illustrates the differences in fitted parameters of these species when commonly detected. From this figure we see that there is no significant offset in centroid velocity or velocity dispersion as derived from the different species. This similarity in velocity distributions is expected if these species are tracing the same molecular gas material.

For the centroid velocities, the median offsets between N_2D^+ and DCO^+, N_2D^+ and DCN, and DCO^+ and DCN are 0.07, 0.09, 0.03 $\mathrm{km\,s^{-1}}$, respectively. The sampling error of the velocity offset distribution due to the finite number of cores is estimated to be about 0.04 $\mathrm{km\,s^{-1}}$, so these offsets are not very significant.

The 1d velocity dispersion σ are generally consistent among different tracers within a factor of 2. The median values of $\sigma_{\mathrm{DCN}}/\sigma_{\mathrm{DCO^+}}$, $\sigma_{\mathrm{N_2D^+}}/\sigma_{\mathrm{DCN}}$ and $\sigma_{\mathrm{N_2D^+}}/\sigma_{\mathrm{DCO^+}}$ are 1.16, 0.99 and 0.95, respectively. The observed scatter is consistent with the fitting uncertainties.

We next compare dense core centroid velocities with the larger-scale gas reservoir (or envelope) traced by $C^{18}O$. Previous studies in relatively low-mass environments have shown that cores mostly have subsonic core-to-envelope motions (e.g., Walsh et al., 2004, 2007; Kirk et al., 2007; Walker-Smith et al., 2013). Our work here provides a measure of core-to-envelope motions within a more massive protocluster. Additionally, most previous works measured the centroid velocity offset between $C^{18}O$ and N_2H^+. Here we have observations of lines from deuterated species like N_2D^+, DCO^+ and DCN, which should be better tracers for the very inner region of a dense core and usually not affected by multiple velocity components that may complicate the interpretation (e.g., Ragan et al., 2015).

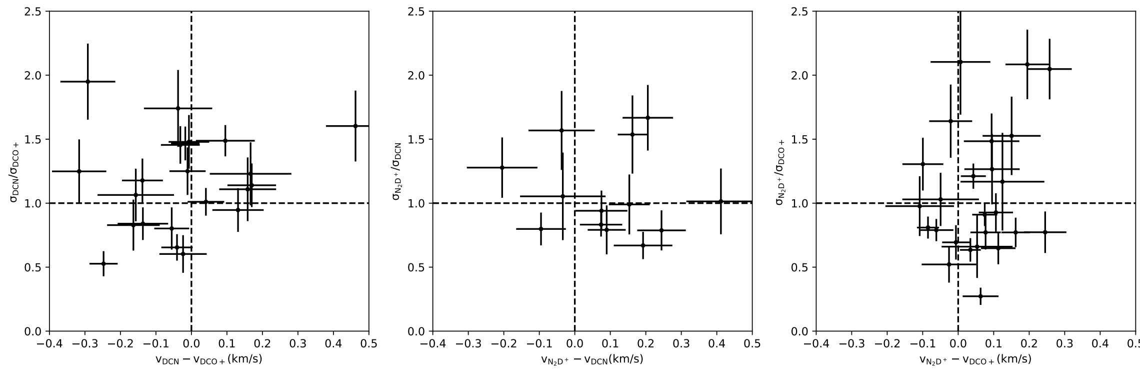

Figure 3.12: Core centroid velocity differences and relative velocity dispersions as measured from N_2D^+(3-2), DCO^+(3-2) and DCN(3-2).

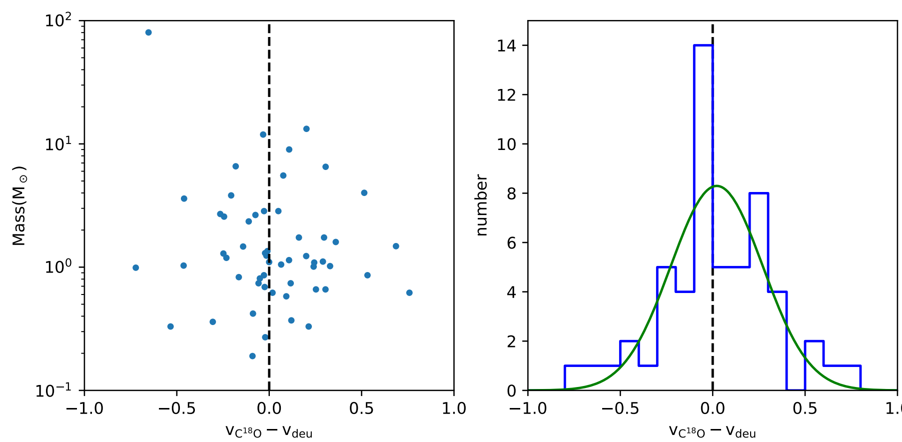

Figure 3.13: *Left:* Distribution of differences between the velocity of dense cores (determined with deuterated tracers) and centroid velocity of $C^{18}O$. *Right:* Histogram of the distribution. The green line shows a gaussian fit to this distribution.

As mentioned above, we have 54 cores that are detected in at least one of the three deuterated species. For those detected in more than one line we define the core velocity, v_c, as an average of the detected centroid velocities, weighted by their measurement uncertainties.

The core velocities v_c are illustrated in Figure 3.11. For cores with only one $C^{18}O$(2-1) component, we compare the difference in centroid velocity between the $C^{18}O$ and v_c directly. If multiple CO velocities are found along line of sight, we assume the component closest to v_c is the one associated with the core, following the discussion in Kirk et al. (2007). This comparison is shown in Figure 3.13.

The median value of the velocity offset is 0.01 $\mathrm{km\,s^{-1}}$, with a standard deviation of about 0.3 $\mathrm{km\,s^{-1}}$. The majority of cores (71%) have core and envelope velocity offsets less than the sound speed of the ambient medium (0.27 $\mathrm{km\,s^{-1}}$ for 20 K temperature). This percentage is higher than that in NGC 1333, for which Walsh et al. (2007) found half of their cores have differences greater than the sound speed, but similar to that seen in the Perseus cloud (Kirk et al., 2007). As discussed in Walsh et al. (2004), small relative motions between cores and envelopes could be interpreted as an indication of quiescence on small scales and this would appear to argue against a competitive accretion scenario for star formation (Bonnell & Bate, 2006), in which dense cores gain most of their mass by sweeping up material as they move through the cloud.

3.5.5 Virial state of dense cores

We now examine the dynamical state of the dense cores, i.e., the comparison of their internal kinetic energy (E_K) and gravitational energy (E_G). This ratio is captured by the virial parameter (Bertoldi & McKee, 1992), defined as

$$\alpha \equiv 5\sigma_c^2 R_c/(GM_c) = 2aE_K/|E_G|, \tag{3.4}$$

where σ is the intrinsic 1D velocity dispersion of the core and R is the core radius.

The dimensionless parameter a accounts for modifications that apply in the case of non-homogeneous and non-spherical density distributions. For a spherical core with a radial density profile that is a power law $\rho \propto r^{-k_\rho}$, then for $k_\rho = 0, 1, 1.5, 2$, $a = 1, 10/9, 5/4, 5/3$. We adopt a fiducial value of $k_\rho = 1.5$ and $a = 5/4$, following McKee & Tan (2003). For a self-gravitating, unmagnetized core without rotation, a virial parameter above a critical value $\alpha_{\rm cr} = 2a$ indicates that the core is unbound and may expand, while one below α_{cr} suggests that the core is bound and may collapse.

We measure core 1D velocity dispersions, σ, from each of the three dense gas tracers, i.e., N_2D^+, DCO^+ and DCN. As shown above, their line widths can vary for the same core, so we calculate the virial parameters separately using each tracer. We derive the intrinsic velocity dispersion from the observed dispersion following equation (3) (replacing $C^{18}O$ with other species). For the core masses, we use the values estimated assuming a temperature of 20 K, as listed in Table A.1.

For core radius we attempt two methods. The first is to use the effective radius calculated from the Dendrogram-returned area (See Sec 5.1). For the second method we adopt a deconvolved size defined as R_c=$\sqrt{(A - A_{\rm beam})/\pi}$, where A and $A_{\rm beam}$ are the core area and synthesised beam size, respectively. Note that in our core identification process, we have allowed for cores with an area smaller than the synthesized beam size. Here for the virial analysis we ignore the cores with areas smaller than $1.5{\times}A_{\rm beam}$, for which the deconvolution sizes could have very large uncertainties. This criterion excludes 34 out of 76 cores.

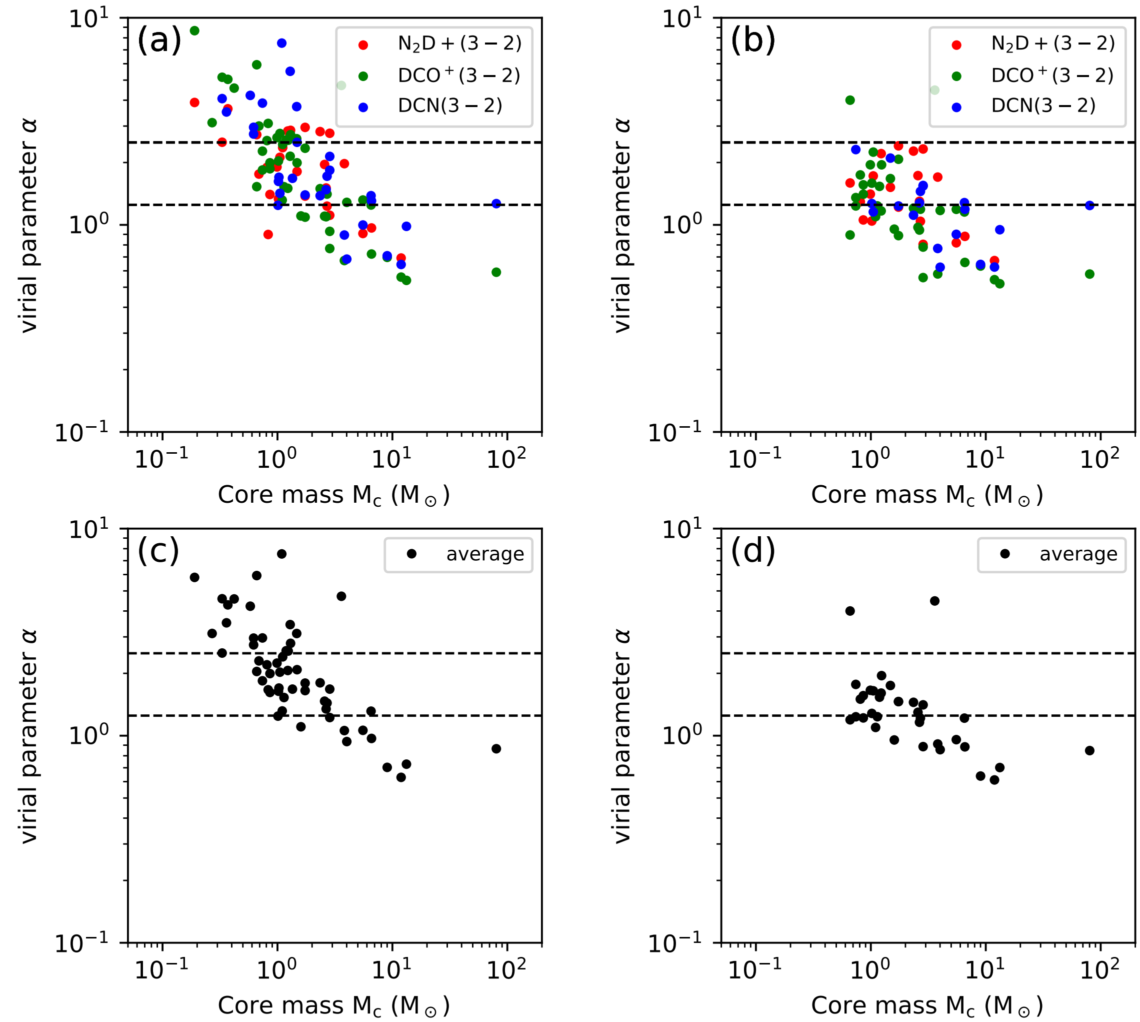

Figure 3.14: *(a)* Virial parameter versus core mass, with radius measured from the dendrogram defined area and velocity dispersion measured with different dense gas tracers, as shown in the legend. The critical value of $\alpha_{\rm cr} = 2a \rightarrow 2.5$ is shown by the upper dashed line: cores below this line are gravitationally bound. The lower dashed line shows the virial equilibrium case of $\alpha = a \rightarrow 5/4$. *(b)* As (a), but with core radius estimated after allowing for beam deconvolution. Small cores, i.e., with areas $> 1.5A_{\rm beam}$ are excluded. *(c)* Same as (a) but we take the linear average of the non-thermal line width measured via different tracers to derive an average virial parameter. *(d)* Same as (c) but using the deconvolved size.

Figure 3.14a and b display the virial parameters measured with different tracers versus core mass for the two methods described above. In Figure 3.14c and d we

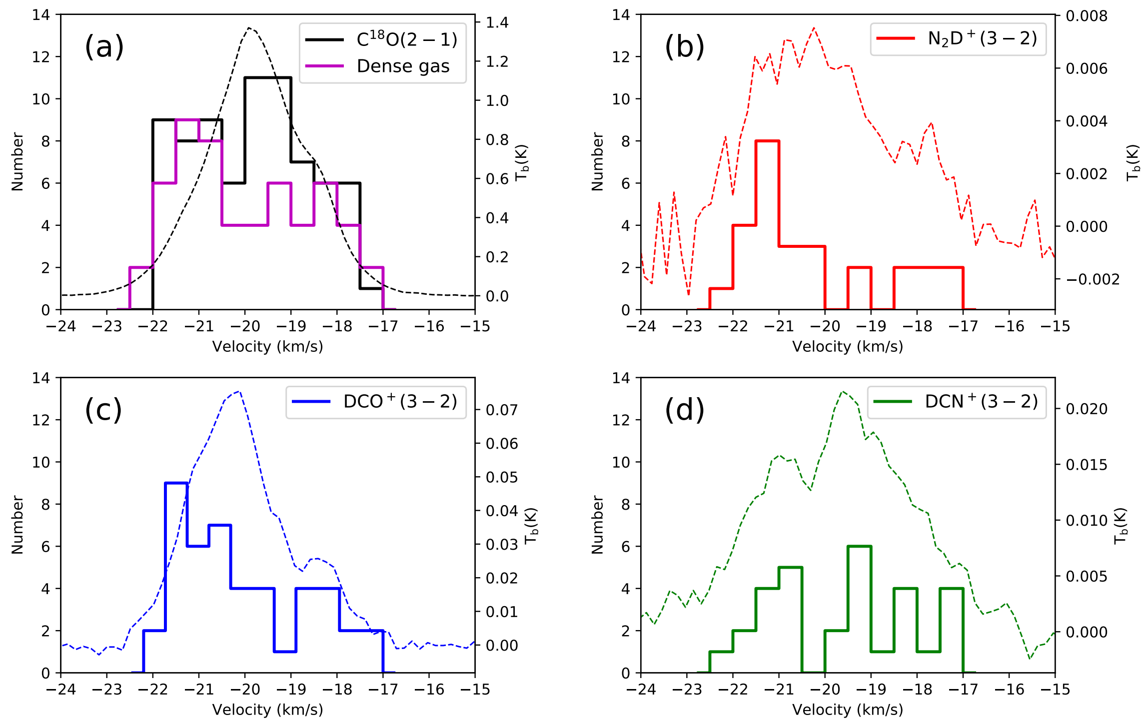

Figure 3.15: *(a)* Distribution of $C^{18}O$(2-1) core centroid velocities (black). Overlaid is the TP $C^{18}O$(2-1) spectrum (averaged over 2.5′ radius aperture) for comparison. The results of core velocities measured with deuterated species are shown in magenta histogram. *(b)* Same as *(a)* but only for N_2D^+(3-2). *(c)* Same as *(a)* but only for DCO^+(3-2). *(d)* Same as *(a)* but only for DCN(3-2). The TP DCN(3-2) spectrum is averaged over 1′ radius aperture.

combine the measurements from different tracers by taking the linear average of their non-thermal velocity dispersion in the virial parameter derivation.

We see virial parameters range from 0.5 to 10 as measured by individual dense gas tracers. There is a trend for more massive cores to have smaller virial parameters, but this is generally expected since $\alpha \propto M_c^{-1}$. The scatter is significantly reduced for the deconvolved size method, with most measurements ranging from 0.5 to 3. This suggests most data points with virial parameter > 5 in panel (a) could arise from overestimation in the core radius. We do not find significant systematic differences between different tracers. The median values are 1.35, 1.19, 1.23 for N_2D^+, DCO^+ and DCN, respectively.

The virial parameters estimated by averaging all the available dense gas data for each core show a further reduction in the scatter. For the second method with deconvolved sizes that focus on the larger cores, most cores have a virial parameter that is consistent with a value expected in virial equilibrium, given the uncertainties.

The uncertainties in the derived virial parameters come from uncertainties in measured 1D line dispersion $\sigma_{\rm obs}$, mass and temperature. The fitting error of $\sigma_{\rm obs}$ is typically $\lesssim$20%, resulting in $\sim$ 40% uncertainty in $\sigma^2_{\rm obs}$. The assumed temperature will systematically affect estimation of the dense core mass and also the thermal line width component in equation (3). For example, with a typical $\sigma_{\rm DCO^+} = 0.36\ {\rm km\,s^{-1}}$, if temperatures of 15 K or 30 K were to be adopted, then the virial parameters would differ by factors of 0.6 and 1.9, respectively. Also considering other uncertainties in the mass estimate, like dust opacity, gas-to-dust mass ratio, dust emission fluxes, and distances, overall, we estimate the absolute virial parameter uncertainties to be about a factor of 2.5.

Therefore, our virial analysis suggests that the dense cores in G286 are consistent with being close to virial equilibrium. Thus self-gravity has been important in forming the cores. This confirms a basic assumption of core accretion models of star formation, such as the turbulent core model (McKee & Tan, 2003). However, given the large systematic uncertainties it is difficult to distinguish whether the dense cores are closer to a supervirial or subvirial state, or whether magnetic fields are playing a role in supporting the cores.

3.5.6 Core to core velocity dispersion

The relative motion between dense cores can be quantified using the core-to-core velocity dispersion $\sigma_{\mathrm{c-c}}$, i.e., the standard deviation of the core centroid velocities. It can be compared with the velocity dispersion of the large scale diffuse gas out of which these dense cores presumably formed or the initial velocity dispersion of newborn stars, and as such, provides important constraints on theoretical models and simulations of star cluster formation (e.g., Kirk et al., 2010; Foster et al., 2015).

Here our target G286 offers an interesting case of a massive protocluster that is still in the gas-dominated phase and actively forming stars. To measure the core velocity despersion, we show the core velocity distributions measured with $C^{18}O$(2-1), N_2D^+(3-2), DCO^+(3-2) and DCN(3-2) in Figure 3.15. For comparision the large scale total power spectra of each line are also overlaid. The results combining velocities measured with deuterated tracers (54 cores, see subsection 3.5.4) are also displayed in Figure 3.15(a). We then calculate the standard deviation of these distributions, obtaining $1.27 \pm 0.11\ \mathrm{km\,s^{-1}}$ for the $C^{18}O$-detected sample, $1.52 \pm 0.21\ \mathrm{km\,s^{-1}}$ for the N_2D^+ sample, $1.40 \pm 0.15\ \mathrm{km\,s^{-1}}$ for the DCO^+ cores, $1.50 \pm 0.20\ \mathrm{km\,s^{-1}}$ for DCN cores and $1.39 \pm 0.13\ \mathrm{km\,s^{-1}}$ for the combined results. The uncertainties here only account for sampling errors due to limited sample size, assuming the data points are drawn from a normal distribution.

In contrast to previous results in nearby cluster-forming clouds like Ophiuchus and Perseus (André et al., 2007; Kirk et al., 2007, 2010), our core velocities cover a wide range from -22.5 to -17 $\mathrm{km\,s^{-1}}$ and the distribution is not well approximated with a single gaussian component. This is particularly clear for N_2D^+ and DCO^+: for these two tracers the core velocities exhibit a bimodal distribution with two velocity groups, which agrees well with the averaged TP spectra. DCN picks up core velocites in a relatively uniform pattern, filling in the gap around -19 $\mathrm{km\,s^{-1}}$, and hence the distribution combining all the deuterated species is more flat, though more cores still cluster in the "blue" group at $\sim$ -21 $\mathrm{km\,s^{-1}}$. On the other hand, though the $C^{18}O$ profile can be characterized with a gaussian (with some skewness) peaking aroud -20 $\mathrm{km\,s^{-1}}$ and we do have more $C^{18}O$-detected cores close to the systemic velocity (-20 $\mathrm{km\,s^{-1}}$ to -19 $\mathrm{km\,s^{-1}}$), the $C^{18}O$-measured core velocity distribution is still relatively flat. This indicates that the core to core velocity dispersion we measured here is largely contributed by the global velocity patterns.

The core velocity dispersion $\sigma_{\rm c-c}$ can be compared with the dispersion required for virial equilibrium on the protocluster clump scale $\sigma_{\rm cl,vir}$, and its actual gas velocity dispersion, $\sigma_{\rm cl}$. For $\sigma_{\rm cl,vir}$ we again follow Bertoldi & McKee (1992):

$$\sigma_{\rm cl,vir} = \frac{aGM_{\rm cl}}{5R_{\rm cl}}. \tag{3.5}$$

As with cores, we again adopt $k_\rho = 1.5$, so that $a = 5/4$. We choose a size of $R_{\rm cl} = 1.54$ pc, which is twice the geometric mean of the Mopra HCO^+(1-0) FWHM major and minor axes (Barnes et al., 2011). SED fitting performed using this aperture with *Herschel* data (Ma et al., in prep.) yields a mass of $\sim 1500\ M_\odot$. Thus, $\sigma_{\rm cl,vir} = 0.89 \pm 0.22\ \mathrm{km\,s^{-1}}$, where the error comes assuming a 50% uncertainty in the mass estimate. The mass here only accounts for the gas component, since we do not expect significant contribution from stellar mass: Andersen et al. (2017a) estimated a total current stellar mass of $\sim 240 M_{\odot}$ in a similarly sized region. Thus the observed values of $\sigma_{\mathrm{c-c}}$ are moderately greater than $\sigma_{\mathrm{cl,vir}}$.

For σ_{cl}, we measure the line width of average TP spectra of $C^{18}O$(2-1) in this region. The purpose here is to compare core-to-core motions with the spread of motions seen over the region as a whole to reveal how connected the dense cores are to the larger scale gas in the region. A gaussian fitting for the $C^{18}O$(2-1) line gives $\sigma_{\mathrm{cl,C^{18}O}} = 1.09 \pm 0.01$ km s^{-1}. To account for the thermal component we correct this value following equation (3) assuming a temperature of 20 K and obtain $\sigma_{\mathrm{cl}} = 1.12$ km s^{-1}. This is close to, but slightly smaller than the values of $\sigma_{\mathrm{c-c}}$.

In summary, the 1D dispersion measured in gas tracers, σ_{cl} (1.12 ± 0.01 km s^{-1}), is close to $\sigma_{\mathrm{cl,vir}}$ (0.89 ± 0.22 km s^{-1}), indicating the G286 clump is gravitationally bound and in approximate virial equilibrium and can be considered as a single, coherent dynamical system. However, both values are smaller than the core to core velocity disperion $\sigma_{\mathrm{c-c}}$. We have a range of $\sigma_{\mathrm{c-c}}$ values using different tracers and the smallest one, i.e., using $C^{18}O$(2-1), is $\sigma_{\mathrm{c-c,C^{18}O}} = 1.27 \pm 0.11$ km s^{-1}. Here the core velocity distribution is more flat, while both the $C^{18}O$ core velocities and the TP $C^{18}O$ spectrum cover similar velocity range. This means there is a deficiency of cores near the systemic velocity (~ 20 km s^{-1}), where the bulk of the $C^{18}O$-traced gas is located. This deficiency is clearer in the distributions traced by N_2D^+ and DCO^+, and hence an even larger $\sigma_{\mathrm{c-c}}$ is measured with these two tracers. The two velocity groups seen in N_2D^+ and DCO^+ (at $\sim$ -21 km s^{-1}and -18km s^{-1}) are actually spatially distinct (see Figure 3.4, Figure 3.8,Figure 3.11), with more redshifted cores mostly located in the NE-SW filament and more blueshifted cores in the NW-SE filament and the E-W filament. A similar velocity pattern is also seen for $C^{18}O$ in Figure 3.4, indicating the dense cores are still well coupled with the large-scale motions within the cloud.

The origin of this velocity pattern is uncertain. In the filament collapse scenario, as observed in some hub-filament systems, accretion flows are channeling gas to the junctions where star formation is often most active (e.g., Kirk et al., 2013; Peretto et al., 2014; Liu et al., 2016). It is possible that these converging flows are reflected in different LOS velocities depending on the 3D configurations. We will presumably have more massive cores in the hub region (near the systemic velocity), but not necessarily a larger number of cores, as suggested by our observations. Smoothly varying velocities along filaments is expected in this picture. We do see indications of a velocity gradient of dense cores along the filaments, but it is not clear in $C^{18}O$, for which the spectra are often complex. Further higher sensitivity observations of N_2H^+ and NH_3 will help investigate the gas velocity gradient along filaments.

Alternatively, the two main velocity components seen in N_2D^+ and DCO^+ could be tracing two interacting clouds/filaments, with the central region as the collision interface (e.g., Nakamura et al., 2014). Such a mechanism could be consistent with a larger-scale cloud-cloud collision scenario that has been reported in other star-forming regions (e.g., Furukawa et al., 2009; Fukui et al., 2014; Gong et al., 2017).

Andersen et al. (2017a) analysed the stellar population in G286 and found evidence for at least three different sub-clusters associated with the molecular clump based on differences in extinction and disk fractions. It is unclear how the dense gas distribution and ongoing cluster formation might be related with these past star formation events. Future studies of the radial velocity of optically revealed stars, e.g., the velocity dispersion and its distribution will be of great interet to understand the cluster formation in G286.

3.6 Conclusion

We have studied the gas kinematics and dynamics of the massive protocluster G286.21+0.17 with ALMA using spectral lines of $C^{18}O$(2-1), N_2D^+(3-2), DCO^+(3-2) and DCN(3-2). The main results are as follows:

1. Morphologically, $C^{18}O$(2-1) traces more extended emission, while N_2D^+(3-2) and DCO^+(3-2) are more closely associated with the dust continuum. DCN(3-2) is strongly concentrated towards the protocluster center, where no or only weak detection is seen for N_2D^+ and DCO^+, possibly due to a relatively evolved evolutionary stage in the central region involving chemical evolution at higher temperatures.

2. Based on 1.3 mm continuum, G286 is composed of several pc-scale filamentary structures: the NE-SW filament in northwest, and the NW-SE filament in the southeast, as well as another filament oriented in the E-W direction that is more clearly seen in DCO^+. The NE-SW filament is associated with redshifted $C^{18}O$ emission while the NW-SE and E-W filament are mainly associated with blueshifted gas. Other tracers show similar velocity structures.

3. We performed a filamentary virial analysis towards the NE-SW filament. We divided the filament into four strips and the values of $m_f/m_{\rm vir,f}$ of the four strips range from 0.60 to 2.39. Within the uncertainties, these values are consistent with the filament being in virial equilibrium, without accounting for surface pressure and magnetic support terms. We also detected a steady velocity gradient of 2.84 $\mathrm{km^{-1}pc^{-1}}$ along the filament, which may arise from infall motion.

4. We analysed the spectra of 74 continuum dense cores and measureed their centroid velocities and internal velocity dispersions. There are no statistically sig-

nificant velocity offsets among different tracers. $C^{18}O$ has systematically larger velocity dispersion compared with other tracers.

5. The majority (71%) of the dense cores have subthermal velocity offsets with respect to their surrounding $C^{18}O$ emitting envelope gas, similar as found in previous studies for low-mass star formation environments (e.g., Kirk et al., 2007).

6. We measured the virial parameter for the dense core sample. Within the uncertainties the virial parameters of the dense cores in G286 are close to unity, suggesting these cores are close to virial equilibrium.

7. The core to core velocity dispersion in G286 is larger than that required for virial equilibrium in the protocluster potential, but with the velocity distribution largely composed of two spatially resolved velocity groups, which indicates that the dense molecular gas has not yet relaxed to virial equilibrium.

Chapter 4

Stellar Variability in G286.21+0.17

4.1 Introduction

Variability is ubiquitous among young stellar objects (YSOs). A low level of variability (i.e., typically below a few 0.1 mag) has been observed in most YSOs in the optical and NIR (e.g., Parihar et al., 2009). Mechanisms to produce such variations include rotationally modulated cool spots, hot spots on the stellar surface, extinction changes, and changes in the inner circumstellar disk (Wolk et al., 2013). Some of these mechanisms, like hot spots and varying extinction, may also produce variability with larger amplitudes (see, e.g., Grankin et al., 2007; Bouvier et al., 2013). Apart from these common causes of variability, a small fraction of YSOs show evidence for eruptive behavior, with variations larger than 1 magnitude in the optical or NIR bands over a few years or decades. This type of variability is thought to be related to the process of accretion from the circumstellar disk on to the protostar. During these bursts the YSO may increase its mass accretion rate by several orders of magnitude compared with quiescent phases, resulting in strong variability. While this episodic accretion scenario is well established, the driving force of this phenomenon is still poorly understood (e.g., Audard et al., 2014). Understanding the underlying mechanisms is crucial not only for building a complete picture of star formation, but also for the potential implications on the planet formation process (e.g., Zhu et al., 2009).

The nature of YSOs favors observations at near and mid-IR wavelengths, which allow for direct detection of optically thick disks, e.g., via excess K-band flux (Lada & Adams, 1992). Over recent years there has been an increasing interest to search for eruptive variables with long-term NIR observations. Scholz (2012) used archival NIR photometry to investigate the long-term variability in a few nearby low-mass star-forming regions and found a low fraction ($\sim$2% in the YSO sample) of large amplitude variable objects. A higher incidence of K band variations > 1 mag ($\sim 13\pm7\%$) has been reported in Class I YSOs in the dark cloud L1003 in Cygnus OB7 (Rice et al., 2012; Wolk et al., 2013). A panoramic search by the UKIRT Infrared Deep Sky Survey (UKIDSS; Lawrence et al., 2007) found a strong concentration of high-amplitude IR variables towards star-forming regions (Contreras Peña et al., 2014), and this is confirmed by recent VVV survey (VISTA Variables in the Via Lactea; Minniti et al. (2010)), in which more than 100 eruptive YSOs are detected (Contreras Peña et al., 2017a).

G286.21+0.17 (hereafter G286) is a massive ($\sim 2000\,M_\odot$) protocluster associated with the η Car giant molecular cloud at a distance of 2.5$\pm$0.3 kpc (Barnes et al., 2010). The gas and dust component is well studied with ALMA, which reveals ~ 80 dense cores in millimeter continuum emission (Cheng et al., 2018). NIR observations reveal a high disk fraction of the YSOs, which suggests the cluster is very young ($\sim$ 1 Myr; Andersen et al., 2017a). Here we present analysis of two-epoch HST NIR

Table 4.1: Photometry of G286.2032+0.1740

Date(y.m)	Instrument	J	H	Ks
2011.5	VLT/HAWK-I	21.14±0.17	19.02±0.11	18.30±0.08
2012.6	VLT/HAWK-I	...	18.90±0.06	...
2013.2	VLT/HAWK-I	...	18.23±0.09	...
2014.10	HST/WFC3	20.82±0.03	18.22±0.02	...
2017.10	HST/WFC3	18.93±0.01	16.43±0.01	...
2019.3	Gemini/GASOI	...	...	14.84±0.01
2019.6	Gemini/F2	18.50±0.03	16.19±0.02	15.02±0.01
2019.12	Gemini/F2	18.38±0.03	16.11±0.02	14.99±0.01

imaging of G286, with the main goal of characterizing variabilities. In particular, we report the discovery of a strong outburst in a low-mass embedded YSO, as well as its photometric and spectroscopic follow-up using Gemini observations.

4.2 Data

4.2.1 HST WFC3/IR imaging

HST-WFC3/IR observations of the central cluster region of G286 were obtained in Cycle 22 and 24 under program IDs 13742 and 14680 (PI: J. Tan), obtained in October 2014 and October 2017, respectively. Observations were carried out in F110W, F160W and F167N filters and in this study we will focus on the two wide band filters. The field of view (FOV) for WFC3 is $136'' \times 123''$, and the pixel scale is $0.128''$. A 3×3 grid (with $10''$ overlap between adjacent pointings) was observed to cover the 6'× 6' central region of G286, as shown in Figure 4.2. In both bands three exposures were obtained for each position in the mosaic with a total integration time of 897 seconds in F110W and 847 seconds in F160W.

The data reduction used the STScI processed flt frames and they were combined using `multidrizzle` with the default parameter settings. For photometry each tile in the mosaic was handled individually to avoid potential issues with slight misalignments. The full width at half-maximum of the point-spread function (PSF) are $0.12''$

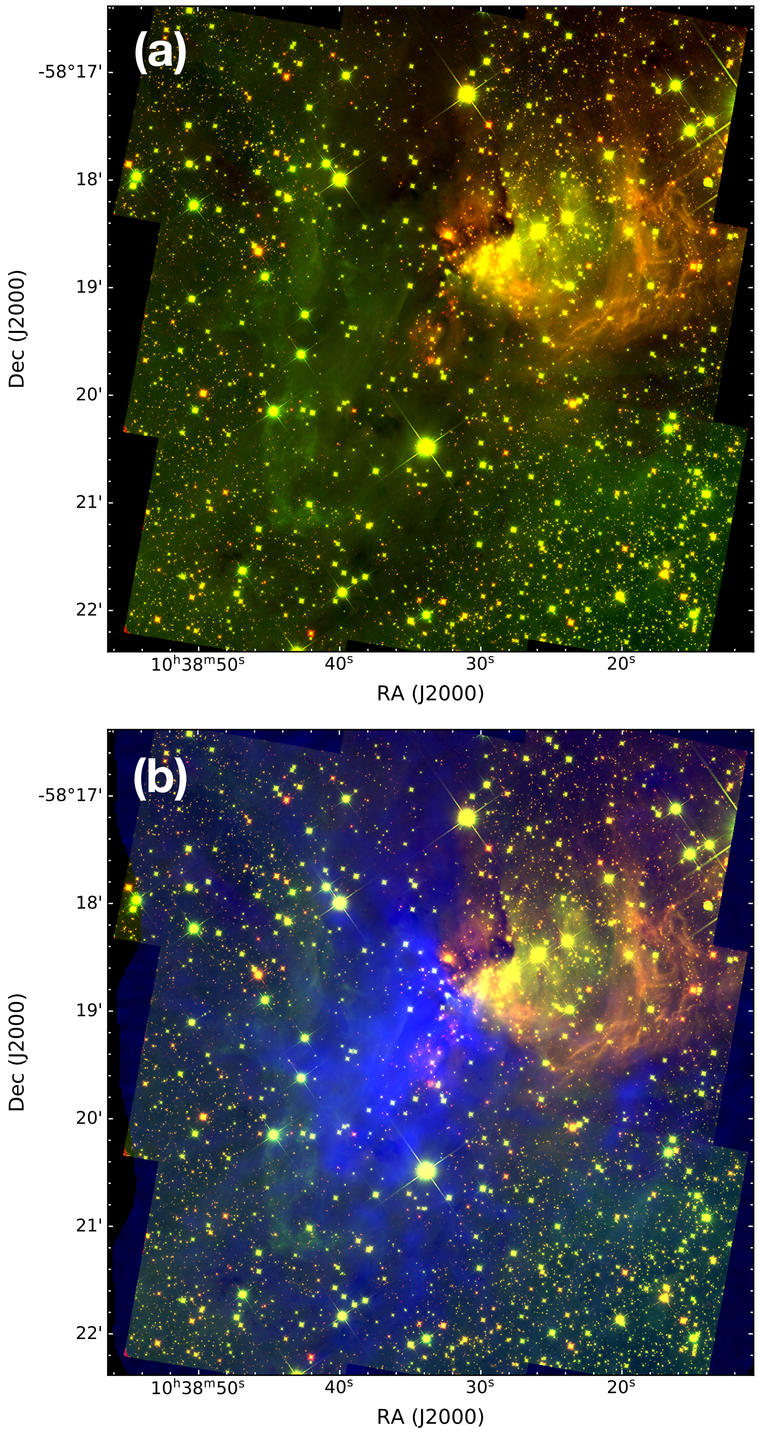

Figure 4.1: *(a)* HST F110W and F160W (green and red, respectively) color mosaic of G286. The field of view is $6' \times 6'$, corresponding to 4.4 pc $\times$ 4.4 pc for a distance of 2.5 kpc. *(b)* Same as *(a)* but overlaid with the ALMA $C^{18}O$(2-1) integrated intensity map (from -23 to -17 km s^{-1}) in blue, which has a spatial resolution of $8.1'' \times 4.8''$(Cheng Y. et al. 2020, in preparation).

and 0.15″ for the F110W and F160W, respectively.

As input for photometry we used the VLT source catalog from Andersen et al. (2017a), which contained 6207 members inside the HST FOV. The completeness is expected to be better than 80% for sources brighter than $K_S = 17$ and 50% for sources down to $K_S = 19$, as suggested by the artificial star experiments. Aperture photometry was performed with the *Daophot* package in *Pyraf*. For stars located in the overlap regions of different tiles, we adopted the photometric measurements with smaller errors. An aperture of 3 pixel radius was used to measure the flux of a source, and the background was measured in an annulus from 20 to 30 pixels. Restricting the list of objects to those with photometric errors smaller than 0.1 mag in both the F110W and F160W bands results in a list of 5273 sources with photometry in both epochs.

4.2.2 VLT and Gemini observations

To provide more photometric constraints on an extreme variable star in this survey (G286.2032+0.1740), we also collected additional observations including the VLT/HAWK-I JHKs imaging, Gemini/GSAOI Ks band imaging and Gemini/Flamingos 2 (F2) JHKs imaging. The VLT observations were obtained in the programs $087.D-0630(A)$ and $089.D-0723(A)$ over the period of 2011-2013 (see Andersen et al. (2017a) for details). The seeing during the observations was 0.4"-0.6". A mosaic of 8'×13' was observed. The total exposure times were 6000s in J, 1500s in H, and 1500s in K_s, respectively. For this study we used the pipeline reduced and mosaiced images obtained from each observing block instead of the combined images in Andersen et al. (2017a) to be able to follow the time evolution of the object.

G286 was observed with Gemini/GSAOI in 2019 March as part of the proposal GS-2019A-DD-103 (PI: M. Andersen). GSAOI has a resolution of 0.02″/pixel and consists of four 2048 $\times$ 2048 pixels detectors, divided by gaps of $\sim$2″, providing a total FOV of almost 85″$\times$85″. Two pointings were obtained, but here we only discuss the one covering the variable source. A total exposure time of 45 minutes on-source, was acquired during the run. The data were reduced in a standard manner using dedicated sky frames and up to date flat fields, using the *gsaoi* package in the Gemini pyraf package. Before co-addition of the individual frames, they were corrected for distortion using the program *discostu*. All the frames were aligned to the first GSAOI frame and then average combined using bad pixel masks for the individual frames. Aperture photometry was performed using the *Daophot* package in *Pyraf*. An aperture of 3.5 pixel radius was used to measure the flux, and the background was measured in an annulus from 20 to 35 pixels.

Gemini/F2 JHK$_s$ imaging was performed in 2019 June and December (proposal DT-2019A-129 and GS-2019B-FT-109, PI: Y. Cheng). For each observation, we obtained a total exposure time of 90 seconds in J, 48 seconds in H and 60 seconds in Ks, respectively. The raw images were reduced using the *Gemini.F2* package provided in the *Pyraf* environment. The aperture photometry was done following similar procedures as the GSAOI data.

In 2019 June we also obtained H and K band spectra of G286.2032+0.1740 using F2 under thin cirrus conditions. We used the 2 pixel slit with the R3K grating resulting in a spectral resolution of 2800 in H and 2900 in K. Ten 120-second exposures were obtained for both the H and K band spectra in a typical ABBA dither pattern. A telluric star was observed for both spectral settings. The data were reduced in a standard manner using flat and Argon lamp observations obtained after the science exposures. Each science frame was dark subtracted, flat fielded and sky subtracted using the temporal nearest offset position before the frames were cross correlated and coadded. The Argon lamp was used for wavelength calibration. The cirrus did result in a rather variable sky that has left several OH lines poorly subtracted in the H band spectrum. These lines are marked in the final spectrum shown in Figure 4.8.

4.3 Results

4.3.1 Overview of the Region

Figure 6.1(a) shows a two-color image of G286 with HST F110W and F160W data (green and red, respectively). The stellar component in this region has been characterized by Andersen et al. (2017a) with VLT NIR observations, but the embedded YSO population is better revealed with our more sensitive and higher resolution HST observations. Some strong diffuse nebulosity is clearly seen in the northwest, which is associated with a shell-like HII region, where the stars are less affected by extinction (Barnes et al., 2010). In the central 30″ region there is a heavily obscured star cluster (i.e., region R1 in Andersen et al. (2017a)), which appears as redder objects in this two-color image. Compared with the background/foreground stars near the edge of the field, there is a relative paucity of stars extending to the north and south from the center, suggesting existence of substantial extincting molecular cloud material. This is confirmed by our ALMA $C^{18}O$(2-1) observations (Cheng Y. et al. 2020, in preparation), as shown in Figure 6.1(b). $C^{18}O$ is known to be a good tracer of high column density regions and the integrated emission has a close correspondence with the dark lanes seen in the HST image.

4.3.2 Near-IR variability

Figure 4.3(a) shows the F110W band variation against first epoch F110W magnitude for the 5273 point sources with photometric errors smaller than 0.1 mag. A larger scatter in magnitude variation is seen towards fainter F110W magnitudes, which is mostly contributed by increasing photometric uncertainties due to the lower signal for fainter sources. A Gaussian fit gives a dispersion of $\Delta m_{\rm F110W} \sim 0.03$ for the whole sample. A similar analysis for F160W band gives a $\Delta m_{\rm F160W} \sim 0.02$ and the distribution is shown in Figure 4.3(b).

To quantitatively select stars that are variable, we use the Stetson variability index (Stetson, 1996), which is defined as

$$S = \sum_{i=1}^{p} sgn(P_i)\sqrt{|P_i|}, \tag{4.1}$$

where p is the number of pairs of simultaneous observations of an object. $P_i = \delta_{j(i)}\delta_{k(i)}$ is the product of the relative error of two observations, which is defined as

$$\delta_i = \sqrt{\frac{n}{n-1}}\frac{m_i - \overline{m}}{\sigma_i} \tag{4.2}$$

for a given band. Here n is the number of measurements used to determine the mean magnitude $\overline{m}$ and σ_i is the photometric uncertainty. The Stetson statistic has been widely used to characterize variability in multi-wavelength observations (e.g., Carpenter et al., 2001; Rice et al., 2012). Since it accounts for the correlated changes in multiband magnitudes, the Stetson index can be used to identify variables with relatively low variability compared with photometric errors.

Figure 4.3(c) shows the Stetson statistics as a function of F110W magnitude. For random noise, the Stetson index should be scattered around zero, and larger positive values indicate correlated variabilities. An outlier-clipped gaussian fitting of the Stetson index distribution gives a mean value of $S = 0.2$ and a dispersion of 0.5. Therefore, objects with $S \geq 2$ can be considered 3σ variables and we use $S \geq 1.7$ as our criterion for variability hereafter. Of all the 5273 objects, we have found that 363 (7%) are variable. The spatial distribution of these variables is illustrated in

Figure 4.2.

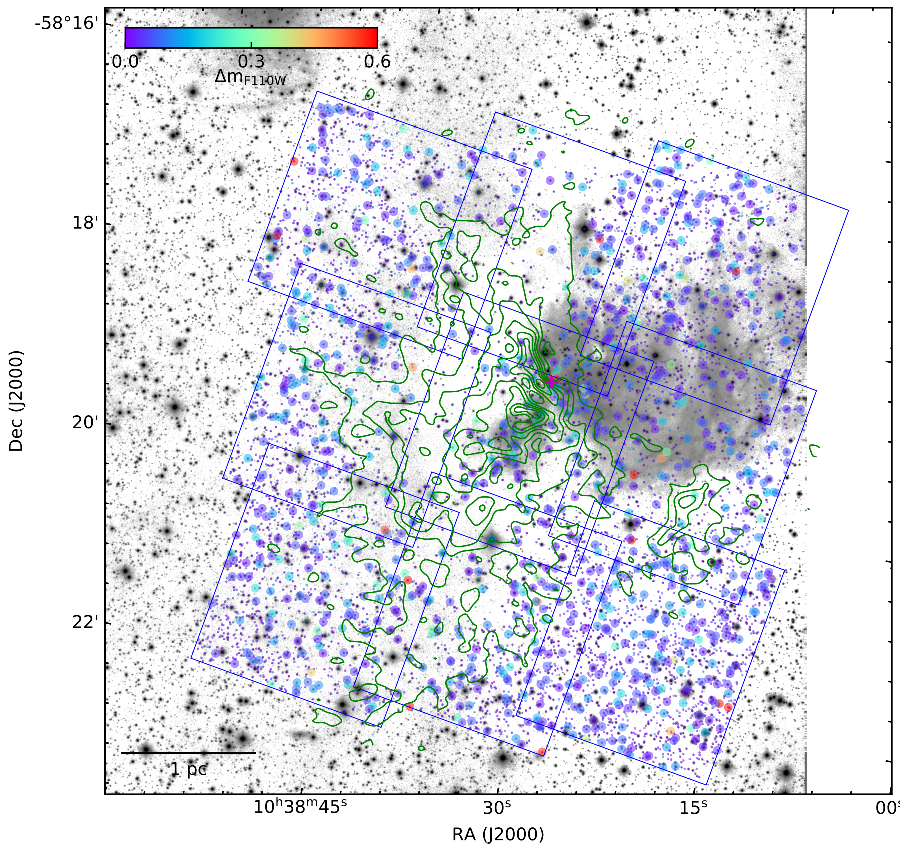

Figure 4.2: VLT HAWK-I Ks-band image of G286 in grey scale. Overplotted in green contours is ALMA $C^{18}O(2\text{–}1)$ integration map. The contours start from 4 Jy beam^{-1}km s^{-1} in steps of 4 Jy beam^{-1}km s^{-1}. The colored circles show the sources detected in the VLT observations, with the color indicating the F110W band magnitude differences between two HST epochs. The variables with Stetson index larger than 1.7 are shown with larger circles. The blue rectangles show the extent of the 3×3 mosaic of HST WFC3/IR FOV. The position of G286.2032+0.1740 is marked with magenta cross.

The sample consists of heterogeneous populations, including foreground and background field stars and cluster members. To characterize the variability for young stars that possess disks, which are mostly cluster members, we plot $J-H$ versus $H-K$ diagrams in Figure 4.4 using the VLT JHKs photometry using the catalog from Andersen et al. (2017a). This color-color diagram is an effective tool to identify objects

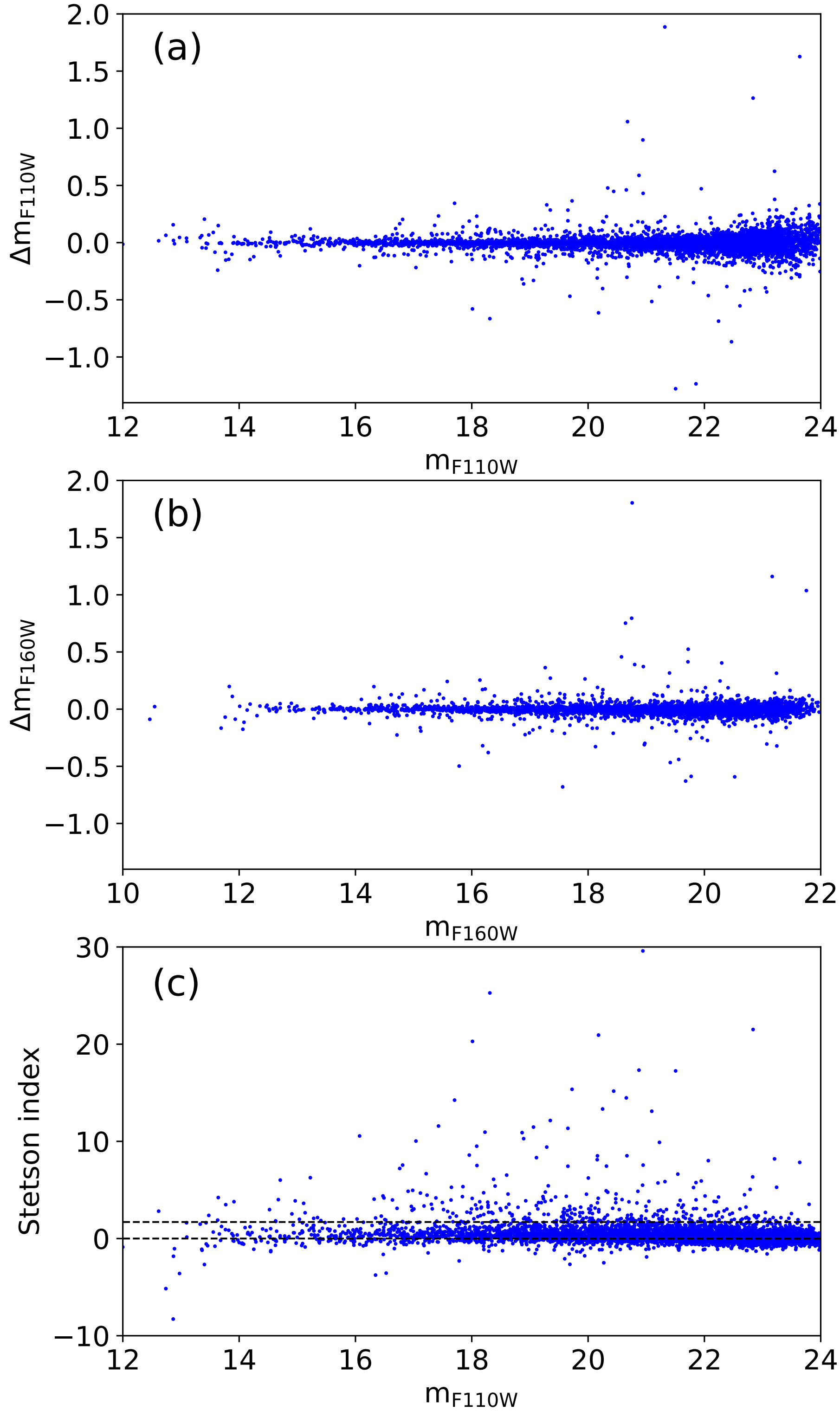

Figure 4.3: *(a)* F110W band variability in two HST epochs against the first epoch F110W band magnitude. *(b)* Same as *(a)* but for F160W band. *(c)* Stetson variability index against the first epoch F110W band magnitude. The dashed lines indicates $S = 0$, corresponding no variability, and $S = 1.7$, above which we identify as significant variability.

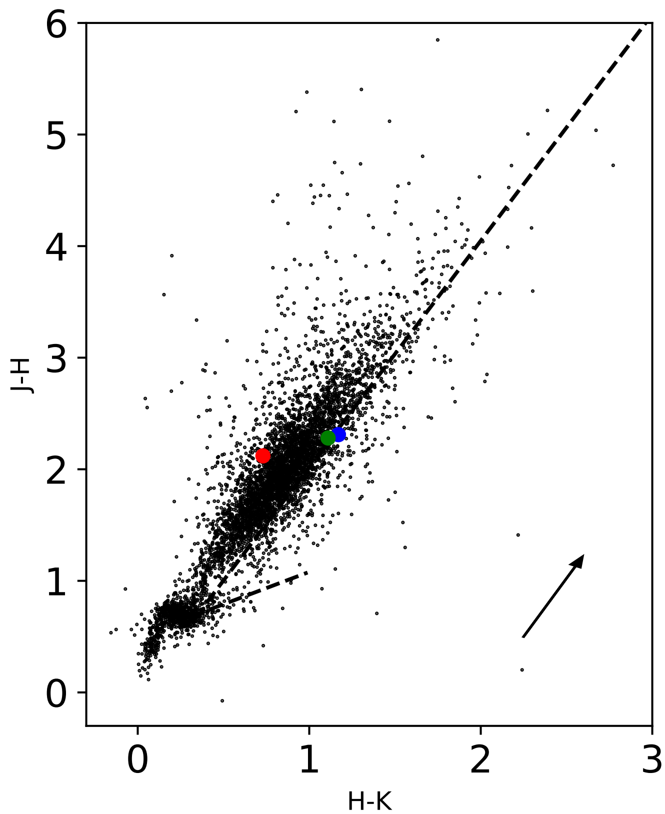

Figure 4.4: $J - H$ vs. $H - K$ color-color diagram. Overplotted are the reddening vector extending from an M6 spectral type and the T-tauri locus from Meyer et al. (1997). The red, blue and green dots denote G286.2032+0.1740 at three epochs, i.e., 2011 May, 2019 June and 2019 December, respectively. An extinction vector with $A_K = 0.5$ is overplotted, using the reddening law of Nishiyama et al. (2009).

with warm circumstellar disks (e.g., Meyer et al., 1997). Following Andersen et al. (2017a), the sample has two distinct populations: a bluer population ($J - H \approx 0.6$), which is mostly field stars in the foreground of the clump, and a redder population ($J - H \approx 2$) consisting of the cluster content and also some field star contamination. To detect optically thick disks, we use the NIR excess criterion devoloped by Lada & Adams (1992). We consider stars to have a NIR excess consistent with an optically thick disk if they are located to the right of the reddening vector from the M6 main sequence colors, as shown in Figure 4.4. The objects also have to be above the empirically derived dereddened T-Tauri locus (Meyer et al., 1997). In addition, all objects with a color $J - H < 1$ are ignored since they are expected to be foreground objects. These criteria yield 562 disk excess candidates, of which 80 are variable at a significant level ($S > 1.7$).

The fraction of variables in our identified YSOs that show evidence for a circumstellar disk is relatively low (14%) compared with other NIR surveys (e.g., Carpenter et al., 2001; Scholz, 2012; Rice et al., 2012), in which most YSOs have been observed to show a low level of NIR variability, with typical K band amplitude of ~ 0.15 mag. This is mainly due to the distance to the cluster. We have increasing photometric errors for fainter objects (e.g., $\sigma_{\rm F110W} \gtrsim 0.05$ for $m_{\rm F110W} > 22$) and hence it is difficult to detect variability at a significant level for these faint objects, assuming a typical variation of 0.15 mag. A higher variable fraction is achieved with a brightness cut. For example, the variable fraction is 57% (24/42) for disk candidates with $m_{\rm F110W} < 19$. Furthermore, we only have HST observations over two epochs separated by 3 years, which may miss some short-term (weeks to months) variability.

Our observational setup is more suitable to survey long-term, large amplitude variations. Typical short-term NIR variations, arising from rotation, hot spots or inner disk inhomogenities, are in the range of 0.1-0.6 mag (Scholz et al., 2013, and references therein). Larger amplitude variations in YSOs are usually associated with accretion outbursts or extinction events. Of all the 5273 objects, 12 have $\Delta m_{\rm F110W} >$ 0.6 and 7 have $\Delta m_{\rm F160W} > 0.6$. The maximum amplitude in F110W and F160W band are 1.89±0.03 and 1.80±0.02, respectively. Of all the 562 YSO candidates with evidence for a circumstellar disk, 3 (0.5%) have $\Delta m_{\rm F110W} > 0.6$ and 1 (0.2%) has $\Delta m_{\rm F160W} > 0.6$. To search for eruptive events, we further require a positive change in luminosity and magnitude variations larger than 0.6 in both bands. This gives 5 candidates, with 1 object also satisfying the disk excess criteria. Detailed inspection suggests that one of them (G286.2182+0.1507) was affected by a bad spot in the detector in the first epoch and hence is excluded in the following analysis.

To investigate the nature of these objects, we have collected more observations, including our early VLT HAWK-I observations (2011-2013) and recent Gemini GSAOI Ks band imaging (March 2019) and F2 $JHKs$ band imaging (June 2019, December 2019). For direct comparison the HST F110W/F160W photometry was converted into the 2MASS system (i.e., corresponding to J/H bands) following similar procedures as in Andersen et al. (2017b). In Figure 4.5 we show light curves and color-magnitude diagrams of the four high amplitude variables in H band, for which we have better sampling. Three of them (G286.2372+0.1503, G286.1676+0.1815, G286.2390+0.2128) show a declining trend from 2012 to 2015, so the brightening between two HST epochs could be understood as returning to their normal luminosity (after a fading event). It is unclear whether we are observing part of a periodic variation or an isolated event. This type of object might be related to either stars going back to quiescent states after an outburst or objects dominated by long-term extinction events similar to the long-lasting fading event in AA Tau (Bouvier et al., 2013) or some of the faders in (Findeisen et al., 2013). The color-magnitude diagram is supportive of the explanation of varying extinction, since most data points of

G286.1676+0.1815 and G286.2390+0.2128 seem to follow the direction of the reddening vector. G286.2372+0.1503 has a steeper slope in the color-magnitude diagram, with significant variation in brightness but relative stable color, and hence its variability may also be contributed by other mechanisms besides extinction. The other object (G286.2032+0.1740) is the only one of these four objects that exhibits continuous brightening over the observation period of ~ 8 years, and thus is more likely to be a long-period accretion outburst event. We discuss its nature further in the following section.

4.3.3 An object with extreme variability

In our variability analysis, we have identified an object with eruptive variability, i.e., G286.2032+0.1740, located at ($\alpha_{J2000} = 10^h38^m31^s.44$, $\delta_{J2000} = -58°18'48.2''$). G286.2032+0.1740 has the most extreme variations in both bands, with an brightening of $\Delta J = 1.89$ and ΔH=1.79. Further literature research indicates this object was a faint, virtually unstudied star prior to the onset of its eruption. G286.2032+0.1740 was not previously detected in early NIR surveys such as 2MASS, DENIS and WISE, due to its faintness before eruption. In Figure 4.6, we show the pre- and post-outburst images of G286.2032+0.1740 in J (top), H (middle) and Ks band (bottom), taken at different dates, which clearly reveals a brightness increase in all three bands. The corresponding lightcurves and photometry are shown in Figure 4.7 and Figure B.2, respectively. The most striking contrast is seen in the Ks band: comparing the Gemini GSAOI results (2019) with the earliest VLT photometry (2011), we measure an amplitude change of $\Delta Ks = 3.5$ mag, i.e., a flux increase by a factor of 25.

Following the light curve morphology categorization in the VVV survey (Contreras Peña et al., 2017a), G286.2032+0.1740 falls in the "eruptive variability" category. In the H band, for which we have better sampling of the light curve, G286.2032+0.1740 exhibits a monotonic rise over 8 years, with $H = 19.02$ in May 2011 increasing to $H = 16.11$ in Dec. 2019, though a lower level scatter is present from 2013 to 2014. On the other hand, the J band luminosity remains roughly constant until 2015 ($J = 21.14$ in May 2011 and $J = 20.82$ in Oct 2014), and rises to $J = 18.38$ in Dec 2019. Judging from the H band light curve, G286.2032+0.1740 went into outburst no later than June 2012, but we caution that this estimate may be affected by our relatively sparse sampling of the light curve. G286.2032+0.1740 appears only slightly brightened from June to December in 2019 and it is not clear if it has reached the plateau phase.

Figure 4.8 shows the H and K band spectra taken during June 2019, when G286.2032+0.1740 was in its bright state. There is a hint of shallow CO absorption at 2.29 μm. The location of the most prominent lines expected for a late-type star are marked but there is no clear evidence for emission or absorption lines, perhaps indicating that they are masked by veiling from the disk. There is no sign of Br_γ emission either, suggesting the accretion disk may extend all the way to the stellar surface during this outburst. We discuss the nature of G286.2032+0.1740 in the next section.

4.4 Discussion

Although the fraction of eruptive variables is very low among YSOs, they could provide unique insights into specific important processes occurring in the vicinity of the star, i.e., the star-disk interface, the inner disk as well as spatial scales beyond 1 AU, depending on specific mechanisms (Audard et al., 2014). A commonly accepted picture is that these objects are undergoing accretion outbursts, during which the accretion rate rapidly increases by several orders of magnitude. A significant fraction of the mass of the star may be accreted in such bursts. The eruptive YSOs

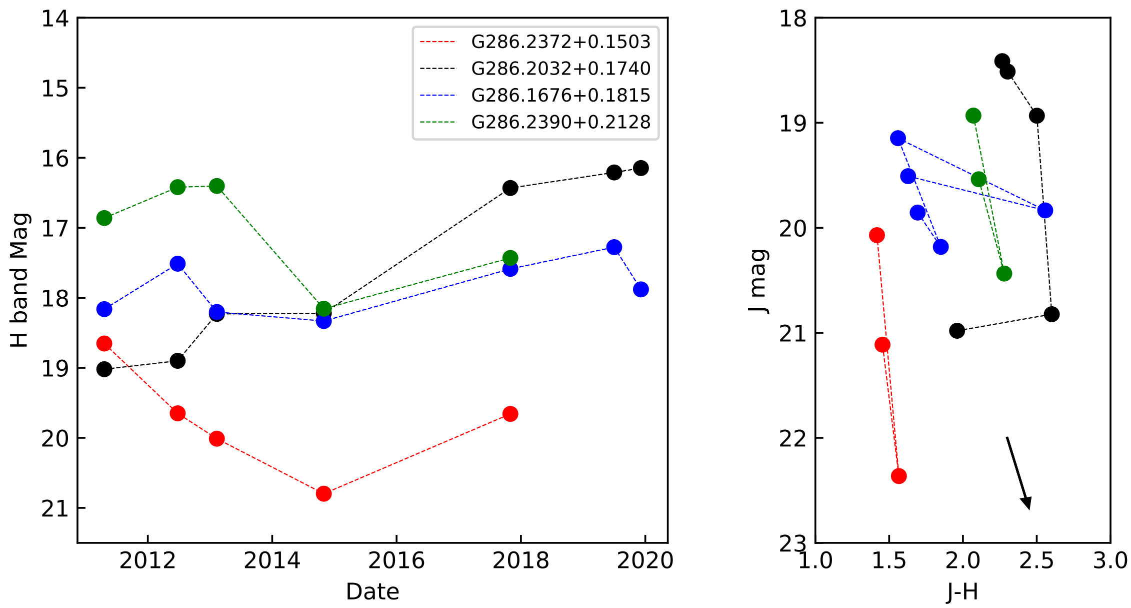

Figure 4.5: *Left:* H band Light curves for the four high amplitude variables. The photometric uncertainties are < 0.1 and not shown here. *Right:* Color-magnitude diagram. Note that for epoch 2012 June and 2013 February only H band photometry is available so no data is plotted in this diagram. An extinction vector with $A_K = 0.2$ is overplotted using the reddening law of Nishiyama et al. (2009).

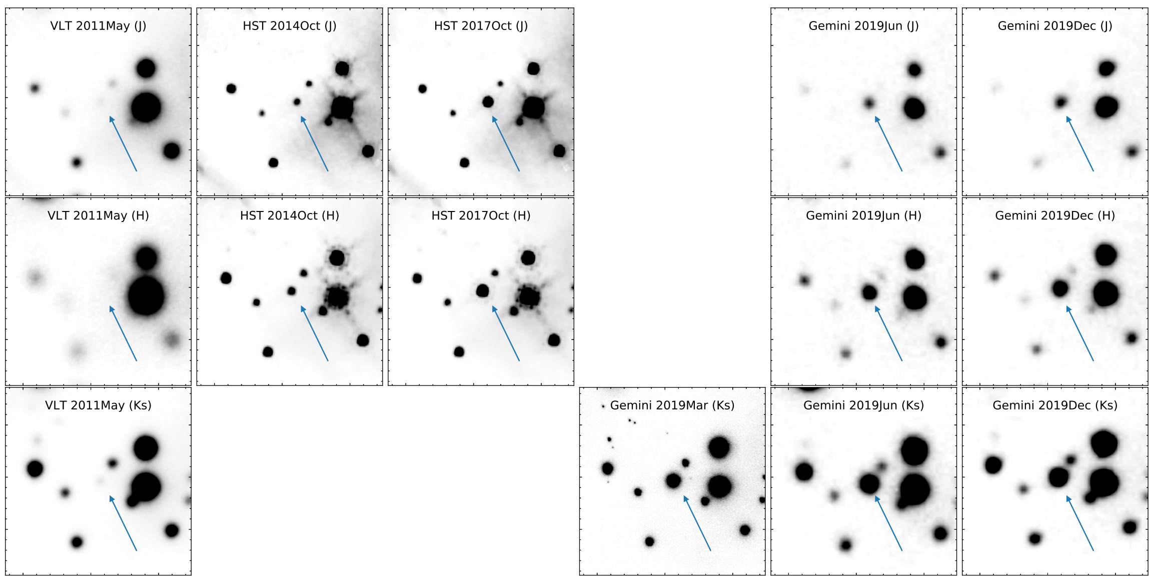

Figure 4.6: A composite of G286.2032+0.1740 images taken in different bands and at different epochs. The filters are J, H and Ks from top to bottom, respectively. From left to right are the J(F110W)/H(F160W)/Ks images with VLT HAWK-I in 2011 May, F110W/F160W images with HST in 2014 October, J/H images with HST in 2017 October, Ks images with Gemini GSAOI in 2019 March, and J/H/Ks images with Gemini F2 in 2019 June and December.

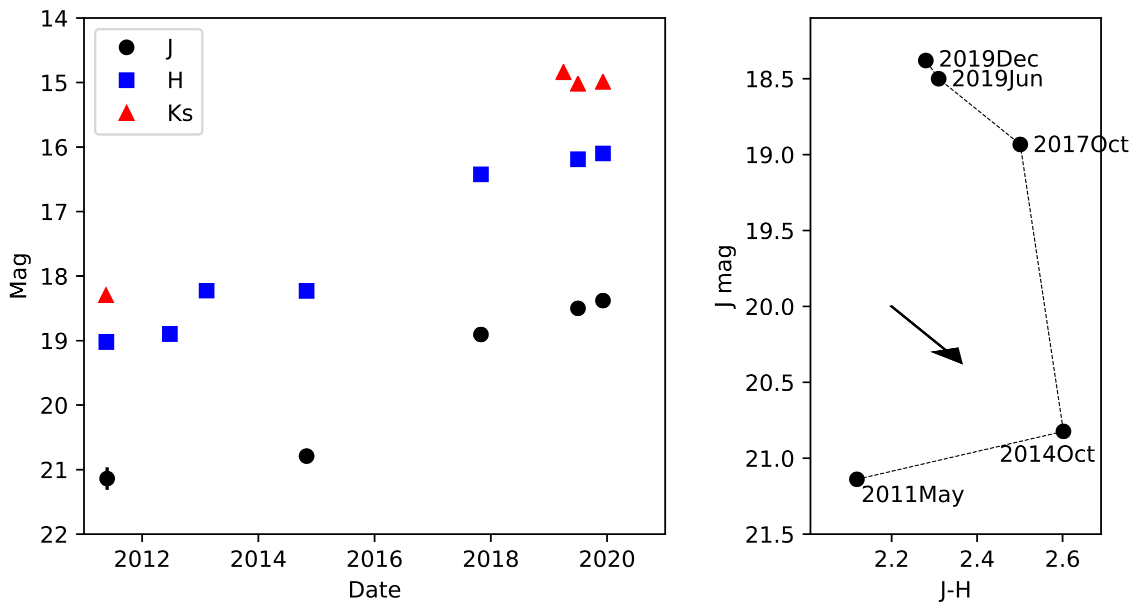

Figure 4.7: *Left:* Light curve for G286.2032+0.1740 over 8 years. J, H, Ks data are represented as circles, squares and triangles, respectively. *Right:* Color-magnitude diagram for G286.2032+0.1740. An extinction vector with $A_K = 0.1$ is overplotted, using the reddening law of Nishiyama et al. (2009).

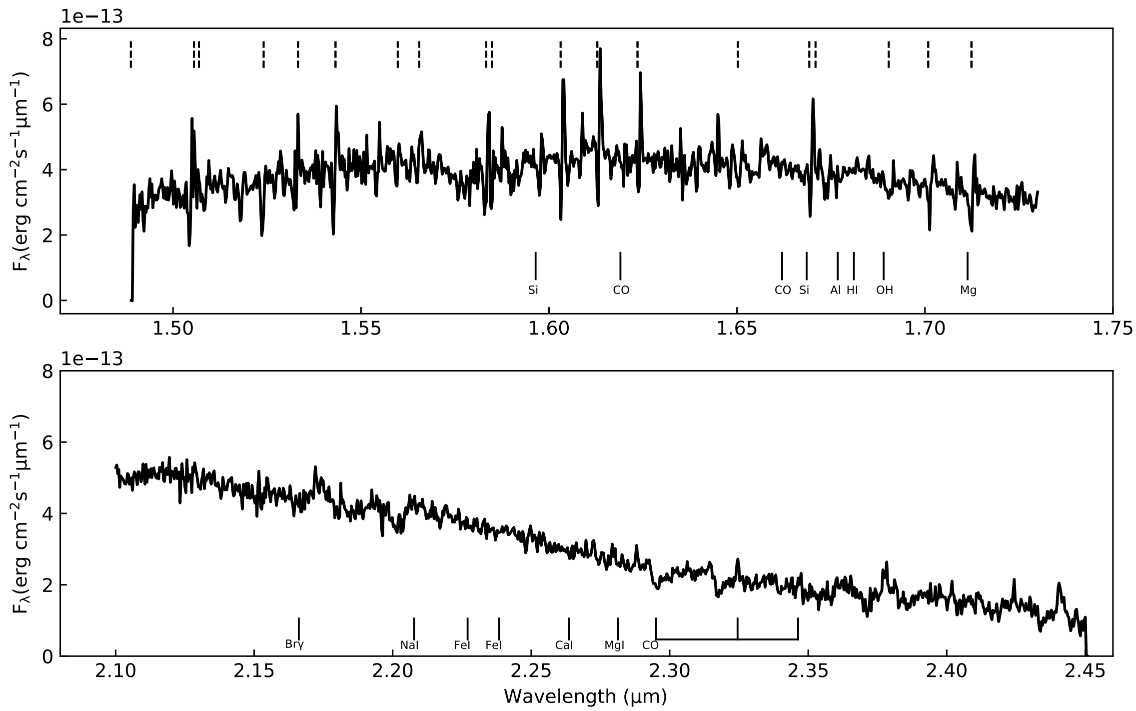

Figure 4.8: H- and K-band spectra of G286.2032+0.1740. Due to highly variable conditions residuals of OH lines are seen in the H band spectrum, as marked by the dashed black lines. The location of metallic lines that are seen in absorption for late type stars are marked. The lack of detection of the lines despite the relatively strong continuum suggests veiling.

have been traditionally divided into two classes: FUors, which have large flux increases and long outburst durations (tens to hundreds of years)(e.g., Herbig, 1977; Hartmann & Kenyon, 1996); and EXors, which have recurrent short-lived outbursts (weeks to months)(e.g., Herbig, 1989, 2008). Episodic accretion has several key implications for star formation and evolution, including solving the "luminosity problem" for embedded sources (Kenyon et al., 1990; Evans et al., 2009) and contributing to the luminosity spread of young star clusters in the Hertzsprung-Russell (HR) diagram (e.g., Baraffe et al., 2009).

However, many aspects of eruptive YSOs, including the recurrence time-scale and its relation with evolutionary stage, are still under active debate(e.g., Scholz et al., 2013; Fischer et al., 2019; Contreras Peña et al., 2019), partly due to limited numbers of examples. Both FUor and EXors categories have fewer than 20 that are known in total (Reipurth & Aspin, 2010; Connelley & Reipurth, 2018).

Comparing with known eruptive variables classes, G286.2032+0.1740, characterized by a long-term large-amplitude rising light curve, resembles an FUor object in its temporal behavior. In principle, high-amplitude variability in the NIR can be produced by various physical phenomena, including evolved giant and supergiant stars like Mira variables, cataclysmic variables and active galactic nuclei (AGN), etc (see Catelan et al., 2013, for a discussion). However, none of these possibilities is consistent with the characteristics of G286.2032+0.1740, including its faintness, NIR color and shape of the light curve. For example, there is no indication of periodicity from the light curve of G286.2032+0.1740, in contrast with what is expected for evolved stars like asymptotic giant branch (AGB) stars. The slowly rising light curve over years is also inconsistent with a nova outburst event(Warner, 2003). The NIR variability of AGN, on the other hand, is relatively smooth, but with smaller amplitude (Enya et al., 2002; Cioni et al., 2013). Furthermore, the fact that G286.2032+0.1704 is located in the Galactic plane with moderate extinction also makes it highly unlikely to be a background object like AGB star or AGN. In Figure 4.4 we overplot the $J-H$ vs. $H-K$ colors of G286.2032+0.1740 for three epochs with sufficient data (i.e., where the different bands were obtained close to each other within 5 days) (2011 May, 2019 June, 2019 December). At the more recent two epochs G286.2032+0.1740 appeared close to the boundary of the disk excess criterion, while in the early epoch G286.2032+0.1740 was to the left of that boundary, indicating a later evolutionary stage without much disk/envelope material. However, JHK observations are known to be less sensitive to disks around young stars, compared with L-band observations or mid-infrared diagnostics (e.g., Haisch et al., 2000) and stars with disks may drift in JHK color space, rendering a smaller detection rate with only single epoch observations (Rice et al., 2012). Overall, given its location in a known active star-forming region and its photometric behavior, we consider that G286.2032+0.1740 is more likely to be an outbursting YSO. Similar to other FUor/FUor candidates, G286.2032+0.1740 has a spectrum lacking emission lines. This relatively featureless spectrum, as well as possible CO absorption, is broadly consistent with the FUor category. A similar example is VVVv721 (Contreras Peña et al., 2017b; Guo et al., 2020), which is classified as a FUor and characterized by having CO absorption and broad H_2O absorption bands, with a lack of other photospheric features. In the case of G286.2032+0.1740 some doubts will remain since the CO absorption features are very weak compared to typical FUors (Reipurth & Aspin, 2010) and some other common characteristics of FUors, like broad band water vapor absorption, are also not clearly seen. G286.2032+0.1740 has a relatively slow rise in its light curve (rise time > 8 years), which is similar to the classical FUor V1515 Cyg (Kenyon et al., 1991)and VVVv721(Contreras Peña et al., 2017b). This slow rise may be explained as resulting from thermal instabilities that spread from the inner regions towards the outer parts of the accretion disc (see e.g., Audard et al., 2014).

Apart from accretion bursts, variable extinction may also be the reason for some extreme variation cases. For example, the variability of ESO-Oph-50 is explained by a low mass star seen through circumstellar matter, with changing inhomogeneities in the inner parts of the disk (Scholz et al., 2015). In the bright state the emission is consistent with a photosphere reddened by circumstellar dust, while in the faint state we are observing bluer scattered light since the direct stellar emission is blocked. However, the color behavior of G286.2032+0.1740 is inconsistent with this scenario. In Figure 4.7 we plot the color-magnitude diagram of G286.2032+0.1740. The trajectory can be divided into two stages: from May 2011 to Oct 2014 G286.2032+0.1740 became redder with slight brigtenning in the H band. In the second stage, G286.2032+0.1740 turned bluer and brighter, which is in contrast to ESO-Oph-50 (bluer when fainter), but consistent with some outburst cases (e.g., Aspin & Reipurth, 2009). The magnitude changes in this stage are also steeper than expected from the reddening vector and thus cannot be attributed to variable extinction. The color variation in the first stage (from 2011 to 2014) is more erratic, in which G286.2032+0.1740 was reddened by 0.5 mag but kept similar J band brightness. Unfortunately we only have a handful of data points in this pre/early outburst stage and thus cannot give more constraint on the nature of its color variation.

In the earliest epoch (2011), G286.2032+0.1740 was a faint object with a K magnitude of 18.3, suggesting its nature as a very low-mass YSO and/or it was observed through substantial extinction. To quantitatively estimate its mass, we compare its JHK photometry with the predictions from the Baraffe et al. (2015) isochrone, assuming a typical age of 1 Myr for G286 (Andersen et al., 2017a). Depending on which two colors are used for de-reddening, we obtain a range of masses from 0.06 to 0.10 $M_{\odot}$. The mass estimation falls in a similar range (0.05 to 0.12 $M_{\odot}$) with varying assumed ages from 0.5 Myr to 2 Myr. Note that even the earliest epoch data here may not represent the pre-outburst quiescent state, so this estimation should be considered as an upper limit. If this is confirmed by further spectroscopic observations, G286.2032+0.1740 provides a unique case to study the extreme variability for YSOs in the very low-mass regime, for which our knowledge is still sparse. Very low-mass stars and brown dwarfs have been observed to have both low-level periodic variability, and more irregular high amplitude variability, but typically only with I-band amplitude changes up to 1 mag (Scholz & Eislöffel, 2005; Bozhinova et al., 2016). In terms of high amplitude variables (> 3 mag) that are likely associated with strong accretion outbursts, there are very few cases reported in the very low-mass range ($< 0.5\ M_\odot$) (e.g., ASASSN-13db, (CTF93)216-2, Holoien et al., 2014; Caratti o Garatti et al., 2011). G286.2032+0.1740, with mass $< 0.12\ M_\odot$, is the lowest mass YSO with a strong outburst found so far. Combining its very low mass and strong outburst, G286.2032+0.1740 is apparently an extreme case of YSO varability. Since the object is currently near its brightest state, it gives a unique chance to characterize a very low mass YSO in its eruption stage.

Chapter 5

Star Formation in a Strongly Magnetized Cloud

5.1 Introduction

Star formation is a complicated process with many open questions, including what sets its rate, overall efficiency, and resulting mass distribution of stars, i.e., the stellar initial mass function (IMF). To help answer these questions, detailed studies of star-forming regions that can resolve individual self-gravitating cores are needed and these regions should span as wide a range of environmental conditions as possible in order to explore potential effects of these conditions. With this goal in mind, we present here a study of a dense star-forming clump in the Vela C giant molecular cloud (GMC) that has been selected to have a low angular dispersion in sub-mm polarization position angles, which likely indicates that it has relatively strong magnetic fields.

The Vela molecular cloud complex is one of the nearest giant molecular cloud complexes in the Galactic disk (Murphy & May, 1991). It is composed of four molecular clouds, of which Vela C is the most massive and the host of the youngest stellar population (Yamaguchi et al., 1999). Vela C is known to harbor low, intermediate and high-mass star formation (Massi et al., 2003; Netterfield et al., 2009) and hence is an ideal laboratory to study different modes of star formation. When contoured at $A_V = 7$ mag, the Vela C cloud appears to segregate into five distinct sub regions (North, Centre-Ridge, Centre-Nest, South-Ridge, and South-Nest), each with distinct morphological characteristics (Hill et al., 2011). In the Centre-Ridge sub region there is a compact HII region, RCW36, which is adjacent to a very prominent dust ridge that hosts the majority of dense cores in the cloud (Hill et al., 2011). Owing to its proximity, i.e., at a distance of 933 ± 94 pc (Fissel et al., 2019), Vela C has been an important target for magnetic field mapping studies through sub-mm polarimetry and near-infrared stellar polarimetry (Fissel et al., 2016; Kusune et al., 2016; Santos et al., 2017). In particular, the relative orientation between gas column density filamentary structures and the magnetic field changes progressively with increasing gas column density, from mostly parallel or having no preferred orientation at low column densities to mostly perpendicular at the highest column densities (Soler et al., 2017; Fissel et al., 2019). This suggests that the magnetic field is strong enough to have influenced the formation of the dense gas structures within Vela C.

The ongoing star formation in Vela C has been investigated in several studies via far-infrared (FIR) to mm continuum imaging (e.g., Netterfield et al., 2009; Giannini et al., 2012; Massi et al., 2019). Giannini et al. (2012) identified 268 dense cores with *Herschel* FIR data. Massi et al. (2019) found 549 cores based on sub-mm continuum mapping using APEX and derived a prestellar core mass function (CMF) that has a similar shape as the stellar IMF at the high mass end. However, these observations are limited by their relatively low spatial resolution, i.e., $\gtrsim 20''$ (0.09 pc), which is unable to resolve down to the scale of dense cores (i.e., a few $\times$ 0.01 pc) relevant to the formation of individual stars or small-N multiple systems.

Table 5.1: Observed transitions

molecular transition	frequency[a] (GHz)	E_u/k (K)	HPBW ($''$)	$\triangle v$ ($km\,s^{-1}$)	sensitivity ($Jy\,beam^{-1}$ per channel)
N_2D^+(3-2)	231.321912	22.2	$7.07''\times4.44''$	0.046	0.20
^{13}CO(2-1)	220.398684	15.9	$7.63''\times4.57''$	0.096	0.20
$C^{18}O$(2-1)	219.560354	15.8	$7.65''\times4.61''$	0.096	0.16
DCN(3-2)	217.238538	20.9	$7.48''\times4.84''$	0.195	0.10
SiO(5-4)	217.104980	31.3	$7.49''\times4.84''$	0.195	0.09
$CH_3OH(5_{1,4}-4_{2,2})$	216.945521	55.9	$7.50''\times4.84''$	0.196	0.09
DCO^+(3-2)	216.112580	20.7	$7.50''\times4.86''$	0.196	0.09
N_2H^+(3-2)	279.511832	26.8	$5.88''\times3.60''$	0.038	0.30
DCN(4-3)	289.644907	34.8	$5.75''\times3.51''$	0.073	0.20
DCO^+(4-3)	288.143858	34.6	$5.71''\times3.51''$	0.073	0.30

[a] Line frequencies from Cologne Database for Molecular Spectroscopy (CDMS; http://www.astro.uni-koeln.de/cdms/catalog) (Müller et al., 2005). For N_2H^+(3-2) and N_2D^+(3-2) we list the frequency of the hyperfine component with the largest A_{ul} emission coefficient in Pagani et al. (2009).

In this paper we present an ALMA 7m-array study in both Band 6 and Band 7 towards a dense clump in the Center Ridge of Vela C (referred as CR1 clump hereafter) and the observations achieve $\sim5''$ resolution for various molecular species (see section 5.1). The CR1 clump is located to the north of a hot pocket of gas (RCW 36) around the OB cluster, but appears to not yet be impacted by it (Hill et al., 2011). The CR1 clump has been selected for this study because it appears to be strongly magnetized as evidenced by having a local minimum of angular dispersion in sub-mm polarization position angles, as shown in Figure 6.1 (see also Figure 6 in Fissel et al., 2016). Thus, the main goal of this paper is to study the dense core population leading to star formation in this example of a strongly magnetized environment. The CR1 clump is close to the #5 $C^{18}O$ clump identified in Yamaguchi et al. (1999) (see also Figure 6.1), for which Kusune et al. (2016) estimated a plane-of-the-sky (POS) magnetic field strength of 120 μG based on near-IR stellar polarimetry. According to the Chandrasekhar-Fermi method (Chandrasekhar & Fermi, 1953), the POS magnetic field strength B_{pos} can be expressed as

$$B_{\mathrm{pos}} = Q\sqrt{4\pi\rho}\frac{\sigma_v}{\sigma_\theta} \tag{5.1}$$

where ρ is the mean density of the cloud, σ_v is the line-of-sight velocity dispersion, σ_θ is the dispersion of the polarization position angles, and $Q \sim 0.5$ is a correction factor for $\sigma_\theta \lesssim 25°$ (Ostriker et al., 2001). In Kusune et al. (2016) the angular dispersion of polarization angles in the #5 $C^{18}O$ clump is estimated to be 18°. However, it is difficult to probe the magnetic field structures in high extinction regions with near-IR polarimetry and most polarization vectors are from the relative diffuse part of the cloud. The angular dispersion of our mapped region (or #5 $C^{18}O$ clump) appears much lower in the BLASTPol survey, i.e., $\sim 2°$ (see also Figure 6.1), leading to a higher B_{pos} estimation of ~ 1 mG. Note that it is likely that the small scale magnetic field variation is not resolved in the BLASTPol survey (reso. $\sim 2.5'$), so future high resolution dust polarization observations are required to clarify the field strength in this region. Nevertheless, the selected region is likely to have a relatively strong magnetic field compared to surrounding regions in Vela C.

Our Band 6 spectral set-up and analysis methods are similar to our previous studies of the G286 protocluster (Cheng et al., 2020) and Infrared Dark Clouds (IRDCs) (e.g., Tan et al., 2013; Kong et al., 2017), which have a goal of studying cores via their mm dust continuum emission and via emission lines from dense gas tracers, especially N_2D^+(3-2). The Band 7 spectral set-up is designed to obtain a sub-mm dust continuum measurement, as well as observation of N_2H^+(3-2) that allows an accurate estimate of the level of deuteration of N_2H^+, which is expected to be boosted in cold, dense conditions and thus may be a useful evolutionary indicator of prestellar and early stage protostellar cores.

This paper is structured as follows: the observations and results are presented in section 5.2 and section 5.3, respectively. We further discuss our results in section 5.4, and present our conclusions in section 5.5.

5.2 Observations

5.2.1 ALMA observations

The observations were conducted with the ALMA 7m-array in Bands 6 and 7 in Cycle 6 (Project ID 2018.1.00227.S, PI: J. C. Tan), during a period from March to April 2019. The entire field ($10' \times 4.5'$) was divided into four strips, each about $150''$ wide and $270''$ long.

For the Band 6 observation we set the central frequency of the correlator sidebands to be the rest frequency of the N_2D^+(3-2) line for SPW0 with a velocity resolution of 0.046 $\mathrm{km\,s^{-1}}$. The second baseband SPW1 was set to 231.00 GHz, i.e., 1.30 mm, to observe the continuum with a total bandwidth of 1.875 GHz, which also covers CO(2-1) with a velocity resolution of 1.46 $\mathrm{km\,s^{-1}}$. SPW2 was split to cover ^{13}CO(2-1) and $C^{18}O$(2-1) line, both with a velocity resolution of 0.096 $\mathrm{km\,s^{-1}}$. The frequency coverage for SPW3 ranged from 215.85 to 217.54 GHz to observe DCN(3-2), DCO^+(3-2), SiO(5-4) and $CH_3OH(5_{1,4} - 4_{2,2})$.

For Band 7 we set the central frequency to be the rest frequency of the N_2H^+(3-2) line for SPW0 with a velocity resolution of 0.038 $\mathrm{km\,s^{-1}}$. The central frequencies of SPW1 and SPW2 were set to 278.88 GHz and 291.10 GHz, respectively, and each band had a bandwidth of 1.875 GHz to observe continuum emission. SPW3 was split equally to observe two lines, i.e., DCN(4-3), DCO^+(4-3), with 58.59 MHz (61 km/s) bandwidth and resolution of 0.073 km/s.

The raw data were calibrated with the data reduction pipeline using *Casa* 5.4.0. The continuum visibility data were constructed with all line-free channels. We per-

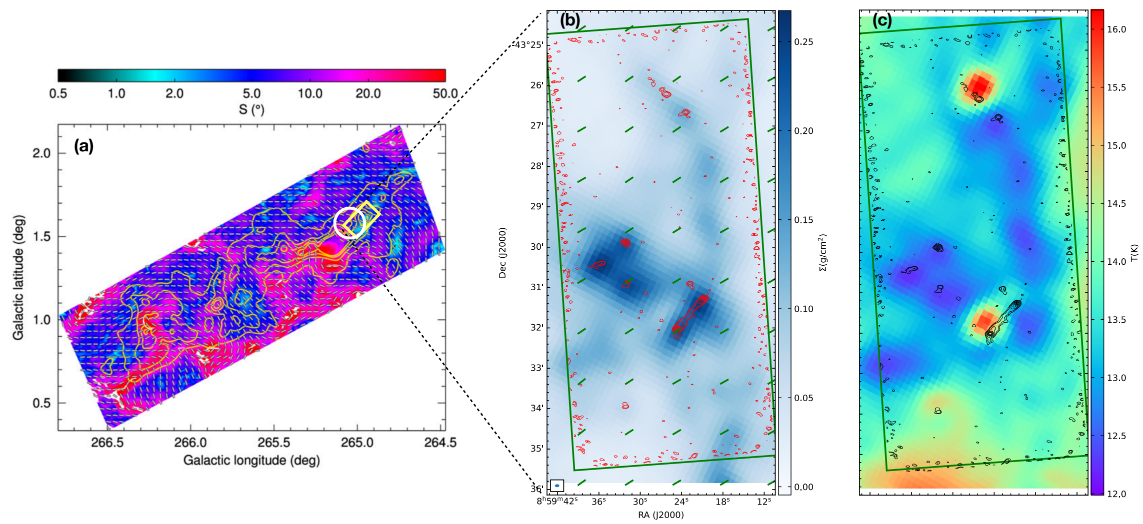

Figure 5.1: (a) Figure 6 from Fissel et al. (2016). BLASTPol map of the dispersion in the polarization-angle in degrees on 0.5 pc scales, shown in colorscale. Line segments show the orientation of the magnetic field as projected on the plane of the sky (Φ), derived from the BLASTPol 500 μm data. The Φ measurements are shown approximately every $2.5'$. Contours indicate 500 μm I intensity levels of 46, 94, 142, and 190 MJy sr^{-1}. The yellow box indicates the region mapped by ALMA in this study, which is selected based on its appearance as a local minimum on the polarization-angle dispersion map. The position of the #5 $C^{18}O$ clump in Yamaguchi et al. (1999) is indicated with a white circle with a radius of $4'$. (b) Mass surface density map derived with the *Herschel* data shown in color scale. The red contours indicate the ALMA 1.3 mm continuum map. The contour levels are $\sigma \ \times$ (4, 6, 10, 20, 40, 80), with $1\sigma = 1.3$ mJy beam^{-1}. The direction of the POS magnetic field in panel (a) is shown in green line segments. (c) Temperature map derived with the *Herschel* data shown in color scale. The black contours show the ALMA 1.3 mm continuum map.

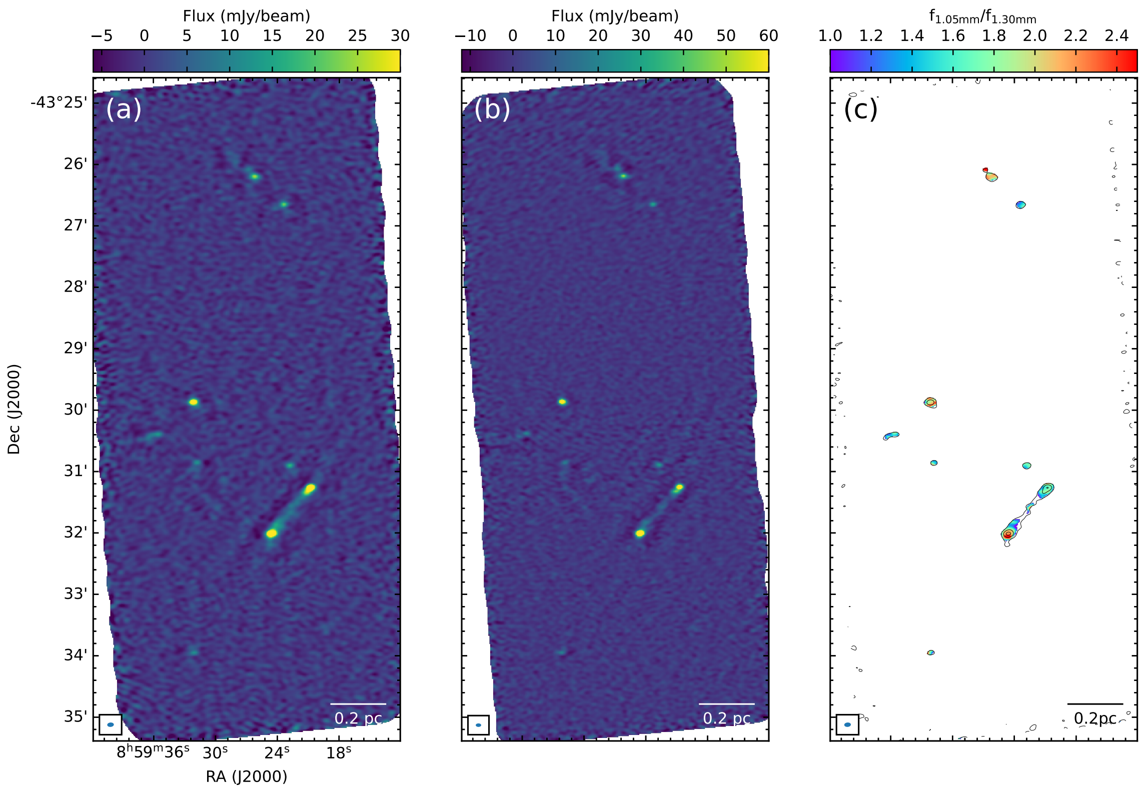

Figure 5.2: (a) ALMA Band 6 (1.3 mm) continuum image of Vela C CR1. (b) ALMA Band 7 (1.05 mm) continuum image of Vela C CR1. (c) Map of flux ratio $f_{1.05\text{mm}}/f_{1.30\text{mm}}$. Only the regions with flux above 3σ in both bands are shown. In deriving this map we found a systematic positional offset $\sim 0\farcs3$ between Band 6 and Band 7 maps, possibly due to imperfect phase calibration. This offset has been corrected in this map.

formed imaging with the *tclean* task in *Casa* and during cleaning we combined data for all four strips to generate a final mosaic map. The 7m-array data were imaged using a Briggs weighting scheme with a robust parameter of 0.5, which yields a resolution of $7.00'' \times 4.29''$ for Band 6, and $5.92'' \times 3.47''$ for Band 7. The 1σ noise levels in the continuum image are 1.3 $\mathrm{mJy\,beam^{-1}}$ and 1.8 $\mathrm{mJy\,beam^{-1}}$ for Band 6 and Band 7, respectively. The resolutions and sensitivities for spectral lines are summarized in section 5.1.

5.2.2 Auxiliary data

We have retrieved archival data to provide auxiliary information at infrared wavelengths. The 3.5 and 4.5 μm maps are from the Spitzer Heritage Archive hosted in the NASA/IPAC Infrared Science Archive. For 12 and 22 μm we use Wide-field Infrared Survey Explorer *WISE* archival data. Continuum images in the wavelengths of *Herschel PACS* (70 and 160 μm) and *SPIRE* (250, 350, and 500 μm) were obtained from the Herschel Science Archive. For this, Vela C was observed on 2010, May 18, as part of the HOBYS (Herschel imaging survey of OB young stellar objects, Motte et al. (2010)) guaranteed time key program.

We also obtained the total hydrogen column density N_{H} (in units of hydrogen nuclei per cm^{-2}) and temperature map (see Figure 6.1), which were first presented in Section 5 of Fissel et al. (2016). These maps are based on dust spectral fits to four far-IR/sub-mm dust emission maps: *Herschel*-SPIRE maps at 250, 350, and 500 μm; and a *Herschel*-PACS map at 160 μm. These maps have the same spatial resolutions as the 500 μm map, i.e., $35.2''$.

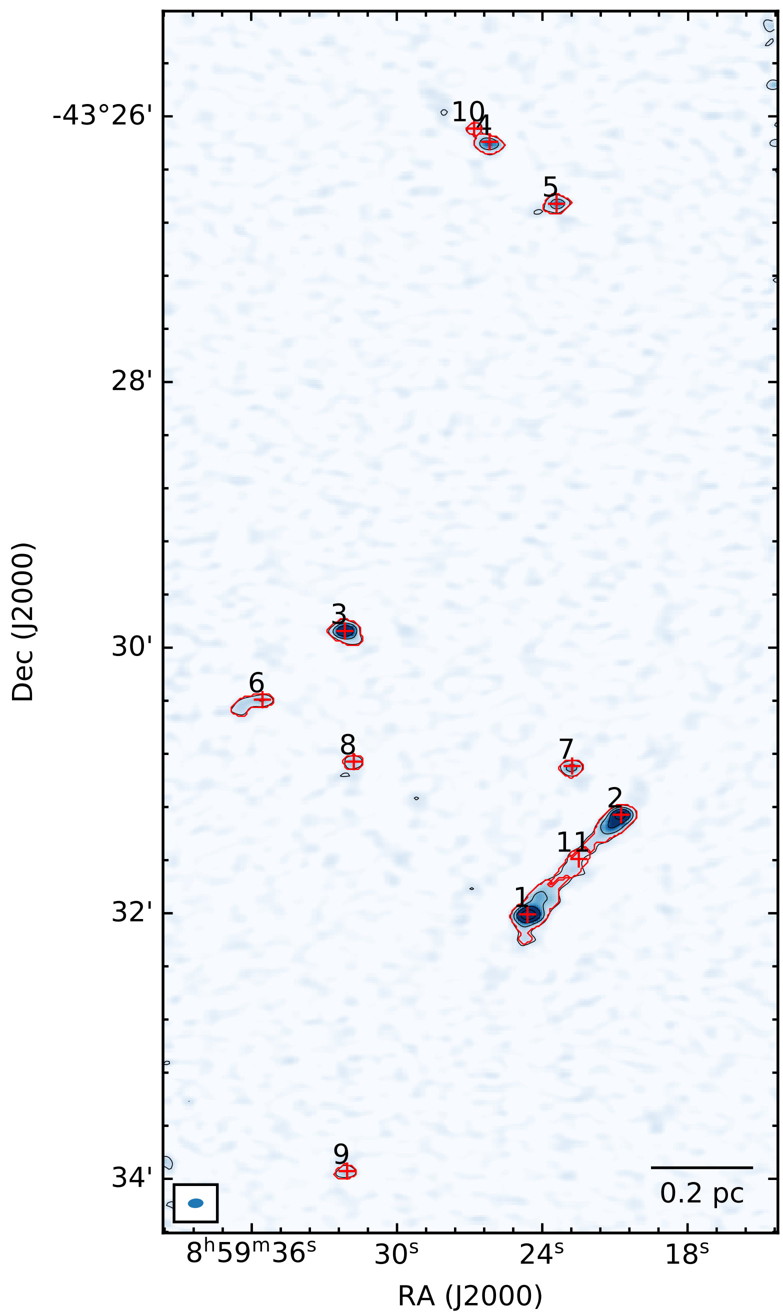

Figure 5.3: Cores identified with *dendrogram* overlaid on the 1.3 mm continuum. The red crosses indicate the peak positions, while the red contours indicate the boundaries returned by *dendrogram*. Note that CR1c11 was identified via N_2D^+ moment 0 map (see text).

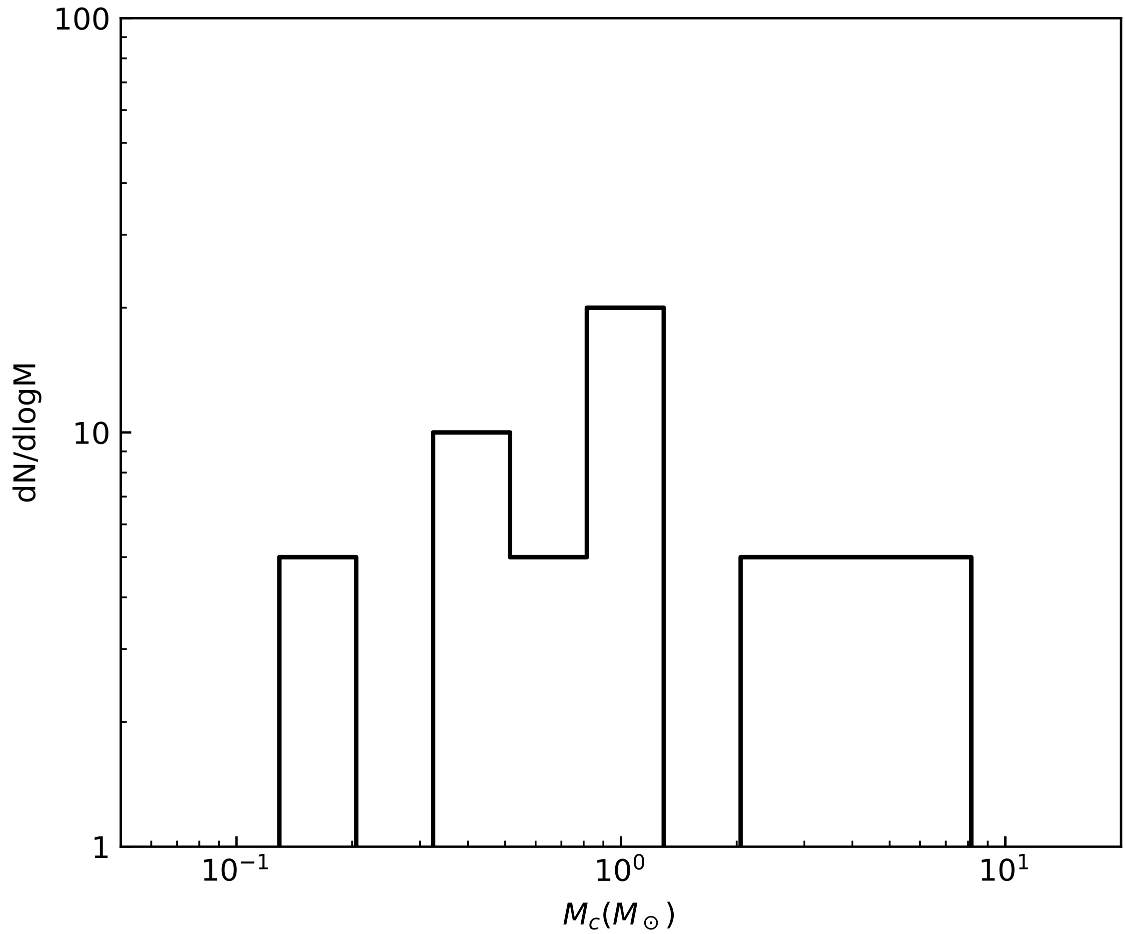

Figure 5.4: The mass distribution of cores detected in the Vela C CR1 region.

Table 5.2: Core properties

Core	R.A. (°)	Dec. (°)	M_c ($M_\odot$)	Area arcsec^2	R_c(") arcsec	R_c (0.01pc)	Σ_c (g cm^{-2})	$n_{\mathrm{H},c}$ 10^5cm^{-3}	$\frac{f_{1.05\mathrm{mm}}}{f_{1.30\mathrm{mm}}}$	T_c[a] (K)	α_{vir}[b]
1	134.85254	-43.53361	6.69	301	9.47	4.27	0.228	6.00	1.83 ± 0.14	$7.8^{+3.6}_{-1.9}$	1.30
2	134.83645	-43.52111	4.86	206	7.83	3.53	0.242	7.70	1.59 ± 0.13	$5.1^{+1.2}_{-0.8}$	1.01
3	134.88394	-43.49805	2.52	117	5.90	2.66	0.222	9.35	1.90 ± 0.16	$9.4^{+7.6}_{-2.8}$	0.98
4	134.85906	-43.43667	1.19	76	4.77	2.15	0.161	8.41	2.02 ± 0.21	$13.6^{+116.6}_{-6.1}$	1.58
5	134.84758	-43.44444	0.88	68	4.50	2.03	0.133	7.35	1.37 ± 0.19	$3.8^{+1.0}_{-0.7}$	1.47
6	134.89812	-43.50666	0.88	92	5.23	2.36	0.098	4.66	1.36 ± 0.21	$3.8^{+1.2}_{-0.8}$	3.00
7	134.84488	-43.51500	0.61	52	3.95	1.78	0.120	7.59	1.59 ± 0.25	$5.1^{+2.9}_{-1.4}$	
8	134.88242	-43.51444	0.35	37	3.33	1.50	0.097	7.30	1.63 ± 0.35	$5.5^{+6.3}_{-2.0}$	
9	134.88358	-43.56583	0.34	37	3.33	1.50	0.094	7.04	1.63 ± 0.36	$5.4^{+6.7}_{-2.0}$	
10	134.86173	-43.43500	0.17	20	2.44	1.10	0.087	8.88	2.48 ± 0.68	>7.4	
11	134.84373	-43.52667	0.88	110	7.72	2.58	0.082	3.56	1.28 ± 0.22	$3.5^{+1.0}_{-0.7}$	4.84

[a] Estimated from ratio of $f_{1.05\mathrm{mm}}/f_{1.30\mathrm{mm}}$ assuming optically thin thermal emission from dust and dust opacities of the moderately coagulated thin ice mantle model of Ossenkopf & Henning (1994).

[b] For each core the virial parameter is derived with a deconvolved core radius, and velocity dispersions combining measurements with different tracers, i.e., the same as panel (d) in Figure 5.8.

5.3 Results

5.3.1 Continuum

Figure 5.2 illustrates the Band 6 (1.3 mm) and Band 7 (1.05 mm) continuum of the Vela C CR1 clump. Overall there are about 10 clearly visible cores sparsely distributed over the field. The detections at 1.05 mm are similar to those at 1.3 mm. The two brightest cores are located in the southern part of the field, with a linear filament or "bridging feature" connecting them. This bridge is about 0.27 pc long and appears more prominent at 1.3 mm. As shown in Figure 6.1, the orientation of this bridging feature is close to the POS direction of the magnetic field derived in the BLASTPol survey, with an offset of ~ 18 °.

We used the *dendrogram* algorithm (Rosolowsky et al., 2008) implemented with *astrodendro* to carry out an automated, systematic search for cores in the continuum images following the method used in Cheng et al. (2018) and Liu et al. (2018). We defined the identified leaves (the base element in the hierarchy of dendrogram that has no further sub-structure) as cores. We set the minimum flux density threshold to 4σ, the minimum significance for structures to 1σ, and the minimum area to half the size of the synthesized beam. We tried *dendrogram* identification on the continuum maps of both bands and found almost equivalent results. Hereafter we define the positions and boundaries of cores based on the 1.3 mm data, which have slightly better signal to noise ratios, as shown in Figure 5.3. The cores are named as CR1c1, CR1c2, etc., with the numbering order from highest to lowest integrated flux. There is an additional core (CR1c11) that is located at the bridging feature and not identified as a core from the 1.3 mm data, but it does appear as an independent condensation in 1.05 mm continuum, and moment 0 maps of some lines like N_2D^+(3-2) and DCO^+(3-

2). So we also include CR1c11 in our sample and adopt a core boundary defined using the N_2D^+ moment 0 map (by running *dendrogram* with the same set up). Then the regions of CR1c1 and CR1c2 that overlap with CR1c11 are excluded from the definition of CR1c1 and CR1c2 when deriving their properties.

We then estimated the masses of cores assuming the 1.3 mm emission comes from optically thin thermal dust emission with a uniform temperature of 15 K following the methods and assumptions used in the study of Cheng et al. (2018), with the only difference being that this previous study adopted a fiducial temperature of 20 K. Our reason to choose a slightly lower temperature is the availability in Vela C of a relatively high resolution temperature map (though not high enough to resolve individual cores themselves) that indicates temperatures closer to 15 K. The estimated masses range from 0.17 to 6.7 $M_\odot$. If temperatures of 10 K or 20 K were to be adopted, then the mass estimates would differ by factors of 1.85 and 0.677, respectively. In Figure 5.4 we plot the CMF of the detected sample. Given the small numbers of detected cores, it is difficult to make meaningful comparison with the CMFs of other regions.

The core radii are evaluated as $R_c = \sqrt{A/\pi}$, where A is the projected area of each core returned by the *dendrogram* algorithm. The median radius is 0.016 pc (i.e., 3300 au), similar to the spatial resolution of 5100 au that is achieved by the $\sim 5.5''$ angular resolution observations. This indicates that most cores are not well resolved. Given masses and radii, the mass surface densities and volume number densities of the cores can be estimated. These properties are summarized in Figure 5.2.2.

In Figure 5.2(c) we present the map of 1.05 mm/1.3 mm flux ratio for positions with fluxes greater than 3σ in both bands (after convolving 1.05 mm data to the angular resolution of the 1.3 mm map). This ratio ranges from 1.0 to 2.5 over the map. We use this ratio to give more constraints on the dust temperature. To do this, we compare the observed ratio $f_{1.05\mathrm{mm}}/f_{1.30\mathrm{mm}}$ with that predicted from models of optically thin thermal dust emission, i.e.,

$$\frac{f_{\nu_1}}{f_{\nu_2}} = \frac{B_{\nu_1}(T_{\rm dust})}{B_{\nu_2}(T_{\rm dust})} \cdot \frac{\kappa_{\nu_1}}{\kappa_{\nu_2}} = \frac{B_{\nu_1}(T_{\rm dust})}{B_{\nu_2}(T_{\rm dust})} \cdot \left(\frac{\nu_1}{\nu_2}\right)^{\beta} \tag{5.2}$$

where f_ν is the dust emission flux at frequency ν, $B_\nu(T_{\rm dust})$ is the Planck function with dust temperature $T_{\rm dust}$, κ_ν is the dust opacity and β is the dust opacity index. For fiducial dust opacity we adopt the same model that we have used for our mass estimates, i.e., the thin ice mantle model of Ossenkopf & Henning (1994) with 10^5 years of coagulation at a density of $n_{\rm H} = 10^6 {\rm cm}^{-3}$. At sub-mm wavelengths, this model exhibits $\kappa_\nu = 0.1(\nu/1000\,{\rm GHz})^\beta {\rm cm}^2{\rm g}^{-1}$ with $\beta \simeq 1.8$. As shown in Figure 5.5, $f_{1.05{\rm mm}}/f_{1.30{\rm mm}}$ increases from 1.5 at $T_{\rm dust} = 5$ K to about 2.1 at $T_{\rm dust} = 20$ K, and grows asymptotically to 2.2 at higher temperatures. For comparison, we also present the predicted $f_{1.05{\rm mm}}/f_{1.30{\rm mm}}$-$T_{\rm dust}$ relation for the equivalent bare grain and thick ice mantle models of Ossenkopf & Henning (1994). We see that for the models with ice mantles (thin/thick), which are expected to be the most relevant for prestellar and early stage protostellar cores, the choice of dust opacity model does not strongly affect the derived $T_{\rm dust}$ for a given flux ratio. More generally, our derived $T_{\rm dust}$ estimates are valid for dust opacity models that have a spectral index β close to 1.8 in the millimeter wavelength regime.

Given the observed values of $f_{1.05{\rm mm}}/f_{1.30{\rm mm}}$, we estimate $T_{\rm dust}$ by looking for the corresponding values on the predicted relation, as shown in Figure 5.5. The uncertainties in $f_{1.05{\rm mm}}/f_{1.30{\rm mm}}$ are also transferred into the uncertainties in $T_{\rm dust}$. Figure 5.2.2 lists these derived temperatures. The fluxes of cores are measured by integrating over the region defined by *dendrogram* and for flux uncertainties we consider both the root-mean-square error and a flux calibration uncertainty of about 5%, and combine them in quadrature.

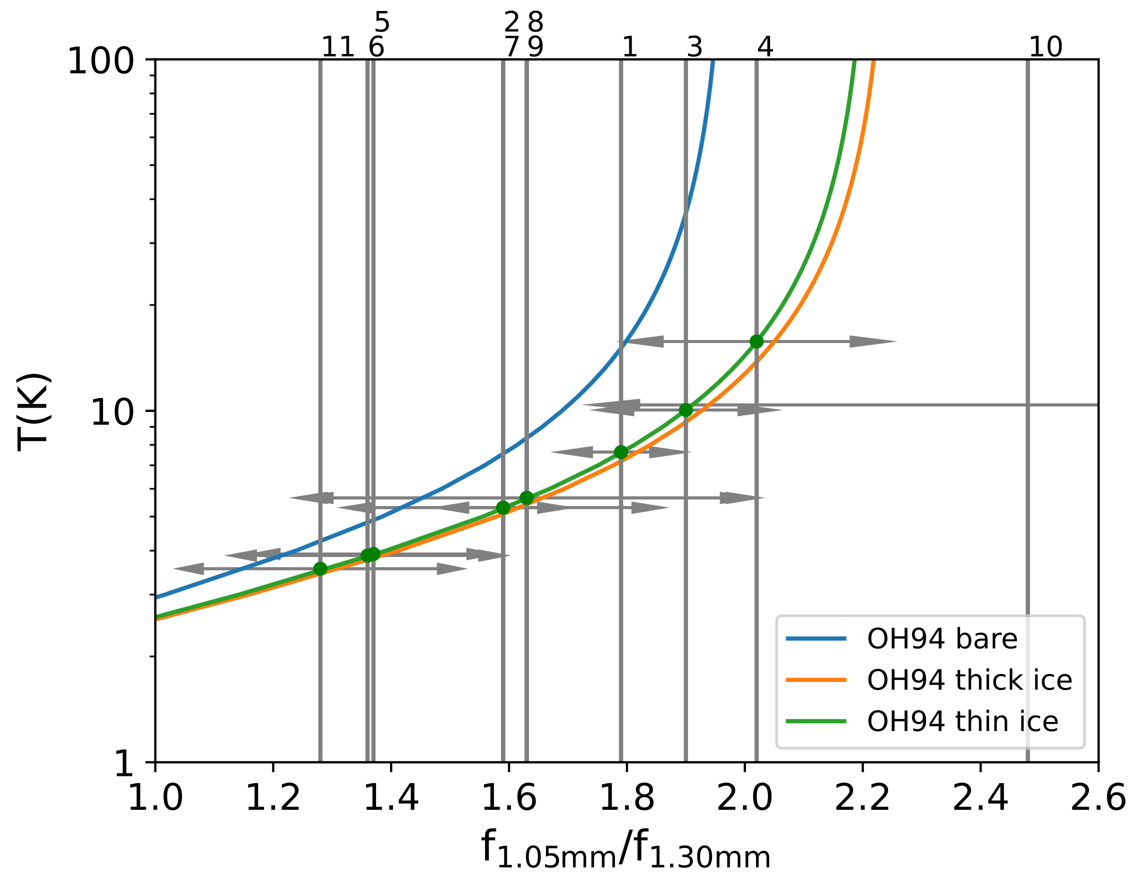

Figure 5.5: The predicted relation between $f_{1.05\mathrm{mm}}/f_{1.30\mathrm{mm}}$ and temperature for three dust models from Ossenkopf & Henning (1994). The measured ratios for the dense cores of Vela C CR1 are shown by the vertical lines, with uncertainties shown as two headed arrows at the location where the vertical line crosses the fiducial OH94 thin ice mantle model (or at 10 K level for CR1c10). The indices of cores as in Figure 5.2.2 are labeled on top of the plot.

The measured $T_{\rm dust}$ values range from 3.5 K to 13.6 K. For CR1c10 the $f_{\rm 1.05mm}/f_{\rm 1.30mm}$ is 2.48 ± 0.68, leading to an unrealistic $T_{\rm dust}$ of $957.0^{+\infty}_{-949.6}$ K, so we only conservatively list the lower limit of 7.4 K. In general the derived core temperatures appear to be relatively low compared to canonical estimates of temperatures in molecular clouds, i.e., typically found to be in the range $\sim 10-20$ K. On the larger scales probed by the *Herschel* sub-mm observations (see Figure 6.1), the CR1 clump is estimated to have dust temperatures of $\sim$ 12-16 K. Still, we note that the centers of some prestellar cores have been measured to have temperatures as low as about 6 K from NH_3 observations (Crapsi et al., 2007). We further note that there are several potential sources of systematic uncertainties in the temperature estimation from $f_{\rm 1.05mm}/f_{\rm 1.30mm}$. The effects of choice of dust model have already been described in Figure 5.5. In addition, since the core boundaries are defined based on the 1.3 mm data, we expect that the estimated flux ratio $f_{\rm 1.05mm}/f_{\rm 1.30mm}$ and correspondingly $T_{\rm dust}$ could be systematically underestimated. Differences in recovered flux fractions could also introduce systematic uncertainties, with a smaller flux recovery fraction generally expected at 1.05 mm. Another potential source of uncertainty is if the cores (or part of the cores) become optically thick, which would occur first at 1.05 mm. This would tend to lower the flux received at 1.05 mm, again causing an underestimation of $T_{\rm dust}$. For example, if a core is moderately optical thick at 1.05 mm with $\tau_{\rm 1.05mm} = 1$, then the resulting $f_{\rm 1.05mm}/f_{\rm 1.30mm}$ will be $\sim$13% lower than the case assuming optical thin. However, most cores in our sample should be optically thin judging from the observed low brightness temperatures T_B. In Band 7 the median T_B seen at the continuum peaks of different cores is about 0.02 K, i.e., even assuming a very low $T_{\rm dust}$ of $\sim$5 K, it is still about a factor of 250 lower. Such a big difference can not be explained purely by a beam filling effect, since it requires a small source size of $\lesssim$ 20 AU (a factor of 250 smaller than the spatial resolution, i.e., around $4.5''$, or $\sim$ 4200 AU in Band 7).

Thus it is more likely due to a small optical depth, i.e., $\tau \ll 1$ in the observed bands, at least averaged on the core scale, although a small inner region that is optically thick is still possible in some cores. These results motivate future work on radiative transfer models of protostellar cores to predict these Band 6 to Band 7 flux ratios.

5.3.2 Spectral lines

Figure 5.6 shows the moment 0 maps of $C^{18}O$(2-1), N_2H^+(3-2), N_2D^+(3-2), DCO^+(3-2), DCN(3-2) and SiO(5-4). Other transitions described in section 5.2 (DCO^+(4-3), DCN(4-3), $CH_3OH(5_{1,4} - 4_{2,2})$) do not have detection above 5σ and hence are not included here. The maps of both ^{13}CO(2-1) and $C^{18}O$(2-1) appear strongly affected by missing large scale information due to the interferometric nature of the observations. It is likely that there exists significant CO line emission from nearby regions that are outside of the field of view, which hinders the performance of the cleaning process, and leads to strong sidelobes. In light of this we only include $C^{18}O$(2-1) here for quantitative analysis, which is more optically thin and relatively less affected. N_2H^+(3-2) has strong detections and appears closely associated with the dust continuum. DCO^+(3-2) is also associated with the dust continuum but slightly more extended. N_2D^+(3-2) and DCN(3-2) have more limited detection compared with N_2H^+(3-2), and are only seen clearly towards a few cores. SiO(5-4) is only detected at the position of CR1c1, possibly tracing shocks related with accretion or outflows.

To investigate the kinematic and dynamical properties of cores, we extract the average spectra of each core, as shown in Figure 5.7. Among the four tracers, N_2H^+ and DCO^+ have clear detections for almost all cores, while other lines are relatively weak and only detected for part of the core sample. The $C^{18}O$ profiles appear to be relatively complicated for some cores, like CR1c3 and CR1c5. To measure the centroid velocity and velocity dispersion of each core we perform a fitting on spectra

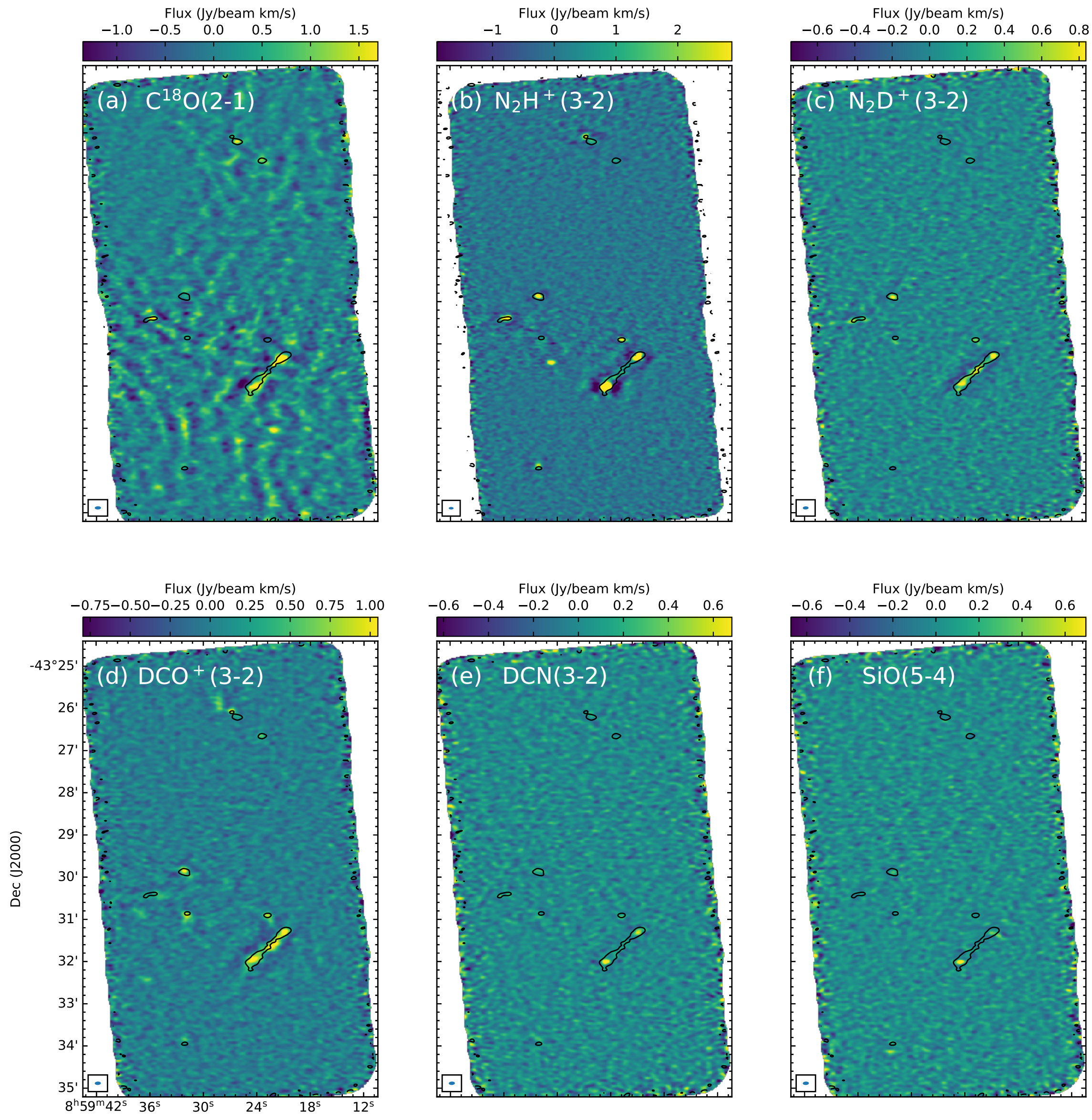

Figure 5.6: Panels from (a) to (f) show the moment 0 maps of $C^{18}O$(2-1), N_2H^+(3-2), N_2D^+(3-2), DCO^+(3-2), DCN(3-2), and SiO(5-4). The 5σ 1.3mm continuum contour is overlaid in black for comparison.

Figure 5.7: Spectra (some with vertical offsets) of N_2H^+(3-2) (blue), N_2D^+(3-2) (red), DCO^+(3-2) (green), DCN(3-2) (magenta) and $C^{18}O$(2-1) (cyan) (see also legend in panel 1) of the 11 cores. In the first panel the relative intensities of hyperfine components of N_2H^+(3-2) and N_2D^+(3-2) are shown underneath the spectra. For spectra with a peak flux greater than 5σ, we perform a Gaussian (or hyperfine profile weighted) fitting. The returned parameters (centroid velocity, velocity dispersion) for each line are displayed in the top left, in the same color as the corresponding line. The dashed vertical lines indicate the centroid velocities from line fitting. If there are multiple components for $C^{18}O$(2-1), only the main component (the one closer to the other dense gas tracers; see text) is shown.

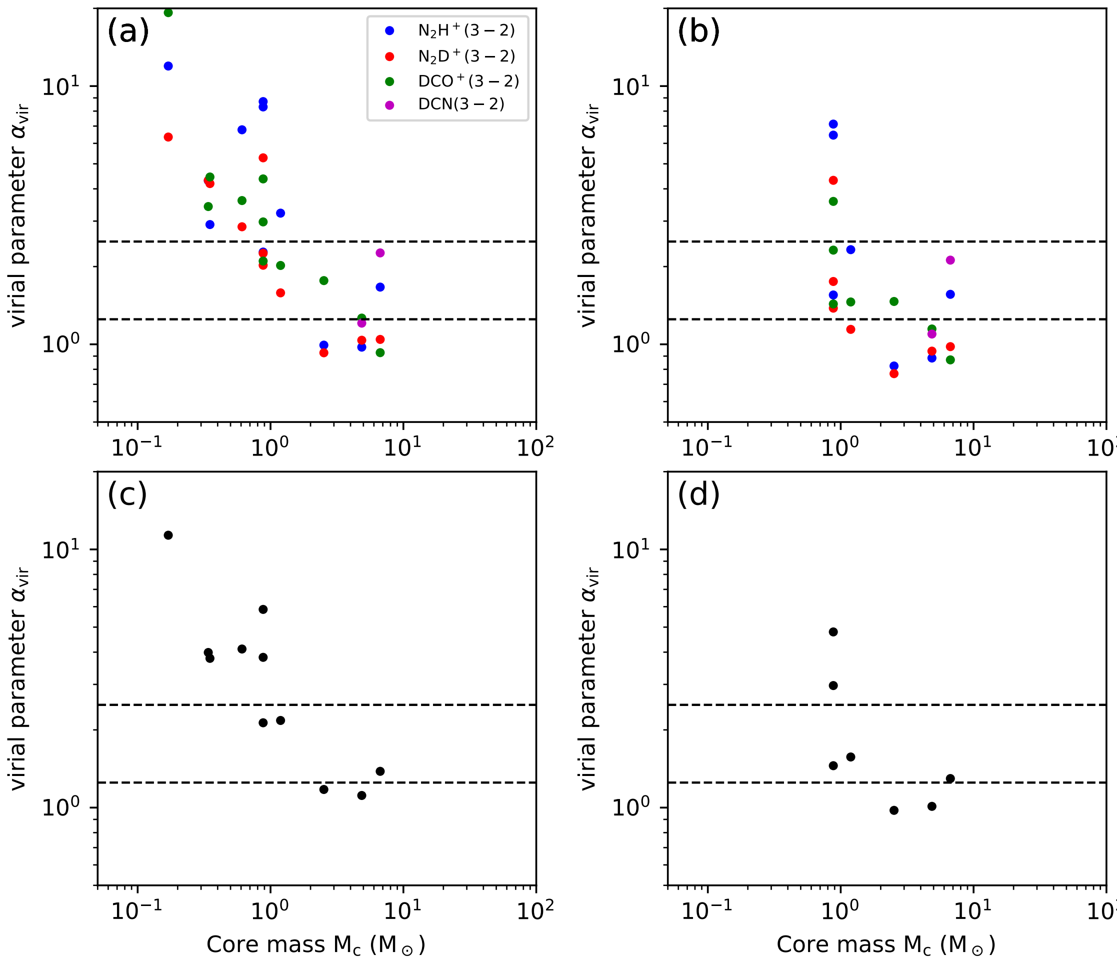

Figure 5.8: (a) Virial parameter, $\alpha_{\rm vir}$, versus core mass, M_c, with core radius measured from the dendrogram defined area and velocity dispersion measured with different dense gas tracers, as shown in the legend. The simple critical value of $\alpha_{\rm vir,cr} = 2a \to 2.5$ (see text) is shown by the upper dashed line: cores below this line are gravitationally bound. The lower dashed line shows the simple virial equilibrium case of $\alpha = a \to 5/4$. (b) As (a), but with core radius estimated after allowing for beam deconvolution. Small cores, i.e., with areas $< 1.5A_{\rm beam}$ are excluded. (c) Same as (a), but we take the linear average of the non-thermal line width measured via different tracers to derive an average virial parameter. (d) Same as (c), but using the deconvolved size.

with well defined profiles, i.e., those with a peak greater than a certain threshold value. Here we adopt a 5σ criterion for this threshold. Since the noise levels of the average spectra vary for different cores (depending on the pixel numbers in the core, etc.), we estimate the rms noise separately for each core and each line using the signal-free channels. This signal-to-noise criterion gives 6 cores for analysis with $C^{18}O$(2-1), 11 for N_2H^+(3-2), 6 for N_2D^+(3-2), 11 for DCO^+(3-2) and 2 for DCN(3-2).

We characterize the $C^{18}O$(2-1) spectra with Gaussian fitting using the *curve_fit* function in the *Scipy.optimize* python module, i.e., the brightness temperature at velocity v, $T_B(v)$, is given by

$$T_B(v) = T_0 \exp\left[-\frac{(v - v_{\rm cen})^2}{2\sigma^2}\right], \tag{5.3}$$

where $T_0 \simeq \tau_0 T_{\rm ex}$ when the line is optically thin. CR1c2 and CR1c6 can be well described with a single Gaussian component. In general, we expect that $C^{18}O$(2-1) traces somewhat lower density envelope gas surrounding the dense core and thus could be more affected by multiple components along the line of sight. In CR1c1, CR1c4, CR1c5 and CR1c9, where the spectra have more complex profiles and hence cannot be well approximated by a single Gaussian, we also allow for a second Gaussian component. The component closest to the velocity determined from other dense gas tracers is assumed to be associated with the core. For the DCO^+(3-2) and DCN(3-2) lines we also perform the Gaussian fitting with the *curve_fit* function.

On the other hand, N_2H^+ and N_2D^+ lines have blended hyperfine components and cannot be approximated with a simple Gaussian. We adopt the frequencies and relative optical depths of N_2H^+ and N_2D^+ taken from Pagani et al. (2009). We further assume the line emission is optically thin to limit the number of free parameters, i.e.,

$$T_B(v) = T_0 \sum_i R_i \exp\left[-\frac{(v - v_i - v_{\rm cen})^2}{2\sigma^2}\right], \tag{5.4}$$

where R_i and v_i are the relative intensity and velocity for the ith hyperfine component, respectively. For CR1c1 the signal to noise ratio is very high ($\sim$20) and three hyperfine groups are clearly detected, so we attempted to include the excitation temperatures ($T_{\rm ex}$), and opacities ($\tau_{\rm tot}$) as free parameters to fit the profile, which is described in section B.1. The best-fit parameters of centroid velocity and velocity dispersion are displayed along with the spectral lines in Figure 5.7. As can be seen, the centroid velocities range from 5.7 to 9.2 $\rm km\,s^{-1}$ and the velocity dispersions $\sigma_{\rm obs}$ range from 0.15 to 0.5 $\rm km\,s^{-1}$ for all species, in which the nonthermal component can be derived via

$$\sigma^2_{\rm nth} = \sigma^2_{\rm obs} - \sigma^2_{\rm th,obs} = \sigma^2_{\rm obs} - \frac{kT}{\mu_{\rm obs} m_{\rm H}} \tag{5.5}$$

where $\mu_{\rm obs}$ is the mass of the particular tracer species. At a temperature of 15 K, the thermal dispersion $\sigma_{\rm th} = \sqrt{kT/\mu m_{\rm H}}$ is 0.23 $\rm km\,s^{-1}$, with $\mu = 2.33$ assuming $n_{\rm He} = 0.1 n_{\rm H}$. Thus the Mach number is measured to range from 0.61 to 2.2, with a median of 1.4 for N_2H^+, 0.77 for N_2D^+ and 1.0 for DCO^+.

5.3.3 Virial state of cores

To further examine the dynamical state of the dense cores, we calculate the virial parameter (Bertoldi & McKee, 1992), defined as

$$\alpha_{\rm vir} \equiv 5\sigma_c^2 R_c/(GM_c) = 2aE_K/|E_G|, \tag{5.6}$$

where σ_c is the intrinsic 1D velocity dispersion of the core and R_c is the core radius. The dimensionless parameter a accounts for modifications that apply in the case of non-homogeneous and non-spherical density distributions and we adopt a fiducial value of $a = 5/4$ following McKee & Tan (2003), which corresponds to a radial density profile of $\rho \propto r^{-1.5}$. For a self-gravitating, unmagnetized core without rotation, a virial parameter above a critical value $\alpha_{\rm vir,cr} = 2a$ indicates that the core is unbound and may expand, while one below $\alpha_{\rm vir,cr}$ suggests that the core is bound and may collapse.

Following the procedures in Cheng et al. (2020), we calculate the virial parameters separately using each tracer, i.e., N_2H^+, N_2D^+, DCO^+ and DCN. The intrinsic velocity dispersion σ_c is derived from the observed dispersion $\sigma_{\rm obs}$ following:

$$\sigma_c = \left(\sigma_{\rm nth}^2 + \sigma_{\rm th}^2\right)^{1/2} = \left(\sigma_{\rm obs}^2 - \frac{kT}{\mu_{\rm obs} m_{\rm H}} + \frac{kT}{\mu m_{\rm H}}\right)^{1/2}, \tag{5.7}$$

where $\mu = 2.33$ is the mean molecular weight assuming $n_{\rm He} = 0.1 n_{\rm H}$ and $\mu_{\rm obs}$ is the molecular weight of different observed species. For the core masses, we use the values from Figure 5.2.2, i.e., derived based on millimeter continuum emission. For core radius, we attempt two methods. The first is to use the effective radius calculated from the dendrogram-returned area in subsection 6.3.1. For the second method, we adopt a deconvolved size defined as $R_c = \sqrt{(A - A_{\rm beam})/\pi}$ for cores with $A > 1.5 A_{\rm beam}$, where A and $A_{\rm beam}$ are the core area and synthesized beam size, respectively. Figure 5.8(a) and (b) display the virial parameters measured with different tracers versus core mass for the two methods described above. In Figure 5.8(c) and (d), we combine the measurements from different tracers by taking the linear average of their nonthermal velocity dispersion in the virial parameter derivation. We note that this procedure may potentially introduce some bias, since cores can vary in the number and type of chemical species that have detected line emission.

We see virial parameters ranging from 1 to 20 as measured by individual dense gas tracers. There is a trend for more massive cores to have smaller virial parameters. The scatter is reduced for the deconvolved size method, suggesting some data points with virial parameter > 5 in panel (a) could arise from an overestimation of the core radius. There are no significant systematic differences between different tracers. For example, with the deconvolved size method (panel (b)), the median values are 1.56, 1.14 and 1.46 for N_2H^+, N_2D^+ and DCO^+. The virial parameters estimated by averaging all the available dense gas data for each core show a further reduction in the scatter. For the second method with deconvolved sizes that focus on the larger cores, we obtain a median value of 1.45, with 2 out of the 7 cores exceeding the critical value of $\alpha_{\rm vir,cr} = 2.5$. For comparison, the virial parameters of the cores appear to be similar to those of the 76 cores in G286, which have a median value of 1.22 (Cheng et al., 2020). Thus we see that most cores have a virial parameter that is consistent with a value expected in virial equilibrium. Note that the derivation of virial ratios relies on the assumption of temperature, which strongly affects the mass estimation. Here an uniform temperature of 15 K has been assumed. If we use a temperature of 20 K, then the median virial parameter rises to 2.58.

Following similar discussions in Cheng et al. (2020), the absolute uncertainties in the derived virial parameters, including uncertainties in measured 1D line dispersion, mass and temperature, can be as high as a factor of 2.5. Therefore, it is difficult to be more certain about whether the dense cores are actually closer to a supervirial or subvirial state. For example, CR1c11 has the highest virial parameter of 4.8, but if a lower temperature of 10 K is adopted, then $\alpha_{\rm vir} = 2.3$, i.e., below the critical value of 2.5, so it is still likely to be gravitational bound. However, we note that the uncertainty factor includes systematic effects, some of which are not expected to vary that much from core to core, so the cores with smallest virial parameters, like CR1c1,

Table 5.3: Estimated column densities, deuteration fractions, CO depletion factors and infrared detections for the cores.

core	$N_{\rm H}$ (10^{22}cm^{-2})	N(C^{18}O) (10^{14}cm^{-2})	N(N$_2$H$^+$) (10^{11}cm^{-2})	N(N$_2$D$^+$) (10^{11}cm^{-2})	$D_{\rm frac}$	f_D	12 μm	70 μm
1	9.75	4.79	310.57	3.32	0.011	62.4	Y	Y
2	10.36	9.54	20.18	3.35	0.17	33.3	Y	Y
3	9.48	1.00	12.46	2.74	0.22	290.7	N	Y
4	6.87	4.79	8.49	<1.47	<0.17	43.9	Y	Y
5	5.68	3.72	3.15	<1.24	<0.39	46.8	N	N
6	4.19	3.39	21.05	2.95	0.14	37.8	Y	Y
7	5.13	<1.42	17.40	2.82	0.16	>110.7	N	Y
8	4.16	2.87	4.29	<2.10	<0.49	44.5	N	Y
9	4.02	1.24	6.60	<1.99	<0.30	99.2	Y	Y
10	3.72	2.04	24.80	3.77	0.15	55.8	N	N
11	3.50	1.62	6.54	5.57	0.85	66.2	N	N

CR1c2 and CR1c3, are more likely to be gravitationally bound and collapsing.

5.3.4 Deuteration and CO depletion

For optically thin lines, following Mangum & Shirley (2015), the column density is calculated from the line integrated intensity by

$$N_{\rm tot}^{\rm thin} = \left(\frac{3h}{8\pi^3 S\mu_{\rm dm}^2 R_i}\right)\left(\frac{Q_{\rm rot}}{g_J g_K g_I}\right)\frac{\exp(\frac{E_u}{kT_{\rm ex}})}{\exp(\frac{h\nu}{kT_{\rm ex}})-1} \times \frac{1}{(J_\nu(T_{\rm ex})-J_\nu(T_{\rm bg}))}\int\frac{T_B dv}{f} \tag{5.8}$$

where $J_\nu(T) \equiv \frac{h\nu/k}{\exp(h\nu/[kT])-1}$; S is the transition line strength; $\mu_{\rm dm}$ is the molecular dipole moment, R_i is the relative transition intensity (for hyperfine transitions), $Q_{\rm rot}$ is the rotational partition function, T_B is the measured brightness temperature; f is the filling factor, and g_J, g_K and g_I are the rotational degeneracy, K degeneracy and nuclear spin degeneracy, respectively. In our calculations we assume a fiducial excitation temperature of 10 K, i.e., moderately cooler than the fiducial dust temperature of 15 K. Such sub-thermal excitation conditions are motivated in part by the results of Kong et al. (2016) who derived and/or considered excitation temperatures from about 4 to 7 K for N_2D^+ and N_2H^+ in massive cores in Infrared Dark

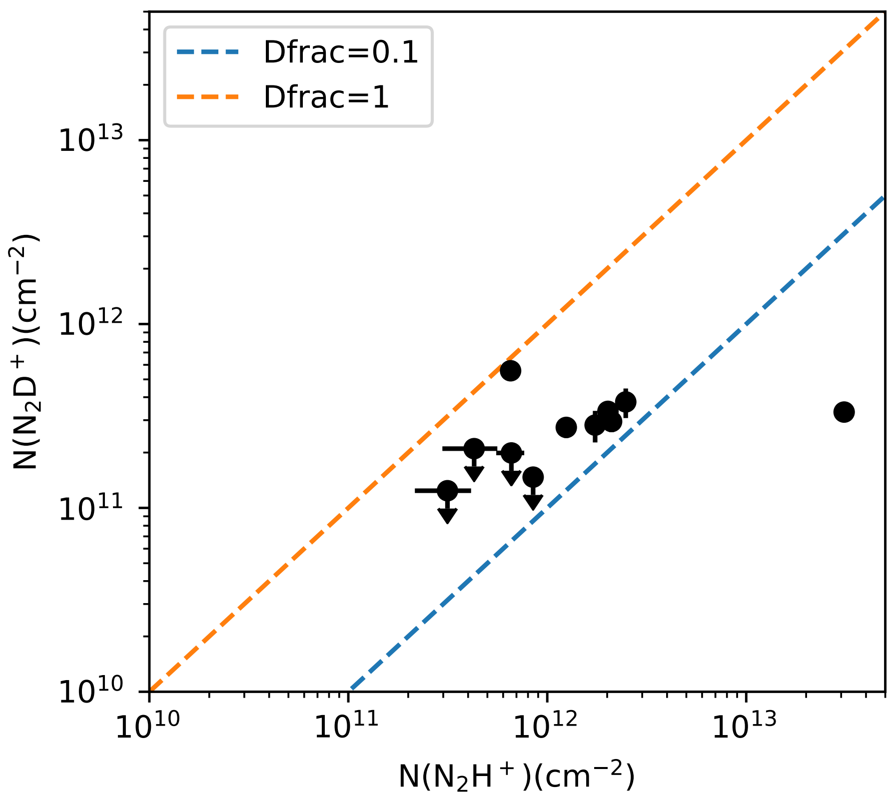

Figure 5.9: Measured N_2H^+ and N_2D^+ column densities for the dense core sample. The two dashed lines are reference lines for D_{frac}= 0.1 and 1, respectively.

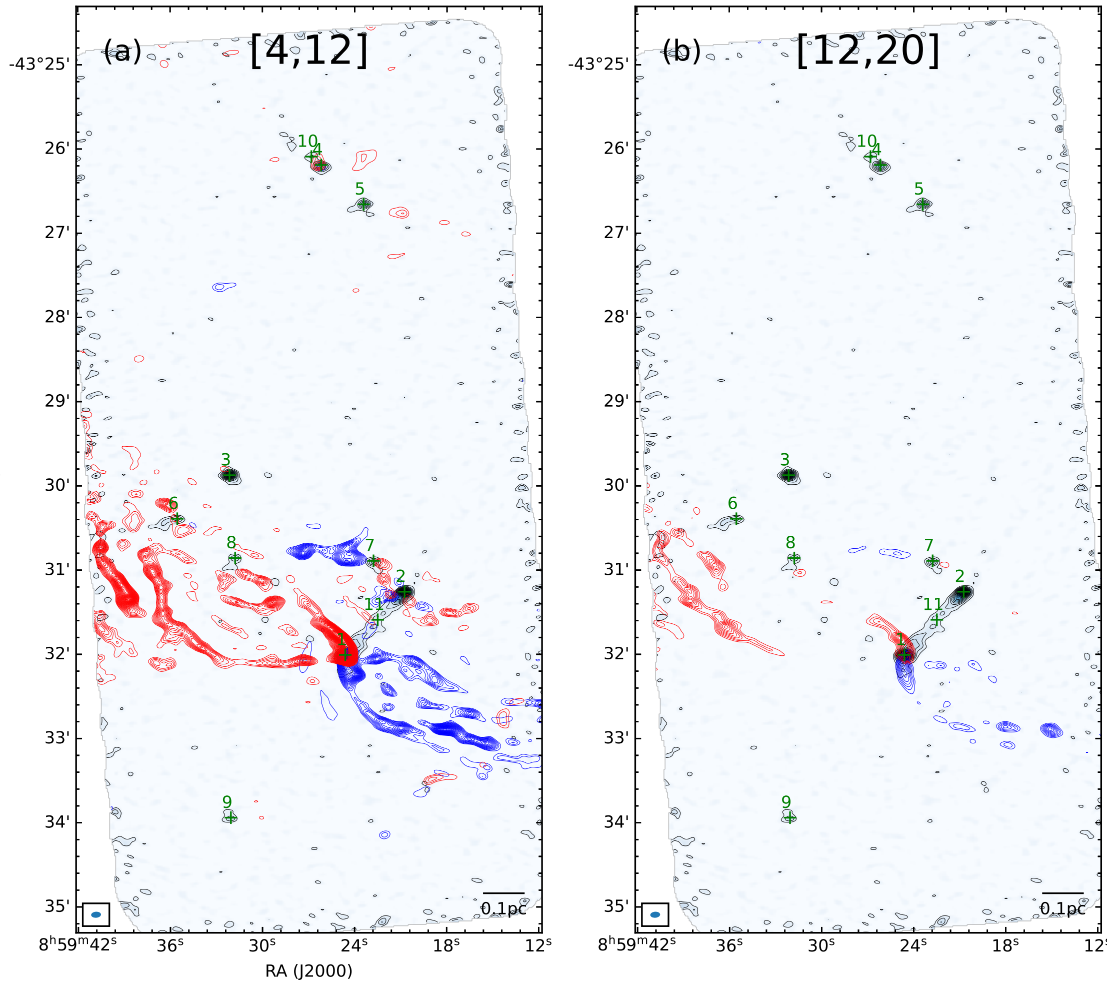

Figure 5.10: (a) CO(2-1) emission integrated from relative velocities from -4 to -12 km s^{-1}for blueshifted and +4 to +12 km s^{-1} for redshifted channels. The continuum is shown in grey scale and black contours for comparison.*(b)* CO(2-1) emission integrated from relative velocities from -12 to -20 km s^{-1} for blueshifted and +12 to +20 km s^{-1}for redshifted channels. The velocity ranges (relative to an averaged system velocity of 7 km s^{-1}) are indicated on top of the panels.

Clouds (IRDCs), with these being significantly lower than gas temperature estimates of ~ 10 to $15\,\mathrm{K}$ from NH_3 observations of the same regions (Kong et al., 2018). Since our observations of N_2D^+ and N_2H^+ are mostly in protostellar core envelopes that are smaller-scale, denser and warmer than the IRDC regions studied by Kong et al. (2016), we consider $T_{\rm ex} = 10\,\mathrm{K}$ to be the most appropriate fiducial choice. However, we will discuss, below, the effects of variation of this choice.

For the derivation of the column densities, we assumed a unity filling factor for all sources. The column density of different species are summarized in Figure 5.3.3. For the N_2H^+ line emission of CR1c1, since the opacity can be determined from the spectral line fitting, the column density is corrected by

$$N_{\rm tot} = N_{\rm tot}^{\rm thin} \frac{\tau}{1 - \exp(-\tau)}. \tag{5.9}$$

Furthermore, with the derived column densities the deuteration ratio for each core is estimated as $D_{\rm frac} = N(N_2D^+)/N(N_2H^+)$. The results are listed in Figure 5.3.3. Figure 5.9 shows the N_2H^+ and N_2D^+ column density measurements of the dense cores. The N_2H^+ column densities are in the range of 3×10^{11} - $3 \times 10^{13}\mathrm{cm}^{-2}$, while the N_2D^+ column densities are in the range 10^{11} - $6 \times 10^{11}\mathrm{cm}^{-2}$. The values of $D_{\rm frac}$ are between 0.011 and 0.85, with a median value of 0.16. This is similar to the value found by Crapsi et al. (2005) in their sample of low-mass starless cores.

The uncertainties in the column density estimation mainly result from the assumption of the excitation temperature $T_{\rm ex}$. If temperatures of 7 K or 15 K were adopted, then $N(N_2H^+)$ would vary by factors of 2.3 and 0.59, respectively, and $N(N_2D^+)$ would vary by factors of 1.9 and 0.69, respectively. Nevertheless, assuming the species have the same excitation temperature, the deuteration ratio $D_{\rm frac}$ is relatively robust and differs only by factors of 0.83 to 1.17 from the low to the high temperature limits of this range. The uncertainties in flux measurement are typically $< 10\%$ for N_2H^+, with only a few exceptions for the cores with weaker N_2H^+ emission, i.e., CR1c5, CR1c8 and CR1c9, that have $\lesssim 30\%$ uncertainties. For N_2D^+ the uncertainties in flux measurement are all $< 20\%$. Additionally, there are flux calibration uncertainties of about 10% for Bands 6 and 7, respectively.

The CO depletion factor, f_D, is defined as the ratio between the "expected" abundance of CO and the "observed" value:

$$f_D = \frac{X^{\rm exp}_{\rm C^{18}O}}{X^{\rm obs}_{\rm C^{18}O}} \tag{5.10}$$

In the abundance calculation we derive the column density of hydrogen nuclei, $N_{\rm H}$ from the mass surface density Σ_c listed in Figure 5.2.2 by $N_{\rm H} = \Sigma_c/\mu_{\rm H} m_{\rm H}$, where $\mu_{\rm H} m_{\rm H} = 1.4 m_{\rm H}$ is the mean mass per H nucleus. To compute $X^{\rm exp}_{\rm C^{18}O}$ we adopt the abundance ratios of $n_{\rm 16O}/n_{\rm 18O} = 327$ from Wilson & Rood (1994) and $n_{\rm 12CO}/n_{\rm H_2} = 2{\times}10^{-4}$ from Lacy et al. (1994). Thus, our assumed abundance ratio of $C^{18}O$ to H_2 is 6.12 $\times 10^{-7}$. The results are listed in Figure 5.3.3. All the cores have f_D measured to be $\gtrsim 40$. Note that the imperfect cleaning due to incomplete uv sampling may have affected the $C^{18}O$ flux measurement, and CO depletion factor accordingly. As mentioned in subsection 5.3.2 the moment 0 map of $C^{18}O$(2-1) in Figure 5.6 does have some artificial ringing features and some cores are not clearly associated with enhanced $C^{18}O$ emission. It is difficult to quantify the uncertainties introduced from the cleaning process, but it may have affected the CO depletion factor by factors of a few for specific cores.

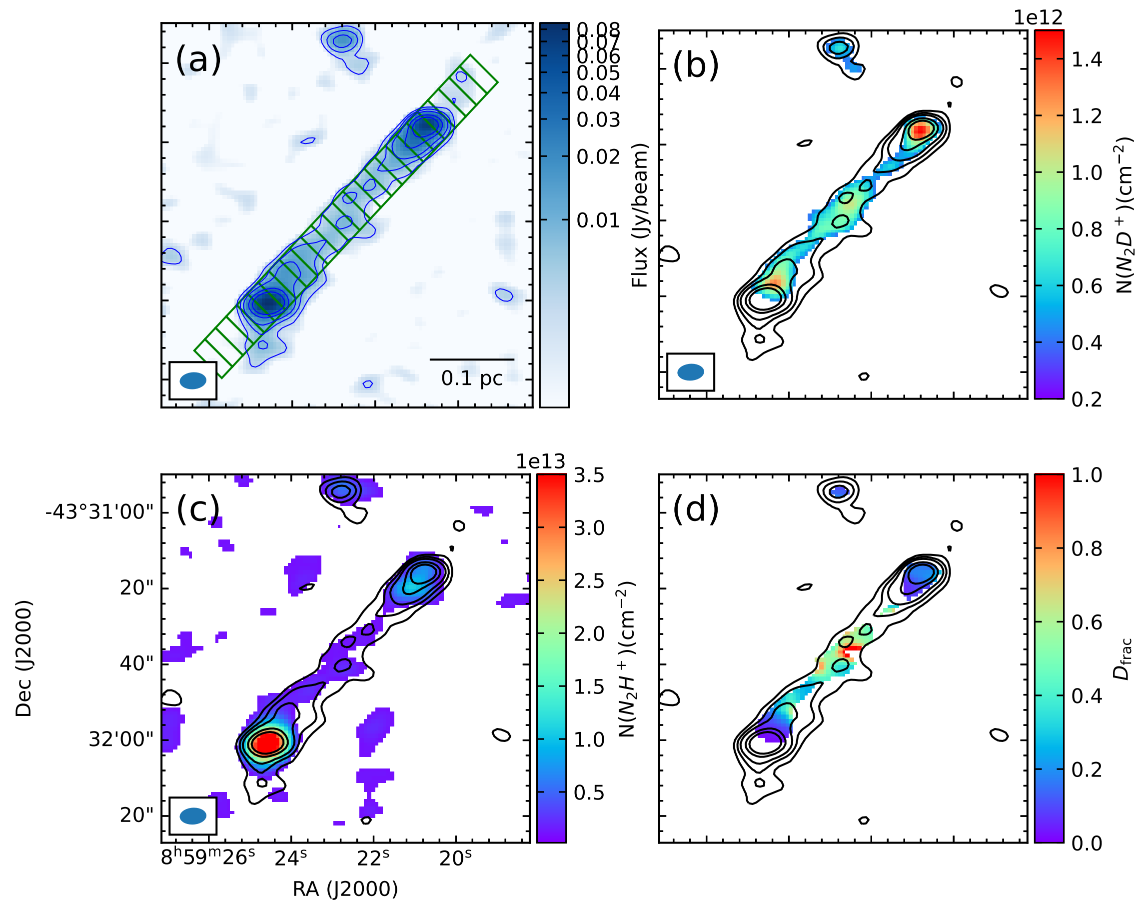

Figure 5.11: *(a)* 1.3 mm continuum map of the bridge feature between the two most luminous cores shown in blue color scale and contours. The contour levels are $\sigma \times$ (5, 10, 15, 30, 50), with $1\sigma = 1.3$ mJy beam^{-1}. As shown in green rectangles we have divided this region into 20 blocks to extract properties along the bridge feature. See text for more details. *(b)* N_2D^+ column density map. The 1.3 mm continuum is overlaid for comparison. *(c)* N_2H^+ column density map. The 1.3 mm continuum is overlaid for comparison. *(d)* D_{frac} map. The 1.3 mm continuum is overlaid for comparison.

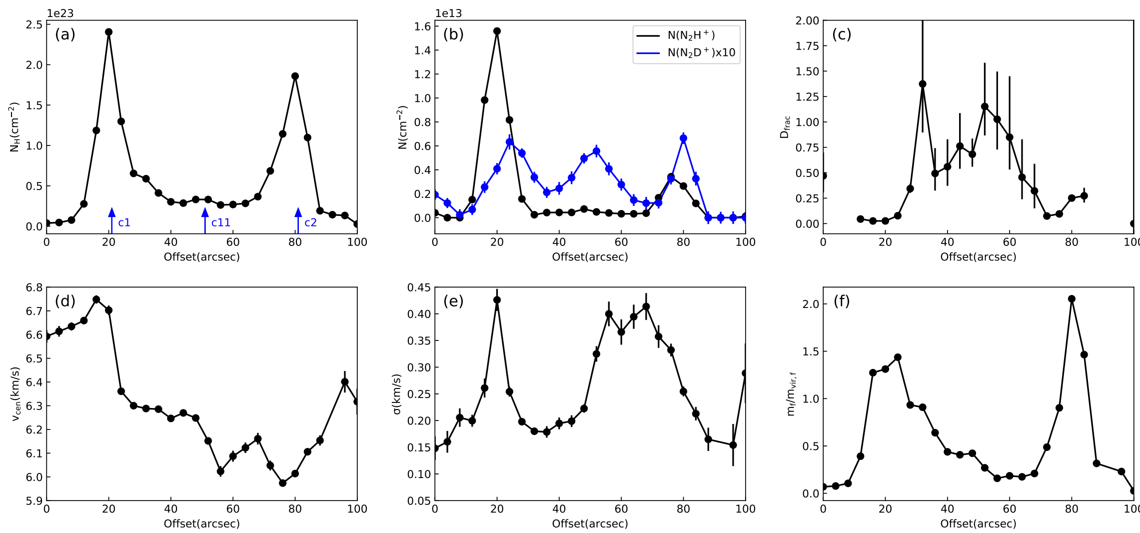

Figure 5.12: Measured properties along the filamentary bridge feature. *(a)* Column density of H nuclei, $N_{\rm H}$. The positions of three cores (CR1c1, CR1c2, CR1c11) are indicated by blue arrows. *(b)* Column density of N_2H^+ and N_2D^+ are shown by black and blue points/lines, respectively. The column density of N_2D^+ is enlarged by a scaling factor of 10 for ease of viewing. *(c)* Deuteration fraction of N_2H^+, $D_{\rm frac}$. *(d)* Centroid velocity measured with the averaged DCO^+ spectrum of each block. *(e)* Velocity dispersion measured with the averaged DCO^+ spectrum of each block. *(f)* Ratio of mass per unit length to virial mass per unit length, $m_f/m_{\rm f,vir}$. The mass per unit length, m_f, is calculated from the 1.3 mm continuum, while the virial mass per unit length, $m_{\rm f,vir}$, is derived with the velocity dispersion measured from the DCO^+ spectra. See text for more details.

5.3.5 CO Outflows

We examined the CO(2-1) data toward this region to see if protostellar outflows are detectable. Figure 5.10(a) illustrates the low velocity CO(2-1) emission integrated over relative velocities ranging from 4 to 12 $\mathrm{km\,s^{-1}}$ (compared to $v_{\mathrm{sys}} \approx 7$ $\mathrm{km\,s^{-1}}$) for blueshifted and redshifted emission, and Figure 5.10 (b) illustrates the high velocity CO(2-1) emission integrated over relative velocities ranging from 12 to 20 $\mathrm{km\,s^{-1}}$. There is a clear bipolar outflow associated with CR1c1, which has an orientation roughly perpendicular with the filamentary bridging feature seen in the continuum. The outflow has a biconical shape with an half opening angle of $\sim 30^{\circ}$. In the vicinity of CR1c2 there appears to be some blueshifted and redshifted CO emission, possibly resulting from a weak outflow, which is also perpendicular to the bridging filament. CR1c7 appears to host a relatively collimated outflow in East-West orientation. The blueshifted lobes has a knotty appearance with a bending feature extending to Northeast direction. There is also a tentative detection of CO outflow from CR1c4 at relatively low velocities in the redshifted lobe, suggesting CR1c4 may also host a protostar.

We also examined the CO channel maps centered on CR1c3, CR1c5, CR1c6, CR1c8, CR1c9, CR1c10 and CR1c11 and did not find evidence for outflows. The strong CO emission from the molecular cloud and the spatial filtering, however, make these nondetections questionable, and observations with higher signal-to-noise are required to properly establish the presence or lack of CO outflows from these sources.

5.3.6 The bridging filament connecting cores CR1c1 and CR1c2

In the continuum map there is an interesting linear filament in which CR1c1, CR1c2 and CR1c11 are located. CR1c1 and CR1c2 are located at the ends of this filament and connected by extended emission seen in 1.3 mm continuum. CR1c11 lies in between CR1c1 and CR1c2 and is further identified from the moment 0 maps of N_2D^+, DCO^+ and 1.05 mm continuum. These three cores exhibit signatures of different evolutionary stages: both CR1c1 and CR1c2 are associated with outflows and have relatively larger values of $f_{1.05\mathrm{mm}}/f_{1.30\mathrm{mm}}$ (1.83, 1.59, respectively), indicating that they already host a protostar that is actively accreting and heating up the surroundings. CR1c11 shows no sign of star formation activity and has a low value of $f_{1.05\mathrm{mm}}/f_{1.30\mathrm{mm}}$ of 1.28. As discussed in subsection 5.3.3, CR1c11 could be gravitationally bound if a lower temperature of $\lesssim 10$ K is assumed. If true, then CR1c11 may be a prestellar core. The chemical properties including D_{frac} are also consistent with these differences in evolutionary stage.

We further divide the bridging filament into 20 strips to derive properties along its length, as shown in Figure 5.11. Each strip has a size of $7'' \times 3.5''$. The column densities of N_2H^+, N_2D^+ are calculated following the procedures in subsection 5.3.2 and also shown in Figure 5.11. Note that in addition to the uncertainties discussed in subsection 5.3.2, spatially filtering of interferometer observations may also lead to an underestimation of flux measurements along the bridge. For example, if there is a more diffuse cocoon component surrounding the bridge we are probably not able to detect it with the current observations. The hydrogen column density N_{H} is calculated from the continuum emission assuming a uniform T_{dust} of 15 K as in subsection 6.3.1. We plot the derived column densities, as well as D_{frac} in Figure 5.12. The evolutionary differences are better illustrated in the D_{frac} profile, which exhibits a plateau around $D_{\mathrm{frac}} \approx 0.8$ from $30''$ to $60''$, i.e., covering the bridging region between CR1c1 and CR1c2. It can also be seen that CR1c1, CR1c2 and CR1c11 have similar $N(N_2D^+)$, but there is a lack of N_2H^+ for CR1c11, thus leading to a high D_{frac}. Therefore, CR1c11 is expected to be in an early stage before the onset of star formation.

To investigate the kinematic properties, we check the line spectra along the bridging filament. DCO^+(3-2) is the best tracer for this purpose, since it is clearly detected throughout the bridge and has a better signal to noise ratio compared to N_2D^+(3-2). We fit the DCO^+ spectra with the same routine as used in subsection 5.3.2. Figure 5.12 illustrates the variation of centroid velocity and velocity dispersion along the bridge. The DCO^+ velocity dispersion ranges from 0.15 to 0.45 $\mathrm{km\,s^{-1}}$. With gas temperatures of 10-20 K, the thermal line broadening is 0.05-0.07 $\mathrm{km\,s^{-1}}$ for DCO^+, so the observed line width is dominated by the nonthermal component. The thermal sound speed of molecular gas is 0.23 $\mathrm{km\,s^{-1}}$ at 15 K, and so the Mach number ranges from 0.6 to 2. The filament appears mildly subsonic at the relative quiescent part, i.e., at offsets from 30″ to 50″. Note that there could be multiple velocity components along the filament that are unresolved in the current observation. There is a clear peak in line dispersion at the position of CR1c1, possibly resulting from an increase in temperature or enhanced nonthermal motions, such as infall and/or outflow due to star formation activity. The case of CR1c2 and CR1c11 is less clear. We see an increase in $\sigma_{\mathrm{DCO^+}}$ from 50″ to 80″ in offset, which is roughly in between CR1c2 and CR1c11.

For v_{cen} there is a decreasing trend from 6.7 $\mathrm{km\,s^{-1}}$ at 20″, to 6.0 $\mathrm{km\,s^{-1}}$ at around 80″, indicating a global velocity gradient of about 2.6 $\mathrm{kms^{-1}pc^{-1}}$. Velocity gradients along filaments have been observed in both nearby low-mass star-forming clouds (e.g., Hacar & Tafalla, 2011) and massive clouds (e.g. Henshaw et al., 2013; Peretto et al., 2014), and often interpreted as flows along filaments, feeding gas into dense cores. However, the global velocity gradient in the filaments may also be attributed to the motion of the filaments themselves (e.g., rotation or oscillation along the line of sight) rather than accretion flows. Interestingly, the positions of CR1c1 and CR1c2 seem to coincide well with local maxima or minima on the v_{cen} profile, possibly suggesting gas infall is taking place in the vicinity of the cores. Figure 5.13 illustrates a possible scenario to explain the observed $v_{\rm cen}$ variations, in which the local bending feature of the velocity profile is caused by infall and/or rotational motion around CR1c1 and CR1c2, while the global velocity gradient between CR1c1 and CR1c2 may arise from other mechanisms like rotation. Summarizing the results, it is likely that the bridging feature is a remnant of a larger filament. CR1c1 and CR1c2 have been accumulating gas material from this filament and have formed protostars, while CR1c11 has condensed from the gas reservoir more recently and is still in a very early, starless evolutionary stage.

To investigate the dynamic state of the filament we perform a filamentary virial analysis following Fiege & Pudritz (2000). As shown by Fiege & Pudritz (2000), a pressure-confined, non-rotating, self-gravitating, filamentary (i.e., length $\gg$ width) magnetized cloud that is in virial equilibrium satisfies

$$\frac{P_e}{P_f} = 1 - \frac{m_f}{m_{\rm vir,f}}\left(1 - \frac{M_f}{|W_f|}\right) \tag{5.11}$$

where P_f is the mean total pressure in the filament, P_e is the external pressure at its surface, m_f is its mass per unit length, $m_{\rm vir,f} = 2\sigma_f^2/G$ is its virial mass per unit length, and M_f and W_f are the gravitational energy and magnetic energy per unit length, respectively. Here, because of the observational difficulties of measuring the surface pressure and magnetic fields, we ignore the surface term and magnetic energy term, i.e., only considering the balance between gravity and internal pressure support.

The $100''$ length of the filament corresponds to 0.45 pc at an assumed distance of 0.93 kpc. Without direct observational constraints, we further assume the filament axis is inclined by an angle $i = 60^\circ$ to the line of sight (90° would be in the plane of the sky). If an inclination angle of 90 or 30° were to be adopted, then the length estimates

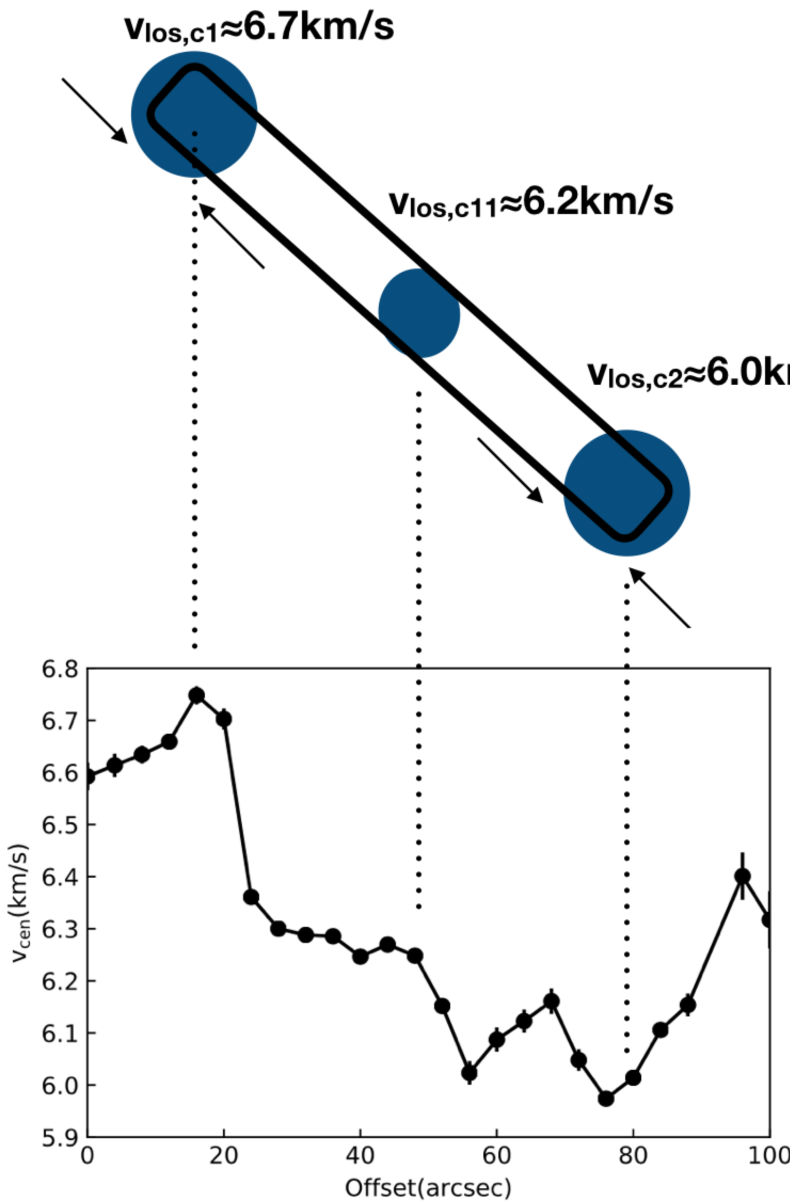

Figure 5.13: Schematic diagram of a possible scenario to explain the centroid velocity profile in Figure 5.12. The observation is made from the bottom of this plot. The global velocity gradient between CR1c1 and CR1c2 may result from mechanisms like filament rotation, while the maxima or minima on the velocity profile are caused by local infall motions around CR1c1 and CR1c2.

would differ by factors of 1.15 and 0.577, respectively. Thus the actual length of the filament is assumed to be 0.52 pc. In Figure 5.12 we plot the ratio $m_{\mathrm{f}}/m_{\mathrm{f,vir}}$. The masses are calculated from the 1.3 mm continuum flux, assuming a temperature of 15 K and other dust properties as in subsection 6.3.1. $m_{\mathrm{f,vir}}$ is calculated using the velocity dispersion measured from DCO^+. The values of $m_f/m_{\mathrm{vir,f}}$ along the filament range from 0.2 to 2.0. $m_f/m_{\mathrm{vir,f}}$ clearly peaks at the positions of CR1c1 and CR1c2, with peak values of 1.4 and 2.0, respectively, and it is relatively small ($\sim$ 0.2-0.6) in regions between the two cores, suggesting that the filament may only be gravitationally bound around the positions of CR1c1 and CR1c2. However, since the ALMA 7m-array observations only probe scales up to $\sim 19''$, they may be missing some flux from the filament leading to an underestimation of the masses. Furthermore, if a temperature of 10 K instead of 15 K is adopted, which is probably more realistic for the less evolved region between CR1c1 and CR1c2, the estimated mass will be larger by a factor of 1.85, thus bringing the $m_f/m_{\mathrm{vir,f}}$ ratio to $\sim$ 0.4-1.2. Also given other systematic uncertainties in measuring lengths of the structure, it is still likely that the majority of the filament is in approximate virial equilibrium, even without accounting for surface pressure and magnetic support terms.

5.4 Discussion

5.4.1 The dense gas fraction: a deficit in compact substructures

An obvious feature in the continuum map of Vela C CR1 clump is an overall deficit of compact substructures at a few 0.01 pc scales. We have identified 11 cores from the 1.3 mm continuum, which add up to a total mass of only 19.4 $M_\odot$. Alternatively, if we sum up the fluxes above 4σ in the 1.3 mm map and convert to masses following the same assumptions as in subsection 6.3.1, it yields 20.7 $M_\odot$, suggesting the bulk of the ALMA 1.3 mm emission is included in our identified dense cores. For comparison, the total clump mass in the field of view estimated from the *Herschel* column density map is about 2300 $M_\odot$, leading to a dense gas fraction, f_{dg}, of only 0.84% (or 0.90%, using the total integrated flux). Therefore, only a very small fraction of gas mass is currently contained in compact prestellar and protostellar cores. The estimation of dense core masses depends on dust opacity, gas-to-dust mass ratio, temperatures and dust emission fluxes, as well as the distance to the region. The major uncertainty of mass estimation arises from the assumption of temperature. For example, if we assume a higher temperature of $T = 20$ K, the total mass will be a factor of 0.677 smaller, leading to a dense gas fraction of 0.57% or 0.61%. Note that for estimating f_{dg}, some of these uncertainties cancel out, i.e., those due to distance and gas-to-dust mass ratio, so we expect the dense gas fraction in VelaC CR1 clump is $\lesssim 2\%$.

We compare the CR1 clump with another well studied region, G286.21+0.17 (G286), which is a protocluster at a distance of 2.5 kpc (Cheng et al., 2018). G286 has a total *Herschel*-estimated mass of around 2900 $M_\odot$ in a 2.6'×1.7' elliptical aperture (Cheng et al., 2020), leading to an average column density, N_{H}, of $\sim 4 \times 10^{22}\mathrm{cm}^{-2}$, similar to the Vela C CR1 clump ($\sim 5 \times 10^{22}\mathrm{cm}^{-2}$). For the compact gas mass we adopt two methods. For method 1 we simply sum up the masses of cores listed in Cheng et al. (2020), which follows the same assumptions as in subsection 6.3.1. For method 2 we integrate the fluxes for pixels above 4 σ using the 1.3 mm continuum image made with only the 12m-array, and then convert to masses following the same assumptions. The 12m-array data of G286 have a maximum recoverable scale of 11″, corresponding to 0.13 pc at the distance of 2.5 kpc, which is close to the 7m-array observation of Vela C (sensitive to structures up to 29″ , $\sim$ 0.13 pc, in Band 6). Methods 1 and 2 yield f_{dg} of 7.3%, and 14.3% in G286, respectively, so both estimations are an order of magnitude higher compared with the Vela C CR1 clump.

One possible explanation for these differences is that the formation of dense substructures in the Vela C CR1 clump has been suppressed by its strong magnetic field. Alternatively, the CR1 clump could simply be in a very early evolutionary stage of collapse, but with core formation not particularly influenced by the B-field. Follow-up observations to constrain the dynamical and chemical history of Vela C CR1, e.g., to measure infall speeds and chemical ages, can help distinguish these possibilities.

There have been a number of other studies of dense gas fractions in the literature. Direct comparison with our results is generally more difficult given the variety of methods used to estimate masses for both the large scale cloud and the dense (or compact) component. For example, Battersby et al. (2020) studied the dense gas fractions of the central molecular zone (CMZ) and compared to similar studies of clouds in the Galactic disk, finding that $f_{\rm dg} \sim 0.1\%$ to 2% in most CMZ clouds (even though these clouds have relatively high column densities), while typical star-forming Galactic clouds have $f_{\rm dg} \sim 2\%$ to 20%. The measured $f_{\rm dg}$ of Vela C CR1 clump appears similar to the CMZ clouds, and lower than typical Galactic disk clouds. But note that the maximum recoverable scale of our observation ($29''$, 0.13pc) is smaller than the scales probed with SMA observations in Battersby et al. (2020) for most sources.

5.4.2 Implication of the deuteration analysis: tests of astrochemical models

The study of deuterated molecules is an important probe of the physical conditions in star-forming regions. Prior to the formation of a star, the cold (T <20 K) and dense ($n_{\rm H} > 10^5$ cm^{-3}) conditions within star-forming molecular cloud cores drive a cold-gas chemistry that has been well studied in recent years. Many molecular species, including CO and its isotopologues, become depleted in the gas phase by

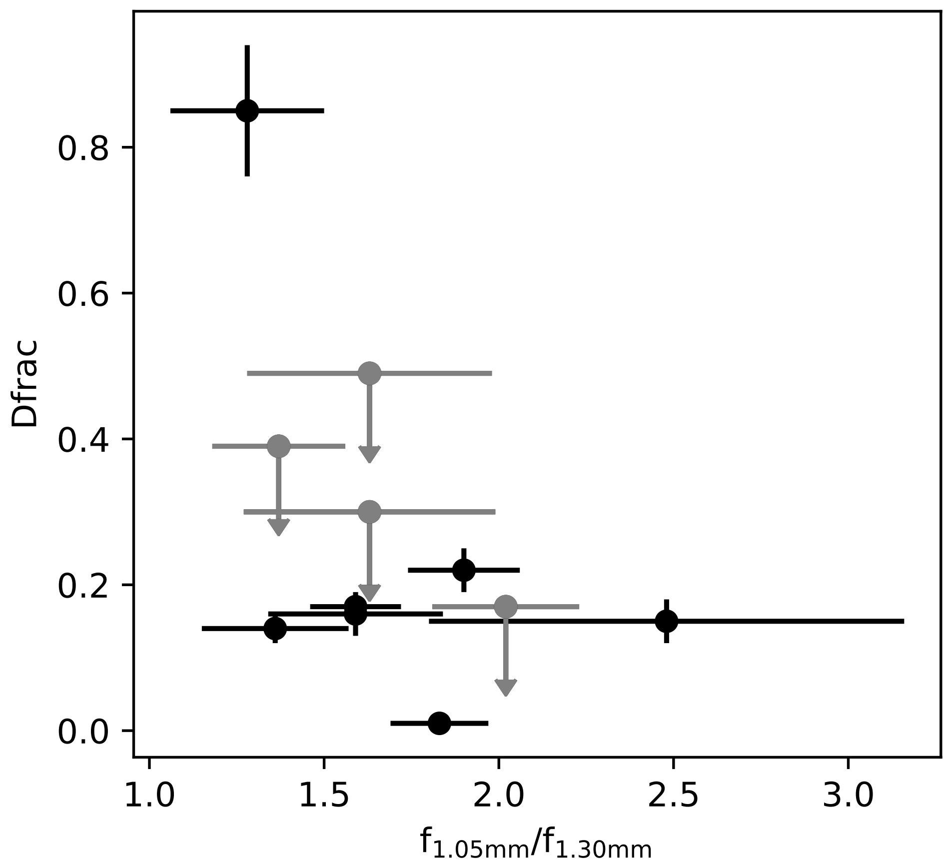

Figure 5.14: Measured D_{frac} v.s. $f_{1.05\mathrm{mm}}/f_{1.30\mathrm{mm}}$ for the dense core sample. The data points that are upper limits are shown in grey.

freezing out onto dust grains. Unlike CO, N-bearing species, in particular NH_3 and N_2H^+, better trace dense and cold gas (e.g., Caselli et al., 1999; Bergin et al., 2002). This is due to the fact that CO, largely frozen out, is unable to effectively destroy their molecular ion precursors. These physical/chemical properties are commonly observed in prestellar cores, where the deuteration fraction (i.e., $D_{\rm frac}$) of non-depleted molecules, defined as the column density ratio of one species containing deuterium to its counterpart containing hydrogen, is orders of magnitude larger than the average interstellar [D/H] abundance ratio, which is $\sim 10^{-5}$ (Oliveira et al., 2003). Therefore, deuterated species, like N_2D^+ are better suited to probe the physical conditions of the earliest stages of star formation. The $D_{\rm frac}(N_2H^+)$ ratio has been found to be a good evolutionary indicator in both low- and high-mass star formation (Friesen et al., 2010; Fontani et al., 2011). In addition, N_2D^+ is probably the best tracer of prestellar cores, e.g., compared to $D_{\rm frac}$ of HNC and NH_3(Fontani et al., 2015).

The $D_{\rm frac}(N_2H^+)$ in the Vela C CR1 clump is found to be in the range of 0.011-0.85. Our observed values are consistent with measurements made in other low-mass star-forming regions (e.g., Caselli et al., 2002; Crapsi et al., 2005; Daniel et al., 2007; Emprechtinger et al., 2009; Friesen et al., 2013). For 4 out of 11 cores, no significant N_2D^+ is detected and only an upper limit of the $D_{\rm frac}$ is given. These cores also have relatively low N_2H^+ column densities and the upper limit on $D_{\rm frac}$ ($\lesssim$0.5) is a rather loose constraint. The extreme value of 0.85, measured towards CR1c11, is among the highest levels of N_2H^+ deuteration reported so far (e.g., Miettinen et al., 2012), indicating the prestellar nature of CR1c11 in a very dense and cold condition. A caveat is that CR1c11 is defined based on the N_2D^+ moment 0 map, which thus biases towards a higher $D_{\rm frac}$ estimation. We note that N_2H^+ could have a greater degree of missing flux compared with N_2D^+, given the properties of the observations in Band 6 and Band 7, however, we do not expect significant flux losses on the scales of the observed cores.

In Figure 5.14 we plot the D_{frac} ratio against other core properties to look for potential correlations. As discussed in subsection 6.3.1, the ratio $f_{1.05\mathrm{mm}}/f_{1.30\mathrm{mm}}$ can be interpreted as a temperature indicator, with higher $f_{1.05\mathrm{mm}}/f_{1.30\mathrm{mm}}$ suggesting higher temperature. There appears to be a weak anti-correlation between $f_{1.05\mathrm{mm}}/f_{1.30\mathrm{mm}}$ and D_{frac}, which is consistent with our expectation, since CO will be released from dust grains at higher temperatures as cores evolve, thus leading to a lower deuteration level.

Given the current available information on core properties it is difficult to assign a precise evolutionary stage for each one, but we do see groups of cores in different evolutionary stages. CR1c1 is probably the most evolved source in CR1. This core has the lowest D_{frac} and drives a powerful, wide-angle CO outflow. CR1c2, CR1c4 and CR1c7 also have associated outflow detections, indicating their protostellar nature. CR1c11 has the highest D_{frac} and is likely a prestellar core that is on the verge of collapsing, although more sensitive observations, especially better temperature measurements, are required to confirm its nature as a gravitationally bound core. A measurement of deuteration on the larger clump scale using single dish observations would be important for understanding the initial astrochemical conditions of prestellar core formation.

The auxiliary infrared data provide extra constraints on the evolutionary stages. Here we focus on two infrared wavelengths, i.e., 12 μm and 70 μm. A more complete investigation of other infrared wavelengths in presented in section B.2. The 12 μm emission usually suggests thermal dust emission heated by protostars and 70 μm data could reveal deeply embedded protostars that are undetected at shorter wavelengths. The detection status is summarized in Figure 5.3.3. As can be seen, CR1c5 and CR1c11 are not detected at 70 μm, suggesting that they are in a very early evolutionary stage, likely prestellar. The detection of CR1c10 is confused by another adjacent bright source (see section B.2). All other cores should have formed a protostar. While CR1c3, CR1c7 and CR1c8 are detected at 70 μm, they are still very faint and not seen at 12 μ and hence they should be in a relatively earlier stage compared with other cores (i.e., CR1c1, CR1c2, CR1c4, CR1c6 and CR1c9), which are bright in both 12 μm and 70 μm and hence more evolved.

5.5 Summary

The Vela C cloud is one of the few regions with magnetic field mapped through both sub-mm emission polarimetry and near-infrared stellar absorption polarimetry, and hence an ideal laboratory to study how the magnetic field strength affects star formation process. To investigate how star formation proceeds in a strong magnetic field environment, we have observed the Center Ridge 1 (CR1) clump in the Vela C with ALMA in Band 6 and Band 7. This clump is a high column density region that shows the lowest level of dust continuum polarization angle dispersion in the BLASTPol survey (Fissel et al., 2016), indicating the presence of a strong magnetic field. We identified 11 dense cores via their mm continuum emission, with masses spanning from 0.17 to 6.7 $M_\odot$. Interestingly, CR1 exhibits a relatively low compact dense gas fraction compared with other typical clouds with similar column densities, which may be a result of the strong magnetic field in this region and/or that it is in a very early evolutionary stage of collapse.

The N_2H^+(3-2) and N_2D^+(3-2) lines in this observation also allow for a precise measurement of the deuteration ratio. In our sample values of $D_{\rm frac}$ span from 0.011 to 0.85 for the dense core sample, with the latter being one of the highest values yet detected. A trend of decreasing $D_{\rm frac}$ from the final prestellar to protostellar phases is inferred by comparison to other indicators, such as presence of outflows and infrared sources. In addition we also report the detection of an bridging feature connecting the two most massive cores (CR1c1, CR1c2) in the region in both continuum and spectral lines. This linear filament is approximately parallel to the large scale plane of sky magnetic field orientation, and roughly orthogonal to the axes of CO bipolar outflows associated with CR1c1 and CR1c2. The kinematics of this filament likely imply that infall is occurring onto the cores.

The presented study uses analysis methods for core identification and characterization from the ALMA Band 6 data that are the same as employed in studies of other star-forming regions, e.g., G286 by Cheng et al. (2018, 2020) and IRDCs by Liu et al. (2018, 2020). Future work will aim to extend such studies to other star-forming environments and thus allow a systematic investigation of many aspects of the star formation process and their dependence on galactic environment.

Chapter 6

Star formation in an Intermediate-mass Star Forming Region

6.1 Introduction

Intermediate mass protostars are observationally defined as young stellar objects (YSOs) that have luminosities between ~ 50 and 2000 $L_{\odot}$ and will eventually reach final masses of 2–8 $M_{\odot}$ (Beltrán, 2015). Intermediate mass protostars constitute the link between low- and high-mass protostars, and hence provide a natural laboratory to test star formation theories that unify the two mass regimes. Unlike their low mass counterparts, intermediate mass stars produce significantly more UV photons and form in more densely clustered environments (e.g., Fuente et al., 2007). In observational terms, intermediate mass star forming regions are on average closer and less extincted than high mass ones, making it easier to trace the primordial configuration of the molecular cloud and to study the earliest stages of star formation.

NGC 2071 IR is an intermediate mass star forming region located in the Orion B molecular cloud, approximately 4′ north of the optical reflection nebula NGC 2071. This region is characterized by an energetic bipolar outflow, which is oriented in the NE-SW direction and extends ∼15′ in length and ∼120 $\mathrm{km\,s^{-1}}$ in velocity. The outflow has been extensively characterized in CO (e.g., Bally, 1982; Scoville et al., 1986; Stojimirović et al., 2008) and H_2 2.12 μm emission (Eislöffel et al., 2000; Walther & Geballe, 2019). At the center of outflow located an infrared cluster with ∼ 30″ diameter, which has a total luminosity of 520 $L_\odot$ (Butner et al., 1990), and harbors ∼ 10 near-IR sources (Persson et al., 1981; Walther et al., 1993; Walther & Geballe, 2019). Most of the near-IR sources are identified as YSOs (Skinner et al., 2009).

Millimeter and centimeter continuum emission has been detected with some of the IR sources (Snell & Bally, 1986; Torrelles et al., 1998; Trinidad et al., 2009; van Kempen et al., 2012; Carrasco-González et al., 2012), in which IRS1 and IRS3 are of particular interest as they are the dominant mid/far-IR luminosity contributors and also presumed driving sources of the the large scale outflow (e.g., Torrelles et al., 1998; Eislöffel et al., 2000). Both IRS1 and IRS3 are resolved into three components in 1.3 cm continuum emission, with the outer components interpreted as ionized gas being ejected by the central objects (Trinidad et al., 2009). Carrasco-González et al. (2012) found variation of elongation direction of IRS1 at 3.6 cm over 4 years, possibly indicating unobserved multiplicity inside IRS1. In both sources, the water maser emission appears to trace parts of a rotating protostellar disk and a collimated outflow (Torrelles et al., 1998; Seth et al., 2002; Trinidad et al., 2009). Based on the spatial-velocity distribution of masers that traces protostellar disks, Trinidad et al. (2009) estimated the central mass of IRS1 and IRS3 to be ∼5, and ∼1 $M_\odot$, respectively.

Building on these previous studies, we have conducted Atacama Large Millimeter/submillimeter Array (ALMA) and Karl G. Jansky VLA observations at 0.87, 1.3

and 9 mm, detecting and resolving the dust and free-free emission from the protostars within the NGC 2071 IR region. Furthermore, the molecular line emission contained within our ALMA bandpass enables us to further characterize the physical conditions of the protostars in the region, and in particular, to give more stringent constraints on the dynamical masses of IRS1 and IRS3. This paper is structured as follows: the observations and results are presented in section 6.2 and section 6.3, respectively. We perform a kinematic modeling of the protostellar disks in section 6.4. We further discuss our results in section 6.5, and present our conclusions in section 6.6.

Table 6.1: Information on the spectral lines in ALMA band 6 observations

Transition	Frequency(GHz)	$E_{\rm up}$	Beam size	Spectral reso. (km s^{-1})	rms (mJy beam^{-1} per channel)
$C^{18}O$ $2-1$	219.560358	15.8	0.″29×0.″26	0.05	5.0
^{13}CO $2-1$	220.398684	15.9	0.″29×0.″26	0.05	8.0
H_2CO $3_{0,3}-2_{0,2}$	218.222195	21.0	0.″29×0.″26	0.20	2.6
H_2CO $3_{2,2}-2_{2,1}$	218.475632	68.1	0.″29×0.″26	0.20	2.6
SO 6_5-5_4	219.949442	35.0	0.″29×0.″26	0.20	3.5
$^{13}CH_3OH$ $5_{1,5}-4_{1,4}$	234.011580	48.3	0.″26×0.″23	1.25	1.2
CH_3OCHO $18_{4,14}-17_{4,13}$	233.777515	114.4	0.″26×0.″23	1.25	1.2
CH_3OH $18_{3,16}-17_{4,13}$	232.783446	446.5	0.″26×0.″23	1.25	1.0
CH_3OH $10_{3,7}-11_{2,9}$	232.945797	190.4	0.″26×0.″23	1.25	1.0
CH_3OH $18_{3,15}-17_{4,14}$	233.795666	446.6	0.″26×0.″23	1.25	1.0
SO_2 $28_{3,25}-28_{2,26}$	234.421588	213.3	0.″26×0.″23	1.25	1.2
SO_2 $16_{6,10}-17_{5,13}$	234.187057	403.3	0.″26×0.″23	1.25	1.2

6.2 Observations

The ALMA and VLA observations presented here are part of the VLA/ALMA Nascent Disk and Multiplicity (VANDAM) Survey of the Orion molecular clouds. Observations were conducted toward 328 protostars (148 for the VLA) in the Orion molecular clouds, all at $\sim$0.1″ resolution. The sample of 328 protostars is derived from the HOPS sample (Furlan et al., 2016), observing the bona fide protostars from Class 0 to Flat Spectrum. The full survey results are presented in Tobin et al. (2020).

6.2.1 ALMA band 7 and VLA observations

The detailed information of ALMA band 7 (0.87 mm) and VLA Ka (9 mm) observations can be found in Tobin et al. (2020). In this work we mainly utilize the continuum images. The beam sizes are $0\farcs13 \times 0\farcs10$ (56 au $\times$43 au) for 0.87 mm and $0\farcs09\,'' \times 0\farcs06$(39 au $\times$ 26 au) for 9 mm, respectively. The 0.87 mm map has a rms noise of 0.55 mJy beam^{-1}, and the 9 mm continuum map has a rms noise of 12 μJy beam^{-1}.

6.2.2 ALMA band 6 Observations

NGC 2071 IR was observed with ALMA in 1.3 mm in six executions from Oct 2 to Nov 23 in 2018. The observations were conducted with 42 – 49 operating antennas and covered sampling baselines from 15 m to 2500 m. The correlator was configured with the first basedband split into two 58.6 MHz spectral windows with 1920 channels each (0.041 km s^{-1} velocity resolution) and centered on ^{13}CO 2–1 and C^{18}O 2–1, respectively. The second baseband was split into four 58.6 MHz spectral windows with 480 channels each (0.168 km s^{-1} velocity resolution) and centered on H_2CO $3_{0,3} - 2_{0,2}$, and H_2CO $3_{2,2} - 2_{2,1}$, H_2CO $3_{2,1} - 2_{2,0}$ and SO $6_5 - 5_4$. The thrid basedband was configured with a 0.94 GHz spectral window (1920 channels, 1.25 km s^{-1}) centered on ^{12} CO 2–1. Finally, the fourth basedband contains a 1.875 GHz continuum band centered at 233.0 GHz with 1920 channels.

The data were reduced using the ALMA calibration pipeline within CASA version (**check the version**). In order to increase the signal-to-noise ratio of the continuum and spectral lines, we performed self-calibration on the continuum. We performed 2 rounds of phase-only self-calibration, the first round used solution intervals that encompassed the length of an entire on-source scan, then the second round utilized the 6.05 s solution interval, corresponding to a single integration. The phase solutions from the continuum self-calibration were also applied to the spectral line bands. The resultant rms noise in the 1.3 mm continuum was $\sim$0.13 mJy beam^{-1}. The continuum and spectral line data were imaged using the *tclean* task within CASA version 5.4.0 with Briggs weighting and a robust parameter of 0.5. The beam sizes of the continuum is $0\farcs24\times0\farcs21$ (103 au $\times$90 au). In Table 6.1 we list the information of lines that are used in this study, including both the lines mentioned above and those identified in the continuum spectral window.

6.3 Results

6.3.1 ALMA and VLA Continuum Images

the protostellar content

Figure 6.1 illustrates the 1.3 mm continuum map of the NGC 2071 IR region. The overall spectral energy distribution (SED) of this region at longer wavelengths has been studied in Furlan et al. (2016) with photometry data from *2Mass*, *Spitzer* and *Herschel* (i.e., the source HOPS-361 following their designation). Tobin et al. (2020) further identified 8 protostar systems based on high resolution ALMA 0.87 mm and VLA 9 mm observations. These sources, named from HOPS-361-A to HOPS-361-G, are labeled with red crosses in Figure 6.1. Five of them are associated with near-

IR point sources (i.e., IRS1, IRS2, IRS3, IRS4, IRS8, Persson et al., 1981; Walther et al., 1993). HOPS-361-G (IRS2) is known to be a binary system (HOPS-361-G-A, HOPS-361-G-B) separated by $\sim$1.4$''$($\sim$580 au). HOPS-361-C (IRS3) and HOPS-361-E appear single in ALMA 0.87 mm continuum but are resolved to be close ($<$ 0$\farcs$2, $\sim$80 au) binary systems in the VLA 9 mm images. In the 1.3 mm map, these sources are all detected at $> 5\sigma$ level and exhibit compact dusty structures at 0$\farcs$2 scale, which arise from their protostellar disks and inner envelopes. With self-calibration, our 1.3 mm map reaches a high dynamical range of $\sim$ 1000, and some weak extended structures have also been revealed. HOPS-361-C appears to be embedded in larger dusty structures, which extends to the SE direction and connects with HOPS-361-B. There also appear to be a couple of filamentary features that are about 0.01–0.02 pc long: one originating from HOPS-361-E and extending to the SW direction, one extending from HOPS-361-G to the west and another one spiraling around HOPS-361-C and extending to the north. The origin of these streamer features are not clear but likely to be related with density enhancements shaped by complex gas motions on a few 0.01 pc scales.

In Figure 6.2 and Figure 6.3 we present the ALMA (0.87 mm, 1.3 mm) and VLA (9 mm) continuum images towards these sources. We fit elliptical Gaussians to these protostellar sources using the *imfit* task in *casa* to measure their flux densities, and sizes in 1.3 mm, as listed in Table 6.2. The fluxes and sizes in 0.87 mm and 9 mm from Tobin et al. (2020), which are measured with the same method, are also listed for comparison. The flux densities are then used to analytically calculate the mass of each continuum source. We make the assumption that the observed emission in 0.87 mm and 1.3 mm purely comes from optically thin isothermal dust emission,

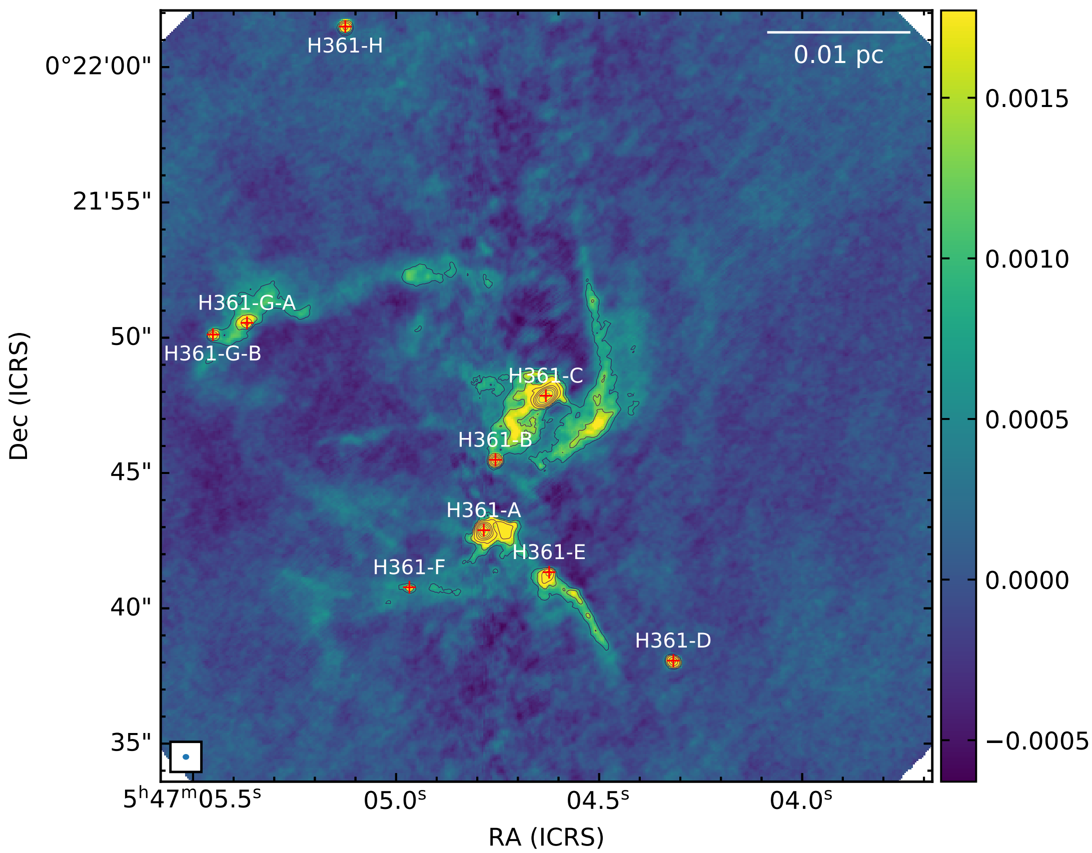

Figure 6.1: Overview of the NGC 2071 IR region. The 1.3 mm continuum is shown in colorscale and contours. The contours levels are (5, 10, 20, 50, 100, 200, 400, 800) $\times\sigma$, where $\sigma = 0.13$ mJy beam^{-1}. The position of identified protostar sources in (Tobin et al., 2020) are marked by red crosses and labeled in white text. The designation "HOPS-361" is abbreviated to "H361" (only in this plot). The beam size is $0\farcs24 \times 0\farcs21$ as shown in the bottom left corner.

enabling us to use the equation

$$M_{\rm dust} = \frac{D^2 F_\nu}{\kappa_\nu B_\nu(T_{\rm dust})}. \tag{6.1}$$

In this equation, D is the distance, F_ν is the observed flux density, B_ν is the Planck function, $T_{\rm dust}$ is the dust temperature and κ_ν is the dust opacity at the observed wavelength. For the distance we adopt 430.4 pc as estimated in Tobin et al. (2020), which is based on Gaia DR2 data for a sample of relatively evolved young stars in Orion. We adopt $\kappa_{0.87\rm mm} = 1.84$ cm^{2}g^{-1} and $\kappa_{1.3\rm mm} = 0.89$ cm^{2}g^{-1} from (Ossenkopf & Henning, 1994) (thin ice mantles, 10^6 cm^{-3} density). We multiply the calculated dust mass by 100, assuming a dust-to-gas mass ratio of 1:100 (Bohlin et al., 1978), to obtain the gas mass. The average dust temperature we adopt for a protostellar system is given by

$$T_{\rm dust} = T_0 \left(\frac{L}{L_\odot}\right)^{0.25}, \tag{6.2}$$

where $T_0 = 43$ K. The average dust temperature of 43 K is reasonable for a $\sim$1 $L_\odot$ protostar at a radius of $\sim$50 au (Whitney et al., 2003; Tobin et al., 2013). For the luminosity (Furlan et al., 2016) has estimated a total $L_{\rm bol}$ of 478 $L_\odot$ in an aperture encompassing both IRS1 and IRS3. For simplicity we calculate the relative $L_{\rm bol}$ ratios among IRS1, IRS2 and IRS3 based on the SOFIA 37.1 μm image, which is the longest infrared wavelength for which we can still resolve the three components (see subsection 6.3.6). Thus the $L_{\rm bol}$ is 368 $L_\odot$, 25 $L_\odot$ and 85 $L_\odot$ for IRS1, IRS2 and IRS3, respectively. For other sources without a measured $L_{\rm bol}$ we adopt 1 $L_\odot$. The $L_{\rm bol}$, $T_{\rm bol}$, derived masses, as well as other available identifiers of the protostars are listed in Table 6.3. The continuum emission from the protostars is likely to be partially optically thick; thus, the masses are likely lower limits, especially at 0.87 mm.

Table 6.2: Source Properties of protostars in NGC 2071 IR[a] derived from 2-D Gaussin fits

Source	Flux(1.3mm) mJy	Size(1.3mm) (arcsec)	PA(1.3mm) degree	Flux(0.87mm) mJy	Size(0.87mm) (arcsec)	PA(0.87mm) degree	Flux(9mm) mJy	Size(9mm) (arcsec)	PA(9mm) degree
HOPS-361-A	208.0	0.24×0.14	12.0	606.4	0.26× 0.15	14.4	5.6	0.10×0.07	64.4
HOPS-361-B	40.3	0.08×0.06	174.4	94.4	0.06× 0.05	174.4	1.9	0.07×0.04	55.5
HOPS-361-C-A	362.5	0.48×0.19	129.5	883.4	0.47× 0.19	130.1	2.3	0.14×0.04	6.7
HOPS-361-C-B	-	-	-	-	-	-	0.2	point	point
HOPS-361-D	22.5	0.19×0.10	44.2	71.3	0.17× 0.09	43.1	0.4	0.09×0.06	50.9
HOPS-361-E	15.3	0.30×0.19	147.0	29.4	0.15× 0.11	111.9	0.2	point	point
HOPS-361-F	4.2	0.26×0.11	79.0	6.6	point	point	0.1	point	point
HOPS-361-G-A	22.6	0.53×0.35	136	31.6	point	point	0.4	0.09 ×0.06	44.3
HOPS-361-G-B	9.3	0.22×0.19	134.0	19.0	point	point	0.3	0.07×0.04	13.3
HOPS-361-H	13.9	0.20×0.19	152.0	-[b]	-	-	0.6	0.08 ×0.06	18.0

[a] The sizes and P.A. are the FWHM and P.A. of deconvolved Gaussian components.
[b] HOPS-361-H is not covered in the 0.87 mm observations.

Table 6.3: Source Properties of protostars in NGC 2071 IR

Source	Other identifiers	R.A.[a] (J2000)	Decl.[a] (J2000)	L_{bol} ($L_\odot$)	T_{dust} (K)	$M_{1.3mm}$ ($M_\odot$)	$M_{0.87mm}$ ($M_\odot$)
HOPS-361-A	IRS1	5:47:4.784	0:21:42.85	368	188	0.0690 ± 0.0017	0.0611 ± 0.0006
HOPS-361-B	VLA1	5:47:4.755	0:21:45.45	1	43	0.0645 ± 0.0012	0.0486 ± 0.0013
HOPS-361-C	IRS3	5:47:4.631	0:21:47.82	85	131	0.1750 ± 0.0039	0.1309 ± 0.0014
HOPS-361-D	IRS8	5:47:4.317	0:21:38.03	1	43	0.0360 ± 0.0004	0.0367 ± 0.0022
HOPS-361-E	-	5:47:4.623	0:21:41.30	1	43	0.0392 ± 0.0053	0.0151 ± 0.0022
HOPS-361-F	-	5:47:4.967	0:21:40.74	1	43	0.0080 ± 0.0009	0.0034 ± 0.0006
HOPS-361-G-A	IRS2A	5:47:5.367	0:21:50.51	25	96	0.0115 ± 0.0015	0.0065 ± 0.0003
HOPS-361-G-B	IRS2B	5:47:5.451	0:21:50.08	25	96	0.0061 ± 0.0006	0.0039 ± 0.0003
HOPS-361-H	IRS4	5:47:5.125	0:22:1.46	1	43	0.0223 ± 0.0006	-

[a] Positions measured from the 1.3 mm continuum by 2-D Gaussin fits.

IRS1 and IRS3

Among these sources, HOPS-361-A (hereafter IRS1) and HOPS-361-C (hereafter IRS3) have the strongest 1.3 mm continuum, with peak fluxes of 0.152 and 0.114 Jy beam^{-1}, respectively. As stated in section 6.1, IRS1 and IRS3 are the dominant mid/far-IR luminosity contributors and also presumed driving sources of the large scale outflow (e.g., Torrelles et al., 1998; Eislöffel et al., 2000). IRS1 is partly resolved in 1.3 mm and no clear elongation is apparent. In 0.87 mm IRS1 appears better resolved. The inner brighter part of IRS1 (i.e., flux above 0.06 Jy beam^{-1}) has a bar-like shape, with an elongation at P.A. of about 30 degrees. This elongated structure is further embedded in low level extended emission (below 0.06 Jy beam^{-1} but still above 20 σ = 11 mJy beam^{-1}, see also Figure 6.4). This weaker component is approximately elliptical and its major axes extends about $0\farcs3$ along the NW-SE direction, i.e., $\sim 75°$ offset in orientation from the inner bright component. There are some hints of spiral-like bending features at the interface between the two components, and may further connect with larger scale spiral-like features extending to $\sim 1''$(see Figure 6.4). These features have added to the complexity on inferring the configuration of the protostellar disk of IRS1. The kinematic information, which

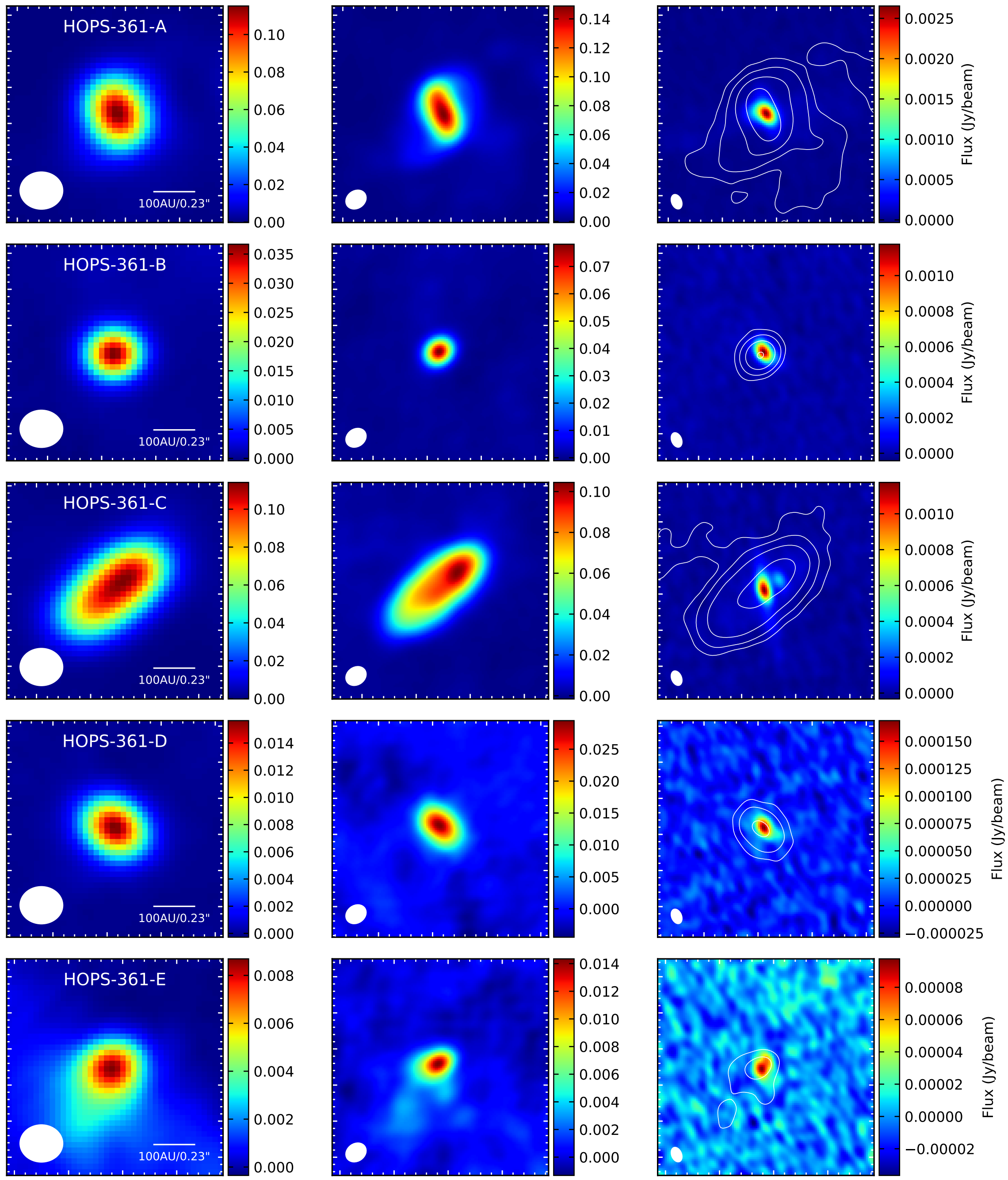

Figure 6.2: 1.3 mm, 0.87 mm and 9 mm Continuum images of protostars in the NGC 2071 IR region from left to right. For the 9 mm images we overplot the 0.87 mm continuum in white contours for comparison. The contours levels are (5, 15, 45, 135) $\times$ 0.55mJy beam^{-1}. The beam sizes are $0\farcs24 \times 0\farcs21$ (104 au $\times$ 91 au) for 1.3 mm, $0\farcs13 \times 0\farcs10$ (56 au $\times$43 au) for 0.87 mm, and $0\farcs09$ $''\times 0\farcs06$(39 au $\times$ 26 au) for 9 mm, as illustrated in the bottom left corner of each panel.

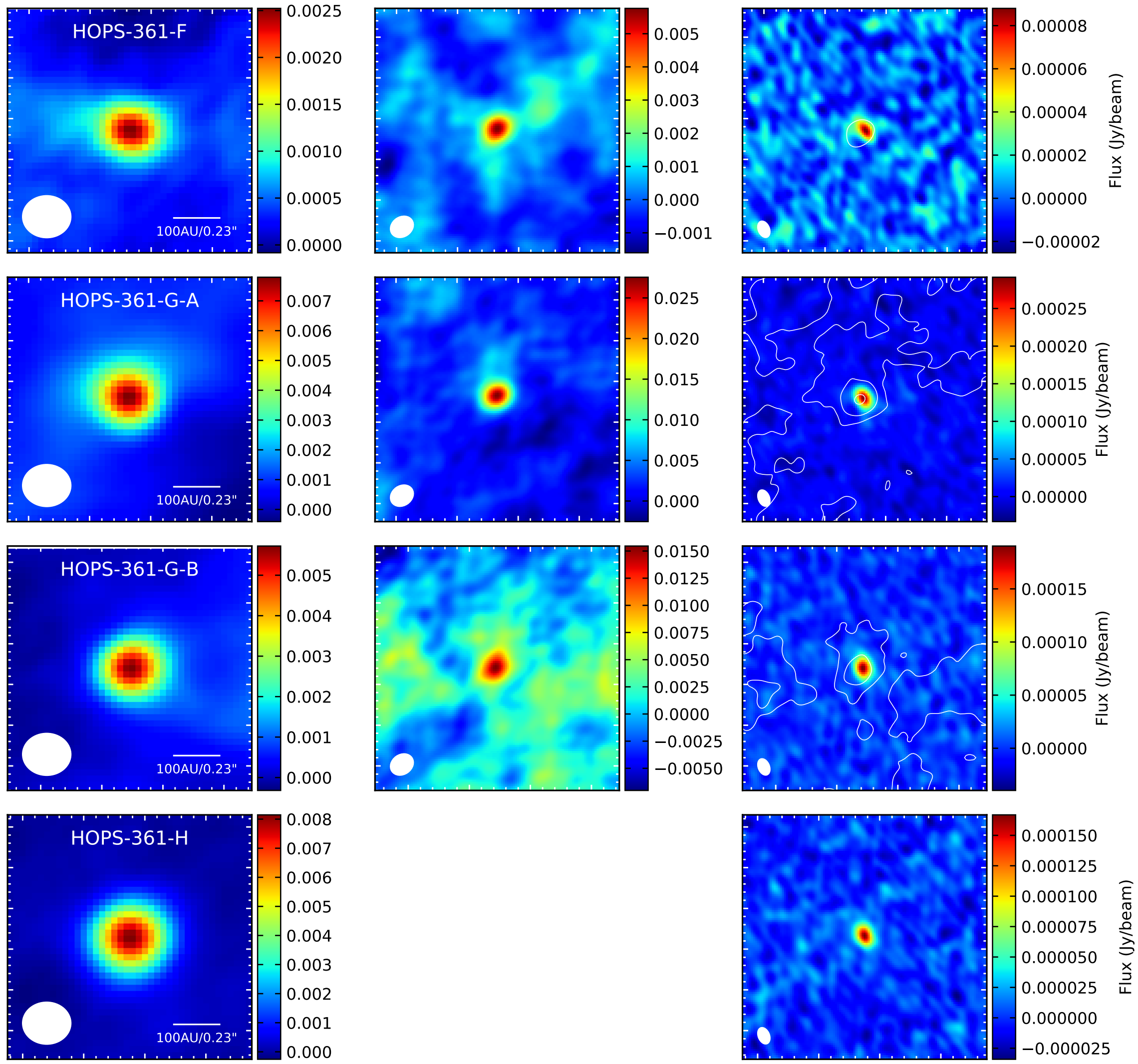

Figure 6.3: Continuation of Figure 6.2. HOPS-361-H is not covered in the FOV of the 0.87 mm observation.

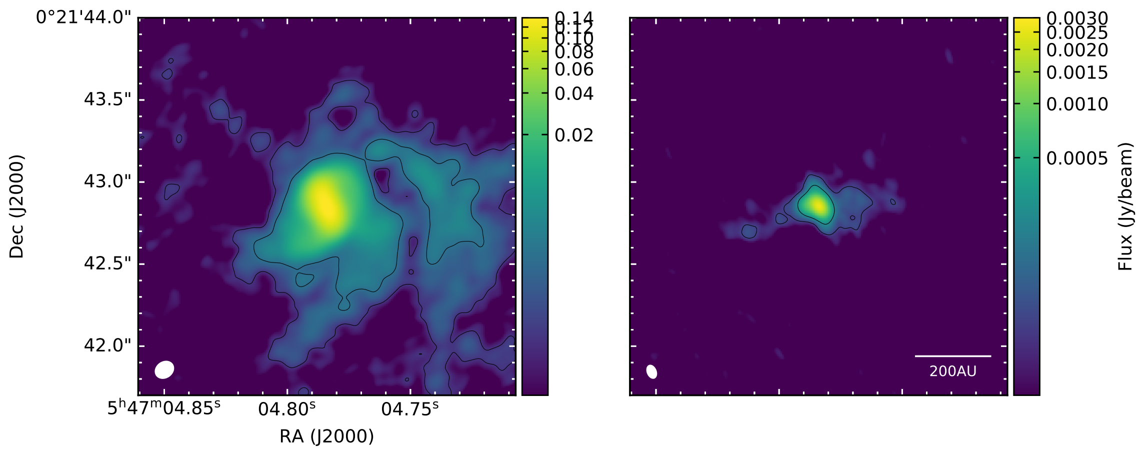

Figure 6.4: 0.87 mm and 9 mm images of IRS1 shown in colorscale with a log stretch. The contours illustrate (5, 20) $\times\sigma$, with $\sigma = 0.55$ mJy beam^{-1} for 0.87 mm data and 12 μJy beam^{-1} for 9 mm data. The beam sizes are shown in the lower left corner.

will be discussed in following sections, are more supportive of a disk oriented in the NW-SE direction, i.e., consistent with the extended component. In this scenario, the inner bright component revealed in 0.87 mm appears as an unusual substructure of the protostellar disk. The deconvolved FWHM from Gaussian fits to the 0.87 mm continuum emission, is $0\farcs25\times0\farcs15$, which is dominated by the inner component.

The VLA 9 mm continuum, has both free-free emission and thermal dust emission, shows a distinctly different morphology with respect to the ALMA images. The 9 mm continuum emission of IRS1 appears as a marginally resolved condensation, which coincides well with the position of 0.87 mm flux peak. The 9 mm emission has a T-shape elongation, i.e., extending along the NE-SW direction (PA $\sim 30°$), and also slightly to the east. The NE-SW extension has a direction similar to the brighter part seen in 0.87 mm. In addition, some low level ($\sim 5\sigma$) diffuse emission is also seen to the east and west of the central source, which extends as far as $0\farcs5$. Trinidad et al. (2009) reported radio knots (IRS1E, IRS1W) ejected from IRS1 along the E-W direction based on VLA 1.3 cm continuum. Comparing with their detections, the weak diffuse emission in the 9 mm could also be tracing a radio jet in the E-W direction; and it is likely that some of the previously detected radio knots, like IRS1W, has dissipated most of its energy and can no longer be detected, thus absent in our map.

On the other hand, IRS3 shows a clear disk at 0.87 mm and 1.3 mm. Gaussian fits to the continuum in both bands give a similar deconvolved size of $0.48''\times0.19''$ with a position angle of 130°. Assuming that the Gaussian semi-major axis corresponds to the disk radius, it has a radius of 103 au, and the inclination can be estimated to be 67° by assuming that it is a geometrically thin disk and then calculating the inverse cosine of the minor axis divided by the major axis. The flux distribution in 0.87 mm continuum appears asymmetric, with the emission peak offset by $0.16''$($\sim$69 au) to the northwest compared with the geometric center. It is less clear if there is similar asymmetric appearance in 1.3 mm due to more limited spatial resolution.

Interestingly, in the center of the disk, the 9 mm continuum further reveals a binary system separated by 0.1″(∼43 au). The two components (IRS3a, IRS3b) has a flux ratio of ∼10 in 9 mm, and the more luminous component, IRS3a, is coincident with the geometric center of the disk structure seen in 0.87 mm and 1.3 mm. IRS3b is located to the northwest of IRS3a and more close to the emission peak in 0.87 mm. IRS3b could be (at least partly) contributing to the asymmetric flux distribution seen in 0.87 mm via enhanced heating towards the surrounding dust/gas. While the detection of IRS3b is a point source, IRS3a is resolved and extends along the NE-SW direction to about 0.24″(∼100 au) on both sides, with a position angle of ∼15°. Extension from IRS3 in this direction has been reported in earlier VLA 1.3 cm and 3.6 cm observations, albeit with a lower resolution (Carrasco-González et al., 2012; Trinidad et al., 2009), and interpreted as a radio jet.

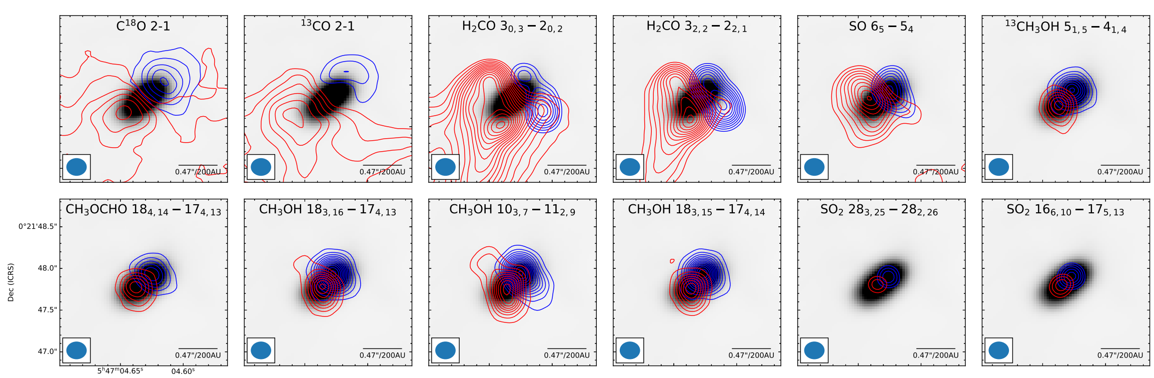

Figure 6.5: Integrated intensity maps of spectral lines toward IRS3 overlaid on the 1.3 mm continuum (gray scale). The transition are marked on top of the panel. The integrated intensity maps are separated into blueshifted velocities at 3 – 8 $\mathrm{km\,s^{-1}}$ and redshifted velocities at 10 – 15 $\mathrm{km\,s^{-1}}$, and plotted with blue and red contours, respectively. The contours start at 10σ and increase on 10σ intervals.

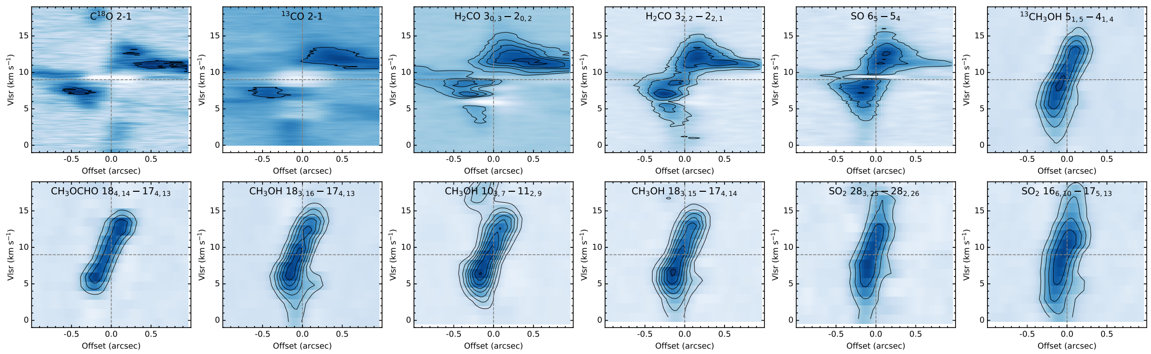

Figure 6.6: PV diagram of spectral lines toward IRS3. The transition are marked on top of each panel. The contours start from 10 σ and increase in steps of 10 σ.

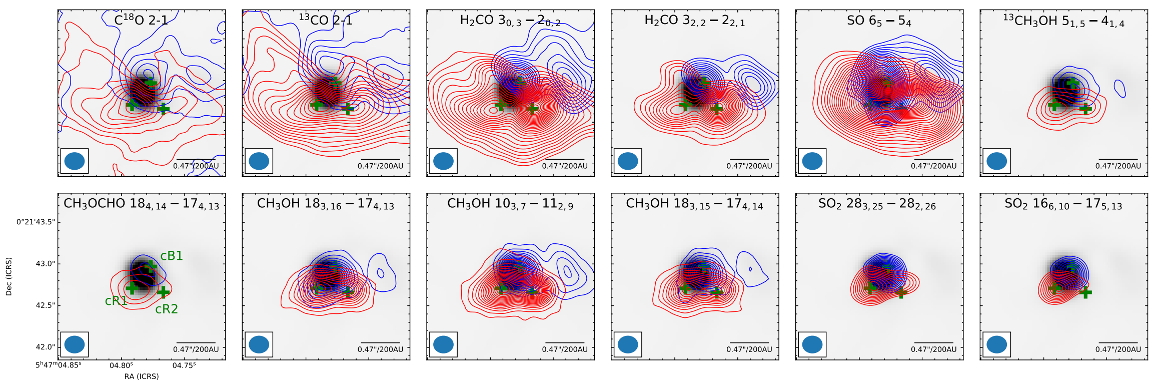

Figure 6.7: Same as Figure 6.5 but for IRS1. For transitions from ^{13}CO, H_2CO and SO the contours start from 40 σ in steps of 10 σ. For other lines The contours start at 10σ and increase on 10σ intervals. We have labeled the positions of cB1, cR1 and cR2 in green crosses (see text for more details).

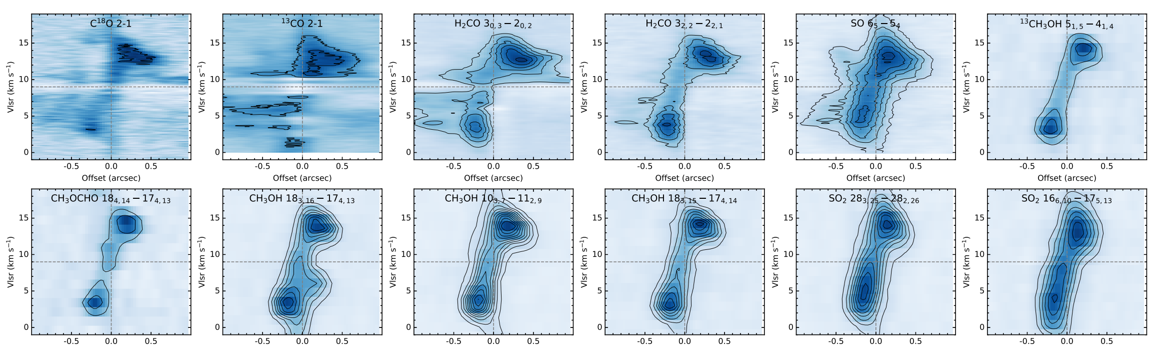

Figure 6.8: Same as Figure 6.6 but for IRS1.

6.3.2 Molecular Line detections

We have detected a series of molecular lines associated with the protostellar disks for both IRS1 and IRS3, including transitions from $C^{18}O$, ^{13}CO, H_2CO, CH_3OH, $^{13}CH_3OH$ and SO_2. In addition to these lines, we have also detected abundant line emission in the continuum spectral window in band 6. Detailed modelling with *Xclass* suggests most of these lines arise from organic molecules like CH_3OCHO and NH_2CHO.

6.3.3 IRS3

Figure 6.5 presents the integrated intensity map of spectral lines toward IRS3. Line emission integrated over two velocity intervals ($1\ \mathrm{km\,s^{-1}} < |\Delta V| < 6\ \mathrm{km\,s^{-1}}$, relative to a systemic velocity of $9\ \mathrm{km\,s^{-1}}$) is shown in blue and red, respectively. Almost all lines exhibit a clear velocity gradient along the major axis of millimeter continuum, with emission transiting from blueshifted in the northwest to redshifted in the southeast. This monolithic velocity transition and its correspondence with the dust continuum are strongly indicative of a Keplerian rotating disk. Figure 6.5 also reveals the difference in spatial distribution of line emission from different molecules. Species including $C^{18}O$, ^{13}CO, H_2CO, SO exhibit strong emission beyond the disk boundary defined by 1.3 mm/0.87 mm dust continuum. The line emission from CH_3OH, SO_2, and other organic molecules is more spatially compact, i.e., within $0\farcs25$ ($\sim$ 108 au) from the center. Hereafter we refer to the two groups of lines with distinct morphology as group A and group B, i.e., group A lines include those from $C^{18}O$, ^{13}CO, H_2CO and SO, while groups B lines include transitions from CH_3OH, SO_2, $^{13}CH_3OH$, as well as most complex organic molecules (CH_3OCHO is shown here as an example).

These two categories are better illustrated in the PV diagram extracted along the the major axis of the dust continuum, as shown in Figure 6.6. The group A, i.e., $C^{18}O$, H_2CO, SO, etc, show bright emission peaks in the first and third quadrant. For ^{13}CO and H_2CO the detection in first quadrant (i.e., blueshifted emission) is stronger. For all species in group A the detection close to the system velocity is relatively weak, possible due to self-absorption of cold gas along line of sight and/or spatial filtering of interferometer observations, especially for $C^{18}O$ and ^{13}CO. For H_2CO and SO the edges on the PV diagram drop from a relative velocity of 7–8 $\mathrm{km\,s^{-1}}$ at the center, to 2–3 $\mathrm{km\,s^{-1}}$ around $1''$and extends further. In contrast with the group A, lines in the group B appear as a continuous linear feature crossing the first and third quadrant, and no low velocity emission extending beyond $0''.5$ ($\sim$215 au) is apparent. The linear feature is consistent with a velocity gradient around 20 $\mathrm{kms^{-1}pc^{-1}}$ and the intensity distribution across it is relatively uniform. The spatial extents of these lines line up well disk boundary inferred from 1.3 mm/0.87 mm continuum. Nevertheless, the outer edges on the PV diagram have a convex shape, i.e., without an obvious extension to higher velocities at offsets closer to zero, in contrast with the expectation for a Keplerian disk, but we will show in section 6.4 that this is mainly due to the limited spatial resolution. Our band 6 observation has a resolution of $\sim 0''.25$ (108 au), comparable with half of the major axis of dust continuum, so the detailed PV structures have been smeared out in this plot. On the other hand, for group A lines, the outer emission extending beyond the $\sim$ 100 au is more likely to be contributed by the envelope gas surrounding the central disk, which constitutes a infalling rotating structure extending to $\gtrsim 1''$(430 au).

6.3.4 IRS1

The kinematics of IRS1 are more difficult to infer since we do not have clear knowledge about the disk orientation from dust continuum. Figure 6.7 presents the integrated intensity map of spectral lines toward IRS1. Interestingly, for most species there appear to be one blueshifted clump (cB1) and two redshifted clumps (cR1, cR2) associated with IRS1. This is most clear for H_2CO, SO and CH_3OH. For an individual rotating disk, one would expect a monolithic velocity gradient along the major axis, as observed for IRS3. Here we think cB1 and cR1 are tracing the protostellar disk, while the third gas clump cR2 is a separate structure that is not associated with IRS1 disk, for the following reasons. Firstly, the position of cR2 is more spatially offset from the emission peak of dust continuum compared with cB1 and cR1. If cB1 and cR2 are tracing the gas rotation on both sides of a disk, then the inferred position of a disk will disagree with that traced by dust continuum. Secondly, not all the lines exhibit clear detection at the position of cR2. cR2 clump is absent in organic molecules like CH_3OCHO and for SO_2 and $^{13}CH_3OH$ only some weak extension from cR1 towards cR2 is seen. Again, this is in contrast with the expectation that if cR2 is tracing one side of the disk since similar chemical/excitation properties are expected for both sides of a disk. Therefore the IRS1 disk, as traced by cB1 and cR1, is oriented in the NW-SE direction.

Figure 6.8 illustrates the PV diagram extracted along the the inferred disk orientation of IRS1. Similarly as IRS3, there are two categories of molecular lines: $C^{18}O$, ^{13}CO, H_2CO and SO show low velocity emission extending beyond $0''.5$, while $^{13}CH_3OH$, CH_3OH, SO_2 and other organic molecules are exclusively tracing the central disk. But different from the canonical case of IRS3, for the lines in the group B, the linear feature is composed of two separate emission peaks in the first and third quadrant, instead of more continuous distributed. In addition, the PV diagram of IRS1 appears more asymmetric against the origin, in terms of both the intensity and the shape. This deviation from pure disk kinematics may arise from an imperfect determination of the disk position/orientation, or confusion by other mechanisms, like ejection, or hidden multiplicity inside IRS1.

6.3.5 Outflows in ^{12}CO

Our observations also allow for a search for protostellar outflows associated with IRS1 and IRS3 via the ^{12}CO 2–1 data. Figure 6.9 presents the channel map of CO 2–1 integrated every 4 $\mathrm{km\,s^{-1}}$ from −55 to 73 $\mathrm{km\,s^{-1}}$. The systemic velocities of IRS1 and IRS3 are around 8.9 and 9.3 $\mathrm{km\,s^{-1}}$, respectively (see section 6.4). A jet-like outflow can be clearly seen in channels from −55 to −19 $\mathrm{km\,s^{-1}}$ for the blueshifted lobe, and from 29 to 73 $\mathrm{km\,s^{-1}}$ for the redshifted lobe. This jet is symmetrically distributed against IRS3 and extends to at least $\sim$ 0.02 pc long on both sides. The orientation of the jet is approximately perpendicular to that of the IRS3 disk. The jet has an extremely high velocity, i.e., a maximum LOS velocity of $\sim$ 70 $\mathrm{km\,s^{-1}}$ relative to IRS3, or a true velocity of $\sim$ 150 $\mathrm{km\,s^{-1}}$ after correcting for an inclination angle of 67°. Overall the jet has a clumpy appearance in most panels. For example, in channels from −43 $\mathrm{km\,s^{-1}}$ to −35 $\mathrm{km\,s^{-1}}$ the jet appears as a chain of several jet knots.

Figure 6.9 also reveals some unusual properties of this jet. Firstly, instead of a continuous linear feature, the jet seems to be composed of a few segments with slightly different directions. This is most clear at panels from −35 to −19 $\mathrm{km\,s^{-1}}$, and from 37 to 69 $\mathrm{km\,s^{-1}}$. Secondly, at velocities from −11 to −3 $\mathrm{km\,s^{-1}}$ the jet gradually turns into a wide angle V-shape outflow with a half opening angle of $\sim$20°. The coexistence of both a collimated jet-like component and a wide-angle biconical

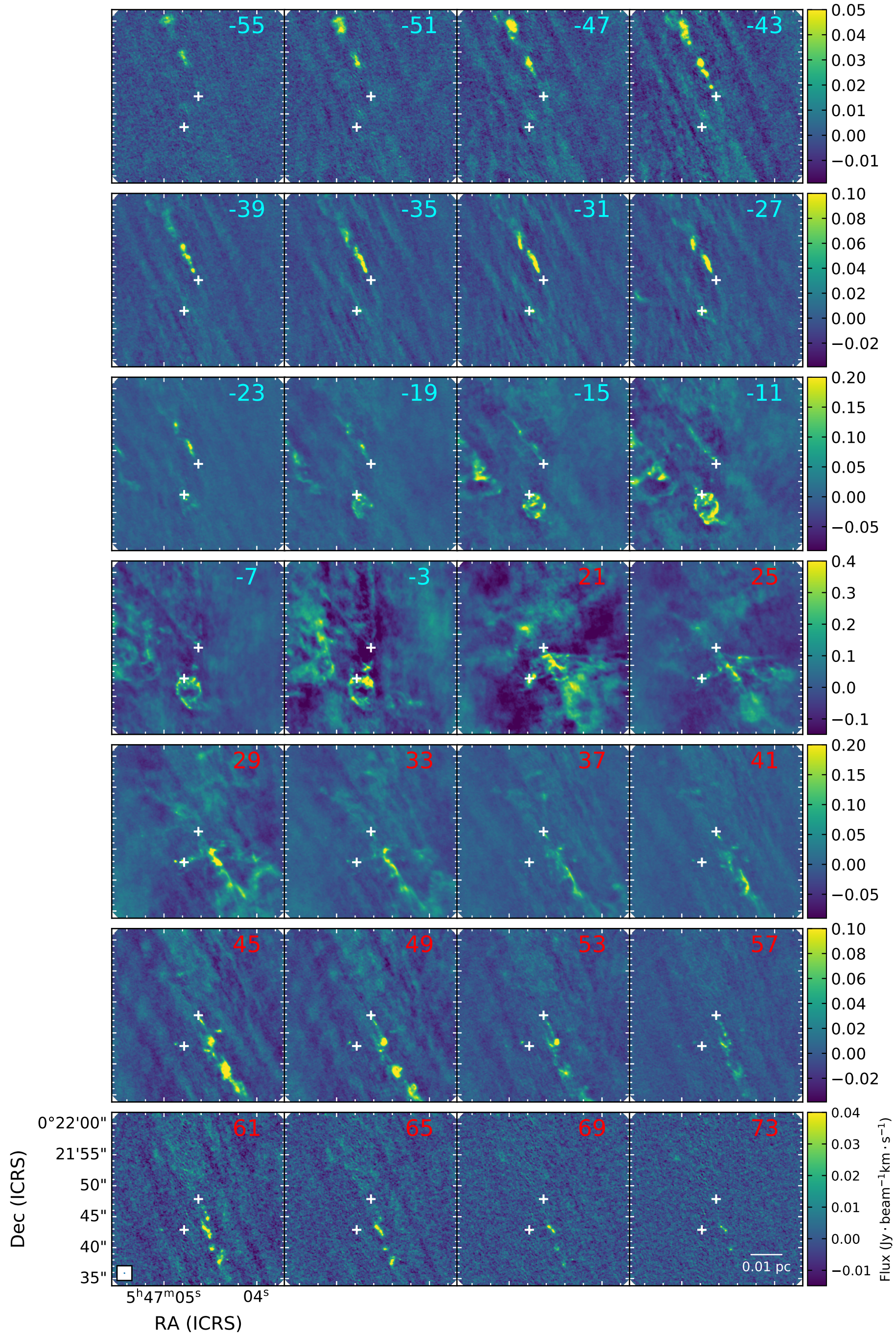

Figure 6.9: CO intensity map integrated over every 4 $\mathrm{km\,s^{-1}}$ from -55 to 73 $\mathrm{km\,s^{-1}}$ shown in colorscale. The center velocity of each panel is marked on the top right corner, with the blueshifted and redshifted velocities shown in blue and red text, respectively. The positions of IRS1 and IRS3 are indicated by white crosses. A scalebar is given in the bottom right panel.

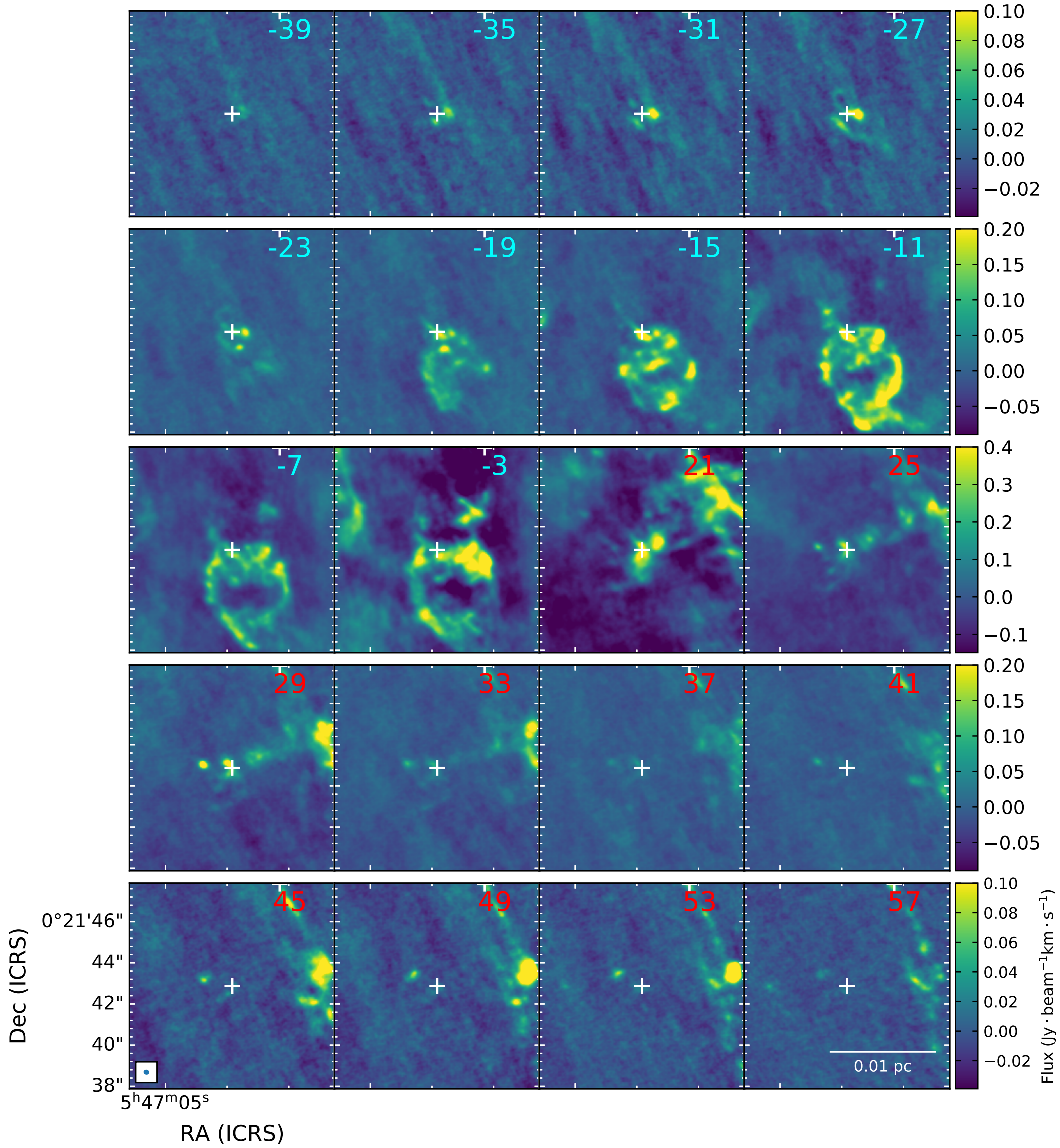

Figure 6.10: Same as Figure 6.9 but a zoom-in view for IRS1. We focuses on CO intensity maps at velocities from -39 to 57 $\mathrm{km\,s^{-1}}$, for which the outflows associated with IRS1 are more prominent.

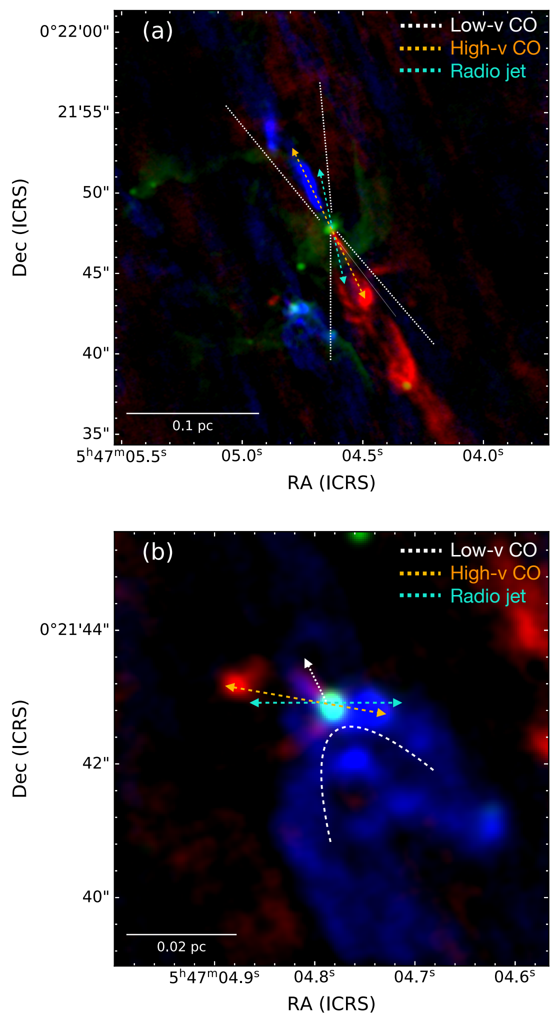

Figure 6.11: *(a)* An overview plot of the CO outflow detections associated with IRS3. The plot is overlaid on a three color image made with integrated blueshifted and redshifted CO emission, as well as the 1.3 mm continuum (in green). The blue and red colorscales represent CO emission integrated over (-51, -16) km s^{-1}and (34, 69) km s^{-1}, respectively. The high velocity CO jet is indicated with a dashed brown line, while the CO cavity seen in low velocities are indicated with a dashed white line. The direction of radio jet, marked in a cyan dashed line, is determined from our 9 mm map (see also Trinidad et al., 2009; Carrasco-González et al., 2012). *(b)* Same as *(a)* but a zoom-in view for IRS1. The blue and red colorscales represent CO emission integrated over (-31, -16) km s^{-1}and (34, 49) km s^{-1}, respectively. For IRS1, the dashed white lines indicate a bubble-like wide angle blueshifited outflow lobe identified in this work, while the dashed brown lines indicate the blueshifted and redshifted CO clumps seen at higher velocities (see text for more details). And the cyan dashed line indicates the approximate direction of the radio ejection reported in (Trinidad et al., 2009). The positions of three redshifted clumps are marked in white crosses.

component has been observed in low-mass outflows (e.g., HH 212, IRAS 04166+2706, Codella et al., 2014; Santiago-García et al., 2009). However, in these sources the jet is usually located at the central axes of the wide angle shell, while for IRS3 the jet is spatially close to the cavity wall of the wide angle component. This wide angle outflow is not apparent in the redshifted lobe at the corresponding velocity range, i.e., from 21 to 30 $\mathrm{km\,s^{-1}}$.

Figure 6.10 presents a zoom-in view of the CO outflow associated with IRS1. The IRS1 outflow is more prominent in the blueshifted lobe from -23 to -3 $\mathrm{km\,s^{-1}}$. It appears as V-shape centered on IRS1 at higher velocities (i.e., panel -23, -19 $\mathrm{km\,s^{-1}}$), with its opening facing towards the SW direction, and turns more like a bubble in shape at lower velocities, which has a radius of $\sim 1.8''$. Such a bubble-like feature is not seen in the redshifted lobe. At higher velocities, i.e., -39 – -27 $\mathrm{km\,s^{-1}}$, the blueshifted outflow turns into a clump, about $0\farcs6$ to the west of IRS1. The redshifted lobe is more complex. There is some weak CO emission originating from IRS1 extending to the NE direction at velocities from 25 to 33 $\mathrm{km\,s^{-1}}$. This redshifted CO emission may be driven by the same source that is responsible for the blueshifted bubble outflow given their roughly aligned direction, but it is unclear why they have such dramatically different appearances. At higher velocities there is a redshifted clump around $1\farcs5$ to the east of IRS1 from 25 to 57 $\mathrm{km\,s^{-1}}$. While this clump appears as a seemingly continuous feature in velocity, detailed inspection suggests that it is actually composed of three clumps with narrower velocity ranges, and the clumps with higher velocities are located more to the NE direction of IRS1. The first clump R1 spans a velocity range from 25 $\mathrm{km\,s^{-1}}$ to 37 $\mathrm{km\,s^{-1}}$. While R1 turns very weak at around 41 $\mathrm{km\,s^{-1}}$, another CO clump (R2) emerges from 41 to 45 $\mathrm{km\,s^{-1}}$, which is very close to, but slightly offset with R1. The highest velocity clump R3 is more prominent from 49 to 57 $\mathrm{km\,s^{-1}}$ and is clearly offset from R1 and R2. The positions of the three clumps are also marked on Figure 6.11. These complicated outflow detections further reveal the complexity in the accretion and ejection process in the vicinity of the IRS1 protostars.

Figure 6.11 provides an overview plot of the outflow detections for IRS1 and IRS3. The plot is overlaid on a three color image made with integrated blueshifted and redshifted CO emission, as well as the 1.3 mm continuum (in green). We have classified the detections into "high-v" and "low-v" and labeled them with different colors. This classification is based on the main velocity range of the outflow detections, using $\Delta V = 25\ \mathrm{km\,s^{-1}}$ as a dividing point between low and high velocity. In summary, both IRS1 and IRS3 exhibit a variety of outflow morphologies at different velocities and there are indication of changes on the ejection direction for both sources. We further overlaid on Figure 6.11 the directions radio jets inferred from this work or literature, which are shown in cyan lines. For IRS3 the direction of radio jet is not consistent with either the high velocity or low velocity CO outflow. For IRS1 the radio jet is close to the high-v outflow. The situation becomes more illusive the with inclusion of disk orientation inferred from continuum and/or line kinematics. While the IRS3 disk is broadly consistent with the radio/molecular ejections, for IRS1 the ejection direction inferred from disk orientation is offset from the observed radio/high-v outflow by $\gtrsim 50°$. We further discuss possible origins in subsection 6.3.5.

6.3.6 SED analysis

To provide more constraints on the physical parameters of IRS1 and IRS3 like protostellar masses, we performed a SED fitting towards the two sources with data from near-IR to sub-mm band. Similar analysis has been conducted in Liu et al. (2020) towards NGC 2071 IR but in their fiducial case a fixed aperture of $9\farcs6$ centered on IRS1 is adopted, which encompasses the emission of both IRS1 and IRS3. Here we follow

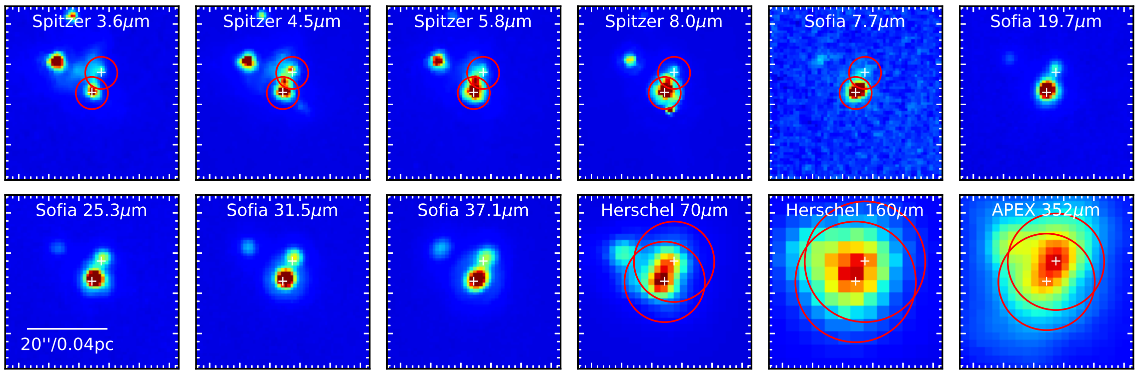

Figure 6.12: Maps of IRS1 and IRS3 in different wavelengths observed with *Spitzer*, *SOFIA* and *Herschel*. The positions of IRS1 and IRS3 are marked with white crosses. The red circles indicate the aperture used for photometry. For the *SOFIA* 19.7 μm, 25.3 μm, 31.5 μm and 37.1 μm images we perform a 2D Gaussian fitting towards IRS1 and IRS3 at the same time to better measure their fluxes.

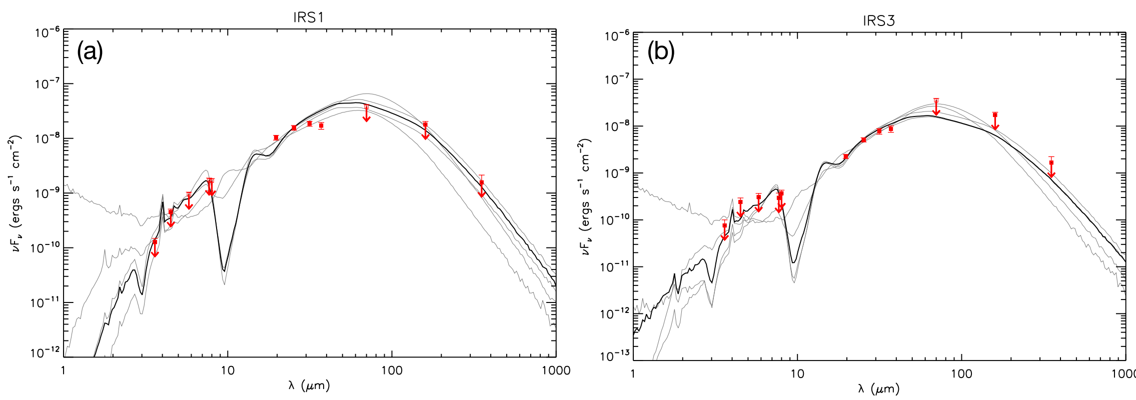

Figure 6.13: Protostar model fitting to the fixed aperture, background-subtracted SED of IRS1 and IRS3 using the ZT model grid. The best-fit model is shown with a solid black line and the next four best models are shown with solid gray lines.

the same fitting routine as in Liu et al. (2020) but attempt to separate the flux between IRS1 and IRS3. We retrieved the same dataset, i.e., *Spitzer/IRAC* 3.5, 4.5, 7.3, 8.0 μm, *SOFIA/FORCAST* 7.7, 19.7, 31.5, 37.1 μm and *Herschel/PACS* 70, 160 μm map as in Liu et al. (2020) (see reference therein). Additional *SOFIA/FORCAST* 25.3 μm, and *APEX/SABOCA* 352 μm data are also included here. In Figure 6.12 we present the multi-wavelength images of IRS1 and IRS3. In short wavelength, e.g. 3.6

to 8.0 μm, IRS1 is clearly seen while the detection IRS3 is relatively weak. In mid-IR wavelength from 19.7 to 7.1μm IRS1 is still the primary flux contributor and IRS3 is also apparent. At longer wavelengths, the resolution of *Herschel* is not sufficient to resolve the two objects.

In order to better disentangle the flux emitted by IRS1 and IRS3, we performed the photometry in a "heterogeneous" way for data at different wavelengths. For wavelengths from 19.7 to 37.1μm, where both objects are clearly detected and partly blended, we performed a two component 2D Gaussian fitting to obtain their fluxes simultaneously. For shorter wavelengths we did aperture photometry with a 4$''$ aperture, which is chosen to cover vast majority of emission from each object. Following the routine in Liu et al. (2020), we carry out a background subtraction using the median flux density in an annular region extending from one to two aperture radii, to remove general background and foreground contamination. Note that for IRS3 the flux measurement is most likely to be overestimated since the adopted aperture also covers part of the emission from IRS1, and there is some contamination of extended nebulosity in 3.6 and 4.5μm. This will not significantly affect our SED fitting results since in our SED modeling the data points of shorter wavelength (< 8.0 μm) are treated as upper limits. For longer wavelengths (70, 160, 352 μm), it is difficult to disentangle the fluxes of blended sources, i.e., IRS1 and IRS3 (and potentially IRS2) with the current resolution. In light of this, we performed an aperture photometry with an aperture that is large enough to encompass the fluxes of both IRS1 and IRS3 (12$''$ in 70μm, 15$''$ in 160μm, 10$''$ in 352 μm) and set the data points as upper limits when performing the SED fitting.

We use Zhang & Tan (2018) RT models (hereafter ZT models) to fit the SEDs and derive key physical parameters of the protostars. The ZT model is a continuum radiative transfer model that describes the evolution of high- and intermediate-mass protostars with analytic and semi-anlytic solutions based on the paradigm of the Turbulent Core model (see Zhang & Tan, 2018, for more details). The main free parameters in this model are the initial mass of the core M_c, the mass surface density of the clump that the core is embedded in $\Sigma_{\rm cl}$, the protostellar mass m_*, as well as other parameters that characterize the observational setup, i.e., the viewing angle i, and the level of foreground extinction A_V. Properties of different components in a protostellar core, including the protostar, disk, infall envelope, outflow, and their evolution, are also derived self-consistently from given initial conditions. In Table B.2, we present the parameters of five best-fitting models, ordered from best to worst as measured by χ^2. From left to right, the parameters are reduced χ^2, the initial core mass M_c, the mean mass surface density of the clump $\Sigma_{\rm cl}$, the current protostellar mass m_*, the viewing angle i, foreground extinction A_V, half opening angle of the outflow cavity $\theta_{\rm w,esc}$, accretion rate from the disk to the protostar $m_{\rm disk}$, the luminosity integrated from the unextincted model SEDs assuming isotropic radiation $L_{\rm bol,iso}$, and the inclination-corrected true bolometric luminosity $L_{\rm bol}$.

The best fitting model of IRS1 indicates a source with a protostellar mass of 4 $M_\odot$ accreting at a rate of $3{\times}10^{-5}$ $\rm M_\odot \cdot\ yr^{-1}$ inside a core with an initial mass of 40 $M_\odot$ embedded in clumps with a mass surface density of 0.1 $\rm g \cdot cm^{-2}$. Nevertheless, the best five models provide similar goodness of fit, judging from the value of χ^2, although there is a significant variation in model parameters like the protostellar mass m_*. For example, similar χ^2 can be achieved with a protostellar source of mass ~ 1 $M_\odot$ accreting at $6{\times}10^{-5}$ $\rm M_\odot yr^{-1}$. This illustrates the model degeneracy that exists in trying to constrain protostellar properties from only their MIR to FIR SEDs (see also De Buizer et al., 2017). In light of this we only consider the typical parameter ranges among the best five models as a reasonable initial constraint for the protostellar system, instead of exploring only the best fitting case. Therefore IRS1

Table 6.4: Estimated physical parameters of IRS1 and IRS3 from SED fitting

Source	χ^2	M_c $M_\odot$	$\Sigma_{\rm cl}$ gcm^{-2}	m_* $M_\odot$	i $^\circ$	A_V mag	$\theta_{\rm w,esc}$ $^\circ$	$m_{\rm disk}$ $M_\odot$	$r_{\rm disk}$ (au)	$\dot{m}_{\rm disk}$ $M_\odot/yr$	$L_{\rm bol,iso}$ $L_\odot$	$L_{\rm bol}$ $L_\odot$
IRS1	4.02	40	0.1	4.0	62	19.3	27	1.3	123	3.0 $\times10^{-5}$	0.8 $\times10^3$	0.4 $\times10^3$
	4.62	10	1.0	1.0	29	16.8	25	0.3	19	6.0 $\times10^{-5}$	0.8 $\times10^3$	0.6 $\times10^3$
	4.69	30	0.1	4.0	65	21.0	33	1.3	136	2.7 $\times10^{-5}$	0.8 $\times10^3$	0.4 $\times10^3$
	5.27	10	3.2	4.0	62	0.0	56	1.3	39	19.0 $\times10^{-5}$	1.9 $\times10^3$	0.3 $\times10^3$
	5.39	50	0.1	4.0	51	32.7	24	1.3	115	3.2 $\times10^{-5}$	0.8 $\times10^3$	0.5 $\times10^3$
IRS3	0.32	30	0.1	2.0	58	6.7	23	0.7	79	2.0 $\times10^{-5}$	0.2 $\times10^3$	0.2 $\times10^3$
	0.74	10	1.0	2.0	44	33.5	39	0.7	34	7.5 $\times10^{-5}$	0.8 $\times10^3$	0.3 $\times10^3$
	0.76	40	0.1	2.0	55	16.8	19	0.7	73	2.2 $\times10^{-5}$	0.3 $\times10^3$	0.2 $\times10^3$
	0.83	30	0.1	1.0	48	0.0	15	0.3	48	1.5 $\times10^{-5}$	0.2 $\times10^3$	0.1 $\times10^3$
	1.04	10	3.2	4.0	71	0.0	56	1.3	39	19.0 $\times10^{-5}$	1.9 $\times10^3$	0.2 $\times10^3$

can be better fitted with a protostellar source with a central mass of 1 – 4 $M_\odot$, with an accretion rate of 3 – 19 $\times10^{-5}$ $M_\odot yr^{-1}$. Similarly, the SED of IRS3 is described with a protostellar source with a central mass of 1 – 4 $M_\odot$, with an accretion rate of 2 – 19 $\times10^{-5}$ $M_\odot \cdot yr^{-1}$. The viewing angle, ranging from 58° to 71°, is broadly consistent with the value derived from ALMA observations (67°). Moreover, for the case of IRS3, the best fit case with $m_* \sim 2$ $M_\odot$ provides a significantly better fitting ($\chi^2 \sim 0.35$) compared with other four models and hence a lower protostellar mass is more favored.

6.4 Kinematic Modeling

The detection of molecular lines has provided an opportunity to quantify the gas kinematics and precisely measure the stellar masses. Different approaches have been developed to measure the dynamical mass based on the kinematic structure of molecular lines. A widely adopted method uses PV diagrams to fit Keplerian rotation, either the outer edge or the intensity maxima (see Seifried et al., 2016, for a discussion). More sophisticated modelling that includes a proper parameterization of the physical structure of the disk, e.g., temperature and density profile, and radiative transfer with code like RADMC-3D (Dullemond et al., 2012), has also been developed (e.g., Czekala et al., 2015, 2016; Sheehan et al., 2019). However, they can be computationally expensive and may have difficulties in the presence of considerable extended emission and multiple sources that is present in NGC 2071 IR. Similarly accurate determination of dynamical mass could be achieved via pure kinematic modeling without detailed treatment of the underlying physical structure of the disk (Boyden & Eisner, 2020). Here we develop a simple analytic model, which is similar as the one in Boyden & Eisner (2020), to interpret the observed PV diagrams and to infer the dynamical masses.

6.4.1 A simplified analytic model

The observed kinematics of molecular lines could arise from two component: a Keplerian rotating disk, and an infalling-rotating envelope. For the disk, we assume an optically thin, uniformly excited disk orbiting around a central object with mass m_* and we assume that the disk has a height $h(r) = 0.2{\times}r$ on both sides of the midplane, and a sharp truncation at the inner boundary $R_{\rm in}$, and the radius at the R. The density distribution of the disk is described by $\rho \propto r^{-2}$. The disk follows Keplerian rotation, i.e,

$$v_r = 0, \tag{6.3}$$

$$v_\phi = \sqrt{\frac{Gm_*}{r}}. \tag{6.4}$$

The envelope starts from R extends to an outer boundary $R_{\rm out}$, with the motion described by

$$v_r = -v_0\frac{\sqrt{R(r-R)}}{r}, \tag{6.5}$$

$$v_\phi = v_0\frac{R}{r}, \tag{6.6}$$

where $v_0 = \sqrt{2Gm_*/R}$ is the the rotation velocity at the so called centrifugal barrier. Based on the density and kinematic distribution above we can generate a 3-D model grids to simulate the disk/envelope system, with each grid assigned with a density ρ_i and velocity v_i. To compare with observations we assume the disk has a systemic velocity of $v_{\rm sys}$ and is viewed at an inclination angle i (i = 0° corresponds to a face-on configuration while i = 90° is edge-on). Thus we may calculate the light of sight velocity $v_{\rm i,los}$ for each grid depending on the viewing angle and the position of the model grid. Each grid then produce line emission with a velocity profile described by

$$\phi_{\rm v,obs} \propto exp\left(-\frac{v_{\rm obs} - v_{\rm i,los}^2}{2\sigma^2}\right), \tag{6.7}$$

where we adopt a σ of 0.4 km s^{-1}, i.e., the thermal broadening line width for T = 43 K. For a specific sky location, the line intensity at $v_{\rm obs}$ can be obtained by integrating $\phi_{\rm v,obs} \cdot \rho_i$ for each model grid along line of sight. In this way we can generate a position-position-velocity (PPV) cube. To mimic the observational setups we match the channel width of our model PPV cube to values in the observation (depending on which line is being fit), and smooth the PPV cube to the same spatial resolution as in the real observations. Then we extract a PV diagram along the disk midplane to compare with our observational results.

In Figure 6.14 we present an example of the model output. The colorscales in Panel (a) and (b) indicate the PV diagram of IRS3 from line CH_3OH $18_{3,15} - 17_{4,14}$ and SO $6_5 - 5_4$, respectively, which are selected as representatives for line groups A and B described in Section 3.2. For panel (a), we overlay in grey contours the model for a pure Keplerian rotating disk with m_*=1.5 $M_\odot$, R = 100 au, $R_{\rm in}$ = 40 au and $v_{\rm sys}$ = 10 km s^{-1}. The model appears reasonably consistent with emission of CH_3OH $18_{3,15} - 17_{4,14}$, suggesting that it indeed can be explained by a Keplerian rotating disk. For panel (b) a disk-only model does not fit the SO $6_5 - 5_4$ data well as it shows significant low velocity emission extending up to $\sim 1''$ from the center. It is highly unlikely that SO is tracing a same disk but in larger radius since the disk radius inferred from continuum is only 103 au. Therefore we add an envelope component with $R_{\rm out} = 430$ au ($1''$). As can be seen the resulting contours gives a much better fit to the data. Therefore, the difference in the two PV groups are most likely arising from different relative contribution from the envelope, i.e., emission of lines in group A mainly originate from the disk, while group B lines have contribution from both disk and envelope.

6.4.2 Dynamical mass estimation

For purpose of dynamical mass estimation we utilize the group B lines, i.e., lines that exclusively trace the disk. This allows us to reduce the number of free parameters, and also the systematic uncertainties since the disk kinematics is much simpler. To further assess the fit quality we use a χ^2 likelihood, defined as

$$\chi^2 = \sum \left(\frac{\mathrm{Data}(x, v) - \mathrm{Model}(x, v)}{\sigma} \right)^2, \tag{6.8}$$

i.e., the sum of χ^2 over all pixels within a localized region in the PV diagram. σ is the rms noise of the PV diagram measured with signal-free regions. In summary, we have in total four parameters for the disk model, $\{m_*,\ R,\ R_{\rm in},\ v_{\rm sys},\ i,\ f_{\rm norm}\}$, including the stellar mass m_*, disk inner/outer radius $R_{\rm in}$ and R, systemic velocity $v_{\rm sys}$, inclination i and a normalization factor $f_{\rm norm}$. In order to explore the parameter space more effectively we adopt the Markov Chain Monte Carlo (MCMC) fitting code *emcee* (Foreman-Mackey et al., 2013). Uniform prior probability distributions for the parameters is assumed, for the mass m_* in a range of $1 - 15\ M_\odot$, $R_{\rm in}$ in a range of $0 - 40$ au, R in a range of 40–200 au and i in a range of $0 - 90\ \mathrm{km\,s^{-1}}$ and $v_{\rm sys}$ in a range of 8 – 12 $\mathrm{km\,s^{-1}}$.

We picked five lines in group B, i.e., CH_3OH $18_{3,15} - 17_{4,14}$, CH_3OH $10_{3,7} - 11_{2,9}$, $^{13}CH_3OH$ $5_{1,5} - 4_{1,4}$, SO_2 $28_{3,25} - 28_{2,26}$ and CH_3OCHO $18_{4,14} - 17_{4,13}$. These lines are relatively strong and isolated so that we can safely avoid the contamination from other lines that are close in frequency. We run the MCMC routine for the PV diagram of each line separately. In practice we found that there are usually some coupling between m_* and i, which is expected. Consider a narrow ring with radius r rotating around a center mass m_*, then on the PV diagram one would get a velocity gradient

$$\frac{\partial v_{\mathrm{LOS}}}{\partial x} = \sqrt{\frac{Gm_*}{r^3}} sini. \tag{6.9}$$

The case for an inner truncated disk is similar, i.e., equivalent to a set of rings with radii from R_{in} to R. So our model is not very effective at optimizing both m_* and i simultaneously, especially when the disk kinematics are not well-resolved. In this case we may overfit the data and the walkers could struggle to achieve global optimization when multiple χ^2 minimums exist. Therefore, we attempted two strategies of parameter setup: one with the inclination i as a free parameter and a prior range of 0 – 90° is given. As for the second strategy, we use a fixed i to avoid overfitting. For IRS3 we adopt the inclination angle inferred from the dust continuum (i.e., 67°). For IRS1 the inclination is not well constrained so we fixed the inclination angle for a range of discrete values, i.e., 90°, 60° and 30°, and then run MCMC routine.

Table 6.5 lists the best-fit parameters for IRS1 and IRS3. We found that different lines return broadly consistent disk parameters. In the fixed-i case, our modeling of IRS3 gives a mass ranging from 1.59 to 1.91 $M_\odot$, and a radius ranging from 88 to 126 au for the different lines. This mass estimation is in reasonable agreement with the SED model results for IRS3, i.e, ~ 2.0 $M_\odot$. The radius estimation also agrees well with the value derived from millimeter continuum ($\sim$103 au). SO_2 $28_{3,25}-28_{2,26}$ gives the lowest mass value of 1.59 ± 0.11 $M_\odot$, while CH_3OH $10_{3,7}-11_{2,9}$ gives the highest mass value of 1.91 ± 0.07 $M_\odot$. The models with free inclination work reasonably well and give very similar results compared with the model with fixed i. The best-fit i ranges from 77 to 89°, indicating that a configuration that is close to edge-on is also favored from the modeling. These values appears larger compared with the fiducial 67°, but the projection term is regulated by sin i, and in the fiducial case $\sin(67°) \approx 0.92$ is already very close to the edge-on configuration $\sin(90°) = 1$.

For IRS1 the returned mass strongly depends on the assumed inclination value. For a moderate inclination $i = 60°$, the modeling returns a mass of 3.85 – 5.40 $M_\odot$ among different lines. High inclination (90°) results in a lower mass estimation, i.e, 3.17 – 4.21 $M_\odot$, while low inclination i=30° tends to give a high mass estimation around 9.82 – 13.87 $M_\odot$, which is unrealistically large for IRS1 given the observed bolometric luminosity. So lower inclinations (i.e., more close to face-on configuration) are not explored. The free-i models further put some constraints on the inclination, with the best-fit values ranging from 49° to 69° for different lines. The corresponding masses span from 3.60 to 6.45 $M_\odot$. We discuss possible range of stellar masses of IRS1 in subsection 6.5.1.

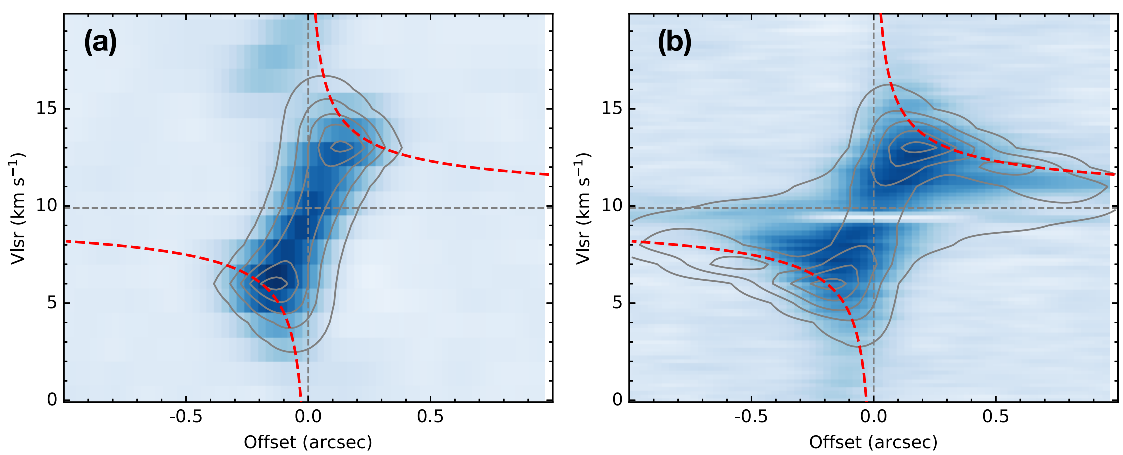

Figure 6.14: PV diagram examples overlaid with the predictions of the analytic model. *(a)* PV diagram of CH_3OH $18_{3,15} - 17_{4,14}$ shown in colorscale. The grey contours indicate the analytic model for a Keplerian rotating disk with m_*=1.5 $M_\odot$, R = 100 au, $R_{\rm in}$ = 40 au and $v_{\rm sys}$ = 10 km s^{-1}. *(b)* PV diagram of SO $6_5 - 5_4$. Overlaid are the model with both a Keplerian rotating disk (same as *(a)*) and an envelope with radius extending to 1″.

Table 6.5: Estimated physical parameters of IRS3 and IRS1 from the kinematic modeling

Source	Molecule/Transition	i (degree)	m_* ($M_\odot$)	R (au)	$R_{\rm in}$ (au)	$v_{\rm sys}$ km s^{-1}	Δx (au)	norm
IRS3	CH_3OH $18_{3,15}-17_{4,14}$	77.18±1.17	1.56±0.10	106.91±2.86	15.80±1.51	9.26±0.06	-16.70±1.44	1.13±0.02
		67	1.68±0.07	106.05±2.75	16.18±0.54	9.22±0.05	-16.27±1.31	1.16±0.02
	CH_3OH $10_{3,7}-11_{2,9}$	87.11±3.63	1.76±0.06	124.30±3.40	8.31±1.44	9.53±0.05	-16.57±1.57	1.09±0.02
		67	1.91±0.07	122.84±3.08	8.48±0.84	9.51±0.06	-18.29±1.29	1.14±0.02
	$^{13}CH_3OH$ $5_{1,5}-4_{1,4}$	77.48±4.48	1.61±0.07	114.96±3.12	17.17±1.83	9.17±0.06	-16.40±1.61	1.13±0.02
		67	1.73±0.05	116.51±2.47	16.18±1.03	9.17±0.05	-16.44±1.21	1.16±0.03
	SO_2 $28_{3,25}-28_{2,26}$	76.88±5.35	1.56±0.17	90.86±5.27	7.79±1.55	9.26±0.14	-18.64±2.13	1.17±0.05
		67	1.59±0.11	88.23±4.13	8.39±0.67	9.26±0.13	-19.50±1.57	1.22±0.04
	CH_3OCHO $18_{4,14}-17_{4,13}$	88.55±4.62	1.72±0.06	119.95±2.63	38.56±2.95	9.30±0.05	-19.58±1.21	1.21±0.03
		67	1.88±0.06	116.68±2.26	41.19±3.01	9.28±0.05	-19.28±1.25	1.29±0.04
IRS1	CH_3OH $18_{3,15}-17_{4,14}$	55.96±2.80	5.22±0.26	132.05±3.51	34.43±1.96	8.73±0.05	4.05±1.42	1.19±0.03
		90	3.78±0.09	125.50±3.42	38.48±1.36	8.71±0.05	4.52±1.23	1.12±0.02
		60	4.87±0.10	133.21±3.64	34.95±2.56	8.71±0.04	4.17±1.21	1.20±0.03
		30	12.53±0.21	129.59±2.73	28.41±1.94	8.70±0.04	4.99±1.51	1.24±0.03
	CH_3OH $10_{3,7}-11_{2,9}$	55.17±3.54	5.03±0.39	143.75±3.90	27.72±3.27	8.99±0.04	-6.67±1.59	1.04±0.03
		90	3.68±0.10	128.30±3.16	45.79±3.62	8.89±0.04	-9.04±1.40	1.05±0.03
		60	4.54±0.11	141.09±4.35	25.52±3.85	8.98±0.05	-6.97±1.23	1.01±0.02
		30	11.86±0.23	139.62±3.03	25.57±2.58	8.94±0.03	-5.38±1.38	1.10±0.02
	$^{13}CH_3OH$ $5_{1,5}-4_{1,4}$	56.72±2.63	5.72±0.31	137.77±3.16	58.06±2.11	8.85±0.03	-4.86±1.38	1.13±0.02
		90	4.21±0.08	135.45±2.95	60.60±1.85	8.81±0.03	-5.81±1.08	1.00±0.02
		60	5.40±0.09	140.91±2.75	58.79±1.81	8.82±0.04	-4.30±1.36	1.13±0.02
		30	13.87±0.31	134.20±3.01	50.40±1.70	8.77±0.04	-3.70±1.38	1.23±0.03
	SO_2 $28_{3,25}-28_{2,26}$	68.69±5.80	3.60±0.31	126.49±3.27	16.27±4.45	9.29±0.07	-8.65±1.25	1.16±0.03
		90	3.17±0.09	122.62±3.06	20.27±3.01	9.36±0.05	-7.75±1.18	1.11±0.02
		60	3.85±0.09	118.19±3.74	20.70±5.14	9.31±0.07	-6.93±1.16	1.21±0.02
		30	9.82±0.32	114.31±3.14	11.32±2.47	9.07±0.07	-6.37±1.27	1.22±0.03
	CH_3OCHO $18_{4,14}-17_{4,13}$	49.41±2.71	6.45±0.50	127.96±2.63	54.96±2.26	8.89±0.03	-5.25±1.51	1.12±0.03
		90	4.17±0.11	120.08±3.72	65.94±2.97	8.90±0.04	-7.53±1.48	1.06±0.04
		60	5.23±0.10	128.82±3.12	57.85±2.45	8.91±0.04	-5.55±1.33	1.06±0.03
		30	13.50±0.29	123.57±3.59	48.68±2.04	8.91±0.04	-4.48±1.61	1.15±0.02

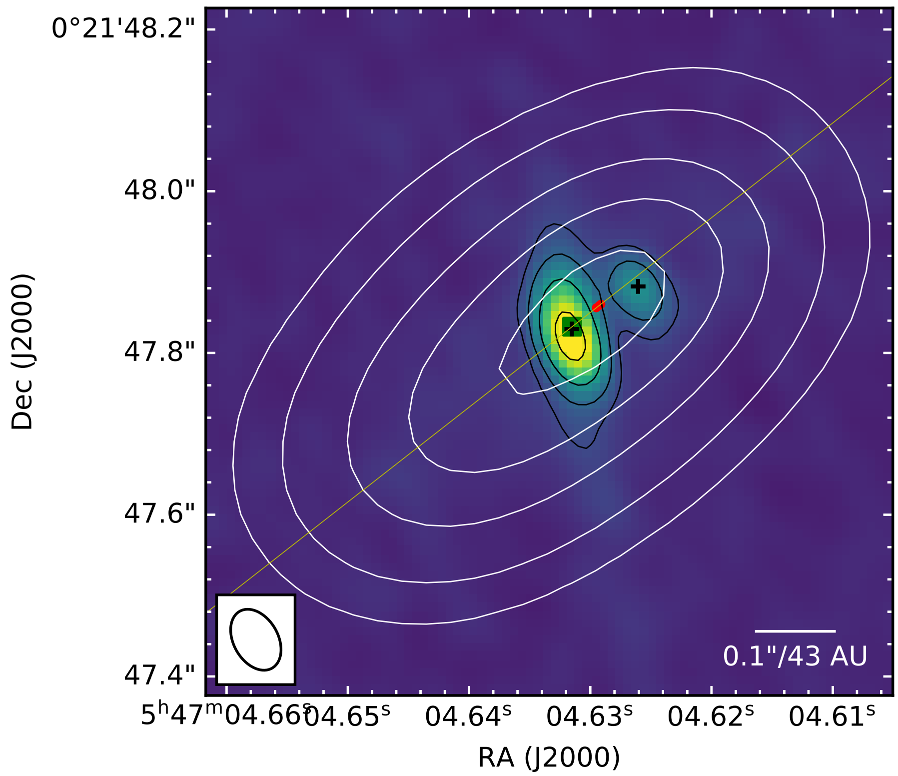

Figure 6.15: A zoom-in view of IRS3. The colorscale and contours illustrate the VLA 9 mm continuum. The contours levels are (10, 20, 40, 80)$\times\sigma$ with $\sigma = 12$ μJy beam^{-1}. The white contours indicate the 1.3 mm continuum and the contour levels are (100, 200, 400, 600, 800)$\times\sigma$ with $\sigma = 1.3$ mJy beam^{-1}. The beam size of 9 mm data is $0\farcs09\times0\farcs06$, shown in the lower left corner. The geometric center of circumbinary disk, determined as the intensity weighted center of the region between 100 σ and 400 σ contours in 1.3 mm, is shown in a green square. The positions of IRS3a and IRS3b, measured from the 9 mm data is indicated by black crosses. The red dots represent the "kinematic center" from the kinematic modeling measured for different lines.

6.5 Discussion

6.5.1 Implication of the protostellar mass

Despite of the fact that NGC 2071 IR is known to be an intermediate mass star formation region based on luminosity considerations, there is no consensus with regard to the protostar masses of the brighest sources, i.e., IRS1 and IRS3. Snell & Bally

(1986) suggests that a single B2 star is required to generate sufficient ionizing flux to account for the observed radio emission of IRS1, whereas the majority of radio emission may arise from thermal jets rather than free-free emission of a compact HII region. Carrasco-González et al. (2012) argues that IRS3 should also host an intermediate mass star by modelling its SED and spatial intensity profile at 3 mm with an irradiated accretion disk model. More constraints are derived from observations of water masers with VLA and VLBA by several investigators (Torrelles et al., 1998; Seth et al., 2002; Trinidad et al., 2009). Based on the spatial-kinematic distribution of the water masers Trinidad et al. (2009) estimated a central mass of 5±3 $M_\odot$ and 1.2±0.4 $M_\odot$ for IRS1 and IRS3, respectively. Nevertheless, the estimation is derived with only a small number of masers (5 for IRS1, 6 for IRS3) and relies on assumptions about the disk inclination and radii. Our ALMA molecular line observations provide a unique chance to clarify the dynamical masses of IRS1 and IRS3.

IRS3

For IRS3 our kinematic modeling gives a central mass estimation of 1.59 – 1.91 $M_\odot$ from fits to different molecules. The variation is probably reflecting systematic differences of molecules in the spatial distribution within the disk, due to variation of abundances and excitation conditions. A more detailed modeling involving physically realistic disk properties and astrochemical evolution is required to better understand the variations of different molecules but is beyond the scope of this paper. Here we take the range 1.59 – 1.91 $M_\odot$ as a reasonable estimation for possible central masses of IRS3. This estimation is further consolidated by our SED fitting in subsection 6.3.6, which prefers a central mass around 2 $M_\odot$. Note that our VLA 9 mm observations have revealed the multiplicity in IRS3. In principle, if the molecular lines are tracing Keplerian orbiting motions around the two components (IRS3a, IRS3b) then the estimated dynamical mass should be treated as the sum of two.

Our kinematic modeling has the ability to constrain the mass ratio of IRS3a/b. In section 6.4 we attempted the modeling of IRS3 with the position offset as a free parameter to allow for a precise measurement of the "kinematic center", which corresponds to the binary barycenter as the disk kinematics are regulated by the center of mass. In the fixed-i case, the best-fit offsets range from -19.6 to -16.3 au for different lines, indicating the kinematic center is about 16.3 – 19.6 au to the NW direction compared with the reference point, as illustrated in Figure 6.15. Therefore the kinematic center is located roughly in the middle of IRS3a/b and one can further estimate a IRS3a/IRS3b mass ratio of 1.1–1.5 by comparing their relative distances from the kinematic center.

It is also interesting to note that IRS3a appears to coincide well with the "geometric center" of the disk. Here the "geometric center" can be defined as the center of symmetry of elliptical contours in 1.3 mm/0.87 mm continuum at relatively low levels, where the emission is not obviously skewed to the NW direction. In Figure 6.15 we marked the position of the intensity weighted center for outer disk (defined by the region between 100σ - 400σ isophotal contours in 1.3 mm). If the disk is in a steady state with its material distribution regulated by the central mass, one would expect its geometric center close to the barycenter of the binary system, whereas in our case there seems to be a non negligible deviation between the two.

However, we note that our spatial resolution is only $0\farcs23$ ($\sim$100 au) in band 6 so it is challenging to infer the position of the kinematic center (or the relative position between ALMA/VLA detections) with a few au precision. One potential issue is the limitation in absolute positional accuracy, which hinders precise determination of the precise relative location between VLA/9 mm and ALMA/band6 detections. The theoretical accuracy limit by signal to noise ratio can be estimated by $\delta p =$

$\theta_{\rm beam}/(S/N)/0.9$ (e.g., Cortes et al., 2021), which is around 0.3 mas for a FWHM beam size $\theta_{\rm beam} = 0\farcs23$ and S/N = 890 for IRS3 in band 6. However, the atmospheric phase fluctuations limit the δp to about $0.05\theta_{\rm beam}$ (Cortes et al., 2021), which is around $0\farcs02$, or 5 au. Secondly, the determination of the kinematic center relies on assumption of symmetrically distributed line emission on both sides of the disk. Nevertheless, we have observed asymmetric intensity distribution in high resolution 0.87 mm continuum, which is heavily skewed to the NW direction. If the asymmetry arises from local enhanced temperature or density (likely due to the existence of IRS3b), then the molecular line emission could be stronger toward the NW side as well, and thus leading to a deviation of the kinematic center to the NW direction. There are some hints for asymmetry in line intensity distribution in some lines (see e.g, Figure 6.6) but follow up observations in future is required to clarify it.

IRS1

The mass of IRS1 is less well constrained mainly due to a lack of knowledge of the inclination angle. In the case of a fixed inclination of 60°, the kinematic modeling gives a central mass in range of 3.85 – 5.40 $M_\odot$ with the scattering from different molecules. If a lower inclination is adopted the model requires a larger central mass to account for the observed PV feature. The lowest mass estimation, i.e., when assuming i = 90°(the edge-on configuration), is 3.17 – 4.21 $M_\odot$ for different tracers. For smaller inclinations like i = 30°, the model results in a mass as high as ∼13 $M_\odot$, which is already physically unrealistic given the observed bolometric luminosity. The free-i cases favor a modestly large inclination of 49°– 69°.

One can also argue against a very small inclination of i $\lesssim$ 30°(close to face-on configuration) for IRS1 based on the observed morphology/kinematics of outflows driven by IRS1. The H_2 1 - 0 S(1) map reveals a strong outflow associated with IRS1 roughly in the E-W direction, with the Eastern lobe extending as far as 30″(∼0.06 pc) (outflow II in Eislöffel et al. (2000), see also Walther & Geballe (2019)). In our CO 2–1 observations the outflow associated with IRS1 appears as a single blueshifted lobe located to the Southwest of the source, in contrast with the face-on configuration for which one would expect more spatially overlapping blueshifted and redshifted line emission. Therefore the IRS1 disk should have a moderate or higher inclination, although we cannot be more certain about the precise range.

The SED analysis in subsection 6.3.6 provides a good constraint on the upper limit of the central mass of IRS1. All the best five fit models of IRS1 have a stellar mass $m_* \lesssim 4\ M_\odot$. A larger stellar mass will typically result in larger fluxes in mid-/far-infrared, and bolometric luminosities compared with the observation. The best fit model with larger stellar mass (i.e., $m_* = 8\ M_\odot$) has a $\chi^2 \gtrsim 10$, significantly worse compared with the minimum χ^2 (~ 5), and hence highly unlikely. Nevertheless, the Zhang & Tan (2018) model grid is rather sparse for smaller m_* and it is difficult to derive a more precise upper limit from the SED fitting. Combining the information from both kinematics and SED, we speculate the stellar mass of IRS1 is about 3 – 5 $M_\odot$. This puts constraints on the inclination angle of IRS1, i.e., i $\gtrsim 60°$ according to Table 6.5. A caveat is that in the SED analysis we have implicitly assumed that IRS1 is dominated by a single protostar. If multiple components exist, IRS1 is likely to harbor a total stellar mass $\gtrsim 5\ M_\odot$(divided between different components), without significantly deviating from the bolometric luminosities constrained by infrared observations.

6.5.2 Accretion rate

In subsection 6.3.6 our SED modeling returns an estimation of the accretion rate onto the protostar $\dot{m}_*$, which spans from 1.5×10^{-5} to $1.9 \times 10^{-4}\ M_\odot\ \mathrm{yr}^{-1}$ for both

IRS1 and IRS3. Much of the large uncertainties arise from emission being blended at wavelength >70 μm and hence the bolometric luminosity for either source is not well constrained. The totol luminosity $L_{\rm bol}$ has been estimated to be 478 $L_{\rm bol}$ in an aperture encompassing both IRS1 and IRS3 in Furlan et al. (2016). If we simply estimate the ratio of the $L_{\rm bol,IRS1}/L_{\rm bol,IRS3}$ based on the *SOFIA* 37.1 μm photometry, as done in subsection 6.3.1, then the $L_{\rm bol}$ of IRS1 and IRS3 are 368 $L_\odot$ and 85 $L_\odot$, respectively. Vast majority of the $L_{\rm bol}$ in IRS3 should be attributed to accretion luminosity since the central object has a mass smaller than 2 $M_\odot$ based on our kinematic modeling (see e.g., Palla & Stahler, 1993). Assuming $L_{\rm acc} \approx L_{\rm bol}$, then the accretion rate can be estimated from the equation

$$L_{acc} = \frac{Gm_* \dot{m}_*}{R_{ps}}, \tag{6.10}$$

where G is the gravitation constant, m_* is the protostar mass, $\dot{m}_*$ is the mass accretion rate from the disk to the protostar, and R_{ps} is the protostellar radius. Here we adopt a stellar radius of 5 $R_\odot$ based on the protostellar structure models in Palla & Stahler (1993). Thus the mass accretion rate is likely between 7.4 $\times10^{-6}$ to 9.6 $\times10^{-6}$ $M_\odot$ yr^{-1} for a protostellar mass in range of $1.59 - 1.91$ $M_\odot$. In this calculation we have assumed the accretion luminosity of IRS3 is dominated by a single protostar, whereas in subsection 6.5.1 we have shown that the secondary component, IRS3b, may have a comparable mass as IRS3a, albeit with the systematic uncertainties in the derivation of mass ratio. From the above equation, the estimated $\dot{m}_*$ will not change if both components have a similar $\dot{m}_*$ and a $R_{\rm ps}$ of 5 $R_\odot$, regardless of their mass ratios. In this case the estimated $\dot{m}_*$, 7.4$\times10^{-6}$ – 9.6$\times10^{-6}$ $M_\odot$ yr^{-1}, should be understood as accretion occurring onto both objects. It is difficult, though, to precisely determine the relative strength of $\dot{m}_*$, and accordingly $L_{\rm acc}$, for IRSa/b since it may depends on their masses, as well as their locations in the disk. And their radii are probably smaller than 5 $R_\odot$ given their smaller masses.

This estimation of $\dot{m}_*$ is smaller (a factor $\gtrsim 2$) compared with that derived in our SED modeling. However, in our SED modeling the returned $L_{\rm bol}$ for all best five models (100 – 300 $L_\odot$) are greater than the assumed $L_{\rm bol}$ (85 $L_\odot$) here, possibly because for λ >70 μm only upper limits of the photometry measurements is given. For the solution with $L_{\rm bol} = 100\ L_\odot$, the Zhang & Tan (2018) model gives a $\dot{m}_*$ of $1.5 \times 10^{-5}\ \ M_\odot\ {\rm yr}^{-1}$, i.e., consistent within a factor of 2 with the derived value from simplified calculations. This remaining discrepancy mainly arises from a different treatment of the accretion luminosity in the Zhang & Tan (2018) SED model, in which half of the accretion energy, i.e., $Gm_*\dot{m}_*/2R_{ps}$ is released when the accretion flow reaches the stellar surface, while the other half is partly radiated from the disk and partly converted to the kinetic energy of the disk wind. So up to half of the accretion luminosity may be converted to the kinematic energy and cannot be observed in radiation, thus a larger accretion rate is needed in ZT model to account for the accretion luminosities.

It is difficult to derive the accretion rate for IRS1 in the same way, due to the less well constrained dynamical mass and unknown multiplicity. If IRS1 contains two low mass protostars with mass $\lesssim 2\ \ M_\odot$, then one can derive an accretion rate of 1.45 $\times 10^{-5}\ \ M_\odot\ {\rm yr}^{-1}$ following similar arguments as we did for IRS3, i.e., assuming $L_{\rm acc} \approx L_{\rm bol}$ and $R_{ps} = 5\ R_\odot$. However, IRS1 could consist of one or multiple protostars with higher masses, which may have larger stellar radii and a larger fraction of the observed luminosity could be dominated by stellar radiation instead of accretion. Indeed, in three out of the best five SED models for IRS1 in subsection 6.3.6 with $m_* = 4\ \ M_\odot$, vast majority of the total luminosity is contributed by the protostar themselves. But still we expect active accretion is currently occurring onto IRS1 based on the detection of high velocity CO outflows close to IRS1.

6.5.3 Jets and outflows in NGC 2071 IR

Jets and outflows provide a fossil record of the mass-loss histories of associated YSOs. The NGC 2071 IR region is characterized by widespread molecular hydrogen emission as revealed by the H_2 1-0 S(1) line, and considerable efforts have been made to identify individual outflows and assigning individual protostars to them (Eislöffel et al., 2000; Walther & Geballe, 2019). IRS3 appears to be the driving source for the largest NW-SE outflow that extends $\sim 3'$ far on both sides (outflow IA, IB following the designation in Eislöffel et al. (2000)). IRS1 is driving another outflow that is more E-W oriented (outflow IIA, IIB, with PA$\sim$70°), although the western lobe (IIB) is much fainter in H_2 lines. Our CO 2-1 observations, for the first time, provide a high resolution view of the molecular outflows within the central $30''$ in the NGC 2071 IR region. We discuss IRS3 and IRS1 separately in the following sections.

IRS3

The CO 2–1 data reveals a high velocity bipolar jet associated with IRS3, with a position angle in a range of 22 – 32° seen in different velocities. This further confirms the association of the large scale NW-SE H_2 outflow with IRS3. Interestingly, there are clear misalignment between the jet/outflow seen in different tracers: the H_2 outflow IA/IB has an average position angle of $\sim$ 45°, with its lateral extents covering a wide range around 10°– 60°. The molecular jet shows a position angle about 22 – 32°. The radio jet in our 9 mm map has a position angle $\sim$ 15°(which is consistent with measurements in literature, see Torrelles et al. (1998); Seth et al. (2002); Trinidad et al. (2009); Carrasco-González et al. (2012)). Furthermore, the disk has a position angle of $\sim$ 130°, approximately perpendicular to the high velocity CO jet (but not the radio jet). The most likely mechanism to account for these observational phenomena is a precessing jet wiggling over a large range of jet position angles, and thus the varius orientations seen in different tracers represent the interaction of jet and environment material at different phases. Jet precession has long been known in both low mass and high mass YSOs (see reviews in Frank et al., 2014; Lee, 2020), and large axis changes of up to $\sim 45^\circ$ is also observed in a few sources (e.g., Cunningham et al., 2009).

The current radio jet seen in centimeter continuum indicates the most recent ejection event from the protostar. It is also suggested in Carrasco-González et al. (2012) that the jet is precessing since they found variations in the jet orientation (a few degrees) of the IRS3 jet over a few years (1995–1999). However, their observations have relatively low resolutions ($\sim 0.3''$ in 3.6 cm) and are unable to resolve the radio jet, and hence the measurements may suffer from more uncertainties due to the imperfect Gaussian fitting, or contaminated by the unresolved binary component. Our high resolution 9 mm data gives a more unambiguous measurement of the jet position angle, i.e, $\sim 15^\circ$, which is close to the value measured for 1998/1999 epochs in Carrasco-González et al. (2012). There is no smoking gun evidence for the changes of radio jet orientation in a few year timescale, and further observations with similar spatial resolutions are needed to confirm/clarify it and better constrain the precession period.

The molecular outflow, seen in CO 2–1, also exhibits changes in ejection angles at different velocities, with a smaller position angle jet at higher velocities. A plausible picture is that the jet axis is moving close to line of sight as the jet wiggles clockwise on the sky. At some velocities the outflow appears as misaligned sections, which are also symmetrically distributed in blueshifted and redshifted lobes (e.g., at ΔV=28 km s^{-1}). Such point-symmetric (i.e., S-shaped) wiggles are expected for precession of the accretion disks because of tidal interactions in noncoplanar binary systems (see, e.g., Raga & Biro, 1993; Terquem et al., 1999). Similar misaligned sections and S-shape wiggle is also tentatively detected in the H_2 emission (see figures in Eislöffel et al., 2000; Walther & Geballe, 2019), but the spatial distribution of H_2 is more complex and may involve other physical processes including deflection or blocking of part of an outflow. At lower velocities we have detected a wide angle component of the CO outflow. Interestingly, the edges of this component line up well with the spatial extent of the H_2 emission. This further consolidates a unified origin of the CO and H_2 emission and suggest that this wide outflow cavity is at least partly shaped by the jet precession.

IRS1

Combining the information in the literature and this work, IRS1 exhibits a similar complexity on the inferred ejection directions. Trinidad et al. (2009) detected a few ejected condensations (IRS1E, 1W) from IRS1 along the East-West direction (P.A. $\sim 100°$) based on VLA 1.3 cm and 3.6 cm observations (see also Carrasco-González et al., 2012). In H_2 emission, IRS1 seems to drive a East-oriented outflow (P.A. $\sim$ 70°). This outflow contains several shock knots and some interspread diffuse emission and are collectively called Outflow IIA in Eislöffel et al. (2000), but there could be contribution from other protostars like IRS2. The western lobe (IIB) is much fainter in H_2. On the other hand, a smaller P.A. ($\sim 45°$) is required to account for the disk kinematics (section 6.4) and the low velocity CO outflow, especially the blueshifted wide angle component. There are some relatively high velocity CO knots distributed close to the E-W orientation as well. The situation is further complicated by the non-ideal disk appearance seen in high resolution 0.87 mm, 1.3 mm and 9 mm continuum. The relatively diffuse part of 0.87 mm emission appears consistent with a NE-SW oriented disk (P.A. $\sim 135°$) but it contains a bright inner part elongated at around

P.A. $\sim 30°$. Extension along similar direction is also seen in 9 mm continuum, as well as a protuberance to the east. This East-orientated extension could be due to a E-W jet, as suggested in Trinidad et al. (2009) based on ejected radio knots, whereas the extension with P.A. $\sim 30°$ is less clear without auxiliary information.

In summary, the observed radio condensations or high velocity CO suggests a jet along or close to the E-W direction, while the disk kinematics and CO outflow agree with a NE-SW orientated outflow direction. The H_2 emission has a spatial content with P.A. approximately in between but may have contributions from other YSOs. Similar to the case of IRS3, one might consider a precessing jet to account for the observed ejection events from IRS1. Carrasco-González et al. (2012) reported that the direction of IRS1 jet appear to be changing slightly over a few years based on the 3.6 cm continuum morphology. In particular, the jet slightly bends to the northwest around $0\farcs5$ to the west of the protostar. Carrasco-González et al. (2012) argued that it could be due to either the superposition of a binary jet or a single jet interacting with the ambient medium. The latter scenario is reminiscent of our 1.3 mm continuum map, where we have also observed a dust clump around $0\farcs5$ to the west of IRS1. This dense clump could be responsible for the bending feature in radio jet. Optionally, we note that a precessing jet can also naturally explain the variations in jet orientation and morphology.

The possibility of unresolved multiplicity cannot be ruled out with current data. Carrasco-González et al. (2012) suggests that the extension in their $0.09''$ resolution 1.3 cm map can be interpreted as a marginally resolved close binary system with a separation $\sim$ 40 au. Our 9 mm map of IRS1 exhibits a similar protuberance to the east. A secondary component could be responsible for the origin of precession. Alternatively, one could assign the observed ejections in different directions to different components in the binary system, e.g., one along E-W and the other along NE-SW.

However, more aggressive weighting of the long baselines in the imaging process does not present any definitive evidence of multiplicity at present. In either case, IRS1 is an interesting target to follow up with higher resolution interferometer observations to resolve possible multiplicity and to investigate the accretion and jet ejection process associated with intermediate mass protostars.

6.6 Conclusion

We have used ALMA and the VLA, in conjunction with previous near- to far-infrared, single-dish submillimeter data to characterize the protostellar content of the intermediate mass star formation region, NGC 2071 IR, and in particular, the dominant sources IRS1 and IRS3. These observations allow for a detailed characterization of the properties of protostellar disks, jets/outflows and multiplicity associated with IRS1 and IRS3. The main findings are summarized as follows:

1. IRS3 shows a clear disk appearance at 0.87 mm and 1.3 mm, which has a measured radius of 103 au and an inclination of $\sim 67^{\circ}$. 9 mm continuum further reveals a close binary system separated by $\sim$43 au. The more luminous component, IRS3a, is coincident with the geometric center of the disk, and drives a radio jet with a position angle around 15°.

2. IRS1 is not resolved in 1.3 mm. In 0.87 mm IRS1 appears to contain both a inner brighter component and a larger diffuse component, with approximately orthogonal orientation. IRS1 is marginally resolved and has a T-shape extension in 9 mm.

3. Both IRS1 and IRS3 exhibit clear velocity gradient across protostellar disks in multiple spectral lines, indicating Keplerian rotation. Inspection of the PV diagrams suggests that the molecular lines can be divided into two groups:

group A, including $C^{18}O$, H_2CO, SO, etc, show bright emission peak in the first and third quadrant extending to $\gtrsim 1''$and should have contribution from both disk and envelope, while lines group B, including CH_3OH, $^{13}CH_3OH$, SO_2 and other organic molecules appears as a continuous linear feature crossing the first and third quadrant without low velocity emission extending beyond $0''.5$ ($\sim$200 au) and are hence exclusively tracing the central disk.

4. We developed an analytic modeling and MCMC method to better constrain the dynamical masses of the central objects of protostellar disks. IRS3 is estimated to have a dynamical mass of 1.59–1.91 $M_\odot$. It is less clear for IRS1 without reliable measurement of the inclination but a minimum mass of $\sim$3 $M_\odot$ is derived assuming the edge-on configuration. In the free-i case, the kinematic modeling gives a range of inclination from 49° to 60°, and mass from 3.60 to 6.45 $M_\odot$.

5. We use the Zhang & Tan (2018) model to fit the SED of IRS1 and IRS3 from near-IR to millimeter wavelength. Reasonably good fit can be obtained with a stellar mass of $\sim$4 $M_\odot$ for IRS1, and $\sim$2 $M_\odot$ for IRS3. Combining the constraints from both SED and kinematic modeling, IRS1 should have central mass in the range 3 – 5 $M_\odot$ assuming it is dominated by a single protostar.

6. Based on our CO 2–1 data, IRS3 drives a high velocity jet as well as a low velocity wide angle outflow, while IRS1 only drives a single lobe low velocity wide angle outflow. For both IRS1 and IRS3, the inferred ejection directions from different tracers, including radio jet, water maser, molecular outflow and H_2 emission, are not always consistent and can be misaligned by up to 50°. IRS3 is better explained with a single precessing jet over a large P.A. $\sim$ 50°.

Similar mechanism may be working in IRS1 as well but unresolved multiplicity cannot be ruled out.

Chapter 7

Summary and Prospect

7.1 Star formation in G286

We study the core mass function (CMF) of the massive protocluster G286.21+0.17 with the Atacama Large Millimeter/submillimeter Array via 1.3 mm continuum emission at a resolution of 1.0″ (2500 au). We have mapped a field of $5.3' \times 5.3'$ centered on the protocluster clump. We measure the CMF in the central region, exploring various core detection algorithms, which give source numbers ranging from 60 to 125, depending on parameter selection. We estimate completeness corrections due to imperfect flux recovery and core identification via artificial core insertion experiments. For masses $M \gtrsim 1\ M_\odot$, the fiducial dendrogram-identified CMF can be fit with a power law of the form $\mathrm{d}N/\mathrm{dlog}M \propto M^{-\alpha}$ with $\alpha \simeq 1.24 \pm 0.17$, slightly shallower than, but still consistent with, the index of the Salpeter stellar initial mass function of 1.35. Clumpfind-identified CMFs are significantly shallower with $\alpha \simeq 0.64 \pm 0.13$. While raw CMFs show a peak near $1\,M_\odot$, completeness-corrected CMFs are consistent with a single power law extending down to $\sim 0.5\,M_\odot$, with only a tentative indication of a shallowing of the slope around $\sim 1\ M_\odot$. We discuss the implications of these results for star and star cluster formation theories.

We study the gas kinematics and dynamics of the massive protocluster G286.21+0.17 with the Atacama Large Millimeter/submillimeter Array using spectral lines of $C^{18}O$(2-1), N_2D^+(3-2), DCO^+(3-2) and DCN(3-2). On the parsec clump scale, $C^{18}O$ emission appears highly filamentary around the systemic velocity. N_2D^+ and DCO^+ are more closely associated with the dust continuum. DCN is strongly concentrated towards the protocluster center, where no or only weak detection is seen for N_2D^+ and DCO^+, possibly due to this region being at a relatively evolved evolutionary stage. Spectra of 76 continuum defined dense cores, typically a few 1000 AU in size, are analysed to measure their centroid velocities and internal velocity dispersions. There are no statistically significant velocity offsets of the cores among the different dense gas tracers. Furthermore, the majority (71%) of the dense cores have subthermal velocity offsets with respect to their surrounding, lower density $C^{18}O$ emitting gas. Within the uncertainties the dense cores in G286 show internal kinematics that are consistent with being in virial equilibrium. However, on clumps scales, the core to core velocity dispersion is larger than that required for virial equilibrium in the protocluster potential. The distribution in velocity of the cores is largely composed of two spatially resolved groups, which indicates that the dense molecular gas has not yet relaxed to virial equilibrium, perhaps due to there being recent/continuous infall into the system.

We present a near-infrared (NIR) variability analysis for an $6' \times 6'$ region, which encompasses the massive protocluster G286.21+0.17. The total sample comprises more than 5000 objects, of which 562 show signs of a circumstellar disk based on their infrared colors. The data includes HST observations taken in two epochs separated by 3 years in the F110W and F160W bands. 363 objects (7% of the sample) exhibit NIR variability at a significant level (Stetson index > 1.7), and a higher variability fraction (14%) is found for the young stellar objects (YSOs) with disk excesses. We identified

4 high amplitude (> 0.6 mag) variables seen in both NIR bands. Follow up and archival observations of the most variable object in this survey (G286.2032+0.1740) reveal a rising light curve over 8 years from 2011 to 2019, with a K band brightening of 3.5 mag. Overall the temporal behavior of G286.2032+0.1740 resembles that of typical FU Ori objects, however its pre-burst luminosity indicates it has a very low mass ($< 0.12 M_{\odot}$), making it an extreme case of an outburst event that is still ongoing.

7.2 Star formation in the Vela C and NGC 2071IR region

We study star formation in the Center Ridge 1 (CR1) clump in the Vela C giant molecular cloud, selected as a high column density region that shows the lowest level of dust continuum polarization angle dispersion, likely indicating that the magnetic field is relatively strong. We observe the source with the ALMA 7m-array at 1.05 mm and 1.3 mm wavelengths, which enable measurements of dust temperature, core mass and astrochemical deuteration. A relatively modest number of eleven dense cores are identified via their dust continuum emission, with masses spanning from 0.17 to 6.7 $M_{\odot}$. Overall CR1 has a relatively low compact dense gas fraction compared with other typical clouds with similar column densities, which may be a result of the strong magnetic field and/or the very early evolutionary stage of this region. The deuteration ratios, $D_{\rm frac}$, of the cores, measured with N_2H^+(3-2) and N_2D^+(3-2) lines, span from 0.011 to 0.85, with the latter being one of the highest values yet detected. The level of deuteration appears to decrease with evolution from prestellar to protostellar phase. A linear filament, running approximately parallel with the large scale magnetic field orientation, is seen connecting the two most massive cores, each having CO bipolar outflows aligned orthogonally to the filament. The filament contains the most deuterated core, likely to be prestellar and located midway between the protostars. The observations permit measurement of the full deuteration structure of the filament along its length, which we present. We also discuss the kinematics and dynamics of this structure, as well as of the dense core population.

We present ALMA band 6/7 (1.3 mm/0.87 mm) and VLA Ka band (9 mm) observations toward NGC 2071 IR, an intermediate-mass star formation region in the L1630 cloud of Orion B. We characterize the continuum and associated molecular line emission towards the most luminous protostars, i.e., IRS1 and IRS3, as well as other protostellar objects, on $\sim$ 40 au ($0\farcs1$) scales. IRS1 is partly resolved in millimeter and centimeter continuum showing a potential disk. IRS3 has a clear disk appearance in millimeter continuum and is further resolved into a binary system in our 9 mm map. Both sources exhibit clear velocity gradient across their protostellar disks in multiple spectral lines including $C^{18}O$, H_2CO, CH_3OH, $^{13}CH_3OH$, SO, SO_2, and organic molecules like CH_3OCHO and NH_2CHO. We use an analytic method to fit the Keplerian rotation motion of disks, and give constraints on physical parameters like the dynamical mass of the central object with a MCMC routine. IRS3 is estimated to have a total mass of 1.59–1.91 $M_\odot$. IRS1 has a central mass of 3–5 $M_\odot$ based on both kinematic modeling and its spectral energy distribution, assuming it is dominated by a single protostar. For both IRS1 and IRS3, the inferred ejection directions from different tracers, including radio jet, water maser, molecular outflow and H_2 emission, are not always consistent and can be misaligned by up to $\sim 50°$. IRS3 is better explained by a single precessing jet with its axis wiggling over a range of position angles. A similar mechanism may be present in IRS1 as well but unresolved multiplicity is also possible.

7.3 Prospect

Development of a complete star formation theory requires testing by observations that span a wide range of environments and evolutionary stages. In this disertation we have presented pioneering studies in the massive protocluster G286, which is representative of typical Galactic environment, as well as the strongly magnetized CR1 region in Vela C. The next crucial step is to conduct a systematic survey in a wide range of Galactic environments. I thus plan to extend my current analysis to other star forming regions, with the general aim of measuring the CMF and IMF across different Galactic environments, to better constraining cluster formation theories. As an example in this section I will outline our planned studies in the low metalicity region Sh2-284.

Metallicity is an environmental variable that is of particular interest, since the formation of stars at low metallicities, and the determination of their characteristic clustering and mass scales, is a central problem in galaxy formation and evolution, i.e., to understand the properties of the high redshift universe. In principle, the abundance of heavy elements affects dust abundance, heating and cooling rates, and trace ionization fractions in molecular gas. In addition to fragmentation and collapse, feedback processes may also vary with metallicity, e.g., since ionizing radiation fields are harder and ionized gas temperatures are higher. Ultimately, metallicity may have an impact on the rate of star formation (e.g., the Kennicutt-Schmidt relation) and the shape of the IMF (e.g., Marks et al., 2012). However, observationally there are currently few constraints on the detailed star formation properties of low metallicity regions. Some fundamental questions are still debated. For example, do low metallicity clouds/clumps/cores have similar fragmentation properties as those of more typical Milky Way star-forming regions of near solar metallicity? Do low metallicity regions have a similar correspondence of CMF and IMF as in local regions? The main limitation is the large distance of extragalactic targets, and the corresponding limited sensitivity and spatial resolution that can be achieved when observing them. Only within the Galaxy can individual unit of star formation, i.e., self-gravitating gas cores and single stars be resolved.

A particularly interesting region is Sh2-284 in the Galaxy that has been found to be metal-poor (see Figure 7.1). It is located in the outer Galactic disk about 5 kpc from the Sun (Negueruela et al., 2015). The metallicity is measured to be -0.3 dex below solar for Si and -0.5 dex below solar for O(Negueruela et al., 2015), making Sh2-284 the most metal-poor star-forming environment known in the Milky Way. Sh2-284 offers the possibility to study star formation in great detail in a metal-poor environment, i.e., being more than a factor of 10 closer than the Magellanic Clouds, where these studies are typically carried out. We have obtained Gemini/F2 J/H/Ks data towards this region in a $6' \times 5'$field of view to measure the shape of IMF down to $\sim$0.5 $M_{\odot}$. I am also leading an approved JWST program (PI: Cheng, ID: 2317) aiming to understand the IMF shape of the stellar population in the low mass end down to 15 $M_{\rm Jup}$. In terms of the dust/gas component, we have also obtained the IRAM 1.3 mm continuum and APEX N_2H^+(3-2) line data. An alma program in band 6 is also proposed in this cycle. We plan to apply the developed methods presented in this thesis to better undertand the star formation process in this metal-poor environment.

Another direct extension of the presented studies is to study protostellar disks in different environments. Most sample studies of protostellar disks focuses on lower-mass, more isolated regime of star formation in solar neighborhood. In cluster environments, the high stellar density, protostellar outflow feedback, and ultraviolet radiation from massive stars may influence disk properties and evolution of low-mass

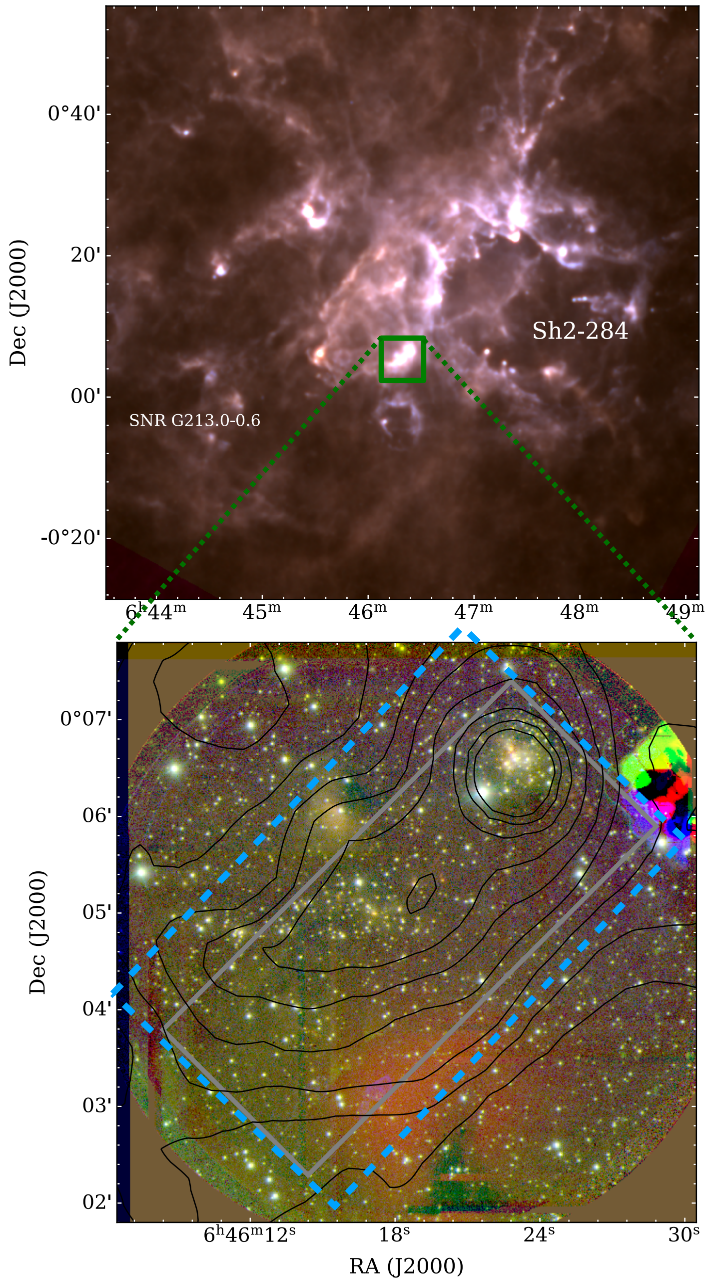

Figure 7.1: *(a)* Three color image of the Sh2-284 region constructed by combining *Herschel* SPIRE 250 μm (blue), 350 μm (green), and 500 μm (red) images. The HII region Sh2-284 and the supernova remnant G213.0-0.6 are labeled. The green dashed rectangle is the region shown in (b). *(b)* JHKs (blue, green, and red, respectively) color mosaic of a dense clump in Sh2-284 made with the Gemini FLAMINGOS-2 data (priv. comm.). The black contours illustrate the *Herschel* 500 μm emission. The contour levels start at 40 MJy/beam in steps of 20 MJy/beam. The region to be mapped by JWST is indicated with the grey rectangle while the proposed ALMA mapping region is shown in blue rectangle.

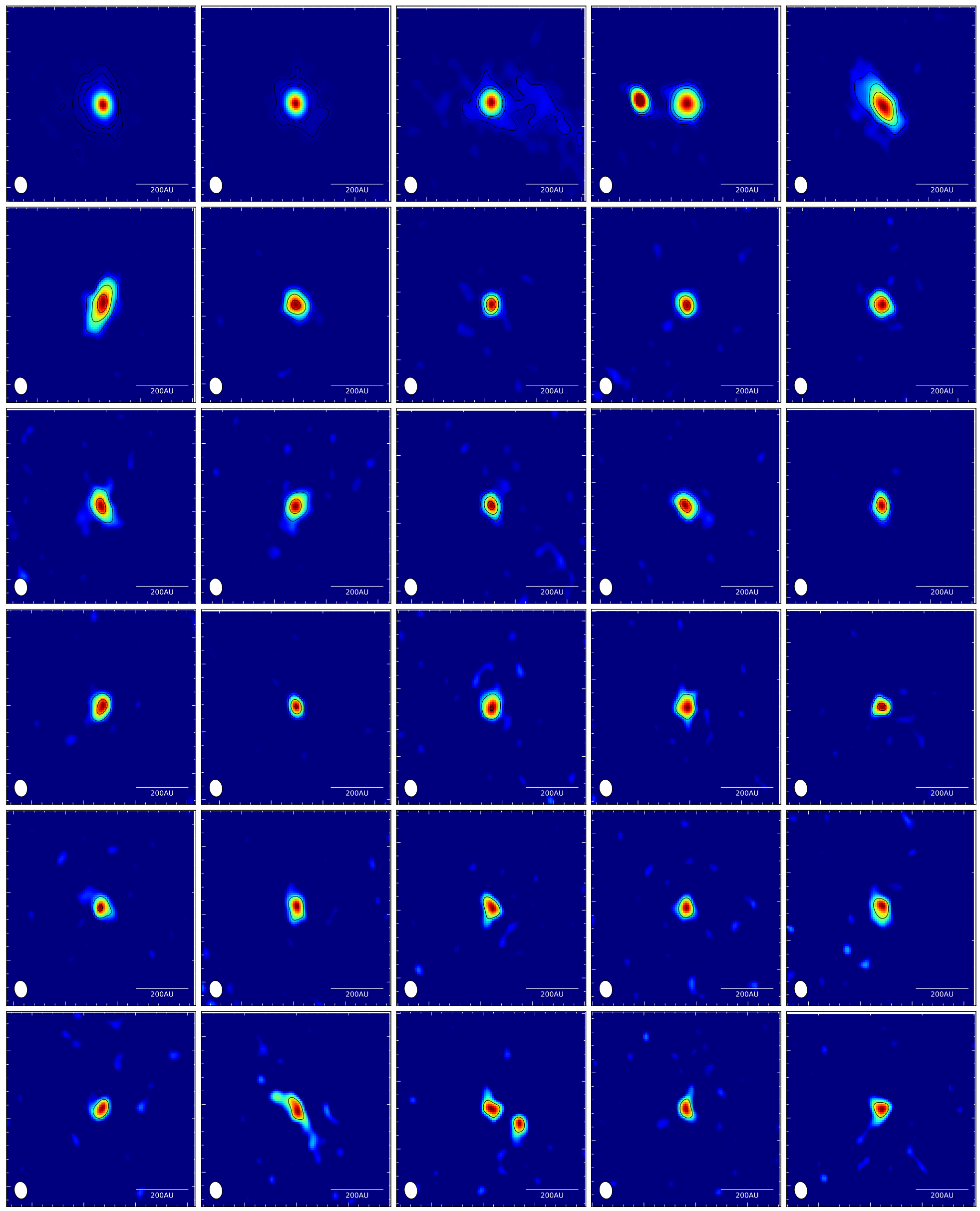

Figure 7.2: Composite of all point sources detected in Cycle 5 long baseline observations of G286. The contours levels are 4,8,12,20 times the local rms. The synthesized beam ($\sim 0.02''$) is shown in the lower left corner of each panel.

cluster members. For example, in the dense environment of the ONC and in σ Ori, the presence of young massive stars can have a dramatic effect: even a young population (∼1–3 Myr) like in the ONC has disks that are significantly less massive than their counterparts in Lupus (Eisner et al., 2018). It is still under debate how the feedback from massive protostars may effect properties of disks. Only recently are we able to unveil disk populations in more distant (>1 kpc) cluster environments using ALMA's capabilities (e.g., Busquet et al., 2019).

To investigate the properties of protostellar disks clustered environments, we conducted a high resolution survey using ALMA long baselines in Cycle 5 (PI: Cheng) towards the well studied target G286. With a spatial resolution of 20 mas and a sensitivity of 0.001 $M_{\odot}$, we have detected 32 point-like continuum sources within a single ALMA pointing, most of which are presumably tracing protostellar disks (see Figure 7.2). These disks have masses ranging from 0.006 to 0.3 $M_{\odot}$ assuming a temperature of 20 K. Besides a triple system near the center of the cluster, we also found two close binary systems (separation <200 AU) in our sample. The mass and radius distribution of the G286 disk population appears similar with those of protostellar disks in local regions like Orion (Cheng et al., in prep.). This study justifies the capabilities of ALMA to detect disk populations in distant regions with long base line configurations and we also plan to extend the study to other environments in the cluster studies mentioned above.

Appendix A

Appendix on the ALMA results of the G286 study

A.1 Properites of dense cores in G286

A.2 Spectra fitting of the core sample

Table A.1: Estimated physical parameters for 1.3 mm continuum cores

core	Ra (°)	Dec (°)	I_{peak} mJy beam^{-1}	S_ν (mJy)	M_c $M_\odot$	R_c (0.01pc)	Σ_c (g cm^{-2})	$n_{H,c}$ 10^6cm^{-3}
1	159.63383	-58.31897	60.14	420.29	80.24	3.63	4.068	11.71
2	159.63524	-58.32063	15.32	47.19	9.01	1.74	1.994	11.99
3	159.64045	-58.32043	11.20	34.13	6.52	1.92	1.179	6.41
4	159.64373	-58.32201	11.10	34.49	6.58	1.76	1.416	8.39
5	159.63973	-58.32167	11.06	69.42	13.25	2.71	1.209	4.66
6	159.63154	-58.31674	10.03	14.94	2.85	1.05	1.713	16.97
7	159.64328	-58.32094	9.43	29.04	5.54	1.68	1.308	8.12
8	159.63153	-58.31933	9.04	7.07	1.35	0.73	1.694	24.24
9	159.64708	-58.32530	8.73	20.00	3.82	1.43	1.244	9.07
10	159.63546	-58.32133	8.52	5.40	1.03	0.66	1.569	24.74
11	159.63163	-58.31720	8.38	3.23	0.62	0.51	1.574	32.16
12	159.63177	-58.31842	8.30	5.69	1.09	0.68	1.570	24.11
13	159.63045	-58.31534	8.29	14.93	2.85	1.34	1.061	8.28
14	159.63572	-58.31830	7.92	5.31	1.01	0.70	1.380	20.58
15	159.66617	-58.32238	7.90	13.47	2.57	1.56	0.710	4.77
16	159.63329	-58.32012	7.57	7.69	1.47	0.83	1.429	18.01
17	159.62948	-58.31815	7.32	6.79	1.30	0.81	1.325	17.11
18	159.66145	-58.32416	7.31	9.14	1.74	1.26	0.740	6.16
19	159.63511	-58.31409	6.87	62.38	11.91	3.09	0.833	2.82
20	159.63008	-58.31798	6.67	6.77	1.29	0.83	1.258	15.86
21	159.63146	-58.31591	6.52	12.32	2.35	1.23	1.045	8.90
22	159.64112	-58.31903	6.45	21.01	4.01	1.79	0.835	4.87
23	159.62922	-58.31562	6.31	14.14	2.70	1.36	0.975	7.49
24	159.63281	-58.31702	6.16	3.02	0.58	0.58	1.144	20.61
25	159.64503	-58.32397	6.12	13.86	2.65	1.44	0.856	6.23
26	159.63331	-58.31758	6.08	3.27	0.62	0.60	1.160	20.21
27	159.63752	-58.31851	6.06	8.92	1.70	1.13	0.896	8.30
28	159.64744	-58.32461	5.79	5.82	1.11	0.87	0.987	11.89
29	159.64422	-58.32289	5.28	4.33	0.83	0.79	0.875	11.52
30	159.64468	-58.32329	5.22	3.61	0.69	0.73	0.866	12.39
31	159.62961	-58.31916	5.13	6.24	1.19	0.91	0.968	11.16
32	159.63175	-58.32042	5.12	5.04	0.96	0.89	0.814	9.57
33	159.62987	-58.32137	4.50	12.73	2.43	1.45	0.769	5.53
34	159.64877	-58.32960	4.43	7.77	1.48	1.34	0.555	4.34
35	159.63103	-58.32106	4.16	2.89	0.55	0.71	0.724	10.60
36	159.62937	-58.32062	4.12	2.70	0.52	0.68	0.745	11.45
37	159.63976	-58.32276	4.02	8.54	1.63	1.45	0.516	3.71
38	159.63000	-58.32016	4.00	5.38	1.03	0.96	0.737	7.99
39	159.63706	-58.31779	3.92	3.64	0.70	0.87	0.614	7.38
40	159.62838	-58.32134	3.86	2.22	0.42	0.62	0.731	12.26
41	159.63368	-58.31362	3.81	5.43	1.04	1.07	0.610	5.98
42	159.62900	-58.31655	3.77	6.43	1.23	1.16	0.612	5.52
43	159.64888	-58.32789	3.77	5.20	0.99	1.08	0.568	5.49
44	159.64251	-58.31957	3.69	6.50	1.24	1.12	0.660	6.15
45	159.63874	-58.31673	3.64	8.38	1.60	1.44	0.514	3.72
46	159.67328	-58.32603	3.63	5.34	1.02	1.17	0.501	4.49
47	159.63370	-58.31682	3.61	1.91	0.36	0.62	0.643	10.93
48	159.64524	-58.32276	3.46	3.46	0.66	0.90	0.549	6.40
49	159.64849	-58.32509	3.43	3.86	0.74	0.91	0.599	6.90
50	159.63991	-58.32611	3.42	4.53	0.86	1.11	0.472	4.45
51	159.67270	-58.32482	3.38	9.11	1.74	1.56	0.477	3.20
52	159.64614	-58.32435	3.32	1.72	0.33	0.60	0.608	10.60
53	159.64167	-58.31675	3.28	18.88	3.60	2.32	0.449	2.03
54	159.64989	-58.32882	3.27	4.23	0.81	1.00	0.545	5.72
55	159.64225	-58.32300	3.23	1.51	0.29	0.58	0.571	10.29
56	159.63973	-58.32419	3.18	3.90	0.74	0.98	0.517	5.50
57	159.63632	-58.32468	3.12	3.64	0.69	1.01	0.460	4.78
58	159.65086	-58.32812	2.98	3.46	0.66	0.99	0.454	4.82
59	159.63897	-58.32474	2.94	5.99	1.14	1.23	0.502	4.25
60	159.63765	-58.32215	2.90	2.61	0.50	0.88	0.432	5.14

Table A.2: Continuation of Table A.1

core	Ra (°)	Dec (°)	I_{peak} mJy beam^{-1}	S_ν (mJy)	M_c $M_\odot$	R_c (0.01pc)	Σ_c (g cm^{-2})	$n_{H,c}$ 10^6cm^{-3}
61	159.63372	-58.31557	2.87	1.43	0.27	0.63	0.460	7.63
62	159.63206	-58.32324	2.84	1.69	0.32	0.68	0.467	7.17
63	159.64094	-58.30845	2.83	5.51	1.05	1.25	0.451	3.77
64	159.67355	-58.32445	2.70	1.74	0.33	0.72	0.425	6.13
65	159.64838	-58.31984	2.68	5.75	1.10	1.31	0.425	3.38
66	159.64144	-58.32606	2.67	4.48	0.86	1.17	0.419	3.75
67	159.63598	-58.31504	2.64	1.38	0.26	0.64	0.429	6.98
68	159.67361	-58.32257	2.61	1.94	0.37	0.76	0.431	5.93
69	159.64169	-58.32479	2.60	1.86	0.36	0.74	0.430	6.05
70	159.63645	-58.32321	2.56	6.47	1.23	1.39	0.424	3.18
71	159.63106	-58.32798	2.56	1.49	0.29	0.66	0.434	6.84
72	159.63961	-58.30961	2.55	1.86	0.36	0.75	0.427	5.99
73	159.63557	-58.31262	2.52	1.20	0.23	0.58	0.460	8.35
74	159.63958	-58.31643	2.49	1.31	0.25	0.62	0.436	7.35
75	159.64786	-58.32908	2.47	0.99	0.19	0.53	0.444	8.69
76	159.63002	-58.32627	2.39	1.16	0.22	0.59	0.423	7.46

Figure A.1: Spectra of $C^{18}O$(2-1), N_2D^+(3-2), DCO^+(3-2) and DCN(3-2) of 76 continuum cores shown in different colors. The core masses are labeled on the top left. For the spectrum with a peak flux greater than 4 σ we perform a gaussian fitting. The returned parameters (centroid velocity, velocity dispersion) for each line are displayed on the top left, in the same color as the corresponding line. The dashed vertical lines indicate the centroid velocity from line fitting (If there are multiple components for $C^{18}O$, only the main component (the one closer to other dense gas tracers, see text) is shown).

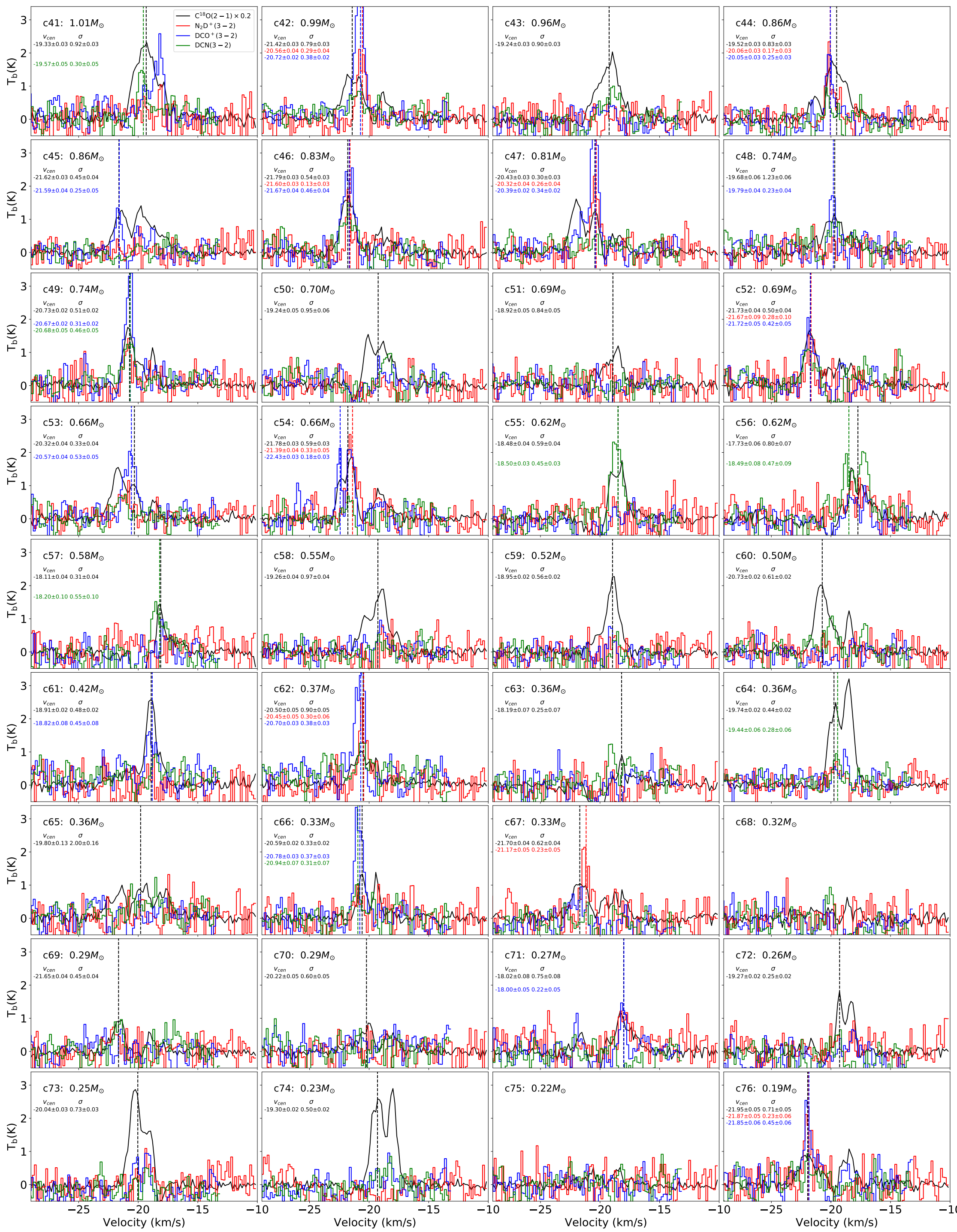

Figure A.2: Continuation of Figure A.1.

Appendix B

Appendix on the ALMA results of the Vela C region

B.1 N_2H^+(3-2) Spectral Fitting of of CR1c1

Under the assumption of constant excitation temperature among the hyperfine components of N_2H^+(3-2), the brightness temperature can be represented as:

$$T_B(v) = [J(T_{\text{ex}}) - J(T_{\text{bg}})][1 - \exp(-\tau(v))] \tag{B.1}$$

where $J(T) \equiv \frac{h\nu/k}{\exp(h\nu/[kT])-1}$ and $T_{\text{bg}} = 2.73$ K and the optical depths of the multiplets are

$$\tau(v) = \tau_{\text{tot}} \sum_i R_i \exp\left[-\frac{(v - v_i - v_{\text{sys}})^2}{2\sigma^2}\right], \tag{B.2}$$

where R_i and v_i are the relative intensity and velocity for the ith hyperfine component, respectively. Figure B.1 shows the best-fit for the N_2H^+(3-2) spectrum of CR1c1 and the returned best-fit parameters are displayed on the top right corner.

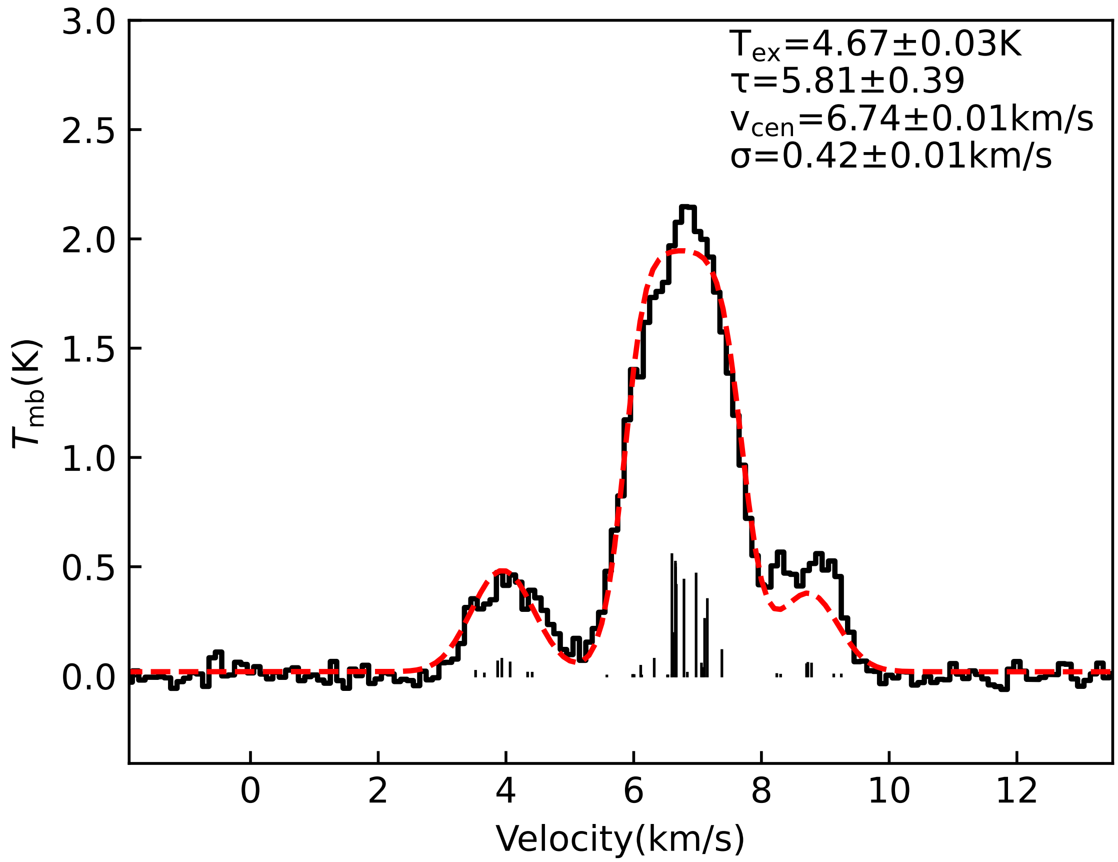

Figure B.1: N_2H^+(3âĂŞ2) spectrum of CR1c1 shown in black. The relative intensities of hyperfine components are shown underneath the spectrum, also in this velocity frame. The dashed red line shows the best-fit spectrum. The returned parameters from fitting (excitation temperature, opacity, centroid velocity, velocity dispersion) are displayed at the top right corner. The opacity listed is the total opacity by summing up the opacities of all the hyperfine components. The peak opacity in the best-fit case is slightly smaller ($\tau_{\mathrm{peak}} = 4.64$).

B.2 Infrared counterparts of the cores in Vela C CR1

In order to determine the evolutionary stages of dense cores, we searched for infrared counterparts from near-IR to far-IR bands. We retrieved the datasets in the archive including *Spitzer* 3.5, 4.5 μm, *WISE* 12, 22 μm and *Herschel* 70, 160, 250, 350, 500 μm maps. For each core we checked the infrared detection at the location and boundary defined by the ALMA 1.3 mm continuum to determine if there is a counterpart. Figure B.2 presents a zoom-in view of the infrared images for each core from 3.6 μm to 250 μm. The detection status is summarized in Figure B.2. Detections at $\lambda > 250$ μm are not included here since the spatial resolution is poor and hence it is in general difficult to disentangle the dense core from the surrounding material.

As can be seen, CR1c11 is presumably in a very early evolutionary stage, since it is undetected in all infrared wavelengths. The detection of CR1c10 is confused by another adjacent bright source. CR1c5 is not seen at wavelengths up to 70 μm, but is detected weakly at 160 μm and 250 μm. CR1c3, CR1c7 and CR1c8, which are detected at 70 μm but not shorter wavelengths, are slightly more evolved and should have formed protostars. The remaining sources, i.e., CR1c1, CR1c2, CR1c4, CR1c6 and CR1c9, are clearly seen in all infrared wavelengths and are thus expected to be of the latest protostellar evolutionary stages among the sample.

For infrared bands that show a counterpart, we also attempt aperture photometry, with the aperture radius fixed to be the equivalent radius of the size measured from 1.3 mm continuum. If the aperture radius is greater than half of the beam FWHM at the corresponding infrared band, then a flux measurement and associated uncertainty are reported. With this criterion only for CR1c1 are we able to measure the fluxes in all wavelengths. The aperture photometry is done following the method of Liu et al. (2020), i.e., we carry out a background subtraction using the median flux density in an annular region extending from one to two aperture radii, to remove general background and foreground contamination. The error bars are set to be the larger of either 10% of the background-subtracted flux density or the value of the estimated background flux density.

To better constrain the physical parameters of dense core, we used Zhang & Tan

(2018) radiative transfer models (ZT models hereafter) to fit the near-IR to millimeter SEDs towards CR1c1. The ZT model is a continuum radiative transfer model that describes the evolution of high- and intermediate-mass protostars with analytic and semi-analytic solutions based on the paradigm of the Turbulent Core model (see Zhang & Tan, 2018, for more details). The main free parameters in this model are the initial mass of the core M_c, the mass surface density of the clump that the core is embedded in $\Sigma_{\rm cl}$, the protostellar mass m_*, as well as other parameters that characterize the observational setup, i.e., the viewing angle i, and the level of foreground extinction A_V. Properties of different components in a protostellar core, including the protostar, disk, infall envelope, outflow, and their evolution, are also derived self-consistently from given initial conditions. Figure B.3 shows an example of the SED fit for CR1c1, with the parameters for the best five fitted models reported in Table B.2. The best fitted model indicates a source with a protostellar mass of 2 $M_\odot$ accreting at a rate of $3{\times}10^{-5}$ $\rm M_\odot \cdot\ yr^{-1}$ inside a core with an initial mass of 10 $M_\odot$ embedded in clumps with a mass surface density of 0.3 $\rm g \cdot cm^{-2}$. Note that the ZT models are designed for high-mass star formation and $M_c = 10\ M_\odot$ is the minimum core mass explored. Thus there could be other viable protostellar properties, e.g., starting with lower M_c, that have not been explored here.

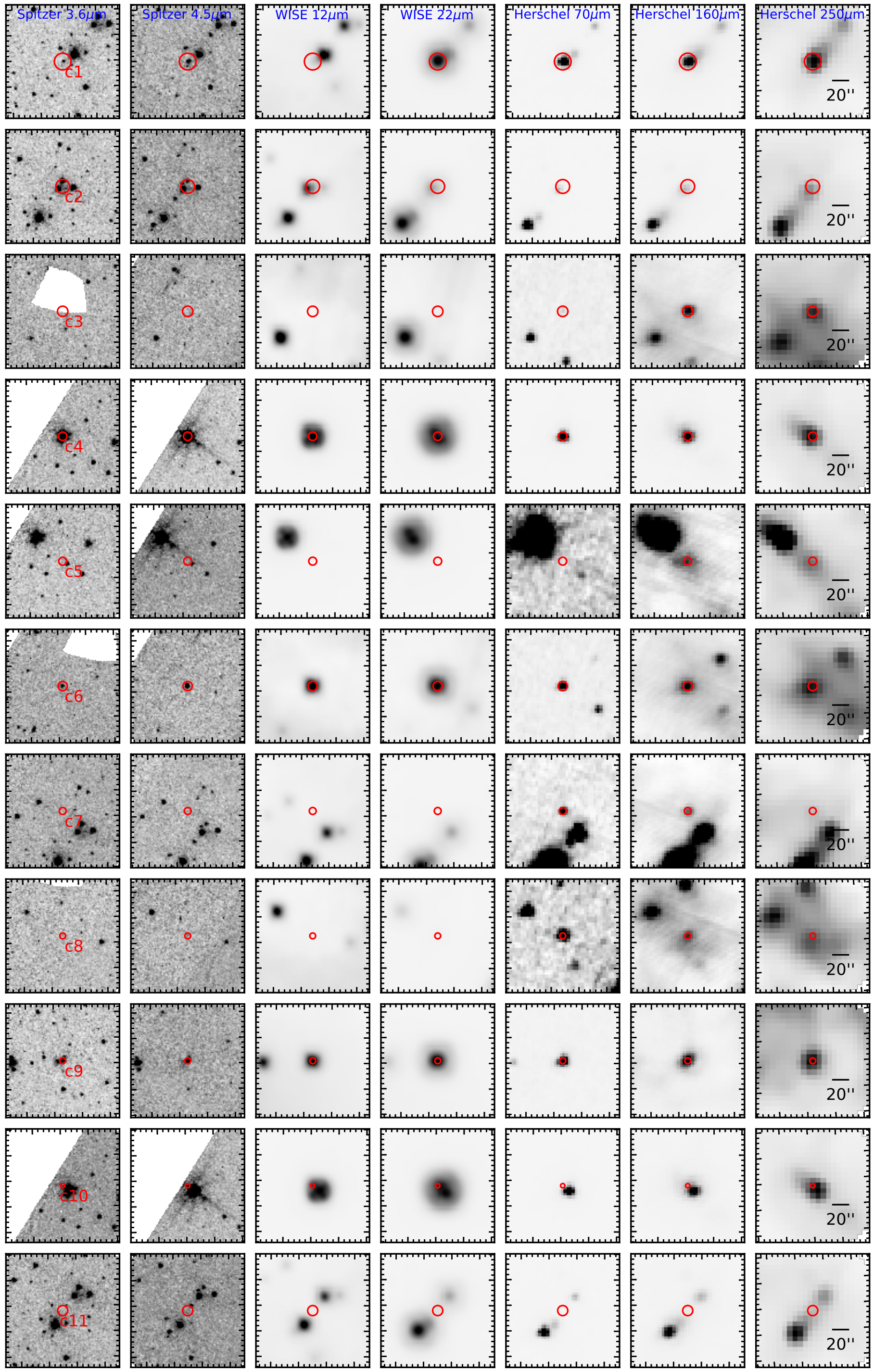

Figure B.2: Infrared counterparts of the cores in the CR1 region. From left to right we present the images of *Spitzer* 3.6/5.8 μm, *WISE* 12/22 μm and *Herschel* 70/160/250 μm, and from top to bottom the images are centered on the position from CR1c1 to CR1c11. The red circles indicate the position and size measured from the ALMA 1.3 mm continuum.

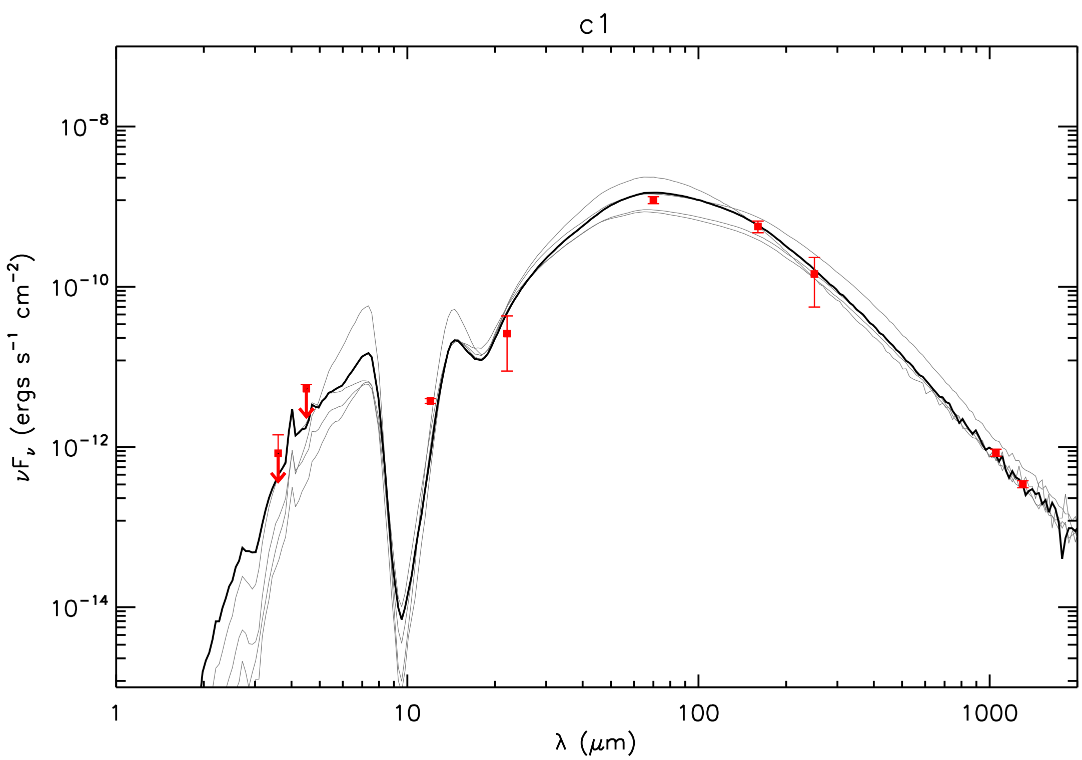

Figure B.3: Protostellar model fitting to the fixed aperture, background-subtracted SED of CR1c1 using the Zhang & Tan (2018) model grid. The best-fit model is shown with a solid black line and the next four best models are shown with solid gray lines. Flux values are those from Figure B.2. The fluxes in 1.05 mm and 1.3 mm are measured with the same background subtraction method, with values of 0.298 Jy and 0.147 Jy, respectively.

Table B.1: Photometry of cores in Vela C CR1 from 3.6 to 250 μm [a]

Core	Wavelength (μm)						
	3.6	5.8	12	22	70	160	250
c1	0.001 (0.0007)	0.008 (0.001)	0.015 (0.001)	0.190 (0.126)	28.189 (2.819)	30.207 (5.041)	11.992 (7.347)
c2	0.017 (0.002)	0.033 (0.003)	0.018 (0.009)	0.035 (0.031)	2.049 (0.205)	5.272 (1.721)	Y
c3	N	N	N	N	0.057 (0.006)	0.935 (0.646)	Y
c4	0.116 (0.012)	0.791 (0.079)	Y	Y	23.118 (3.764)	Y	Y
c5	N	N	N	N	N	Y	Y
c6	0.002 (0.0002)	0.016 (0.002)	Y	Y	0.499 (0.070)	Y	Y
c7	N	N	N	N	0.093 (0.027)	Y	Y
c8	N	N	N	N	Y	Y	Y
c9	0.003 (0.0003)	0.013 (0.001)	Y	Y	Y	Y	Y
c10	N	N	N	N	N	N	N
c11	N	N	N	N	N	N	N

[a] The fluxes are in unit of Jy. Cores with and without an counterpart at corresponding wavelengths are indicated with 'Y' and 'N', respectively. If an infrared counterpart is detected and the core has a radius greater than half of the FWHM beam at corresponding infrared wavelength, we perform an aperture photometry (see text for more details) and the measured fluxes and uncertainties are shown (instead of 'Y').

Table B.2: Parameters of the best five fitted models for CR1c1

Source	χ^2	M_c $M_\odot$	$\Sigma_{\rm cl}$ $\rm g \cdot cm^{-2}$	$R_{\rm core}$ pc	m_* $M_\odot$	$\theta_{\rm view}$ $^\circ$	A_V mag	$\theta_{\rm w,esc}$ $^\circ$	$m_{\rm disk}$ $M_\odot$	$r_{\rm disk}$ (AU)	$\dot{m}_{\rm disk}$ $M_\odot/yr$	$L_{\rm bol,iso}$ $L_\odot$	$L_{\rm bol}$ $L_\odot$
CR1c1	0.68	10	0.3	0.04	2.0	62	74.2	43	0.7	63	3.0×10^{-5}	2.8×10^{2}	0.7×10^{2}
$R_{\rm ap} = 9''.5$	1.80	10	0.1	0.07	0.5	71	79.6	20	0.2	37	0.8×10^{-5}	0.8×10^{2}	0.5×10^{2}
(0.04 pc)	2.46	10	0.1	0.07	1.0	68	82.2	31	0.3	63	1.0×10^{-5}	1.1×10^{2}	0.5×10^{2}
	5.07	20	0.1	0.10	0.5	86	72.9	13	0.2	32	1.0×10^{-5}	0.9×10^{2}	0.7×10^{2}
	6.27	10	1.0	0.02	4.0	65	184.5	59	1.3	76	7.7×10^{-5}	11.4×10^{2}	1.7×10^{2}

Load the bibliography, biographical sketch, and CV

References

Adams, F. C. 2010, ARA&A, 48, 47

Alves, J., Lombardi, M., & Lada, C. J. 2007, A&A, 462, L17

Andersen, M., Barnes, P. J., Tan, J. C., Kainulainen, J., & de Marchi, G. 2017a, ApJ, 850, 12

Andersen, M., Gennaro, M., Brandner, W., et al. 2017b, A&A, 602, A22

André, P., Belloche, A., Motte, F., & Peretto, N. 2007, A&A, 472, 519

André, P., Men'shchikov, A., Bontemps, S., et al. 2010, A&A, 518, L102

Andrews, S. M., Wilner, D. J., Zhu, Z., et al. 2016, ApJL, 820, L40

Ansdell, M., Williams, J. P., Manara, C. F., et al. 2017, AJ, 153, 240

Ansdell, M., Williams, J. P., van der Marel, N., et al. 2016, ApJ, 828, 46

Armitage, P. J. 2011, ARA&A, 49, 195

Aspin, C., & Reipurth, B. 2009, AJ, 138, 1137

Audard, M., Ábrahám, P., Dunham, M. M., et al. 2014, in Protostars and Planets VI, ed. H. Beuther, R. S. Klessen, C. P. Dullemond, & T. Henning, 387

Bally, J. 1982, ApJ, 261, 558

Baraffe, I., Chabrier, G., & Gallardo, J. 2009, ApJL, 702, L27

Baraffe, I., Homeier, D., Allard, F., & Chabrier, G. 2015, A&A, 577, A42

Barenfeld, S. A., Carpenter, J. M., Ricci, L., & Isella, A. 2016, ApJ, 827, 142

Barnes, P. J., Yonekura, Y., Ryder, S. D., et al. 2010, MNRAS, 402, 73

Barnes, P. J., Yonekura, Y., Fukui, Y., et al. 2011, ApJS, 196, 12

Bastian, N., Covey, K. R., & Meyer, M. R. 2010, ARA&A, 48, 339

Bate, M. R. 2005, MNRAS, 363, 363

—. 2009, MNRAS, 392, 590

—. 2012, MNRAS, 419, 3115

Battersby, C., Keto, E., Walker, D., et al. 2020, ApJS, 249, 35

Beltrán, M. T. 2015, Astrophysics and Space Science, 355, 283

Bergin, E. A., Alves, J., Huard, T., & Lada, C. J. 2002, ApJL, 570, L101

Bergin, E. A., & Tafalla, M. 2007, ARA&A, 45, 339

Bertoldi, F., & McKee, C. F. 1992, ApJ, 395, 140

Beuther, H., Walsh, A. J., Johnston, K. G., et al. 2017, A&A, 603, A10

Beuther, H., Zhang, Q., Greenhill, L. J., et al. 2004, ApJL, 616, L31

Bohlin, R. C., Savage, B. D., & Drake, J. F. 1978, ApJ, 224, 132

Bonnell, I. A., & Bate, M. R. 2006, MNRAS, 370, 488

Bonnell, I. A., Bate, M. R., Clarke, C. J., & Pringle, J. E. 2001, MNRAS, 323, 785

Bonnell, I. A., Larson, R. B., & Zinnecker, H. 2007, in Protostars and Planets V, ed. B. Reipurth, D. Jewitt, & K. Keil, 149

Bontemps, S., Motte, F., Csengeri, T., & Schneider, N. 2010, A&A, 524, A18

Bouvier, J., Grankin, K., Ellerbroek, L. E., Bouy, H., & Barrado, D. 2013, A&A, 557, A77

Boyden, R. D., & Eisner, J. A. 2020, ApJ, 894, 74

Bozhinova, I., Scholz, A., & Eislöffel, J. 2016, MNRAS, 458, 3118

Bressert, E., Bastian, N., Gutermuth, R., et al. 2010, MNRAS, 409, L54

Busquet, G., Fontani, F., Viti, S., et al. 2017, A&A, 604, A20

Busquet, G., Girart, J. M., Estalella, R., et al. 2019, A&A, 623, L8

Butner, H. M., Evans, Neal J., I., Harvey, P. M., et al. 1990, ApJ, 364, 164

Caratti o Garatti, A., Garcia Lopez, R., Scholz, A., et al. 2011, A&A, 526, L1

Carpenter, J. M., Hillenbrand, L. A., & Skrutskie, M. F. 2001, AJ, 121, 3160

Carrasco-González, C., Osorio, M., Anglada, G., et al. 2012, ApJ, 746, 71

Carrasco-González, C., Henning, T., Chandler, C. J., et al. 2016, ApJL, 821, L16

Caselli, P., Walmsley, C. M., Tafalla, M., Dore, L., & Myers, P. C. 1999, ApJL, 523, L165

Caselli, P., Walmsley, C. M., Zucconi, A., et al. 2002, ApJ, 565, 344

Catelan, M., Minniti, D., Lucas, P. W., et al. 2013, arXiv e-prints, arXiv:1310.1996

Chabrier, G. 2005, The Initial Mass Function: From Salpeter 1955 to 2005, ed. E. Corbelli, F. Palla, & H. Zinnecker, Vol. 327, 41

Chandrasekhar, S., & Fermi, E. 1953, ApJ, 118, 113

Cheng, Y., Tan, J. C., Liu, M., et al. 2018, ApJ, 853, 160

Cheng, Y., Tan, J. C., Liu, M., Lim, W., & Andersen, M. 2020, ApJ, 894, 87

Cioni, M. R. L., Kamath, D., Rubele, S., et al. 2013, A&A, 549, A29

Clark, P. C., Klessen, R. S., & Bonnell, I. A. 2007, MNRAS, 379, 57

Codella, C., Cabrit, S., Gueth, F., et al. 2014, A&A, 568, L5

Connelley, M. S., & Reipurth, B. 2018, ApJ, 861, 145

Contreras Peña, C., Naylor, T., & Morrell, S. 2019, MNRAS, 486, 4590

Contreras Peña, C., Lucas, P. W., Froebrich, D., et al. 2014, MNRAS, 439, 1829

Contreras Peña, C., Lucas, P. W., Minniti, D., et al. 2017a, MNRAS, 465, 3011

Contreras Peña, C., Lucas, P. W., Kurtev, R., et al. 2017b, MNRAS, 465, 3039

Cortes, P., Remijan, A., Biggs, A., et al. 2021, ALMA Cycle 8 2021 Technical Handbook, Additional contributors to this edition: Tim Bastian, Crystal Brogan, John Carpenter, Chinshin Chang, Geoff Crew, Paul Fisher, Misato Fukagawa, Melissa Hoffman, Chat Hull, Hugo Messias, Todd Hunter, Ruediger Kneissl, Andy Lipnicky, Ryan Loomis, Sergio Martin, Lynn Matthews, Luke Maud, Yusuke Miyamoto, Tony Mroczkowski, Hiroshi Nagai, Kouichiro Nakanishi, Masumi Shimojo, Richard Simon, Jeremy Thorley, MCarmen Toribio, Catarina Ubach, Catherine Vlahakis, Martin Zwaan, doi:10.5281/zenodo.4612218

Crapsi, A., Caselli, P., Walmsley, C. M., et al. 2005, ApJ, 619, 379

Crapsi, A., Caselli, P., Walmsley, M. C., & Tafalla, M. 2007, A&A, 470, 221

Csengeri, T., Bontemps, S., Wyrowski, F., et al. 2017, A&A, 600, L10

Cunningham, N. J., Moeckel, N., & Bally, J. 2009, ApJ, 692, 943

Czekala, I., Andrews, S. M., Jensen, E. L. N., et al. 2015, ApJ, 806, 154

Czekala, I., Andrews, S. M., Torres, G., et al. 2016, ApJ, 818, 156

Daniel, F., Cernicharo, J., Roueff, E., Gerin, M., & Dubernet, M. L. 2007, ApJ, 667, 980

De Buizer, J. M., Liu, M., Tan, J. C., et al. 2017, ApJ, 843, 33

Dore, L., Caselli, P., Beninati, S., et al. 2004, A&A, 413, 1177

Draine, B. T. 2011, Physics of the Interstellar and Intergalactic Medium

Dullemond, C. P., Juhasz, A., Pohl, A., et al. 2012, RADMC-3D: A multi-purpose radiative transfer tool, , , ascl:1202.015

Eislöffel, J., Smith, M. D., & Davis, C. J. 2000, A&A, 359, 1147

Eisner, J. A., Arce, H. G., Ballering, N. P., et al. 2018, ApJ, 860, 77

Elmegreen, B. G. 2007, ApJ, 668, 1064

Elmegreen, B. G., Efremov, Y., Pudritz, R. E., & Zinnecker, H. 2000, in Protostars and Planets IV, ed. V. Mannings, A. P. Boss, & S. S. Russell, 179

Emprechtinger, M., Caselli, P., Volgenau, N. H., Stutzki, J., & Wiedner, M. C. 2009, A&A, 493, 89

Enya, K., Yoshii, Y., Kobayashi, Y., et al. 2002, ApJS, 141, 45

Evans, Neal J., I., Dunham, M. M., Jørgensen, J. K., et al. 2009, ApJS, 181, 321

Fiege, J. D., & Pudritz, R. E. 2000, MNRAS, 311, 85

Findeisen, K., Hillenbrand, L., Ofek, E., et al. 2013, ApJ, 768, 93

Fischer, W. J., Safron, E., & Megeath, S. T. 2019, ApJ, 872, 183

Fissel, L. M., Ade, P. A. R., Angilè, F. E., et al. 2016, ApJ, 824, 134

—. 2019, ApJ, 878, 110

Fontani, F., Busquet, G., Palau, A., et al. 2015, A&A, 575, A87

Fontani, F., Commerçon, B., Giannetti, A., et al. 2018, A&A, 615, A94

Fontani, F., Palau, A., Caselli, P., et al. 2011, A&A, 529, L7

Fontani, F., Commerçon, B., Giannetti, A., et al. 2016, A&A, 593, L14

Foreman-Mackey, D., Hogg, D. W., Lang, D., & Goodman, J. 2013, Publications of the Astronomical Society of the Pacific, 125, 306

Foster, J. B., Cottaar, M., Covey, K. R., et al. 2015, ApJ, 799, 136

Frank, A., Ray, T. P., Cabrit, S., et al. 2014, in Protostars and Planets VI, ed. H. Beuther, R. S. Klessen, C. P. Dullemond, & T. Henning, 451

Friesen, R. K., Di Francesco, J., Shimajiri, Y., & Takakuwa, S. 2010, ApJ, 708, 1002

Friesen, R. K., Kirk, H. M., & Shirley, Y. L. 2013, ApJ, 765, 59

Fuente, A., Ceccarelli, C., Neri, R., et al. 2007, A&A, 468, L37

Fukui, Y., Ohama, A., Hanaoka, N., et al. 2014, ApJ, 780, 36

Furlan, E., Fischer, W. J., Ali, B., et al. 2016, ApJS, 224, 5

Furukawa, N., Dawson, J. R., Ohama, A., et al. 2009, ApJL, 696, L115

Giannini, T., Elia, D., Lorenzetti, D., et al. 2012, A&A, 539, A156

Ginsburg, A., & Mirocha, J. 2011, PySpecKit: Python Spectroscopic Toolkit, , , ascl:1109.001

Ginsburg, A., Goddi, C., Kruijssen, J. M. D., et al. 2017, ApJ, 842, 92

Gong, Y., Fang, M., Mao, R., et al. 2017, ApJL, 835, L14

Grankin, K. N., Melnikov, S. Y., Bouvier, J., Herbst, W., & Shevchenko, V. S. 2007, A&A, 461, 183

Guo, Z., Lucas, P. W., Contreras Peña, C., et al. 2020, MNRAS, 492, 294

Gutermuth, R. A., Megeath, S. T., Myers, P. C., et al. 2009, ApJS, 184, 18

Hacar, A., & Tafalla, M. 2011, A&A, 533, A34

Hacar, A., Tafalla, M., Kauffmann, J., & Kovács, A. 2013, A&A, 554, A55

Haisch, Karl E., J., Lada, E. A., & Lada, C. J. 2000, AJ, 120, 1396

Hartmann, L., Ballesteros-Paredes, J., & Heitsch, F. 2012, MNRAS, 420, 1457

Hartmann, L., & Burkert, A. 2007, ApJ, 654, 988

Hartmann, L., & Kenyon, S. J. 1996, ARA&A, 34, 207

Hennebelle, P., & Chabrier, G. 2008, ApJ, 684, 395

Hennemann, M., Motte, F., Schneider, N., et al. 2012, A&A, 543, L3

Henshaw, J. D., Caselli, P., Fontani, F., Jiménez-Serra, I., & Tan, J. C. 2014, MNRAS, 440, 2860

Henshaw, J. D., Caselli, P., Fontani, F., et al. 2013, MNRAS, 428, 3425

Herbig, G. H. 1977, ApJ, 217, 693

Herbig, G. H. 1989, in European Southern Observatory Conference and Workshop Proceedings, Vol. 33, European Southern Observatory Conference and Workshop Proceedings, 233–246

—. 2008, AJ, 135, 637

Hernandez, A. K., Tan, J. C., Caselli, P., et al. 2011, ApJ, 738, 11

Hernandez, A. K., Tan, J. C., Kainulainen, J., et al. 2012, ApJL, 756, L13

Hill, T., Motte, F., Didelon, P., et al. 2011, A&A, 533, A94

Holoien, T. W. S., Prieto, J. L., Stanek, K. Z., et al. 2014, ApJL, 785, L35

Hosek, Matthew W., J., Lu, J. R., Anderson, J., et al. 2019, ApJ, 870, 44

Johnstone, D., Wilson, C. D., Moriarty-Schieven, G., et al. 2000, ApJ, 545, 327

Kenyon, S. J., Hartmann, L. W., & Kolotilov, E. A. 1991, Publications of the Astronomical Society of the Pacific, 103, 1069

Kenyon, S. J., Hartmann, L. W., Strom, K. M., & Strom, S. E. 1990, AJ, 99, 869

Kirk, H., Johnstone, D., & Tafalla, M. 2007, ApJ, 668, 1042

Kirk, H., Myers, P. C., Bourke, T. L., et al. 2013, ApJ, 766, 115

Kirk, H., Pineda, J. E., Johnstone, D., & Goodman, A. 2010, ApJ, 723, 457

Kong, S., Caselli, P., Tan, J. C., Wakelam, V., & Sipilä, O. 2015, ApJ, 804, 98

Kong, S., Tan, J. C., Caselli, P., et al. 2017, ApJ, 834, 193

—. 2018, ApJ, 867, 94

—. 2016, ApJ, 821, 94

Kramer, C., Stutzki, J., Rohrig, R., & Corneliussen, U. 1998, A&A, 329, 249

Krause, M., Charbonnel, C., Decressin, T., Meynet, G., & Prantzos, N. 2013, A&A, 552, A121

Krause, M. G. H., Offner, S. S. R., Charbonnel, C., et al. 2020, SSRv, 216, 64

Kroupa, P., & Boily, C. M. 2002, MNRAS, 336, 1188

Krumholz, M. R., Leroy, A. K., & McKee, C. F. 2011, ApJ, 731, 25

Krumholz, M. R., & McKee, C. F. 2005, ApJ, 630, 250

Krumholz, M. R., Bate, M. R., Arce, H. G., et al. 2014, in Protostars and Planets VI, ed. H. Beuther, R. S. Klessen, C. P. Dullemond, & T. Henning, 243

Kunz, M. W., & Mouschovias, T. C. 2009, MNRAS, 399, L94

Kusune, T., Sugitani, K., Nakamura, F., et al. 2016, ApJL, 830, L23

Lacy, J. H., Knacke, R., Geballe, T. R., & Tokunaga, A. T. 1994, ApJL, 428, L69

Lada, C. J., & Adams, F. C. 1992, ApJ, 393, 278

Lada, C. J., & Lada, E. A. 2003, ARA&A, 41, 57

Lada, C. J., Margulis, M., & Dearborn, D. 1984, ApJ, 285, 141

Lawrence, A., Warren, S. J., Almaini, O., et al. 2007, MNRAS, 379, 1599

Lee, C.-F. 2020, A&A Rv, 28, 1

Lim, W., Tan, J. C., Kainulainen, J., Ma, B., & Butler, M. J. 2016, ApJL, 829, L19

Liu, M., Tan, J. C., Cheng, Y., & Kong, S. 2018, ApJ, 862, 105

Liu, M., Tan, J. C., De Buizer, J. M., et al. 2020, ApJ, 904, 75

Liu, T., Zhang, Q., Kim, K.-T., et al. 2016, ApJ, 824, 31

Lu, X., Zhang, Q., Liu, H. B., et al. 2018, ApJ, 855, 9

Ma, B., Tan, J. C., & Barnes, P. J. 2013, ApJ, 779, 79

Mangum, J. G., & Shirley, Y. L. 2015, Publications of the Astronomical Society of the Pacific, 127, 266

Marks, M., Kroupa, P., Dabringhausen, J., & Pawlowski, M. S. 2012, MNRAS, 422, 2246

Marsh, K. A., Kirk, J. M., André, P., et al. 2016, MNRAS, 459, 342

Martins, F., Hillier, D. J., Paumard, T., et al. 2008, A&A, 478, 219

Massi, F., Lorenzetti, D., & Giannini, T. 2003, A&A, 399, 147

Massi, F., Weiss, A., Elia, D., et al. 2019, A&A, 628, A110

Matzner, C. D., & McKee, C. F. 2000, ApJ, 545, 364

McKee, C. F., & Tan, J. C. 2003, ApJ, 585, 850

Meyer, M. R., Calvet, N., & Hillenbrand, L. A. 1997, AJ, 114, 288

Miettinen, O., Harju, J., Haikala, L. K., & Juvela, M. 2012, A&A, 538, A137

Millar, T. J., Bennett, A., & Herbst, E. 1989, ApJ, 340, 906

Minniti, D., Lucas, P. W., Emerson, J. P., et al. 2010, Nature, 15, 433

Molinari, S., Swinyard, B., Bally, J., et al. 2010, A&A, 518, L100

Molinari, S., Schisano, E., Elia, D., et al. 2016, A&A, 591, A149

Motte, F., Andre, P., & Neri, R. 1998, A&A, 336, 150

Motte, F., Zavagno, A., Bontemps, S., et al. 2010, A&A, 518, L77

Müller, H. S. P., Schlöder, F., Stutzki, J., & Winnewisser, G. 2005, Journal of Molecular Structure, 742, 215

Murphy, D. C., & May, J. 1991, A&A, 247, 202

Nakamura, F., & Li, Z.-Y. 2007, ApJ, 662, 395

Nakamura, F., Sugitani, K., Tanaka, T., et al. 2014, ApJL, 791, L23

Negueruela, I., Simón-Díaz, S., Lorenzo, J., Castro, N., & Herrero, A. 2015, A&A, 584, A77

Netterfield, C. B., Ade, P. A. R., Bock, J. J., et al. 2009, ApJ, 707, 1824

Nishiyama, S., Tamura, M., Hatano, H., et al. 2009, ApJ, 696, 1407

Ohashi, S., Sanhueza, P., Chen, H.-R. V., et al. 2016, ApJ, 833, 209

Oliveira, C. M., Hébrard, G., Howk, J. C., et al. 2003, ApJ, 587, 235

Ossenkopf, V., & Henning, T. 1994, A&A, 291, 943

Ostriker, E. C., Stone, J. M., & Gammie, C. F. 2001, ApJ, 546, 980

Padoan, P., & Nordlund, Å. 2002, ApJ, 576, 870

—. 2004, ApJ, 617, 559

—. 2011, ApJ, 730, 40

Padoan, P., Nordlund, Å., Kritsuk, A. G., Norman, M. L., & Li, P. S. 2007, ApJ, 661, 972

Pagani, L., Daniel, F., & Dubernet, M. L. 2009, A&A, 494, 719

Palla, F., & Stahler, S. W. 1993, ApJ, 418, 414

Parihar, P., Messina, S., Distefano, E., Shantikumar, N. S., & Medhi, B. J. 2009, MNRAS, 400, 603

Peretto, N., Fuller, G. A., André, P., et al. 2014, A&A, 561, A83

Persson, S. E., Geballe, T. R., Simon, T., Lonsdale, C. J., & Baas, F. 1981, ApJL, 251, L85

Pineda, J. E., Rosolowsky, E. W., & Goodman, A. A. 2009, ApJL, 699, L134

Qian, L., Li, D., & Goldsmith, P. F. 2012, ApJ, 760, 147

Raga, A. C., & Biro, S. 1993, MNRAS, 264, 758

Ragan, S. E., Henning, T., Beuther, H., Linz, H., & Zahorecz, S. 2015, A&A, 573, A119

Reid, M. A., & Wilson, C. D. 2005, ApJ, 625, 891

Reipurth, B., & Aspin, C. 2010, in Evolution of Cosmic Objects through their Physical Activity, ed. H. A. Harutyunian, A. M. Mickaelian, & Y. Terzian, 19–38

Rice, T. S., Wolk, S. J., & Aspin, C. 2012, ApJ, 755, 65

Rodón, J. A., Beuther, H., & Schilke, P. 2012, A&A, 545, A51

Rosolowsky, E. W., Pineda, J. E., Kauffmann, J., & Goodman, A. A. 2008, ApJ, 679, 1338

Sadavoy, S. I., Di Francesco, J., Bontemps, S., et al. 2010, ApJ, 710, 1247

Salji, C. J., Richer, J. S., Buckle, J. V., et al. 2015, MNRAS, 449, 1769

Salpeter, E. E. 1955, ApJ, 121, 161

Santiago-García, J., Tafalla, M., Johnstone, D., & Bachiller, R. 2009, A&A, 495, 169

Santos, F. P., Ade, P. A. R., Angilè, F. E., et al. 2017, ApJ, 837, 161

Scholz, A. 2012, MNRAS, 420, 1495

Scholz, A., & Eislöffel, J. 2005, A&A, 429, 1007

Scholz, A., Froebrich, D., & Wood, K. 2013, MNRAS, 430, 2910

Scholz, A., Mužić, K., & Geers, V. 2015, MNRAS, 451, 26

Scoville, N. Z., Sargent, A. I., Sanders, D. B., et al. 1986, ApJ, 303, 416

Seifried, D., Sánchez-Monge, Á., Walch, S., & Banerjee, R. 2016, MNRAS, 459, 1892

Seth, A. C., Greenhill, L. J., & Holder, B. P. 2002, ApJ, 581, 325

Sheehan, P. D., Wu, Y.-L., Eisner, J. A., & Tobin, J. J. 2019, ApJ, 874, 136

Shu, F. H., Adams, F. C., & Lizano, S. 1987, ARA&A, 25, 23

Skinner, S. L., Sokal, K. R., Megeath, S. T., et al. 2009, ApJ, 701, 710

Snell, R. L., & Bally, J. 1986, ApJ, 303, 683

Sokolov, V., Wang, K., Pineda, J. E., et al. 2018, A&A, 611, L3

Soler, J. D., Ade, P. A. R., Angilè, F. E., et al. 2017, A&A, 603, A64

Stetson, P. B. 1996, Publications of the Astronomical Society of the Pacific, 108, 851

Stojimirović, I., Snell, R. L., & Narayanan, G. 2008, ApJ, 679, 557

Tan, J. C. 2015, in EAS Publications Series, Vol. 75-76, EAS Publications Series, 105–114

Tan, J. C., Kong, S., Butler, M. J., Caselli, P., & Fontani, F. 2013, ApJ, 779, 96

Tan, J. C., Krumholz, M. R., & McKee, C. F. 2006, ApJL, 641, L121

Tanaka, K. E. I., Tan, J. C., & Zhang, Y. 2017, ApJ, 835, 32

Terquem, C., Eislöffel, J., Papaloizou, J. C. B., & Nelson, R. P. 1999, ApJL, 512, L131

Testi, L., & Sargent, A. I. 1998, ApJL, 508, L91

Tobin, J. J., Chandler, C. J., Wilner, D. J., et al. 2013, ApJ, 779, 93

Tobin, J. J., Sheehan, P. D., Megeath, S. T., et al. 2020, ApJ, 890, 130

Torrelles, J. M., Gómez, J. F., Rodríguez, L. F., et al. 1998, ApJ, 505, 756

Trinidad, M. A., Rodríguez, T., & Rodríguez, L. F. 2009, ApJ, 706, 244

Turner, B. E. 2001, ApJS, 136, 579

van Kempen, T. A., Longmore, S. N., Johnstone, D., Pillai, T., & Fuente, A. 2012, ApJ, 751, 137

Walker-Smith, S. L., Richer, J. S., Buckle, J. V., et al. 2013, MNRAS, 429, 3252

Walsh, A. J., Myers, P. C., & Burton, M. G. 2004, ApJ, 614, 194

Walsh, A. J., Myers, P. C., Di Francesco, J., et al. 2007, ApJ, 655, 958

Walther, D. M., & Geballe, T. R. 2019, ApJ, 875, 153

Walther, D. M., Robson, E. I., Aspin, C., & Dent, W. R. F. 1993, ApJ, 418, 310

Warner, B. 2003, Cataclysmic Variable Stars, doi:10.1017/CBO9780511586491

Whitney, B. A., Wood, K., Bjorkman, J. E., & Cohen, M. 2003, ApJ, 598, 1079

Williams, J. P., & Cieza, L. A. 2011, ARA&A, 49, 67

Williams, J. P., de Geus, E. J., & Blitz, L. 1994, ApJ, 428, 693

Wilson, T. L., & Rood, R. 1994, ARA&A, 32, 191

Wolk, S. J., Rice, T. S., & Aspin, C. 2013, ApJ, 773, 145

Yamaguchi, N., Mizuno, N., Saito, H., et al. 1999, Publications of the Astronomical Society of Japan, 51, 775

Yuan, J., Li, J.-Z., Wu, Y., et al. 2018, ApJ, 852, 12

Zhang, Q., Wang, K., Lu, X., & Jiménez-Serra, I. 2015, ApJ, 804, 141

Zhang, Y., & Tan, J. C. 2018, ApJ, 853, 18

Zhang, Y., Tan, J. C., & Hosokawa, T. 2014, ApJ, 788, 166

Zhou, S., Evans, Neal J., I., Koempe, C., & Walmsley, C. M. 1993, ApJ, 404, 232

Zhu, Z., Hartmann, L., Gammie, C., & McKinney, J. C. 2009, ApJ, 701, 620